

**Department of Electrical and Computer Engineering**

**Enhanced Control of DFIG-Based Wind Power Plants  
to Comply with the International Grid Codes**

**Mansour Mohseni**

**This thesis is presented for the Degree of  
Doctor of Philosophy  
of  
Curtin University**

**February 2011**

## **Declaration**

To the best of my knowledge and belief this thesis contains no material previously published by any other person except where due acknowledgment has been made.

This thesis contains no material which has been accepted for the award of any other degree or diploma in any university.

Signature: .....

Date: .....

## **ABSTRACT**

A review of the latest international grid codes shows that large wind power plants are stipulated to not only ride-through various fault conditions, but also exhibit adequate active and reactive power responses during the fault period in order to support the network stability. In particular, modern grid codes require wind power plants to: (1) ride-through various voltage sag and swell conditions, (2) inject reactive current into the grid during the fault period, and (3) attain swift active power restoration after the fault clearance. This thesis proposes a transient control scheme for DFIG-based wind power plants to comply with these requirements.

In the first part of this thesis, the latest regulations enforced on large wind power plants are studied and compared. This study identifies the most stringent regulations defined by the international grid codes, to be further investigated in the following chapters. In the second part of this thesis, extensive simulation studies are carried out to examine the transient response of DFIG-based wind turbines under various symmetrical and asymmetrical fault conditions. Supplementary theoretical analyses are also presented to justify the observations made in the time-domain simulations results. For the first time, the impacts of phase-angle jump, voltage recovery process and sag parameters on the DFIG response are explored. The results of this study can assist researcher to identify the difficulties that hinder successful fault ride-through response of DFIG-based wind turbines, as requested by the international grid codes.

In the third part of the thesis, an enhanced hysteresis-based current regulator (referred to as VBHCR) is proposed to be implemented in the rotor-side and grid-side converters of DFIG-based wind turbines. The main advantages of this current regulator are very fast transient response, simple control structure and insensitivity to the machine parameters variations. Simulation results show that on one hand the VBHCR has very good steady-state performance and on the other hand, it presents very fast/robust tracking response. Therefore, the DFIG equipped the proposed current regulator can fulfill the most stringent low-voltage ride-through requirements imposed by the international grid codes, i.e., those stipulated by the Australian grid code. In the fourth part of the thesis, a new hybrid current control scheme is

introduced to enhance both low and high voltage ride-through capabilities of DFIG-based wind turbines. The proposed control scheme uses the standard PI current regulators under steady-state conditions but upon a voltage sag or swell occurrence, the supervisory control unit transfers the switching strategy of the rotor-side and grid-side converters to the hysteresis-based method. The VBHCR remains in action until the oscillation in the rotor current and dc-link voltage of DFIG suppress below the safety limit and then, the PI current regulator are activated through a re-initialization process.

Finally, the conventional vector control scheme of DFIG-based wind power plants is modified to fulfill the regulations imposed on the active and reactive power responses of wind farms subject to various faults. New design strategies are suggested and their corresponding  $P$ - $Q$  capability curves are thoroughly studied. Simulations results show that the proposed control scheme can meet the Australian regulations as the most demanding grid code. The best design strategy, with enhanced active and reactive power responses, permits the rotor-side and grid-side converters of DFIG to be temporarily overloaded during the fault period and also exploits the free capacity of the GSC to inject further reactive power to the grid. As a result, the active power generation of DFIG-based wind power plant can be retained during the fault period while its reactive power injection capacity of DFIG is also increased to further support the grid.



## **DEDICATION**

*To my parents, Abbas and Mina, for their endless love and support throughout my life, and to my dearest friend, Yosef, who left this world sooner than I can believe.*

## **ACKNOWLEDGMENT**

I would like to express my special thanks to my supervisor, Professor Syed M. Islam, for his invaluable advice, guidance and support all throughout my PhD studies. I am also greatly indebted to my co-supervisor, Associate Professor Mohammad A.S. Masoum who has been abundantly helpful and offered me constant assistance and encouragement during the course of my study. Finally, financial support from Curtin University through Curtin International Postgraduate Research Scholarship (CIPRS) is gratefully acknowledged. Last but not least, I wish to express my love and gratitude to my family and friends for their endless support and love.

# TABLE OF CONTENTS

<b>Abstract</b> .....	<b>ii</b>
<b>Table of Contents</b> .....	<b>vi</b>
<b>Chapter 1. Introduction</b> .....	<b>1</b>
1.1 Statement of the problem .....	1
1.2 Literature review .....	2
1.2.1 Control schemes for DFIG-based WTs.....	2
1.2.2 Transient response of DFIG under fault conditions.....	4
1.2.3 LVRT and HVRT capabilities of DFIG-based WTs .....	5
1.2.4 Reactive power control of DFIG during faults .....	6
1.3 Research objectives.....	7
1.4 Thesis structure .....	8
1.5 List of publications .....	9
<b>Chapter 2. Comparison of the international grid codes for large wind power plants</b> .....	<b>13</b>
2.1 Introduction .....	13
2.2 Current global wind power capacity .....	14
2.2.1 Wind power capacity in Australia.....	16
2.3 Review of the grid connection requirements .....	17
2.4 Comparison of the international grid codes .....	21
2.4.1 LVRT requirement.....	21
2.4.2 HVRT requirement.....	22
2.4.3 Regulations on the $P$ - $Q$ responses of WPPs during faults.....	23
2.4.4 Regulations on the extended range of the frequency variations ..	24
2.4.5 Active power control and frequency regulation.....	25
2.4.6 Reactive power control and voltage regulation.....	26
2.5 Discussions and future trends .....	28
2.5.1 Global harmonization of the grid codes.....	28
2.5.2 Future trends in the grid code regulations.....	29
2.6 Conclusions .....	30

<b>Chapter 3. Transient Response of DFIG-based WTs under symmetrical and asymmetrical voltage sags .....</b>	<b>31</b>
3.1 Introductions .....	31
3.2 Characteristic and classification of voltage sags .....	33
3.2.1 Symmetrical faults and phase-angle jump .....	33
3.2.2 Asymmetrical faults and sag classification .....	35
3.2.3 Fault clearance and voltage recovery process .....	36
3.3 Modelling and control of DFIG-based WTs .....	39
3.3.1 Machine modelling.....	41
3.3.2 GSC modelling .....	41
3.3.3 Vector control of the RSC.....	42
3.3.4 Vector control of the GSC .....	47
3.4 Theoretical analysis of the DFIG response .....	48
3.4.1 DFIG operation under normal operation conditions .....	49
3.4.2 DFIG operation under symmetrical sag conditions .....	50
3.4.3 DFIG operation under asymmetrical sag conditions.....	52
3.5 Simulation results .....	55
3.5.1 Symmetrical faults and voltage recovery process.....	55
3.5.2 Asymmetrical faults and phase-angle jump .....	60
3.5.3 Influences of sag parameters on the DFIG response .....	65
3.6 Conclusions .....	69
<b>Chapter 4. Enhanced hysteresis-based current regulators in the vector control of DFIG-based WTs.....</b>	<b>71</b>
4.1 Introduction .....	71
4.2 Discrete formulation of the RSC voltage vector .....	71
4.3 The proposed vector control scheme for DFIG .....	73
4.3.1 Grid-flux-orientation .....	73
4.3.2 Vector control of the DFIG-based WTs.....	74
4.4 Principles and control structure of the proposed VBHCR.....	76
4.4.1 Principle of the proposed VBHCR implemented in the RSC .....	77
4.4.2 Control structure of the proposed VBHCR.....	78
4.4.3 Variable hysteresis bands.....	81

4.5	Simulation results .....	82
4.5.1	Operation under changing wind speed.....	86
4.5.2	Comparison of the steady-state performances .....	90
4.5.3	Comparison of the transient performances .....	93
4.6	Conclusions .....	97
<b>Chapter 5. Low and high voltage ride-through of DFIG-based WTs using hybrid current controlled converters .....</b>		<b>99</b>
5.1	Introduction .....	99
5.2	Proposed hybrid current control scheme .....	100
5.2.1	Conventional PI current controller.....	100
5.2.2	Vector-based hysteresis current controller.....	101
5.2.3	Transition mechanism .....	104
5.2.4	Re-initialization process.....	106
5.3	Simulation results .....	106
5.3.1	Operation under symmetrical voltage sag.....	107
5.3.2	Operation under asymmetrical voltage sag .....	110
5.3.3	Operation under voltage swell .....	112
5.3.4	Reactive power support.....	113
5.4	Conclusions .....	115
<b>Chapter 6. Active and reactive power responses of DFIG-based WPPs following faults in the grid.....</b>		<b>116</b>
6.1	Introduction .....	116
6.2	<i>P-Q</i> capability curves of DFIG-based WPP .....	117
6.2.1	Maximum current capacity of converters .....	117
6.2.2	<i>P-Q</i> capability curve of DFIG – Design 1 .....	118
6.2.3	<i>P-Q</i> capability curve of DFIG – Design 2 .....	119
6.2.4	<i>P-Q</i> capability curve of DFIG – Design 3 .....	121
6.3	Proposed DFIG control scheme .....	122
6.4	Simulation results .....	125
6.4.1	Impacts of the DFIG operation on the nearby grid .....	133
6.5	Conclusions .....	134

<b>Chapter 7. Conclusions</b> .....	<b>136</b>
7.1 Contributions .....	138
7.2 Future works .....	139
<b>References</b> .....	<b>140</b>
<b>Appendix A – Voltage sag classification</b> .....	<b>145</b>
<b>Appendix B – Simulation parameters</b> .....	<b>147</b>
<b>Appendix C – The UTSP system</b> .....	<b>149</b>
<b>Appendix D – Paper in IEEE Transaction on Power Electronics</b> .....	<b>154</b>

## TABLE OF FIGURES

Figure 2-1 Global installed wind power capacity from 2001 to 2010. -----	15
Figure 2-2 Installed wind power capacity in Australia from 2001 to 2010. -----	16
Figure 2-3 Wind power capacity in different states of Australia at the end of 2009. -----	17
Figure 2-4 Spanish LVRT requirement. -----	18
Figure 2-5 Australian HVRT requirement.-----	19
Figure 2-6 German reactive power injection requirement. -----	19
Figure 2-7 Irish active power regulation curve. -----	25
Figure 2-8 German reactive power regulation curve.-----	20
Figure 2-9 Spanish regulation on the reactive current injection. -----	23
Figure 2-10 Danish active power curtailment regulation.-----	26
Figure 2-11 German regulation on the reactive power control. -----	27
Figure 3-1 Voltage divider model ( <i>italic</i> figures are the real parameters for Horns- Rev wind farm). -----	33
Figure 3-2 Voltage sag magnitude vs. phase-angle jump for various impedance angles. -----	35
Figure 3-3 Schematic diagram of a DFIG-based WT-----	39
Figure 3-4 The overall model and control structure of a DFIG-based WT -----	40
Figure 3-5 Equivalent circuit of the DFIG system -----	42
Figure 3-6 Phasor diagram of DFIG in the synchronous stator-flux frame. -----	43
Figure 3-7 Field-oriented vector control of the RSC and GSC-----	44
Figure 3-8 PI current regulator in the RSC-----	46
Figure 3-9 PI current regulator in the GSC -----	48
Figure 3-10 Equivalent circuit of the machine viewed in the rotor frame. -----	49
Figure 3-11 Initial value of $V_m$ with and without phase-angle jump.-----	52
Figure 3-12 Voltage decomposition into the positive and negative sequence components, with and without phase-angle jump (sag types C and D). -----	54
Figure 3-13 Schematic circuit diagram of the simulated network. -----	55
Figure 3-14 Supply voltage (zoomed at the fault clearance instant) under three-phase faults (type A) with different possibilities of the voltage recovery. -----	57
Figure 3-15 Rotor current under three-phase faults (type A) with different possibilities of the voltage recovery. -----	58

Figure 3-16 Dc-link voltage under three-phase faults (type A) with different possibilities of the voltage recovery. -----	59
Figure 3-17 Influence of the fault current angle, $\psi$ , on the dc-link voltage during the voltage recovery process. -----	60
Figure 3-18 Three-phase supply voltage under 60% type C voltage sag with different initial point-on-wave instants, without and with phase-angle jump. -----	62
Figure 3-19 Rotor current and dc-link voltage under 60% type C voltage sag with different initial point-on-wave instants, without and with phase-angle jump. --	63
Figure 3-20 Stator flux trajectory under 60% type C voltage sag with different initial point-on-wave instants, without and with phase-angle jump. -----	64
Figure 3-21 Influence of the initial point-on-wave instant on the transient response of DFIG-based WTs subjected to phase-to-phase faults (sag types C and D). ----	67
Figure 3-22 Influence of the sag depth on the transient response of DFIG-based WTs subjected to different types of faults. -----	68
Figure 4-1 (a) Power circuit of the RSC, (b) Discrete representation of the RSC output voltage vector. -----	72
Figure 4-2 Phasor diagrams for vector control of DFIG; (a) conventional stator-flux-oriented frame, (b) Proposed grid-flux-oriented frame-----	74
Figure 4-3 Schematic diagram of the proposed grid-flux-oriented vector control scheme for DFIG-based WT -----	76
Figure 4-4 Derivatives of the current error vectors when the $\mathbf{V}_r^{r*}$ vector is located in Sector I -----	78
Figure 4-5 (a) Implementation of the proposed VBHCR in the RSC (b) Four-level hysteresis comparator -----	79
Figure 4-6 The RSC switching pattern for the proposed VBHCR -----	80
Figure 4-7 Circuit diagram of a PWM-VSI supplying an induction motor -----	82
Figure 4-8 $\mathbf{I}_{\alpha-\beta}$ , $\mathbf{V}_n$ , $I_a$ , and $V_{ab}$ for small counter-emf voltage ( $R=0.7 \Omega$ , $L=5 \text{ mH}$ , and $e_o=25 \angle 60^\circ$ )-----	84
Figure 4-9 $\mathbf{I}_{\alpha-\beta}$ , $\mathbf{V}_n$ , $I_a$ , and $V_{ab}$ for large counter-emf voltage ( $R=0.7 \Omega$ , $L=5 \text{ mH}$ , and $e_o=75 \angle 60^\circ$ )-----	84
Figure 4-10 (a) Number of switching with small counter-emf voltage (b) Number of switching with large counter-emf voltage -----	85



Figure 4-11 Circuit diagram of the simulated network -----	85
Figure 4-12 Simulation results as the wind speed varies from 7.8 m/s to 10.5 m/s. -	88
Figure 4-13 Detailed operation of the proposed VBHCR subjected to a step-change in $I_{rd}$ (zero voltage vectors are shown as $V_0$ for the sake of clarity). -----	89
Figure 4-14 Harmonic spectrum of the DFIG output current with (a) PI current regulator (b) Proposed equidistant-band VBHCR -----	91
Figure 4-15 Number of switching in phase 'a' of the RSC when DFIG operates with (a) $s = 0.05$ and (b) $s = 0.25$ . -----	92
Figure 4-16----- Stator voltage, rotor current, dc-link voltage, and electrical torque for DFIG under a three-phase fault with: (a) the standard PI current regulator, (b) the proposed current regulator. -----	95
Figure 4-17 Stator voltage, rotor current, dc-link voltage, and electrical torque for DFIG under a two-phase fault with: (a) the standard PI current regulator, (b) the proposed current regulator. -----	96
Figure 4-18 Synchronization signal estimated by the conventional PLL system and the proposed UTSP under single-phase-to-ground fault -----	97
Figure 5-1 Schematic diagram of the proposed hybrid current controller. -----	102
Figure 5-2 Practical implementation of the VBHCR in the RSC. -----	103
Figure 5-3 Schematic current-time diagram of the proposed hybrid current controller under voltage sag conditions. -----	105
Figure 5-4 Stator voltage, rotor current, dc-link voltage, and electrical torque for DFIG under symmetrical voltage sag with: (a) the standard PI current controller, (b) the proposed hybrid current controller. -----	109
Figure 5-5 Detailed operation of the hybrid current controller at the fault instant -	110
Figure 5-6 Stator voltage, rotor current, dc-link voltage, and electrical torque for DFIG under asymmetrical voltage sag with: (a) the standard PI current controller, (b) the proposed hybrid current controller. -----	111
Figure 5-7 Stator voltage, rotor current, dc-link voltage, and electrical torque for DFIG under a symmetrical voltage swell of 1.3 PU with: (a) the standard PI current controller, (b) the proposed hybrid current controller. -----	113
Figure 5-8 Reactive power support of the PI and the proposed hybrid controller according to Australian regulations for a 50% type A voltage sag -----	114

Figure 6-1 $P$ - $Q$ response of DFIG with control Design 1: (a) quadrature components of the rotor current, (b) active and reactive powers of the stator. -----	119
Figure 6-2 $P$ - $Q$ response of DFIG with control Design 2: (a) quadrature components of the rotor current, (b) active and reactive powers of the stator. -----	120
Figure 6-3 $P$ - $Q$ response of GSC with control Design 3: (a) quadrature components of the GSC, (b) active and reactive powers of the GSC. -----	122
Figure 6-4 Schematic diagram of the proposed control scheme.-----	124
Figure 6-5 Circuit diagram of the simulated network.-----	125
Figure 6-6 Tracking performance of the proposed UTSP: (a) three-phase grid voltage, (b) estimated magnitudes of the sequence components, (c) tracking error signals, and (d) extracted synchronizing phase-angle. -----	126
Figure 6-7 Conventional controller: (a) quadrature components of the rotor current (b) DFIG active and reactive powers. -----	128
Figure 6-8 Design 1: (a) quadrature components of the rotor current (b) DFIG active and reactive powers.-----	129
Figure 6-9 Design 2: (a) quadrature components of the rotor current (b) DFIG active and reactive powers.-----	129
Figure 6-10 Design 3: (a) quadrature components of the rotor current (b) DFIG active and reactive powers.-----	130
Figure 6-11 Components of the GSC current with (a) Design 1 (b) Design 2. -----	131
Figure 6-12 Voltage profile at B120 and B25 during the fault with different control designs adopted in the DFIG-based WPP. -----	132
Figure 6-13 Rotor speed with Design 1 (dashed line) and Design 2 (solid line).---	132
Figure 6-14 Active and reactive power of DFIG with the conventional design strategy (dashed line) and the proposed Design 3 (solid line). -----	133
Figure 6-15 (a) Voltage at B25, (b) shaft speed of the induction generator, and (c) electromagnetic torque of the induction generator with the conventional design strategy (dashed line) or with the proposed Design 3 (solid line).-----	134

## TABLE OF TABLES

Table 2-1 Continental share of the global wind power capacity at the end of 2009--	15
Table 2-2 Wind power capacity for different countries in 2009 -----	15
Table 2-3 LVRT requirements outlined in the international grid codes.-----	22
Table 2-4 HVRT requirements in international grid codes. -----	22
Table 2-5 Frequency limits in international grid codes.-----	25
Table 2-6 Power Factor limits in international grid codes. -----	27
Table 3-1 Voltage sag propagation through the wind farm -----	36
Table 3-2 Voltage recovery sequences and fault clearance instants-----	38
Table 3-3 Decomposition of the supply voltage into positive/negative sequences---	64
Table 3-4 Summarized simulation results for different types of faults -----	67
Table 4-1 Three-phase switching states, RSC output voltage vector, and their respective x-y components -----	72
Table 4-2 Switching table for the proposed VBHCR-----	79
Table 4-3 Average switching frequency in the RSC and GSC -----	93

## **List of abbreviations**

DFIG	Doubly fed induction generator
GSC	Grid-side converter
HVRT	High voltage ride-through
LVRT	Low voltage ride-through
PCC	Point of common coupling
PI	Proportional-integral
PLL	Phase locked loop
RSC	Rotor-side converter
SVM	Space vector modulation
TSO	Transmission system operator
UTSP	Unified three-phase signal processor
VBHCR	Vector-based hysteresis current regulator
VSC	Voltage source converter
WPP	Wind power plant
WT	Wind turbine

## List of symbols

### *Vectors and parameters*

$\mathbf{V}, \mathbf{I}, \Phi$	Voltage, current, and flux vectors.
$\omega, \theta$	Angular speed and angle.
$L_m, L_\sigma$	Mutual and leakage inductances.

### *Subscripts*

$s, r, g$	Stator, rotor, grid.
$\alpha\text{-}\beta$	Stationary frame.
$x\text{-}y$	Rotor frame.
$d\text{-}q$	Synchronous grid-flux frame.

### *Superscripts*

$a, s, r, e$	Arbitrary, stationary, rotor, and grid-flux reference frames.
*	Reference value for the controllers.
$\wedge$	Complex conjugate operator

---

## **Chapter 1. Introduction**

### **1.1 STATEMENT OF THE PROBLEM**

In the last decade there has been growing public opposition toward the installation of conventional electricity generation systems due to their huge CO<sub>2</sub> emissions, contributing to the global warming problems. Moreover, fossil energy resources are very limited while the global energy demand is expected to tremendously increase in the near future, especially in newly industrializing countries such as China and India. Owing to these facts, the global energy market has recently witnessed an increasing tendency for the integration of renewable energy resources into the electrical networks. Among different sources of renewable energy, wind power has proven as the most dominant option due to its mature technology, reduced costs and minimal environmental impacts.

Renewable energy resources, including wind power, are naturally intermittent and fluctuating. Therefore, their steady state and transient responses in the power systems are different to those of the conventional power generation systems. In the past, the penetration levels of wind power in electric networks were extremely small as compared to the conventional generation units; hence, grid connection requirements for wind power plants were not included in the international grid codes. However, as wind power penetration started to reach to a significantly high level in many countries such as Denmark, Germany and Spain, the impacts of WPPs on the existing power system became more crucial and TSOs had to redefine their grid codes and impose more stringent regulations on large WPPs [1].

In modern grid codes, WPPs are requested to not only remain connected to the power network under various types of grid disturbances, but also contribute to the network stability support as do conventional generation units. That is, recent international grid codes stipulate WPPs to act as active components in the grid and take over the control tasks that are traditionally assigned to conventional power plants [1]-[4]. A

review of the international grid codes shows that large WPPs are nowadays required to (1) ride-through various types of voltage sag and swell conditions, (2) provide reactive power support during the fault period, and (3) swiftly restore their active power production after the fault clearance.

This thesis proposes an enhanced control scheme for DFIG-based WPPs to comply with the most stringent regulations enforced by the international grid codes. The variable-speed DFIG technology is selected because it is the most dominated and well-recognized technology employed around [1]. The key contribution of this study is an integrated control and protection scheme that can fulfil all regulations imposed on the transient response of large WPPs, whereas previous studies have focused individually on the low and high voltage ride-through response of DFIG, its reactive power support capability or its active power control.

## **1.2 LITERATURE REVIEW**

In this section, a comprehensive literature review is carried out to (1) evaluate different control schemes adopted for DFIG-based WTs, (2) study the transient response of DFIG-based WTs under various fault conditions, (3) examine different approaches proposed to enhance LVRT and HVRT capabilities of DFIG-based WTs, and (4) investigate active and reactive power response of DFIG-based WPPs in compliance with the international grid code regulations.

### **1.2.1 Control schemes for DFIG-based WTs**

Field-oriented vector control schemes, using rotational transformations and linear PI controllers, is the most popular control technique used in DFIG-based WTs [5]-[8]. In this double-closed-loop approach, the outer power control loop is employed to attain an independent control over the active and reactive power outputs of the machine. In cascade, synchronous-frame PI current regulators are used to control the output current of the RSC and GSC [5].

However, there are two main drawbacks associated with implementing standard PI current regulators in the vector control of DFIG-based WTs: the discrete operation of the converters is not taken into account and the DFIG is modelled as a linear time-invariant system. Based on these simplifying assumptions, the gains of PI

compensators are tuned using the small signal analysis of the nonlinear equations describing the DFIG behaviour [9]-[10]. Therefore, the system formulation is only valid around a specific operating point and it will deviate if the operating point of the system changes largely. This will lead to the non-optimal response of the overall control scheme for a wide operation range. This problem is especially pertinent to wind generator applications where the machine is required to properly function at the operating points largely deviated from the nominal condition, e.g., voltage sag or swell conditions requested in modern grid codes. Hence, the gains of the PI compensators must be carefully tuned with a trade-off between maintaining the system stability over the whole operation range and achieving adequate dynamic response under transient conditions. This will noticeably degrade the transient performance of the overall vector control scheme and jeopardize the stability of the controller under changing operation conditions.

Nonlinear control approaches, such as direct torque/power control methods (DTC/DPC), are proposed to address the above-mentioned problems [11]-[13]. In these techniques, the current control loop is eliminated and the control signal is directly selected from a look-up table, aimed to control both active and reactive powers during one sample time. The main advantages of DTC/DPC methods are their enhanced transient response, minimum use of the machine parameters, and non-complex control structure. However, there is always a significant torque/power ripple due to the high bandwidth of the controller, the switching frequency of converters varies depending on the operating conditions, and the controller performance may deteriorate during the machine starting and low speed operations. Modified methods have been proposed to overcome these problems [14]-[16], but extra drawbacks were introduced, such as the inclusion of additional PI controllers [14], reduced robustness to the machine parameters variations [14]-[15], and complex online calculation requirements [16].

Based on the same principle used in DTC/DPC, Xu et al. have suggested replacing the conventional PI current regulator with a non-linear predictive current regulator [19]. This method is fully compatible with digital control platforms and shows very fast transient response and excellent robustness under various operation conditions. However, its performance depends on the accurate estimation of the machine



parameters and it suffers from a complex control structure.

Other nonlinear current controllers are recently proposed in the literature [17]-[18]. Barros et al. suggested a new control strategy based on the system states optimal feedback [17]. The proposed strategy includes the nonlinear rotor current control and provides a methodology to compute the controller parameters. Simulation results are presented to compare the transient performance of the proposed control scheme with the standard PI current regulators. It is shown that not only are the rotor current overshoots reduced significantly, but also faster damping of the terminal voltage oscillations can be achieved. The main drawback of the proposed control strategy is that the control design process involves trial and error in order to select the value of the linearized system parameters. As a result, there is no systematic approach to assure that the most optimal control tuning is achieved.

Finally in [18], the conventional indirect current-mode controller (CMC) in the RSC is replaced with a novel direct CMC. Simulation results show that the proposed current regulator improves the tracking capability of the rotor-side controller, which, in turn, enhances the LVRT capability of the DFIG-based WTs. The proposed method proves to be very effective under both systematically and asymmetrical faults; however, it increases the complexity of the control scheme as it combines positive and negative sequence controllers to manage the machine during unbalance faults.

### **1.2.2 Transient response of DFIG under fault conditions**

The transient response of DFIG-based WTs under various fault conditions has been investigated in [20]-[41]. Initial works were mainly aimed to develop reduced-order models for DFIG-based WTs in dynamic and stability studies [20]-[25]. This type of model is restricted to the fundamental frequency response of the DFIG under three-phase faults. However, it was shown that asymmetrical faults (e.g., phase-to-phase faults) are more likely to occur and have more detrimental impacts on DFIGs [27]-[29]. Therefore, recent works focused on the detailed transient response and LVRT capability of DFIG-based WTs under asymmetrical sag conditions [30]-[41]. The main shortcoming is that most of the reported studies examine very limited sag conditions, which cannot adequately represent the broad range of LVRT regulations

specified in international grid codes. The gap becomes even more evident in [38] where simulation studies are carried out for the voltage sag conditions that cannot be practically experienced at the DFIG terminals. Moreover, it is known that not only the magnitude of the voltage but also its phase-angle can be affected by faults in the grid. This issue is especially crucial for wind farms directly connected to the distribution systems or offshore wind farms with AC submarine cables [42]. Detrimental impacts of this phenomenon, referred to as “phase-angle jump”, on the operation of DFIG-based WPPs have not been explored in the literature. These shortcomings are briefly discussed in [42], but no theoretical or simulation studies were presented to support the work. Finally, the effect of voltage recovery process and sag parameters on DFIG-based WT are not addressed in the literature.

### 1.2.3 LVRT and HVRT capabilities of DFIG-based WTs

Voltage sag have been reported as the most common power quality disturbance experienced in industrial power systems and for this reason, the LVRT requirements are included in the majority of grid codes around the world [3]. Therefore, extensive research has been so far conducted on the LVRT capability enhancement of DFIG-based WTs [20]-[42]. On the contrary, the HVRT behaviour of DFIG-based WTs is an emerging issue that has not been adequately explored in the literature [43].

The early researches on the voltage sag behaviour of DFIG-based WTs identified two major problems that need close attention: (1) overcurrents in the rotor winding and (2) overvoltages in the dc-link capacitor [27]-[29]. The initial solution to protect the RSC from destructive overcurrents was to place short-circuit at the rotor slip ring terminals via the so called crowbars and then, disconnect the DFIG from the grid [20]-[21]. This solution was only acceptable when the wind power constituted an insignificant part of the system generation. Therefore, other approaches have been recently proposed to increase the LVRT capacity of DFIGs.

The LVRT strategies proposed in the literature can be divided into three main categories: (1) placing active crowbars at the RSC terminals [24]-[26], (2) installing additional converters/dynamic resistors in the DFIG structure [30]-[33], and (3) modifying the conventional control schemes [34]-[40]. Active crowbars have proven to be effective under balanced fault conditions, but they cannot assist the DFIG to

ride-through deep asymmetrical sags such as those observed under phase-to-phase faults. The second approach can improve the LVRT capability of DFIG-based WTs under various sag conditions, but increases the overall cost and complexity of the system. Finally, modified control schemes were proposed as the most successful LVRT strategy. These control techniques are typically structured in two main steps: decomposition of the voltage/current signals into the symmetrical components and regulation of the rotor current in two opposite rotating frames, using dual PI current regulators [36]-[40]. However, it is shown that these control schemes have very limited control bandwidth and suffer from stability problems (mainly due to the sluggish transient response of PI current regulators) [19],[39]. This will result in degraded transient response of DFIG under voltage sag conditions and as a result, strict LVRT regulations cannot be fulfilled.

In [41], the issue of overvoltage in the dc-link capacitor of DFIG-based WTs is addressed by adopting a modified control scheme in the GSC. The proposed GSC control loop includes a feedback from the instantaneous rotor power, but still uses the standard PI current controllers. Therefore, it suffers from the sluggish transient response and limited LVRT capability similar to [36] and [37].

#### **1.2.4 Reactive power control of DFIG during faults**

Modern grid codes stipulate WPPs to contribute to the network stability support as do conventional generation units. That is, WPPs must be able to inject reactive current during the fault period in order to enhance the voltage stability limits of the network. Also, the active power generation of the WPP must swiftly restore to the prefault value after the fault clearance in order to assist the short-term frequency stability of the system. There have been only a few papers published on these issues and there are still some gaps and ambiguities.

In [44] and [45], dynamic simulation studies are conducted to illustrate the voltage control action of DFIG-based WTs under small disturbances. However, the GSC operation is not taken into account and the system response to large disturbance (e.g., short-circuit faults) is not investigated. In [46], the GSC control scheme is modified to attain different voltage control objectives, but the reactive power capability of the stator winding is neglected. In [47], coordinated control of the RSC and GSC is

proposed to fully exploit the reactive power control capability of DFIG-based WTs. The voltage control responses under varying wind speed and large disturbances are also studied. However, this study assumes that the DFIG-based WPP can successfully ride-through fault conditions and provide the reactive power support for the post-fault period. The validity of this assumption cannot be guaranteed under severe fault conditions. Finally in [48], a modified control scheme is presented to utilize the free capacity of the RSC for reactive power generation/absorption when the WPP works below the maximum wind speed. It is shown that the proposed control approach can help the system operation under various operating conditions. However, the DFIG response during fault period is neglected and it is presumed that the WPP can ride-through severe sag conditions. Similar shortcomings are observed in the works that are reported on the active power response of DFIG-based WPPs [49]-[51].

### **1.3 RESEARCH OBJECTIVES**

The ultimate objective of this research is to develop an enhanced transient control scheme for DFIG-based WPPs to fulfil the international grid code requirements. In particular, the DFIG-based WPP must ride-through various voltage sag and swell conditions, provide reactive power support during the fault period, and exhibit fast active power restoration after the fault clearance. Accordingly, the objectives of this thesis can be summarized as follows:

- 1- compare the latest versions of international grid codes in order to identify the most stringent regulations enforced on large WPPs.
- 2- study the transient response of DFIG-based WTs under various fault conditions. It will help researchers to identify the difficulties that hinder successful LVRT response of DFIG-based WTs under various symmetrical and asymmetrical voltage sags, considering phase-angle jump, voltage recovery and sag parameters.
- 3- replace the standard PI current regulators in the RSC and GSC of DFIG-based WTs with new variable-band vector-based hysteresis current regulators. The steady-state and transient performances of the proposed

- current regulator must be examined according to the IEEE limits and operating constraints of the semi-conductor switches used in the converters.
- 4- proposes a novel hybrid current control scheme that integrates the optimal steady-state performance of PI current regulators and very fast transient response of the proposed hysteresis-based current regulator under various voltage sag and swell conditions.
  - 5- test the low and high voltage ride-through capabilities of DFIG-based WTs with the proposed current control schemes, under the most stringent LVRT and HVRT regulations outlined in the international grid codes.
  - 6- modify and improve the conventional control scheme of DFIG-based WPPs in compliance with the reactive power support and active power recovery regulations requested in the international grid codes.

## 1.4 THESIS STRUCTURE

This thesis includes seven chapters. Chapter 2 presents a comparative study on the latest international grid code regulations imposed on large WPPs. This study concentrates mainly on the transient response requirements stipulated by the international TSOs, namely LVRT and HVRT curves, reactive current injection and active power restoration. Chapter 2 identifies the most stringent regulations defined by international grid codes that will be examined in later chapters through extensive simulations.

Chapter 3 examine the transient response of DFIG-based WTs under various symmetrical and asymmetrical voltage sags. Detrimental impacts of phase-angle jump are investigated through theoretical analysis as well as time-domain simulation studies. Also, the operational constraints of circuit breakers and their impacts on the voltage sag recovery process are studied. Finally, the influences of voltage sag parameters on the transient response of DFIG-based WTs are examined. In Chapter 3, the main difficulties associated with successful LVRT response of DFIG are identified to be tackled in the following chapters.

In Chapter 4, an enhanced hysteresis-based current regulator is proposed for implementation in the RSC and GSC of DFIG-based WTs. The operating principles

of the proposed VBHCR are thoroughly investigated, followed by exploring its control structure. Finally, extensive time-domain simulation studies are conducted to evaluate its steady-state and transient performances. It is shown that the proposed VBHCR can fulfil the LVRT requirements outlined in the Australian grid code.

In Chapter 5, a novel hybrid current control scheme is proposed to enhance the LVRT and HVRT capabilities of DFIG-based WTs in compliance with the international grid codes. The proposed hybrid current controller uses the PI current controller under normal operating conditions and VBHCRs for protecting DFIG under fault conditions. Simulations results show that the proposed hybrid current controller can fulfil the LVRT and HVRT requirements outlined in the Spanish and Australian grid codes, respectively.

Chapter 6 presents modified control schemes for DFIG-based WPPs to provide the reactive power support and active power restoration stipulated by the international grid codes. Different design strategies are proposed to enhance the  $P$ - $Q$  response of DFIG under various fault conditions. Extensive simulation studies are also carried out to illustrate the WPP response according to the Australian grid code and its positive impacts on the nearby grid.

Finally, conclusions and proposals for future research are presented in Chapter 7.

## 1.5 LIST OF PUBLICATIONS

The main content of the thesis is based on the following published/submitted articles:

- **Journal papers:**

**J1.** M Mohseni and S Islam, "A New Vector-Based Hysteresis Current Control Scheme for Three-Phase PWM Voltage-Source Inverters," *IEEE Trans. on Power Electronics*, vol. 25, no. 9, pp. 2299-2309, Sep. 2010.

**J2.** M Mohseni, S Islam, and M.A.S. Masoum, "Enhanced Hysteresis-Based Current Regulators in Vector Control of DFIG Wind Turbines," *IEEE Trans. on Power Electronics*, vol. 26, no. 1, pp. 223-234, Jan. 2011.

**J3.** M Mohseni, S Islam, and M.A.S. Masoum, "Impacts of Symmetrical and Asymmetrical Voltage Sags on DFIG-Based Wind Turbines Considering

---

Phase-Angle Jump, Voltage Recovery, and Sag Parameters,” *IEEE Trans. on Power Electronics*, vol. 26, no. 5, pp. 1587-1598, May 2011.

**J4.**        **M Mohseni**, S Islam, and M.A.S. Masoum, “Variable-Band Vector-Based Hysteresis Current Regulator for DFIG Wind Turbines,” *Electrical Power System Research*, vol. 81, no. 5, pp. 1151-1160, May 2011.

**J5.**        **M Mohseni**, M.A.S. Masoum, and S Islam “Fault Ride-Through Capability Enhancement for Doubly Fed Induction Wind Generators,” Accepted for publication in *IET Renewable Power Generation*.

**J6.**        **M Mohseni**, M.A.S. Masoum, and S Islam “Low and High Voltage Ride-Through of DFIG Wind Turbines using Hybrid Current Controlled Converters,” Accepted for publication in *Electrical Power System Research*.

**J7.**        M Mesbah, **M Mohseni**, S Islam, and M Masoum, “A New Approach for Three Phase Rectification with Minimum Measurement and Computational Requirements for Wind Power Applications,” Accepted for publication in *Australian Journal of Electrical & Electronics Engineering*.

**J8.**        **M Mohseni**, M Mesbah, S Islam, and M.A.S. Masoum, “Vector-Based Hysteresis Current Regulator for DFIG Wind Turbines under Non-Ideal Supply Conditions,” Accepted for publication in *Australian Journal of Electrical & Electronics Engineering*.

**J9.**        **M Mohseni**, S Islam, and M.A.S. Masoum, “Improved Modeling of DFIG-Based Wind Farms under Symmetrical and Asymmetrical Voltage Dips with Phase-Angle Jump,” In the second review in *Australian Journal of Electrical & Electronics Engineering*.

**J10.**       **M Mohseni** and S Islam “Transient Control of DFIG-Based Wind Power Plant in Compliance with the Australian Grid Code,” In the second revision for publication in *IEEE Trans. on Power Electronics*.

**J11.**       **M Mohseni** and S Islam “Enhanced Vector Control of DFIG-Based Wind Turbines to Comply with the Australian Grid Code Requirements,” Submitted to the *Australian Journal of Electrical & Electronics Engineering*.

**J12.**     **M Mohseni** and S Islam “Technical connection requirements for large wind power plants- comparison, future trend, and compliant technologies” to be submitted to *Renewable and Sustainable Energy Review*.

- **Conference Papers:**

**C1.**     **M Mohseni** and S Islam “International regulations on the transient response of large wind power plants,” Accepted in the proceeding of *IEEE IECON 2011*, Melbourne, Australia.

**C2.**     **M Mohseni**, M.A.S Masoum, and S Islam “Low voltage ride-through of DFIG wind turbines complying with the Western-Power Grid Code in Australia,” Accepted in the proceeding of *IEEE PES General Meeting 2011*, Detroit, USA.

**C3.**     **M Mohseni** and S Islam “Comparing technical requirement for large wind farms,” Accepted in the proceeding of *IEEE PES General Meeting 2011*, Detroit, USA.

**C4.**     **M Mohseni**, M.A.S Masoum, and S Islam “Emergency Control of DFIG-Based Wind Turbines to Comply with New European Grid Code Requirements,” Accepted for publication in the proceeding of *IEEE Innovative Smart Grid Technologies 2011*, Anaheim, USA.

**C5.**     **M Mohseni**, S Islam, and M.A.S. Masoum, “Low Voltage Ride-Through Requirements at the PCC versus Wind Generator Terminals,” in the proceeding of *AUPEC 2010*, Christchurch, New Zealand.

**C6.**     **M Mohseni**, M.A.S. Masoum, and S Islam “Robust Sensorless Decoupled P-Q Control of Doubly Fed Induction Generators for Wind Power Applications,” in the proceeding of *AUPEC 2010*, Christchurch, New Zealand.

**C7.**     **M Mohseni**, M Mesbah, S Islam, and M.A.S Masoum, “A Novel Current Regulator for DFIG Wind Turbines with Enhanced Performance under Unbalanced Supply Voltage Condition,” in the proceedings of *IEEE PES General Meeting 2010*, Minneapolis, USA, July 2010.



- 
- C8.**      **M Mohseni** and S Islam, “A Space Vector-Based Current Controller for Doubly Fed Induction Generators”, in the proceedings of the *IEEE IECON 2009*, Porto, Portugal, Nov. 2009.
- C9.**      **M Mohseni** and S Islam, “A Novel Current Controller for Three-Phase Voltage-Source Inverters”, in the proceedings of *IEEE IECON 2009*, Portugal, Nov. 2009.
- C10.**     **M Mohseni** and S Islam, “Translating Fault Ride-Through Requirements of Wind Farms from PCC to the Generators Terminals”, in the proceedings of *PEECS 2009*, Perth, Australia, Oct. 2009.
- C11.**     **M Mohseni** and S Islam, “An Improved Modelling and Control Approach for DFIG-Based Wind Generation Systems”, in the proceedings of *AUPEC 2009*, Adelaide, Australia, Sept. 2009.

## **Chapter 2. Comparison of the international grid codes for large wind power plants**

### **2.1 INTRODUCTION**

Grid codes are defined by network operators to outline rights and responsibilities of all generation units/consumers connected to the transmission system. In the past, grid codes did not include any regulations for large WPPs because the penetration level of wind power was extremely small compared to conventional generation systems. However, the situation has radically changed in the last decade as many countries witnessed a tremendous increase in the number and capacity of WPPs integrated into their electric networks. The shift from conventional to the renewable energy resources raised serious stability concerns regarding the impacts of large WPPs, as intermittent generation units, on the operation of existing power networks. To safeguard the system against these problems, network operators around the world have recently defined stringent technical requirements for large wind farms that seek connection to their transmission systems. Modern grid codes require WPPs to not only withstand various grid disturbances, but also participate in the ancillary service provision and contribute to the network stability support as do conventional generation units. If wind generation cannot provide appropriate network support, then as the proportion of conventional and wind generation varies, changes produced in the operating characteristics of the network will make it increasingly difficult for the system operators to provide the required level of security and efficiency [49].

This chapter presents a comprehensive study on the international grid code regulations defined for large WPPs, covering grid codes of Australia (AEMC),

Denmark (Energinet), Canada (Hydro Quebec), Germany (E.ON Netz), Ireland (Eirgrid), New Zealand (Transpower), Spain (REE), UK (NGET) and USA (FERC and WECC). The presented study will assist wind turbine manufacturers to identify the most stringent regulations defined in the international grid codes. It also helps TSOs to compare their existing regulations with those of other countries or establish their statutory regulations for the first time.

This chapter is organized as follows. A brief review of the current global wind power capacity, specifically in Australia, is presented in section 2.2. Section 2.3 explores the most common regulations included in majority of international grid codes, namely LVRT and HVRT requirements, active and reactive power responses during and after faults, extended range of frequency variations, active power control (frequency regulation), and reactive power control (voltage regulation). Section 2.4 compares international grid codes and section 2.5 presents a discussion on the global harmonization of grid codes as well as future trends of the regulations.

## **2.2 CURRENT GLOBAL WIND POWER CAPACITY**

During the last decade, the global energy market has witnessed a large increase in the number and capacity of WPP installed around the world. Figure 2-1 shows the cumulative global installed wind power capacity from 2001 to 2010. It can be seen that the wind power capacity has doubled every three years and is projected to exceed 203 GW by the end of 2010 [52].

Table 2-1 shows the continental share of the wind power capacity in 2009. Europe's share accounts for 47.9% of the global capacity while Asia and North America each accommodates around 25% of the global wind power capacity. Third place belongs to Australia/Pacific with 1.5% of the global share, but Asia has had the largest continental growth rate in 2009, equal to 40.4% of the global new installation. It is followed by North America and Europe that had 28.4% and 27.3% of the global new capacity, respectively. Table 2-2 presents the latest statistics on the wind power capacity for different countries. It can be seen that at the end of 2009, USA had the largest installed wind power capacity equal to 35.16 GW, followed by China and Germany with the wind capacity of 26.0 and 25.77 GW, respectively. The next places belonged to Spain, India, Italy, France, UK, Portugal and Denmark,

respectively. However, the largest annual capacity growth was observed in China and USA, with the new capacity of 13,800 MW and 9,922 MW, respectively.

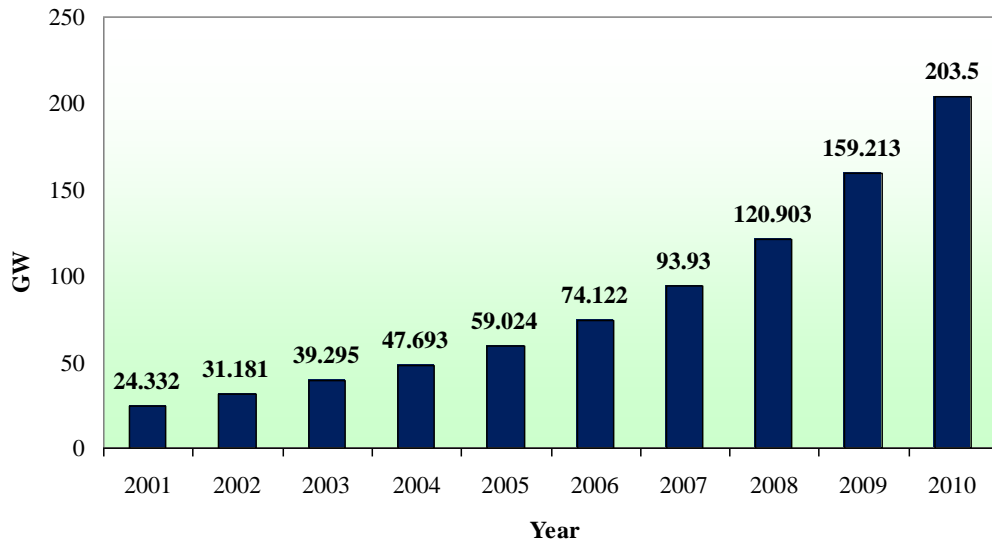


Figure 2-1 Global installed wind power capacity from 2001 to 2010.

Table 2-1 Continental share of the global wind power capacity at the end of 2009 [12].

Continent	Global share	Share in the new capacity
Europe	47.9%	27.3%
Asia	25.1%	40.4%
North America	24.2%	28.4%
Australia/Pacific	1.5%	1.4%
Latin America	0.9%	1.9%
Africa	0.5%	0.4%

Table 2-2 Wind power capacity for different countries in 2009 [12].

Country	USA	China	Germany	Spain	India
Total capacity [MW]	35,159	26,010	25,777	19,140	10,925
New in 2009 [MW]	9,922	13,800	1,880	2,454	1,338

### 2.2.1 Wind power capacity in Australia

Australia is blessed with one of the best wind resources in the world, namely Forties Winds in Southern Australia. This country has recently experienced a considerable increase in the integration level of wind power into its power system. Figure 2-2 shows the cumulative installed wind power capacity in Australia for the last decade, increased from 32 MW in 2000 to 2,019 MW in 2010 [52]. According to the IEA, Australia had 51 wind farms with a total operating wind capacity of 1,712 MW at the end of 2009, supplying 1.6% of its national electric demand (equal to 4,284 GWh). The Australian wind power capacity is installed in all seven states of the country, but South Australia has the largest contribution of more than 43% of the national wind power (see Figure 2-3). In 2009, four projects were commissioned, adding 406 MW new wind power capacity to the Australian electricity grid. Another nine projects are currently under construction and are expected to add an additional 772 MW within the next few years. Also, a further 12,000 MW of wind projects are either in the evaluation phase or undergoing the development approval process. This upwards is expected to continue in the future in view of the fact that the Australian parliament has just passed the expanded Renewable Energy Target scheme, which mandates the country to source 20% of its electricity supply from renewable energy by 2020. This target is four times of the previous target introduced in 2001. South Australian has set even more ambitious renewable energy target of 33% by 2020 [54].

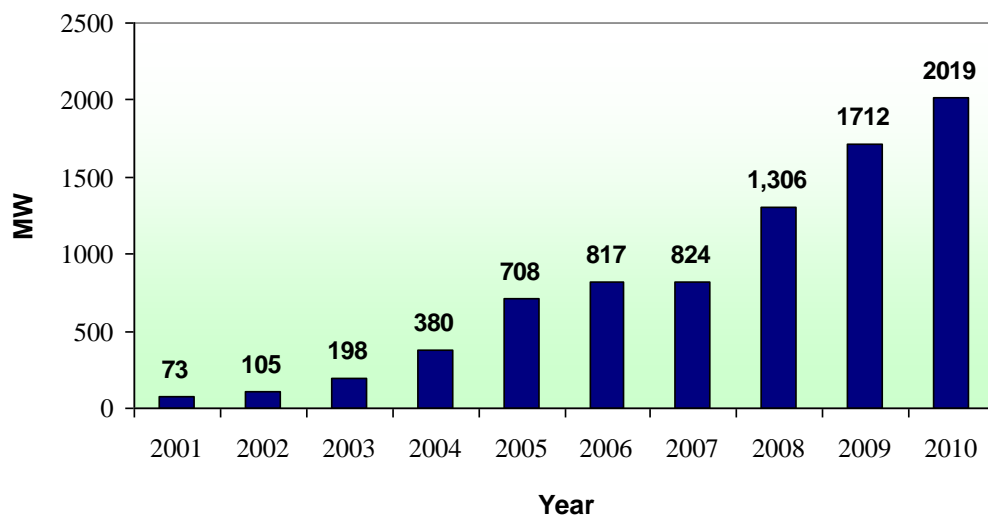


Figure 2-2 Installed wind power capacity in Australia from 2001 to 2010.

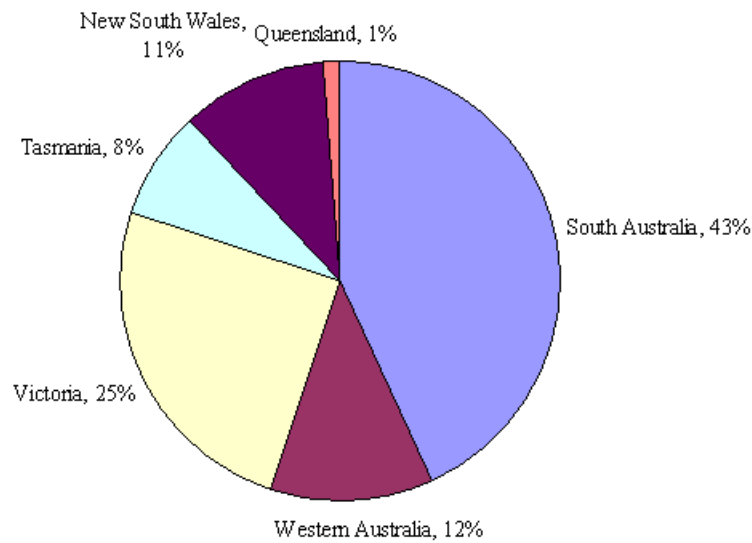


Figure 2-3 Wind power capacity in different states of Australia at the end of 2009.

### 2.3 REVIEW OF THE GRID CONNECTION REQUIREMENTS

The connection requirements for large WPPs vary from one country to another depending on the installed wind power level, robustness on the existing network, local utility practises, and government policies towards renewable energy resources. However, a review of the international grid codes shows that the technical requirements specified for large wind farms are largely classified in five groups

1. low and high voltage ride-through curves;
2. active and reactive power responses following faults;
3. extended variation range for the supply frequency;
4. active power control or frequency regulation facility;
5. reactive power control or voltage regulation capability.

When a fault occurs at some points in the electric network, the voltage drops to the lower levels until the protection devices detect the faulty area and isolate it from the rest of the network. During this interval, wind farms, like other system components, experience a voltage sag condition at their terminals, depending on the type and location of the fault. As a result of this disturbance, wind generators (specifically those using modern variable-speed technologies) may disconnect from the grid due to severe stability problems. A practical example of this incident was reported in the

European outage on 4 November 2006, which caused losing 4,892 MW of wind power generation in Western-Europe [55].

The disconnection of WPPs under voltage disturbances is not acceptable when wind power constitutes a significant part of the total network generation. Thus, modern grid codes require large wind farms to continue their uninterrupted operation under various fault conditions, according to given voltage-time profiles. Such requirements are usually referred to as low voltage ride-through (LVRT) regulations. Figure 2-4 shows a practical example of LVRT profile defined by the Spanish TSO (REE) for wind generators connected to the transmission system: “a wind power plant shall remain connected to the transmission system under the fault conditions when the voltage measured at the HV terminals of the grid connected transformer (at the PCC) remains above the dashed line for two-phase faults and above the solid line for other types of faults” [56].

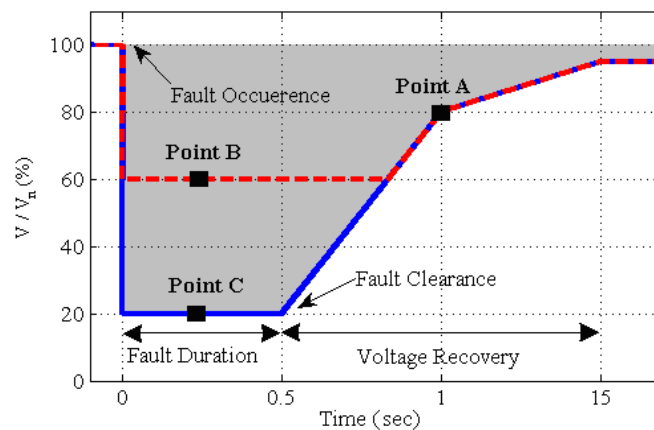


Figure 2-4 Spanish LVRT requirement.

In very recent years, grid codes of countries like Australia and Spain have become even more stringent and defined similar voltage-time profiles for voltage swell conditions. Supply voltage rise can be caused by switching off large loads, energizing capacitor banks, or faults in the transmission system. This requirement is referred to as high voltage ride-through (HVRT) regulations. As a practical instance, the Australian HVRT curve is shown in Figure 2-5, which requires WPPs to withstand voltage swell of 1.3 PU for 0.07 s [57]. Modern grid codes also stipulate WPPs to withstand large frequency excursions that can occur under grid disturbances with large mismatch between the generation and consumption.

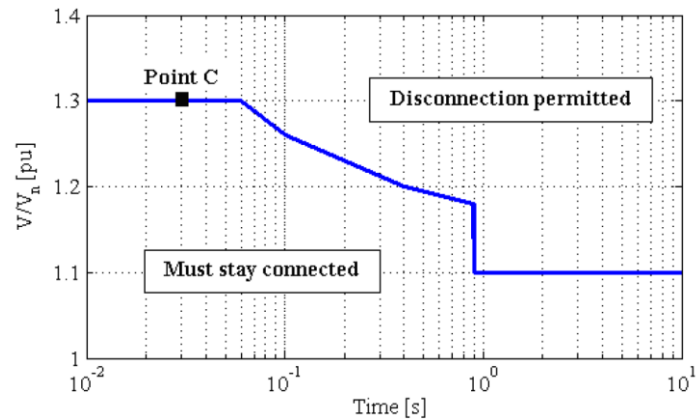


Figure 2-5 Australian HVRT requirement.

In addition to LVRT and HVRT regulations, new grid codes require reactive power injection from WPPs during the fault period and fast active power restoration after the fault clearance. These regulations are imposed by TSOs to exploit the control capability of modern wind farms in the provision of system stability support during and shortly after the grid disturbances. For example, German TSO (E.ON Netz) requests wind farms to support the transient voltage stability through providing the reactive current according to the characteristic shown in Figure 2-6: “as the PCC voltage exceeds 10% dead-band around the nominal value, the reactive current output from the WPP must increase by 2% (on a PU base) for each 1% drop in the supply voltage, within 20 ms after the fault detection”. Australian TSO has imposed more demanding regulations on the reactive current injection. This grid code also requires active power restoration to 95% of the pre-fault value within 100 ms after the supply voltage recovery.

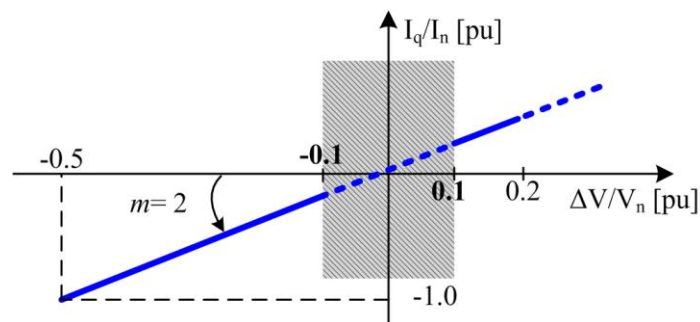


Figure 2-6 German reactive power injection requirement.



Apart from the regulations on the transient response of large wind farms to different voltage disturbances, TSOs usually require WPPs to actively participate in the ancillary service provision. In particular, wind farms must be able to control their active power output and thereby, contribute to the short- and long-term frequency supports. A typical power-frequency response curve (requested by the Irish grid code) is shown in Figure 2-7. Similarly, WPPs must be able to provide reactive power support through contentiously working at a wide range of capacitive/inductive power factor. Figure 2-8 shows typical regulation on the power factor control, defined by German TSO for offshore wind farms.

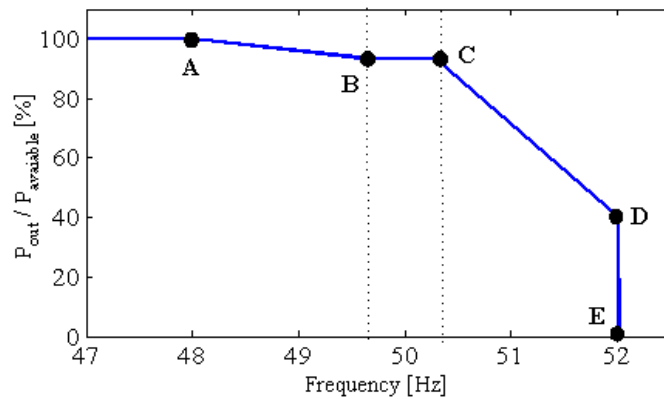


Figure 2-7 Irish active power regulation curve.

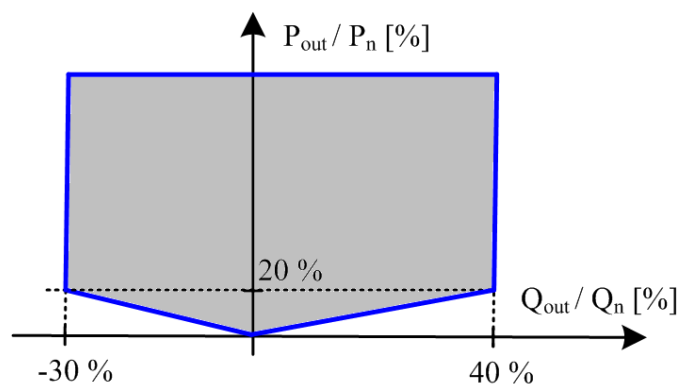


Figure 2-8 German reactive power regulation curve.

## **2.4 COMPARISON OF THE INTERNATIONAL GRID CODES**

### **2.4.1 LVRT requirement**

The LVRT curves defined in international grid codes are relatively similar to the profile shown in Figure 2-4, although their quantitative characteristics may vary between different system operators. From Figure 2-4, it can be seen that the Spanish grid code requires wind farms to withstand three-phase and single-phase faults with voltage drop down to 0.2 PU for 0.5 s, followed by the linear voltage restoration to 0.8 PU during the next 0.5 s. For two-phase faults, on the other hand, continuous operation of WPPs are requested for voltage sags with the retained voltage of 0.6 PU and the maximum duration of 0.8 s. Danish grid code has enforced more stringent LVRT regulations and requires WPPs to ride-through symmetrical and asymmetrical sags with the voltage down to zero for 150 ms, followed the voltage restoration to 0.9 PU in 1.5 s. According to Australian regulations, wind farm must remain connected under symmetrical and asymmetrical sags with the voltage drop to zero for 140 ms and 400 ms, respectively. The supply voltage must then restore to 0.7 PU in 2 s and 0.8 PU in 10 s. The German grid code has defined no regulations for asymmetrical faults, but requires ride-through capability for three-phase faults with voltage drop to zero for the maximum duration of 150 ms, followed by the voltage recovery to 0.8 PU in 1.5 s. The older version of the German LVRT curve is now adopted by FREC (USA) and Eirgrid (Ireland). This curve has the minimum voltage of 0.15 PU for 0.625 s and voltage recovery period of 3 s. The parameters of LVRT profiles defined in other grid codes are summarized in Table 2-3.

From Table 2-3, it can be seen that the most stringent LVRT regulations are requested by the Australian grid code, which requires continues operation of WPPs under asymmetrical sags with the voltage down to zero for 400 ms. For symmetrical sags, on the other hand, the grid codes of Australia, Canada, Denmark, Germany, New Zealand and USA (WECC) have similar regulations. Finally, it is worth noting that if the typical impedance values for the step-up transformers and interconnecting lines inside the wind farms are taken into account, the minimum voltage sag at the terminals of wind generators are very likely to be above 0.15 PU [6]. This will obviously facilitate compliance with the LVRT regulations as the voltage at the WT terminals will be higher than the PCC.

Table 2-3 LVRT requirements outlined in the international grid codes.

Grid code country	During fault		Fault clearance	
	$V_{min}$ [PU]	$T_{max}$ [s]	$V_{min}$ [PU]	$T_{max}$ [s]
Australia	0.0	0.4	0.7	2
Canada	0.0	0.15	0.75	2
Denmark	0.0	0.15	0.6	0.7
Germany	0.0	0.15	0.9	1.5
Ireland	0.15	0.625	0.9	3
New Zealand	0	0.2	0.9	1
Spain	0.2	0.5	0.8	1
UK	0.15	0.14	0.8	1.2
USA (FERC)	0.15	0.625	0.9	3
USA (WECC)	0.0	0.15	0.9	1.5

#### 2.4.2 HVRT requirement

HVRT is a new requirement that has been included in the grid codes of Australia, Denmark, Spain, Germany and USA. The Australian grid code presents a HVRT characteristic curve (shown in Figure 2-5), whereas the HVRT requirements for other grid codes are only defined quantitatively. Table 2-4 compares the HVRT requirements of different grid codes. It is evident that the Australian and Spanish grid codes have the most demanding HVRT regulations, stipulating WPPs to withstand voltage swell of 1.3 PU.

Table 2-4 HVRT requirements in international grid codes.

Country	During swell	
	$V_{max}$ [PU]	$T_{max}$ [s]
Australia	1.3	0.07
Denmark	1.2	0.2
Germany	1.2	0.1
Spain	1.3	0.25
USA (WECC)	1.2	1

### 2.4.3 Regulations on the $P$ - $Q$ response of WPPs following faults

In countries with significant penetration level of wind power or countries with weakly interconnected networks, TSOs have imposed stringent regulations on the active and reactive power responses of WPPs during and after short-circuit faults. These strict regulations are needed to secure the system stability following various disturbances. Regulations on the active power response assist the system to maintain its frequency stability while the reactive power support of wind farms can enhance voltage stability limits of the network.

The regulations on the reactive power response of WPPs during fault periods are enforced in grid codes of Australia, Germany, Spain and UK. Australian grid code requires wind farms to provide capacitive reactive current of at least 4% of their maximum continuous current for each 1% reduction in the PCC voltage once the voltage drops to less than 90% of its rated value. This means that wind farms must generate their maximum reactive current when the PCC voltage reduces beyond 0.75 PU. The German grid code has similar regulation, but requires 2% of reactive current for each percent reduction in the PCC voltage (see Figure 2-6). In Spain, wind farms must not draw reactive power within 100 ms after the fault occurrence and also, must be able to inject reactive power in 150 ms after the fault clearance according to the characteristic shown in Figure 2-9. Finally, the British grid code states that wind farms must produce their maximum reactive current during a voltage dip caused by a short-circuit fault.

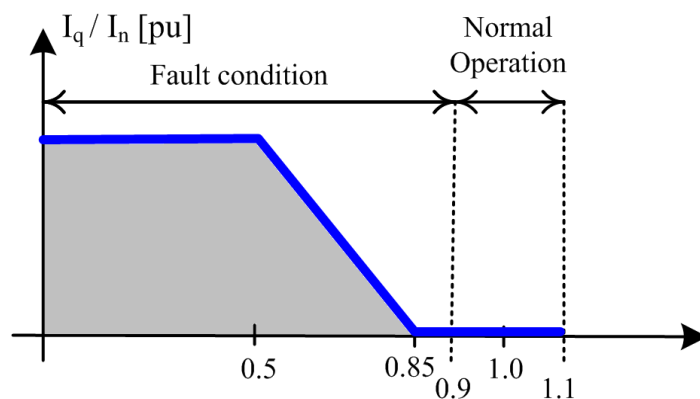


Figure 2-9 Spanish regulation on the reactive current injection.

Regulations on active power restoration are defined in Australia, Ireland, Germany and UK. Australian grid code requires WPPs to restore their active power output to 95% of the pre-fault value within 100 ms after the fault clearance. In Ireland, wind farms must continue active power production during the fault in proportion to the retained voltage. Also, the active power output must restore to 90% of the maximum available power within 1 s after the voltage recovery to 0.9 PU. German grid code stipulates active power restoration to the pre-fault value immediately after the fault clearance, with the gradient larger than 20% of the rated power per second. In UK, WPPs must restore their active power output to 90% of the pre-fault value with 500 ms after the grid voltage returns to 90% of the nominal value. By comparing these requirements, it is observed that the Australian and Irish grid codes have the most stringent requirements. This can be justified by their weakly interconnected power networks, which demands for fast active power restoration in order to maintain the network frequency stability. On the other hand, regulations in Germany are much less demanding because this country has strong interconnection to UCTE.

#### **2.4.4 Regulations on the extended range of frequency variations**

International grid codes require WPPs to continuously operate within extended ranges of frequency variations for given times. In Australia, WPPs must operate continuously under the frequency range of 49.5 to 50.5 Hz, operate under the frequency range of 49 to 51 Hz for 10 minutes, under the frequency range of 48 and 51 Hz for 2 minutes, and under the frequency range of 47.5 Hz and 52 Hz for 9 s. Similar frequency ranges have been defined in other international grid codes, as summarized in

Table 2-5. It is evident that the most onerous transient frequency limits are outlined in Canada (with 7.5% reduction permitted for 0.35 s), whereas the continuous frequency variations in the British grid code appears to have the widest operating range ( $47.5 < f < 52.0$ ).

Table 2-5 Frequency limits in international grid codes.

Country	Frequency limit [Hz]	Maximum duration
Australia	$49.5 < f < 50.5$	Continuous
	$49.0 < f < 51.0$	10 min
	$48.0 < f < 51.0$	2 min
	$47.5 < f < 52.0$	9 sec
Canada	$59.4 < f < 60.6$	Continuous
	$58.5 < f < 61.5$	11 min
	$57.5 < f < 61.7$	1.5 min
	$57.0 < f < 61.7$	10 sec
	$56.5 < f < 61.7$	2 sec
	$55.5 < f < 61.7$	0.35 s
Denmark	$48.5 < f < 51$	Continuous
	$48.0 < f < 51.0$	25 min
	$47.5 < f < 52.0$	5 min
	$47.0 < f < 52.0$	10 sec
Germany	$49.0 < f < 50.5$	Continuous
	$48.5 < f < 51.5$	30 min
	$47.5 < f < 51.5$	10 min
	$46.5 < f < 53.5$	10 sec
Ireland	$49.5 < f < 50.5$	Continuous
	$47.5 < f < 52.0$	60 min
	$47.0 < f < 52.0$	20 sec
UK	$47.5 < f < 52.0$	Continuous
	$47.0 < f < 52.0$	20 sec

#### 2.4.5 Active power control and frequency regulation

According to the international grid codes, WPPs must control their output active power in response to the frequency variations and thereby, contribute to the frequency regulation. Since there is no control on the prime mover of wind

generators, they are usually exempted from active power increase that would be needed in the case of frequency drop. However, active power curtailment is requested in the grid codes of Denmark, Germany and Ireland. The active power reduction can be attained through either disconnecting some wind turbines from the grid or pitching the blades of turbines. The Irish regulation on the active power control is shown in Figure 2-7. In this figure, points B and C denote the range of normal operating conditions and thus, power control action must be taken for the frequency range outside  $49.7 < f < 50.3$  Hz. Danish grid code requires active power curtailment according to the power-frequency curve shown in Figure 2-10 (active power reduction to zero as the frequency exceeds 51.5 Hz). In Germany, WPPs must reduce their active power production with a gradient of 40% of the available power per hertz when the frequency exceeds 52 Hz.

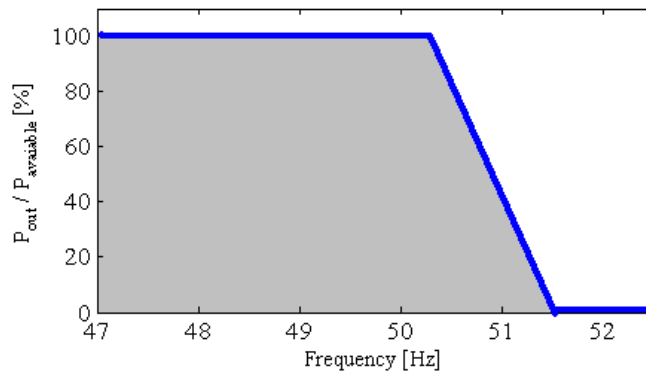


Figure 2-10 Danish active power curtailment regulation.

#### 2.4.6 Reactive power control and voltage regulation

Modern grid codes also require WPPs to provide reactive power control and in turn, offer voltage regulation service to the network operator. According to the Australian regulations, WPPs must be able to continuously operate at their rated output power with the power factor varying from 0.93 capacitive to 0.93 inductive, based on the command signal received from the system operator. In Canada, the reactive power requirements are specified under continuous and dynamic operating conditions. For continuous operation, WPPs must be able to work with the power factor varying from 0.9 capacitive to 0.95 inductive, whereas the minimum range for dynamic conditions is from 0.95 capacitive to 0.985 inductive. The Canadian grid code also requires wind farms to have a voltage regulation system that acts under the voltage



set-point control mode. This voltage control loop must be calibrated to achieve 95% of the reference reactive power in 0.1 to 1 s after the step change in the voltage set-point. The reactive power regulations for other countries are summarized in Table 2-6. Note that in Germany, Spain, and UK, reactive power control must change as the PCC voltage reduces or increases from the rated value (shown for the German grid code in Figure 2-11). Therefore, comparing the international regulations of the reactive power control of wind farms is not possible as some grid codes consider the variation of the supply voltage.

Table 2-6 Power Factor limits in international grid codes.

Grid code country	Power factor	
	Cap.	Ind.
Australia	0.93	0.93
Canada	0.9	0.95
Denmark	0.995	0.995
Germany	0.95	0.925
Ireland	0.95	0.95
New Zealand	0.95	0.95
Spain	0.91	0.91
UK	0.95	0.95
USA	0.95	0.95

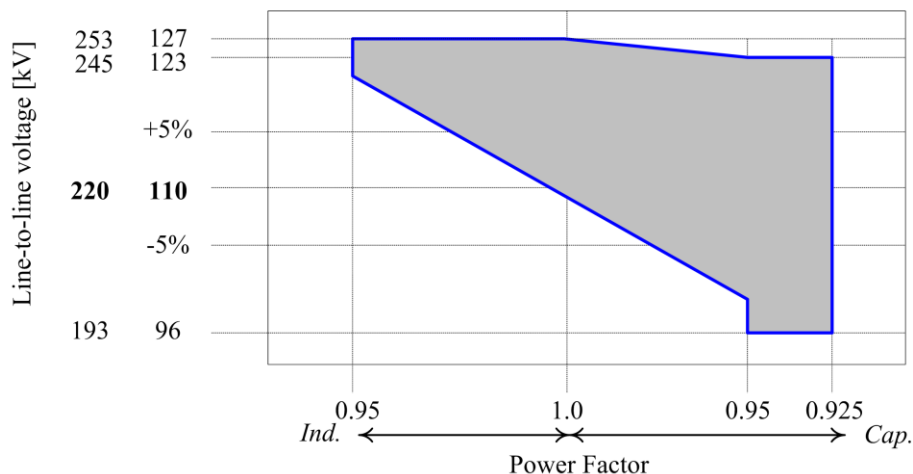


Figure 2-11 German regulation on the reactive power control.

## **2.5 DISCUSSIONS AND FUTURE TRENDS**

Comparative study presented in Section 2.4 shows that the grid code regulations may vary significantly from one country to another. This is usually difficult to find a systematic technical justifications about the existing regulations; however, system operators usually define their grid codes based on the robustness of the existing power networks, integration level of wind power and their local utility practices. For instance, the regulations in weakly interconnected network such as Ireland and Australia are expected to be more stringent compared to the regulations of USA and Germany with robust networks.

### **2.5.1 Global harmonization of the grid codes**

EWEA (European Wind Energy Association) recommends that the technical regulations for European countries should be developed in a more consentient manner in order to attain harmonized requirements in the coming years [58]. Consistency in the regulations would assist wind turbine manufacturers to move from ‘market-oriented’ products to more ‘universal’ approaches. In other words, at the present time, manufacturers are constantly challenged to adapt their hardware and software designs in compliance with specific requirements of each country, rather than adopting a globally optimized design. This trend must change in near future as the global wind power capacity is expected to increase notably. In addition, harmonization of international grid codes will help system operators to share their experience and learn from past operating incidents recorded in other countries.

Besides globally consistent regulations, it is highly recommended that international grid codes avoid posing costly regulations on WPPs unless they are truly needed for the stable operation of the power system. An optimal balance between the cost and technical regulations would help wind farm developers to attain more economically efficient solutions. The realistic design of grid codes is especially important for the inclusion of low/high voltage ride-through requirements as these requirements reportedly increase the overall of cost of wind generators by more than 5% [59].

### 2.5.2 Future trends in the grid code regulations

Studying the latest drafts of international grid codes reveals that more stringent requirements are expected to be defined for large WPPs in the near future. Specifically, WPPs will be required to (1) provide reactive power support during faults, (2) emulate synchronizing power characteristic, i.e., inertia response, and (3) provide power oscillation damping, i.e., power system stabilization. The reactive power injection during the fault period is already requested in Australia, Germany, UK and Spain. Recent studies show that modern variable-speed wind turbines boast very versatile reactive power control capability that is decoupled to their output active power; therefore, system operators can readily rely on wind farms to further support system voltage stability [47]-[51].

Since variable-speed wind turbines are connected to the main grid through back-to-back converters, their operation is essentially decoupled from the grid conditions [49]. In other words, they cannot provide synchronizing power characteristic as do conventional synchronous generators and as a result, the total inertia of the system reduces. To address this problem, some system operators, such as REE, strongly recommend wind power plants to have the ability to emulate inertia response of conventional synchronous generators. This requirement is not compulsory at the present time, but it is expected to be included in grid codes of Spain, Ireland, and New Zealand in the near future. Accordingly, an extra PI controller must be fitted in the wind turbine control scheme, which acts on the frequency variations as the input and changes the output power accordingly in order to suppress the frequency variations [59]. For instance, the Spanish regulations on the inertia response are as follow: (1) the gains of PI controller must be adjusted such that the active power output can vary by 5% within 50 ms; (2) energy storage devices must be used to assist wind power plants to inject or absorb at least 10% of the output active power for 2 s; (3) the deadband of frequency variations is equal to  $\pm 10$  mHz; and (4) the inertia response must be disabled for voltage sags with voltage below 0.85 PU [56].

Future grid codes will also require WPPs to participate in power oscillation damping with the low frequency range of 0.15 Hz to 2.0 Hz. To provide power system stabilizer facility, WPPs must integrate an additional lead-lag compensators that act

on the power oscillation (probably at remote area) as the input signal and increase/reduces the wind power output accordingly. Recent studies show that variable-speed wind turbines can present superior power system stabilizer performance compared to the conventional generation system [49].

## **2.6 CONCLUSIONS**

In conclusion, this chapter presents a comparative study on the international grid code regulations defined for large WPPs. It is found that

- Australia and Spain have the most onerous LVRT and HVRT regulations.
- Australia has the most stringent regulations on the active and reactive power responses following a fault.
- Canada and UK have the most demanding frequency variations ranges for transient and steady-state operating conditions, respectively.
- Strict regulations on active power curtailment (frequency regulation) are defined in Ireland, Germany and Denmark.
- Spain and Canada have the most demanding reactive power capability requirements for voltage regulation.

The main focus of this study is on the transient response of WPPs under fault conditions. It was shown that the Australian grid code has the most stringent regulations on the LVRT/HVRT, reactive power injection and active power restoration; therefore, this grid code is selected for the compliance studies in the following chapters.

## **Chapter 3. Transient response of DFIG-based WTs under symmetrical and asymmetrical voltage sags**

### **3.1 INTRODUCTIONS**

Achieving recent LVRT requirements, enforced by the international grid codes, is a significant technical issue for wind turbine manufacturers. To fulfil this objective, a thorough insight into the LVRT regulations and what they practically imply at the wind generator terminals are of the utmost importance. The relevant features and constraints of power networks must be taken into account, including the effects of transformers' configuration, submarine/underground AC cables and fault clearing mechanism of the circuit breakers. This would help to accurately identify the realistic voltage sag conditions that are expected at wind generator terminals under different types of faults. Following this, detailed transient models of wind generators can be incorporated to predict the evolution of electrical and mechanical variables of the wind generator under different sag conditions. Thereby, researchers and designers will be able to identify the difficulties associated with successful fault ride-through of wind generators and accordingly, modifications to the conventional control techniques can be suggested to address these problems and enhance the LVRT capability of WTs.

Among different technologies proposed for wind generation systems, the DFIG concept has been recognized as the most popular option due to many technical/economical advantages compared to other concepts. The DFIG concept has several advantages as compared to the fixed-speed generators, including maximized power capture, reduced mechanical stresses on the turbine, and reduced acoustical

noise. In addition, this technology is more economically viable than the full-converter variable-speed concept since it employs voltage-source converters (VSCs) rated at 30-35% of the generator size for the rotor speed variation range of  $\pm 25\%$  [1]. Hence, this chapter presents a new analysis into the impacts of various symmetrical and asymmetrical voltage sags on DFIG-based WTs.

The LVRT requirements are usually defined by the grid codes at the high-voltage side of the wind farm coupling transformer to the grid (i.e. at the PCC). However, it is known that depending on the network characteristics and constraints, the voltage sag conditions experienced at the wind generator terminals can be significantly different from the conditions at the PCC. Therefore, it is very important to identify the voltage sags that can practically reach the wind generator terminal. In this thesis, extensive simulation studies are carried out to investigate the transient overshoots and ripples that appear in the rotor current and dc-link voltage when the DFIG is subjected to various types of (a)symmetrical faults. For the first time, the impacts of phase-angle jump and operational constraints of circuit breakers are examined. Furthermore, the influences of sag parameters including type, initial point-on-wave instant, depth, and impedance angle are investigated. Theoretical analyses are also presented to support the validity of observations made in the simulation studies.

This chapter is organized as follows. Section 3.2 presents the characterization and classification of various voltage sag conditions, considering the transformers configurations, impedance angle of the grid, and the natural current zero-crossing operation of circuit breakers. Section 3.3 explores the modelling and conventional vector control of DFIG-based WTs. Section 3.4 presents a theoretical study of the DFIG-based WT under fault conditions, which will be used to analyse the simulation results. In section 3.5, a 1.5 MW DFIG-based WT is simulated in Matlab/Simulink and is subjected to various sag conditions in order to examine the transient overshoots and steady-state ripples that appear in the rotor current and dc-link voltage under different types of faults. This section also examines the effects of phase-angle jump and voltage recovery process. Finally, the influence of sag parameters (type, initial point-on-wave instant, depth, and impedance angle) on the peak values of the rotor current and dc-link voltage are investigated.

## 3.2 CHARACTERISTIC AND CLASSIFICATION OF VOLTAGE SAGS

When a fault occurs at some points in the power network, the supply voltage drops to the lower levels until a protection device trips and circuit breakers isolate the fault. During this interval, wind generators connected to the same bus as the faulted feeder will experience a voltage sag condition. This section aims to characterize and classify the voltage sag conditions caused by different types of faults in the grid.

### 3.2.1 Symmetrical faults and phase-angle jump

The voltage divider model can be used to formulate the voltage sag conditions caused by three-phase faults in radial systems, as displayed in Figure 3-1 [42]. In this figure, T1 represents the step-up transformer that is located in the nacelle of each WT to increase the low-level voltages generated at the DFIG terminals to the medium-voltage used in the collection-grid of the wind farm. In cascade to the nacelle transformers, a large step-up transformer (T2), sized at the nominal capacity of the wind farm, will be used to increase the collection-grid voltage to the transmission-level voltage. Real parameters for the transforms used in one of the largest offshore wind farms in the world, Horns Rev, have been given in Figure 3-1 to provide further insight [60]. According to this figure, the voltage at the PCC, i.e., at the HV side of T2, can be defined as

$$\mathbf{V}_{sag} = \mathbf{V}_s \frac{\mathbf{Z}_f}{\mathbf{Z}_f + \mathbf{Z}_s} \quad 3-1$$

where  $\mathbf{V}_s$  is the pre-fault voltage,  $\mathbf{Z}_s$  is the source impedance at PCC, and  $\mathbf{Z}_f$  is the impedance between the PCC and fault location.

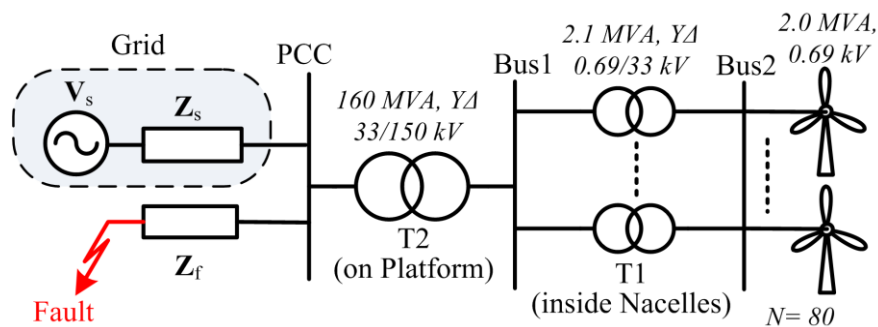


Figure 3-1 Voltage divider model (*italic* figures are the real parameters for Horns-Rev wind farm).

Three-phase sags are normally characterized by the magnitude of the remnant voltage and the duration. However, if the X/R ratios of the impedance  $\mathbf{Z}_s$  and  $\mathbf{Z}_f$  are different, the three-phase fault causes not only a drop in the voltage magnitudes, but also a sudden change in the phase-angle of the three-phase voltage. This phenomenon is referred to as “phase-angle jump” and is defined by

$$\delta = \arg(\mathbf{V}_{sag}) = \arg(\mathbf{Z}_f) - \arg(\mathbf{Z}_s + \mathbf{Z}_f) \quad 3-2$$

For the conventional transmission systems, both  $\mathbf{Z}_s = R_s + jX_s$  and  $\mathbf{Z}_f = R_f + jX_f$  are mainly formed by overhead transmission lines and large transformers, so the phase-angle jump would be very small. However, for wind farm connected to the distribution systems or offshore wind farms with high-voltage submarine cables, the X/R ratio of the source impedance is noticeably larger than the  $\mathbf{Z}_f$  impedance. Thus, three-phase faults cause large sudden variations of the voltage phase-angles.

If (3-1) is rewritten with  $\mathbf{Z}_f / \mathbf{Z}_s = \lambda e^{j\alpha}$ , it can be observed that the ‘ $\lambda$ ’ value varies depending on the fault distance but the ‘ $\alpha$ ’ parameter is a fixed for any given source–fault impedance combination (known as impedance angle). Consequently, a unique relationship between the sag magnitude and its phase-angle jump can be established for any specific impedance angle. It is not however practical to consider individual characteristics of each network for testing the LVRT capability of wind generators. Instead, this work focuses on the typical impedance angles proposed by [61], including  $0^\circ$  (the most common value for transmission systems),  $-20^\circ$  (typical value for distribution systems), and  $-60^\circ$  (the minimum value for wind farms located offshore with submarine/underground AC cables). Figure 3-2 shows the relationship between the sag magnitude and the corresponding phase-angle jump for various impedance angles. It can be seen that the voltage sag conditions specified in the Spanish Grid Code (e.g., Point B in Figure 2-4) are mapped to different voltage vectors depending on the network impedance angle, e.g., to Points  $B_1$  ( $\mathbf{V}_{sag} = 0.6 \angle 0^\circ$ ),  $B_2$  ( $\mathbf{V}_{sag} = 0.6 \angle -12^\circ$ ), and  $B_3$  ( $\mathbf{V}_{sag} = 0.6 \angle -31^\circ$ ) for  $\alpha = 0^\circ$ ,  $\alpha = -20^\circ$ , and  $\alpha = -60^\circ$ , respectively. Similar comments can be made about Points A and C.



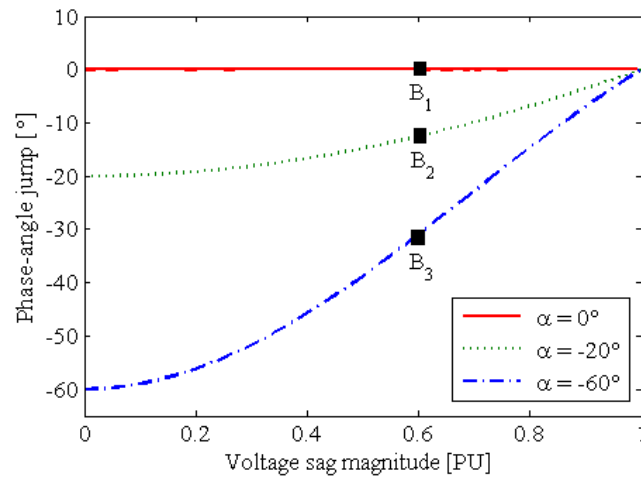


Figure 3-2 Voltage sag magnitude vs. phase-angle jump for various impedance angles.

### 3.2.2 Asymmetrical faults and sag classification

If an asymmetrical fault occurs in the power network, six types of voltage sags (types B to G) can appear at the PCC and the wind generator terminals [61]. The phasor expressions of various sag types are given in the Appendix A. The magnitude and angle of the characteristic voltage ( $V_{sag}$ ) define the retained voltage and phase-angle jump, respectively. Ref. [61] has demonstrated that the transformers' configuration cannot affect the voltage sag conditions caused by three-phase faults, i.e., sag type A propagates unchanged throughout the network from the PCC towards Bus1 and Bus2 in Figure 3-1. However, the voltage sag experienced at the wind generator terminals during asymmetrical faults can be substantially different from the PCC, due to the transformers' configuration. The coupling transformer (T2) is usually connected in  $Y\Delta$  configuration, which filters out the zero-sequence component in the secondary-side (Bus1 in Figure 3-1). The sag type at Bus2, experienced at the wind generator terminals, is defined based on the configuration of the nacelle transformer, as listed in the last two columns of Table 3-1.

From Table 3-1, it is evident that sag types B and E cannot reach the generator terminals as they include zero-sequence components. On the other hand, sag types D, F, and G will be observed only if the transformers' configurations are taken into account. It is finally concluded that to thoroughly examine the operation of DFIG-based WTs under fault conditions, the wind generator must be subjected to the sag types of A, C\*, D\*, C, D, F, and G.

Table 3-1 Voltage sag propagation through the wind farm

Fault	Sag at PCC	Sag at Bus1, YΔ Trans.	Sag at Bus2, YΔ Trans.	Sag at Bus2, Other Trans.
3Φ	Type A	Type A	Type A	Type A
Φ-g	Type B	Type C*	Type D*	Type C*
Φ-Φ	Type C	Type D	Type C	Type D
2Φ-g	Type E	Type F	Type G	Type F

\*) The characteristic voltage is not equal to  $V_{sag}$  but to  $(1/3+2/3 V_{sag})$ .

### 3.2.3 Fault clearance and voltage recovery process

Protection relays may trip at any time during the fault, but the pole of the circuit breakers can only function and isolate the fault at the natural zero-crossing points of the corresponding phase current. As a result, short-circuit faults that involve more than two phases (e.g., two-phase to ground, three-phase, and three-phase to ground faults) will be cleared in two or three steps. This is because when the circuit breaker operates in one phase, the fault will develop into another type and the full voltage recovery will take place with the operation of circuit breakers in other faulted phases. For instance, if a two-phase to ground fault occurs between phases  $a$  and  $b$ , the circuit breaker can first operate in the zero crossing point of phase  $a$ , then the single-phase to ground fault in phase  $b$  will be cleared, leading to the full voltage recovery.

Ref. [61] has listed fourteen types of sags corresponding to different possibilities of voltage recovery, as given in Table 3-2. It can be seen that the three-phase faults (type A voltage sags) can be cleared in five different ways (involving two or three steps), two-phase to ground faults that generate types E, F, or G voltage sags can be cleared in two different ways (involving two steps), and faults that generate other sag types will be cleared in a single way. In Table 3-2, ' $t_i$ ' is the initial point-on-wave instant that the fault occurs and ' $t_{f1}$ ' is the final point-on-wave instant that the first pole of the circuit breaker clears the fault. If the fault is to be cleared in two or three steps, ' $t_{f2}$ ' and ' $t_{f3}$ ' denote the instants that the second and third phases of the circuit breaker clear the fault, respectively. Note that the final point-on-wave instant ( $t_{f1}$ ) is defined according to the fault current angle ( $\psi$ ) and the other two recovery instants

---

( $t_{f2}$  and  $t_{f3}$ ) are delayed by  $60^\circ$ ,  $90^\circ$ , or  $120^\circ$  with respect to  $t_{f1}$ . The typical value of the fault current angle is equal to  $75^\circ$  to  $85^\circ$  for overhead transmission systems and  $45^\circ$  to  $60^\circ$  for distributions systems or transmission systems with submarine or underground cables. Therefore, it can be said that the voltage recovery instants is discrete and nearly constant for any network with a given fault current angle  $\psi$  [61].

Table 3-2 Voltage recovery sequences and fault clearance instants with identical fault current angles for different sag types.

Sag Type	Sequence of sags*	First recovery $\omega t_{f1}$	Second recovery $\omega t_{f2}$	Third recovery $\omega t_{f3}$	Fault-clearing delay
A <sub>1</sub>	A <sub>1</sub> → C <sub>a</sub>	$n.360^\circ - \alpha_a + \psi$	$n.360^\circ - \alpha_a + \psi + 90^\circ$	–	$\omega t_{f2} - \omega t_{f1} = 90^\circ$
A <sub>2</sub>	A <sub>2</sub> → D <sub>a</sub>	$n.360^\circ - \alpha_a + \psi + 90^\circ$	$n.360^\circ - \alpha_a + \psi + 180^\circ$	–	$\omega t_{f2} - \omega t_{f1} = 90^\circ$
A <sub>3</sub>	A <sub>3</sub> → E <sub>2a</sub> → B <sub>b</sub>	$n.360^\circ - \alpha_a + \psi$	$n.360^\circ - \alpha_a + \psi + 60^\circ$	$n.360^\circ - \alpha_a + \psi + 120^\circ$	$\omega t_{f3} - \omega t_{f1} = 120^\circ$
A <sub>4</sub>	A <sub>4</sub> → F <sub>2a</sub> → C <sub>b</sub> *	$n.360^\circ - \alpha_a + \psi + 90^\circ$	$n.360^\circ - \alpha_a + \psi + 150^\circ$	$n.360^\circ - \alpha_a + \psi + 210^\circ$	$\omega t_{f3} - \omega t_{f1} = 120^\circ$
A <sub>5</sub>	A <sub>5</sub> → G <sub>2a</sub> → D <sub>b</sub> *	$n.360^\circ - \alpha_a + \psi$	$n.360^\circ - \alpha_a + \psi + 60^\circ$	$n.360^\circ - \alpha_a + \psi + 120^\circ$	$\omega t_{f3} - \omega t_{f1} = 120^\circ$
B <sub>a</sub>	–	$n.360^\circ - \alpha_a + \psi$	–	–	–
C <sub>a</sub> or C <sub>a</sub> *	–	$n.360^\circ - \alpha_a + \psi + 90$	–	–	–
D <sub>a</sub> or D <sub>a</sub> *	–	$n.360^\circ - \alpha_a + \psi$	–	–	–
E <sub>1a</sub>	E <sub>1a</sub> → B <sub>c</sub>	$n.360^\circ - \alpha_a + \psi + 120^\circ$	$n.360^\circ - \alpha_a + \psi + 240^\circ$	–	$\omega t_{f2} - \omega t_{f1} = 120^\circ$
E <sub>2a</sub>	E <sub>2a</sub> → B <sub>b</sub>	$n.360^\circ - \alpha_a + \psi - 120^\circ$	$n.360^\circ - \alpha_a + \psi - 60^\circ$	–	$\omega t_{f2} - \omega t_{f1} = 60^\circ$
F <sub>1a</sub>	F <sub>1a</sub> → C <sub>c</sub> *	$n.360^\circ - \alpha_a + \psi - 150^\circ$	$n.360^\circ - \alpha_a + \psi - 30^\circ$	–	$\omega t_{f2} - \omega t_{f1} = 120^\circ$
F <sub>2a</sub>	F <sub>2a</sub> → C <sub>b</sub> *	$n.360^\circ - \alpha_a + \psi + 150^\circ$	$n.360^\circ - \alpha_a + \psi + 210^\circ$	–	$\omega t_{f2} - \omega t_{f1} = 60^\circ$
G <sub>1a</sub>	G <sub>1a</sub> → D <sub>c</sub> *	$n.360^\circ - \alpha_a + \psi + 120^\circ$	$n.360^\circ - \alpha_a + \psi + 240^\circ$	–	$\omega t_{f2} - \omega t_{f1} = 120^\circ$
G <sub>2a</sub>	G <sub>2a</sub> → D <sub>b</sub> *	$n.360^\circ - \alpha_a + \psi - 120^\circ$	$n.360^\circ - \alpha_a + \psi - 60^\circ$	–	$\omega t_{f2} - \omega t_{f1} = 60^\circ$

\*) Sag types B<sub>a</sub>, C<sub>a</sub>, D<sub>a</sub> .... denote that space vectors  $\mathbf{V}_{bn}$  and  $\mathbf{V}_{cn}$  are symmetrical with respect to phase *a*, as in Table A-I.

Sag types B<sub>b</sub>, C<sub>b</sub>, D<sub>b</sub> .... denote that space vectors  $\mathbf{V}_{an}$  and  $\mathbf{V}_{cn}$  are symmetrical with respect to phase *b*.

Sag types B<sub>c</sub>, C<sub>c</sub>, D<sub>c</sub> .... denote that space vectors  $\mathbf{V}_{an}$  and  $\mathbf{V}_{bn}$  are symmetrical with respect to phase *c*.

### 3.3 MODELLING AND CONTROL OF DFIG-BASED WTS

This section presents a brief overview of the modelling and the conventional vector control of DFIG-based WTs. Figure 3-3 shows the overall configuration of a DFIG-based WT, consists of a pitch-controlled turbine that is mechanically coupled to a wound rotor induction generator through shaft and gear-box system. The gear-box must be used to increase the low rotation speed of wind turbine to near the synchronous speed of the generator. The stator winding of the machine is directly connected to the grid whereas the rotor winding is connected through back-to-back VSCs to the coupling transformer. Vector control of the RSC provides a decouple control over the active and reactive powers of the machine. The GSC vector controller, on the other hand, is designed to keep the dc-link voltage constant. The VSCs are sized at a fraction of the generator rating, normally in the range between 25 to 35 percent, for a give speed variation range of  $\pm 25\%$ . Since the VSCs can operate in bi-directional power mode, the DFIG can be operated either in sub-synchronous or in super-synchronous operational modes. The conventional protection scheme of DFIG includes the crowbar that protects the RSC from destructive overcurrent and the chopper that protects the dc-link capacitor from severe overvoltages. The protection of DFIG under fault various fault conditions will be studied in Chapter 4 and Chapter 5.

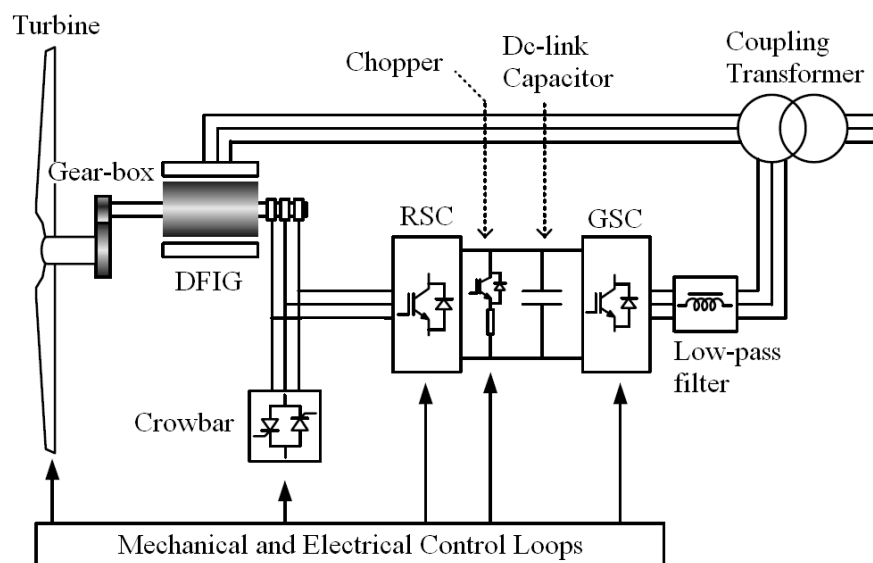


Figure 3-3 Schematic diagram of a DFIG-based WT

Figure 3-4 illustrates the overall model and control structure of a DFIG-based WT, including the mechanical and electrical components [62]. The mechanical parts, with large time constants, are constituted of (1) a wind model, (2) an aerodynamic model of the turbine, (3) a drive train model, and (4) blade angle and output power control blocks. On the other hand, the electrical part of the model consists of (1) the generator model, (2) the RSC control block, and (3) the dc-link and GSC blocks. The input and output variables of each component and the interconnection between different parts of the overall model are shown in Figure 3-4. A comprehensive discussion on the modelling and control of DFIG-based WTs is presented in [1], [5]-[7]. A review of the electrical parts of the model is however needed in this thesis because it helps to theoretically analyse the transient response of DFIG-based WT under various operating conditions including voltage sags and swells.

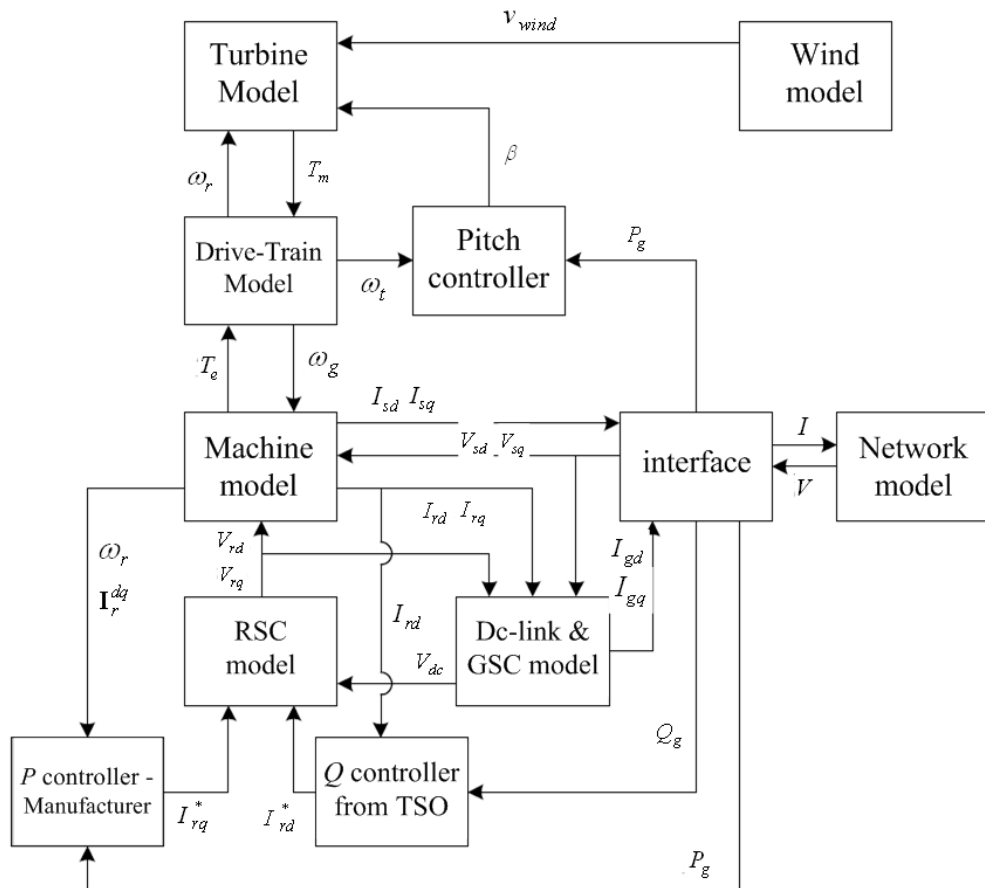


Figure 3-4 The overall model and control structure of a DFIG-based WT

### 3.3.1 Machine modelling

Induction machines are usually modelled using the well-known ‘T-form’ equivalent circuit with self and mutual inductances [5]-[7]. However, the T-form equivalent circuit is more complex than necessary. Therefore, this thesis uses a more convenient ‘Γ-form’ equivalent circuit without losing the model accuracy [63]. The Γ-form equivalent circuit is graphically presented in Figure 3-5 (the machine-side), where  $\omega$  is the angular speed of the arbitrary reference frame. According to this model, the stator and rotor voltage vectors in the arbitrary frame are given by

$$\mathbf{V}_s^a = R_s \mathbf{I}_s^a + \frac{d\Phi_s^a}{dt} + j\omega \cdot \Phi_s^a \quad 3-3$$

$$\mathbf{V}_r^a = R_r \mathbf{I}_r^a + \frac{d\Phi_r^a}{dt} + j(\omega - \omega_r) \cdot \Phi_r^a \quad 3-4$$

and the flux vector are defined as

$$\Phi_s^a = L_m (\mathbf{I}_s^a + \mathbf{I}_r^a) = L_m \mathbf{I}_m^a \quad 3-5$$

$$\Phi_r^a = L_\sigma \mathbf{I}_r^a + L_m (\mathbf{I}_s^a + \mathbf{I}_r^a) \quad 3-6$$

Using (3-5) and (3-6), the stator current and rotor flux can be expressed by

$$\mathbf{I}_s^a = \frac{\Phi_s^a}{L_m} - \mathbf{I}_r^a \quad 3-7$$

$$\Phi_r^a = \Phi_s^a + L_\sigma \mathbf{I}_r^a \quad 3-8$$

Substituting (3-8) in (3-4) gives the rotor voltage equation in the arbitrary frame as

$$\mathbf{V}_r^a = R_r \mathbf{I}_r^a + L_\sigma \frac{d\mathbf{I}_r^a}{dt} + \frac{d\Phi_s^a}{dt} + j(\omega - \omega_r) \cdot (L_\sigma \mathbf{I}_r^a + \Phi_s^a) \quad 3-9$$

Also, the stator power is defined by

$$\mathbf{S}_s = P_s + jQ_s = -1.5 \mathbf{V}_s^a \cdot \hat{\mathbf{I}}_s^a \quad 3-10$$

### 3.3.2 GSC modelling

The GSC of a DFIG-based WT is mainly aimed to keep the dc-link voltage constant while if desired, it can also provide a limited reactive power support. According to dc-side model shown in Figure 3-5, the differential equation describing the capacitor voltage can be defined as

$$C \cdot V_{dc} \frac{dV_{dc}}{dt} = P_r - P_g \tag{3-11}$$

In (3-11), the rotor power ( $P_r$ ) is an independent variable that is controlled by the outer power control loop of the RSC. Therefore, the dc-link voltage can be controlled only through the GSC active power ( $P_g$ ). If the power losses in the ac filter of the GSC are neglected, the output power of the GSC can be defined as

$$\mathbf{S}_g = P_g + jQ_g = 1.5\mathbf{V}_s^a \cdot \mathbf{I}_g^a \tag{3-12}$$

Also, referring to the GSC-side model in Figure 3-5, the voltage equation of this converter in the arbitrary frame can be expressed by

$$\mathbf{V}_g^a = R_g \mathbf{I}_g^a + L_g \frac{d\mathbf{I}_g^a}{dt} + j\omega L_g \mathbf{I}_g^a + \mathbf{V}_s^a \tag{3-13}$$

Based on (3-13), it is evident that the operation of the GSC is identical to the conventional grid-connected VSCs.

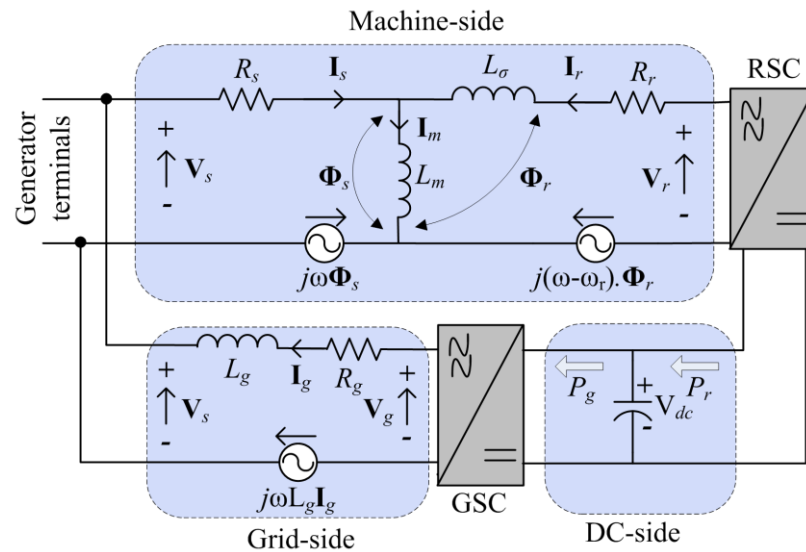


Figure 3-5 Equivalent circuit of the DFIG system

### 3.3.3 Vector control of the RSC

This section presents the overall field-oriented vector control scheme that has been widely adopted in the RSC of DFIG. In this control technique, the synchronous reference frame is usually aligned with the stator-flux space vector, providing a decoupled control of the active and reactive powers of the machine [5]-[8]. The  $d$ -axis of the complex frame is fixed to the stator-flux space-vector and rotates anti-



clockwise at the synchronous speed of  $\omega_s$  ( $\omega = \omega_s$ ). If the slip angle is defined by  $\theta_{\text{slip}} = \theta_s - \theta_r$ , the space-vector relationship between the stationary frame, the rotor frame rotating at  $\omega_r$ , and synchronous frame rotating at  $\omega_s$  can be defined as shown in Figure 3-6. It is clear that

$$\mathbf{F}^e = \mathbf{F}^s \cdot e^{-j\theta_s} \quad 3-14$$

$$\mathbf{F}^r = \mathbf{F}^e \cdot e^{-j(\theta_s - \theta_r)} = \mathbf{F}^e \cdot e^{-j\theta_{\text{slip}}} \quad 3-15$$

where  $\mathbf{F}$  represents the voltage, current, or flux space vector.

The stator voltage is usually a constant quantity in the stator-flux frame; therefore, the term  $(d\Phi_s^e / dt)$  can be assumed equal to zero. If the  $R_s$  value is also neglected in (3-3), this equality can be simplified to

$$\mathbf{V}_s^e = j\omega_s \Phi_s^e \Rightarrow \mathbf{V}_s^e = jV_{sq} = j\omega_s \cdot L_m |\mathbf{I}_m^e| \quad 3-16$$

Substituting (3-16) in (3-10) and making use of (3-5) and (3-7) give the stator active and reactive power as

$$\begin{cases} P_s = 1.5\omega_s L_m |\mathbf{I}_m^e| \cdot I_{rq} \\ Q_s = 1.5\omega_s L_m |\mathbf{I}_m^e| \cdot (I_{rd} - |\mathbf{I}_m^e|) \end{cases} \quad 3-17$$

From (3-17), it is observed that the stator active and reactive power can be independently control through regulating  $I_{rq}$  and  $I_{rd}$ , respectively. Accordingly, the field-oriented vector control scheme for the RSC can be configured as shown in Figure 3-7:

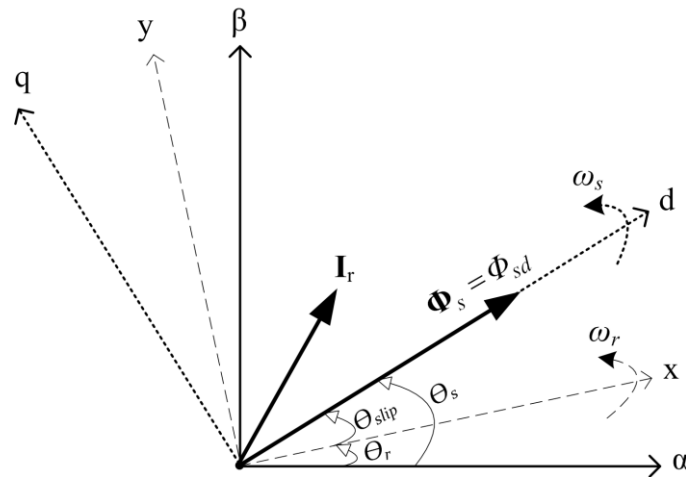


Figure 3-6 Phasor diagram of DFIG in the synchronous stator-flux frame.

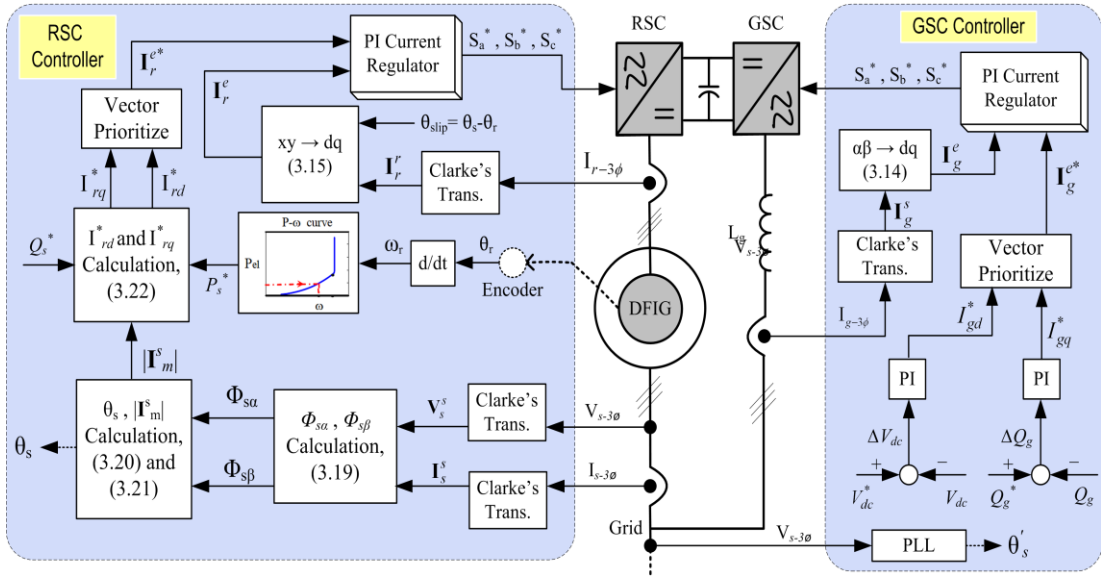


Figure 3-7 Field-oriented vector control of the RSC and GSC

1. Clarke's transformation is used to obtain the vector representation of the measured three-phase signals. Stator voltage and current signals are measured in the stationary frame ( $I_{s-3\phi}^s$  and  $V_{s-3\phi}^s$ ); hence, their corresponding vectors will also be calculated in the same frame, giving  $V_s^s$  and  $I_s^s$  vectors. The rotor current vector, on the other hand, will be obtained in the rotor reference frame ( $I_r^r$ ).
2. According to (3-14) and (3-15), the stator-flux angle  $\theta_s$  and rotor angle  $\theta_r$  are needed for the current vector transformation. The rotor angle is directly measured using a position encoder, whereas the stator-flux phase-angle can be estimated by expressing (3-3) in the stationary frame, as

$$V_s^s = R_s I_s^s + \frac{d\Phi_s^s}{dt} \quad 3-18$$

From (3-18), the quadrature components of the stator-flux vector in the stationary frame can be calculated by the integrations given in (3-19),

$$\begin{aligned} \Phi_{s\alpha} &= \int (V_{s\alpha} - R_s I_{s\alpha}) dt \\ \Phi_{s\beta} &= \int (V_{s\beta} - R_s I_{s\beta}) dt \end{aligned} \quad 3-19$$

However, using pure integration leads to several problems such as dc-offset and dc-drift in practice. Therefore, the integral operator in (3-19) is solved using digital band-pass filters [5]-[6]. These will immune the overall control scheme to the variations of machine parameters (i.e. stator resistance) and eliminate the resultant steady-state errors.

3. The stator-flux angle at each instant can be calculated by

$$\theta_s = \arctan(\Phi_{s\beta} / \Phi_{s\alpha}) \quad 3-20$$

Also, the amplitude of the magnetization current can be estimated using (3-3) as

$$|\Phi_s^s| = L_m |\mathbf{I}_m^s| \Rightarrow |\mathbf{I}_m^s| = \frac{\sqrt{\Phi_{s\alpha}^2 + \Phi_{s\beta}^2}}{L_m} \quad 3-21$$

4. The amplitude of the magnetization current vector does not change in different reference frames, i.e.,  $|\mathbf{I}_m^s| = |\mathbf{I}_m^e|$ . Therefore, the rotor command vector in the stator-flux frame can be calculated using (3-17):

$$\mathbf{I}_r^{e*} = I_{rd}^* + jI_{rq}^* \rightarrow \begin{cases} I_{rq}^* = \frac{P^*}{1.5\omega_s L_m \cdot |\mathbf{I}_m^s|} \\ I_{rd}^* = \frac{Q^*}{1.5\omega_s L_m \cdot |\mathbf{I}_m^s|} + |\mathbf{I}_m^s| \end{cases} \quad 3-22$$

5. In (3-22), the active power command signal ( $P^*$ ) is obtained based on the optimal power-speed curve given by the WT manufacturers, whereas the  $Q^*$  value is defined through the grid code regulations stipulated by the system operators. It must be noted that the outer power control loop is not discussed here because the transient response of DFIG-based WT is mainly dominated by their inner control loop with much smaller time constants.

6. The rotor command vector in (3-22) is expressed in the stator-flux frame whereas the RSC output current is measured in the rotor reference frame. Thus, the  $\mathbf{I}_r^r$  vector must be transformed to the synchronous frame using (3-15).

7. Finally, the rotor command vector and the measured current vector are fed to a PI current regulator to generate the appropriate gating signals for the RSC.

### 3.3.3.1 Using PI current regulator in the RSC

In this current regulator, the tracking error between the reference and the actual rotor current vectors (i.e., the difference between  $\mathbf{I}_r^{e*}$  and  $\mathbf{I}_r^e$ ) is processed by a PI compensator to estimate the RSC output voltage vector. The rotor voltage equation in the synchronous frame is obtained by substituting  $\omega$  with  $\omega_s$  in (3-9) as

$$\mathbf{V}_r^e = R_r \mathbf{I}_r^e + L_\sigma \frac{d\mathbf{I}_r^e}{dt} + j\omega_{slip} \cdot (L_\sigma \mathbf{I}_r^e + \mathbf{\Phi}_s^e) \quad 3-23$$

Separating (3-23) into the  $d$ - and  $q$ - components yields

$$\frac{d}{dt} \begin{bmatrix} I_{rd} \\ I_{rq} \end{bmatrix} = [\mathbf{A}] \cdot \begin{bmatrix} I_{rd} \\ I_{rq} \end{bmatrix} + \frac{\omega_{slip}}{L_\sigma} \cdot \begin{bmatrix} \Phi_{sq} \\ -\Phi_{sd} \end{bmatrix} + \frac{1}{L_\sigma} \cdot \begin{bmatrix} V_{rd} \\ V_{rq} \end{bmatrix} \quad 3-24$$

where

$$[\mathbf{A}] = \begin{bmatrix} -R_r/L_\sigma & \omega_{slip} \\ -\omega_{slip} & -R_r/L_\sigma \end{bmatrix}.$$

According to (3-24), the auxiliary input voltage of  $[U_{rd} \ U_{rq}]$  is defined as

$$\begin{aligned} U_{rd} &= dI_{rd}/dt = k_{pr}(I_{rd}^* - I_{rd}) + k_{ir} \int (I_{rd}^* - I_{rd}) dt \\ U_{rq} &= dI_{rq}/dt = k_{pr}(I_{rq}^* - I_{rq}) + k_{ir} \int (I_{rq}^* - I_{rq}) dt \end{aligned} \quad 3-25$$

where  $k_{pr}$  and  $k_{ir}$  are the proportional and integral gains of the PI compensator, respectively. Based on (3-23) and (3-24), the rotor control voltages in the synchronous frame are obtained as

$$\begin{bmatrix} V_{rd} \\ V_{rq} \end{bmatrix} = L_\sigma \begin{bmatrix} U_{rd} \\ U_{rq} \end{bmatrix} - L_\sigma [\mathbf{A}] \cdot \begin{bmatrix} I_{rd} \\ I_{rq} \end{bmatrix} - \omega_{slip} \begin{bmatrix} \Phi_{sq} \\ -\Phi_{sd} \end{bmatrix} \quad 3-26$$

The rotor voltage vector in the  $d$ - $q$  frame is then transferred to the rotor frame using (3-14). Finally, the control voltage vector ( $\mathbf{V}_r^{xy}$ ) is fed to a space vector modulation (SVM) unit to generate the gating signals for the RSC switches. The control structure of the studied PI current regulator is shown in Figure 3-8.

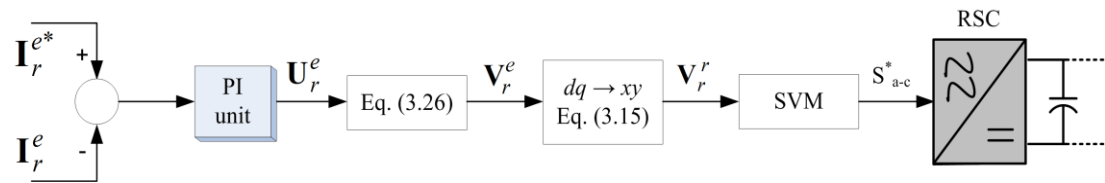


Figure 3-8 PI current regulator in the RSC

From Figure 3-8, it is observed that when the standard PI current regulator is used in the RSC, the rotor current vector follows the command vector through changing the RSC output voltage vector. Therefore, the RSC must be represented in the DFIG equivalent circuit as a current-regulated voltage source. This means that the rotor current waveform can be affected by the stator voltage under grid fault conditions.

### 3.3.4 Vector control of the GSC

The output current of the GSC can be controlled using the same vector control scheme. However, the GSC controller is usually synchronized with the grid-voltage space vector, readily extractable by a PLL system. If (3-3) is rewritten in the voltage-oriented frame (with  $\mathbf{V}_s = V_{sd}$ ), the active and reactive powers of the GSC will be obtained as

$$P_g = 1.5V_{sd}I_{gd} \quad 3-27$$

$$Q_g = 1.5V_{sd}I_{gq} \quad 3-28$$

Substituting (3-27) in (3-11) defines the variations of the dc-link voltage as

$$C \cdot V_{dc} \frac{dV_{dc}}{dt} = P_r - 1.5V_{sd}I_{gd} \quad 3-29$$

According to (3-29), the variation of the dc-link voltage can be controlled through the  $d$ -component of the GSC current ( $I_{gd}$ ). On the other hand, the reactive power of the GSC is controlled through the  $q$ -component of the current vector. Accordingly, the GSC vector control scheme can be configured as shown in Figure 3-7:

1. A PLL system is used to extract the synchronization signal from the voltage.
2. Two PI control blocks are used to calculate the  $I_{gd}^*$  and  $I_{gq}^*$  current components from the error signals of  $\Delta V_{dc}$  and  $\Delta Q_g$ , respectively.
3. Clarke's transformation is used to obtain the vector representation of the measured GSC three-phase current ( $\mathbf{I}_{g-3\phi}^s$ ), followed by transforming it to the synchronous frame.
4. The resulting current vector ( $\mathbf{I}_g^s$ ) along with the GSC command vector ( $\mathbf{I}_g^{s*}$ ) are fed to a PI current regulator that aims to generate the appropriate gating signals in the GSC.

#### 3.3.4.1 Using PI current regulator in the GSC

The control structure of the GSC current regulator is similar to the one used in the RSC. The GSC voltage equation in the synchronous frame is obtained by substituting  $\omega$  with  $\omega_s$  in (3-13), which gives

$$\mathbf{V}_g^e = R_g \mathbf{I}_g^e + L_g \frac{d\mathbf{I}_g^e}{dt} + j\omega_s L_g \mathbf{I}_g^e + \mathbf{V}_s^e \quad 3-30$$

Separating (3-30) into the  $d$ - and  $q$ - components yields

$$\frac{d}{dt} \begin{bmatrix} I_{gd} \\ I_{gq} \end{bmatrix} = [\mathbf{A}] \cdot \begin{bmatrix} I_{gd} \\ I_{gq} \end{bmatrix} + \frac{1}{L_g} \cdot \begin{bmatrix} V_{gd} - V_{sd} \\ V_{gq} \end{bmatrix} \quad 3-31$$

where

$$[\mathbf{A}] = \begin{bmatrix} -R_g/L_g & +\omega_s L_g \\ -\omega_s L_g & -R_g/L_g \end{bmatrix}.$$

According to (3-31), the auxiliary input voltage of  $[U_{gd} \ U_{gq}]$  is defined as

$$\begin{aligned} U_{gd} &= dI_{gd}/dt = k_{pg}(I_{gd}^* - I_{gd}) + k_{ig} \int (I_{gd}^* - I_{gd}) dt \\ U_{gq} &= dI_{gq}/dt = k_{pg}(I_{gq}^* - I_{gq}) + k_{ig} \int (I_{gq}^* - I_{gq}) dt \end{aligned} \quad 3-32$$

where  $k_{pg}$  and  $k_{ig}$  are the proportional and integral gains of the PI compensator, respectively. Based on (3-31) and (3-32), the GSC control voltages in the synchronous frame are obtained as

$$\begin{bmatrix} V_{gd} \\ V_{gq} \end{bmatrix} = L_g [\mathbf{A}] \cdot \begin{bmatrix} I_{gd} \\ I_{gq} \end{bmatrix} + L_g \begin{bmatrix} U_{gd} \\ U_{gq} \end{bmatrix} + \begin{bmatrix} V_{sd} \\ 0 \end{bmatrix} \quad 3-33$$

The overall control structure for the GSC current regulator is shown in Figure 3-9.

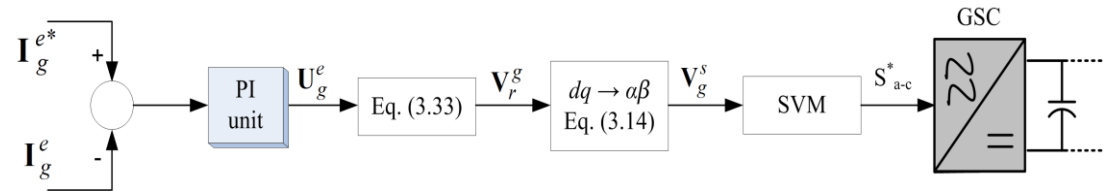


Figure 3-9 PI current regulator in the GSC

### 3.4 THEORETICAL ANALYSIS OF THE DFIG BEHAVIOUR

This section presents the theoretical analysis of the DFIG response under various fault conditions. The presented analysis aims to address the shortcomings of [64] and [65], i.e., the effect of phase-angle jump is taken into account and the rotor winding is not assumed in the open-circuit condition. As a result, this study is not restricted to overvoltages appear under fault conditions, but explains the origin of large overcurrents observed in the rotor winding during different types of voltage sags.

The  $\mathbf{V}_r$  vector can be expressed in the rotor frame by substituting  $\omega = \omega_r$  in (3-9),

$$\mathbf{V}_r^r = \mathbf{V}_{ro}^r + (R_r \mathbf{I}_r^r + L_\sigma \frac{d\mathbf{I}_r^r}{dt}) \quad \text{where} \quad \mathbf{V}_{ro}^r = \frac{d\Phi_s^r}{dt} \quad 3-34$$

It is seen from (3-34) that the rotor voltage is jointly defined by two components: the electromagnetic force (EMF) induced by the stator-flux space vector and the voltage drops across  $R_r$  and  $L_\sigma$ , as shown in Figure 3-10. Parameters  $R_r$  and  $L_\sigma$  are usually very small; therefore, the first term in (3-34) can be neglected as compared to the induced EMF, i.e.,  $\mathbf{V}_r^r \approx \mathbf{V}_{ro}^r$  [64].

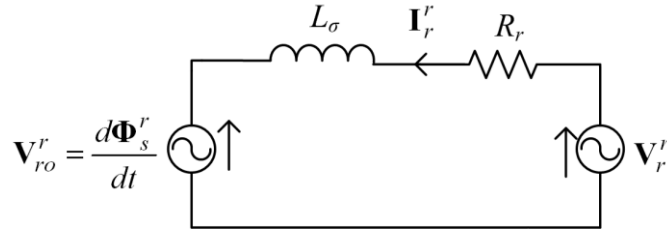


Figure 3-10 Equivalent circuit of the machine viewed in the rotor frame.

### 3.4.1 DFIG operation under normal operation conditions

Eq. (3-16) is valid under normal operation conditions, where the stator-flux vector is fixed with respect to the synchronous frame. Transforming this equation from the stationary to the rotor frame yields to

$$\Phi_s^r = \Phi_s^s \cdot e^{-j\omega_r t} = (\mathbf{V} / j\omega_s) \cdot e^{j(\omega_s - \omega_r)t} \quad 3-35$$

Replacing (3-35) in (3-34) gives the rotor voltage equation as

$$\mathbf{V}_{ro}^r = \frac{d\Phi_s^r}{dt} = \frac{\omega_s - \omega_r}{\omega_s} \cdot \mathbf{V} \cdot e^{j(\omega_s - \omega_r)t} = s \cdot \mathbf{V} \cdot e^{js\omega_s t} \quad 3-36$$

From (3-36), it can be seen that the induced EMF is proportional to the machine slip and rotates slowly with the frequency of  $s\omega_s$ . The DFIG technology is to be used in the applications with limited slip range (less than  $\pm 0.3$  pu); thus, the rotor voltage will be equal to a reduced fraction of the stator-voltage. This fact will be used to design the RSC devices and calculate, with some safety margin, the maximum voltage needed at the RSC output terminals. The nominal output voltage of the RSC must be large enough to dominate the induced EMF and in turn, be capable of controlling the rotor current according to the adopted vector control scheme.

### 3.4.2 DFIG operation under symmetrical sag conditions

Now assume that a balanced three-phase fault occurs at  $t = 0$  s, causing a type A voltage sag with depth  $p$  and phase-angle jump of  $\delta$  at generator terminals. Accordingly, the stator-flux can be defined by

$$\mathbf{V}_s^s(t) = \begin{cases} \mathbf{V} \cdot e^{j\omega_s t} & , \text{for } t < 0 \\ (1-p) \cdot \mathbf{V} \cdot e^{j(\omega_s t + \delta)} & , \text{for } t \geq 0 \end{cases} \quad 3-37$$

Based on (3-16) and (3-37), the steady-state component of the stator-flux, imposed by the supply voltage, can be defined by

$$\Phi_{sf}^s(t) = \begin{cases} \frac{\mathbf{V}}{j\omega_s} \cdot e^{j\omega_s t} & , \text{for } t < 0 \\ \frac{(1-p) \cdot \mathbf{V}}{j\omega_s} \cdot e^{j(\omega_s t + \delta)} & , \text{for } t \geq 0 \end{cases} \quad 3-38$$

However, the stator-flux is a state variable and cannot instantaneously vary from the first to the second value in (3-38). To fulfil this constraint, the stator-flux response must include a transient part that guarantees its gradual change at the fault onset. Eq. (3-34) indicates that the induced EMF is equal to the rotor voltage when the rotor winding is in open-circuit condition ( $\mathbf{I}_r' = 0$ ). By applying this in (3-3) and (3-5), the differential equation describing the stator-flux behaviour can be obtained as

$$\mathbf{V}_s^s(t) = \frac{d\Phi_s^s(t)}{dt} - \frac{R_s}{L_m} \Phi_s^s(t) \quad 3-39$$

The solution of (3-39) is constituted of two parts, the homogenous and non-homogenous components. The non-homogenous part, referred to as the forced or steady-state flux ( $\Phi_{sf}$ ), is defined by (3-38): its amplitude is instantaneously proportional to the stator-flux; thus, it suddenly changes to  $(1-p) \cdot \mathbf{V} \cdot e^{j\delta}$  at the fault instant. On the other hand, the homogenous part corresponds to the natural response of the stator-flux to the sudden variations in the grid voltage. This transient term, referred to as the natural flux component ( $\Phi_{sn}$ ), can be generally expressed by

$$\Phi_{sn}^s(t) = \Phi_{sn} \cdot e^{-t/\tau_s} \quad 3-40$$

where  $\tau_s = R_s/L_m$  is the stator time constant and  $\Phi_{sn}$  is the initial value of the natural flux. This vector is calculated based on the fact that the stator-flux value must be identical immediately before and after the sag, i.e.,  $\Phi_s^s(0_-) = \Phi_s^s(0_+)$ . Accordingly,



$$\Phi_s^s(0_-) = \Phi_{sf}^s(0_+) + \Phi_{sn}^s(0_+) \quad 3-41$$

The stator-flux vector for  $t > 0$  is obtained by substituting (3-38) and (3-40) in (3-41), which finally results in

$$\Phi_s^s(t) = \frac{(1-p) \cdot V}{j\omega_s} e^{j(\omega_s t + \delta)} + \frac{(1-e^\delta + pe^\delta) \cdot V}{j\omega_s} e^{-t/\tau_s} \quad 3-42$$

To calculate the rotor voltage, Eq. (3-42) needs to be expressed in the rotor frame

$$\begin{aligned} \Phi_s^r(t) = \Phi_{sf}^r(t) + \Phi_{sn}^r(t) &= \frac{(1-p) \cdot V}{j\omega_s} e^{j(\omega_s t + \delta - \omega_r t)} \\ &+ \frac{(1-e^\delta + pe^\delta) \cdot V}{j\omega_s} e^{-t/\tau_s} e^{-j\omega_r t} \end{aligned} \quad 3-43$$

Therefore, the induced EMF originated from the forced and the natural flux components of flux can be defined as

$$\mathbf{V}_{ro}^r(t) = \mathbf{V}_{rf}^r(t) + \mathbf{V}_{rn}^r(t) = d\Phi_{sf}^r(t)/dt + d\Phi_{sn}^r(t)/dt \quad 3-44$$

The forced component of EMF can be obtained by substituting the first term of (3-43) in (3-44), as

$$\mathbf{V}_{rf}^r(t) = s \cdot (1-p) \cdot V \cdot e^{j(s\omega_s t + \delta)} \quad 3-45$$

From (3-45), it is evident that the  $\mathbf{V}_{rf}^r$  vector (rotating with the slip frequency of  $s\omega_s$ ) is defined by the retained supply voltage and always has a small amplitude proportional to the machine slip. On the other hand, the natural induced EMF corresponds to the second term of (3-43), which is defined by

$$\mathbf{V}_{rn}^r = -V \cdot (1-e^\delta + pe^\delta) \cdot \frac{(1/\tau_s + j\omega_r)}{j\omega_s} \cdot e^{-t/\tau_s} e^{-j\omega_r t} \quad 3-46$$

If the term ' $1/\tau_s$ ' is neglected in (3-46), it can be simplified to

$$\mathbf{V}_{rn}^r = -V \cdot (1-e^\delta + pe^\delta) \cdot (1-s) \cdot e^{-t/\tau_s} e^{-j\omega_r t} \quad 3-47$$

Based on (3-47), the natural induced EMF (rotating with  $\omega_r$ ) appears just after the fault occurrence and exponentially decays to zero with the stator time constant ( $\tau_s$ ). However, the initial value of natural EMF can be severely large as it is proportional to ' $1-s$ '. Therefore, this is very likely that the natural induced EMF exceeds the RSC voltage rating just after the fault instant. Consequently, the control of rotor current will be lost temporarily due to the severe overvoltages that appear in the rotor winding. Referring to Figure 3-10, these transient overvoltages are imposed on the

impedance formed by ' $R_s + j\omega_r L_\sigma$ '. The rotor impedance at this frequency is small (typically less than 0.5 pu); thus, overcurrents with magnified amplitudes can flow in the rotor winding and cause the destruction of semi-conductor switches of the RSC if no protection device is incorporated.

The situation becomes even worse when the sag is associated with large phase-angle jumps. Figure 3-11 compares the initial values of  $\mathbf{V}_m$  for two extreme impedance angles ( $\alpha = 0^\circ$  and  $\alpha = -60^\circ$ ), when the machine operates at three various slips preceding the fault ( $s = +0.25, 0$ , or  $-0.25$  pu). It can be observed that the presence of phase-angle jump always leads to larger natural EMFs. The adverse impact of phase-angle jump is more notable for sags with the remnant voltage of 20–80% where the initial value of  $\mathbf{V}_m$  increases by 25–45%. It is also evident that the initial value of  $\mathbf{V}_m$  is proportional to the machine speed, i.e. larger natural EMFs will be produced at higher rotation speeds. Finally, it can be concluded that the most onerous LVRT conditions will be imposed on the DFIG-based WT when the machine is operating at the highest speed and the sag is associated with large phase-angle jumps.

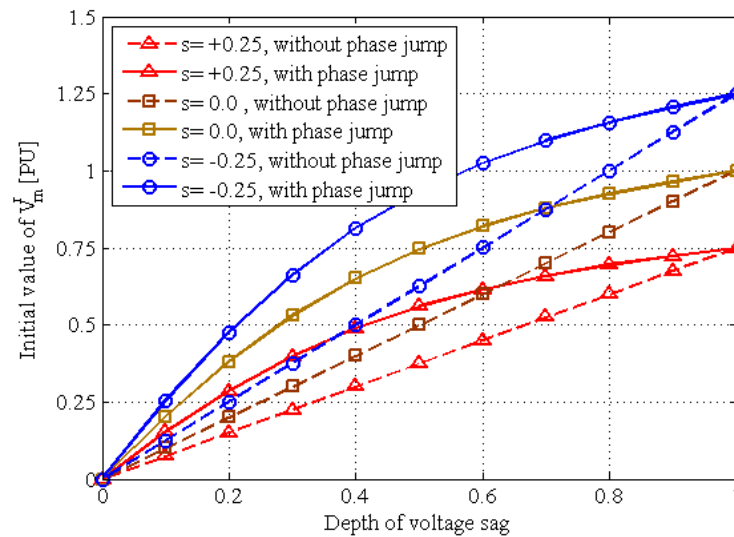


Figure 3-11 Initial value of  $\mathbf{V}_m$  with and without phase-angle jump.

### 3.4.3 DFIG operation under asymmetrical sag conditions

It is already discussed that the zero-sequence component of voltage cannot reach the DFIG terminals because it will be filtered by the  $Y\Delta$  transformers used between the PCC and individual wind generators. Therefore, asymmetrical voltage sags, caused

by any unbalanced fault, can be decomposed into positive and negative-sequence components, expressed by

$$\mathbf{V}_s^s = \mathbf{V}_1 e^{j\omega_s t} + \mathbf{V}_2 e^{-j\omega_s t} \quad 3-48$$

where  $\mathbf{V}_1$  and  $\mathbf{V}_2$  represent the initial vectors of the positive and negative sequence components, respectively. The positive sequence of the stator voltage generates a flux component rotating anti-clockwise at the synchronous speed whereas the negative sequence of the stator flux rotates at the same speed but in the opposite direction. The forced stator-flux is thus defined by

$$\Phi_{sf}^s = \Phi_1^s + \Phi_2^s = \frac{\mathbf{V}_1 e^{j\omega_s t}}{j\omega_s} - \frac{\mathbf{V}_2 e^{-j\omega_s t}}{j\omega_s} \quad 3-49$$

Transferring (3-49) to the rotor reference frame results in

$$\Phi_{sf}^r = \Phi_{sf}^s e^{-j\omega_r t} = \frac{\mathbf{V}_1 e^{j(\omega_s - \omega_r)t}}{j\omega_s} - \frac{\mathbf{V}_2 e^{-j(\omega_s + \omega_r)t}}{j\omega_s} \quad 3-50$$

Accordingly, the EMF induced by the forced flux is obtained by

$$\mathbf{V}_{rf}^r = d\Phi_{sf}^r / dt = \mathbf{V}_1 \cdot s \cdot e^{js\omega_s t} - \mathbf{V}_2 \cdot (2-s) \cdot e^{-j(2-s)\omega_s t} \quad 3-51$$

Based on (3-51), it can be seen that the positive sequence component rotates at the slip frequency with a small amplitude proportional to the machine slip. On the contrary, since the second term of (3-51) includes a factor close to 2, its amplitude can be considerably large for sags with even very small negative-sequence component of the stator voltage. The resulting negative-sequence EMF, with the frequency approximately equal to twice the grid frequency, is imposed to the rotor winding impedance of ' $R_s + j(2-s)\omega_s L_\sigma$ '. This will generate large steady-state current ripples during the sag.

In addition, a natural flux component must be included to insure the continuity of the stator-flux trajectory at the beginning and end of fault. However, there is a distinctive difference in this case compared to the symmetrical faults: the initial value of the natural flux component depends not only on the depth and type of sag but also on the fault occurrence instant. In other words, to calculate the initial value of the natural response, positive and negative sequence components of the forced flux must be calculated for the simulated sag condition. Referring to (3-51), the highest natural flux occurs when the positive and negative sequence components are aligned in the

opposite direction. In such an extreme case, the stator forced flux, which is equal to the vector summation of positive and negative components, has the minimum possible amplitude just after the fault instant. Therefore, the highest value of the natural flux is needed to avoid abrupt changes of the stator-flux vector. Since the impedance of the rotor winding for the negative-sequence is almost twice the impedance seen by the natural EMF, the transient overshoots of the rotor current are usually larger than the oscillating component.

Figure 3-12 shows the supply voltage decomposition when the wind generator is subjected to the asymmetrical sag types of C or D. It can be seen that higher negative sequence is always resulting if the sag is associated with phase-angle jump. This, in turn, produces oscillations with larger peak-to-peak ripples. Since the positive sequence component decreases at the same time, amplitudes of positive and negative components of the voltage become closer. Consequently, there is a notable reduction in the magnitude of the minimum possible forced flux, so larger natural components might be needed to avoid the flux discontinuity. This means higher voltage and current overshoots in the rotor winding at the start and end of the sag.

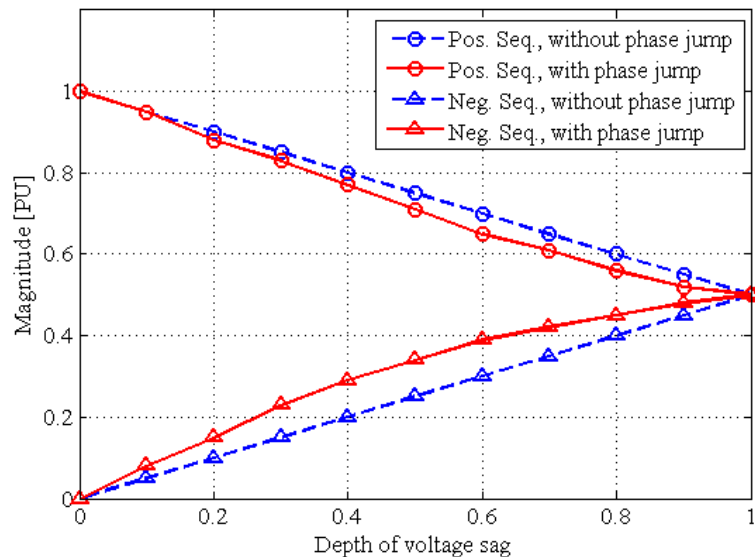


Figure 3-12 Voltage decomposition into the positive and negative sequence components, with and without phase-angle jump (sag types C and D).

### 3.5 SIMULATION RESULTS

In this section, extensive simulation studies are carried out to examine the operation of DFIG-based WTs under different types of voltage sags. It is shown that symmetrical and asymmetrical grid faults affect the DFIG operation in different ways and phase-angle jumps have large detrimental impacts on the DFIG transient response. Moreover, the effects of initial point-on-wave instant and the voltage recovery parameters are examined.

The simulation analysis is conducted using Matlab/Simulink. Figure 3-13 shows the schematic diagram of the simulated network with the parameters given in the Appendix B. The vector control schemes adopted in the RSC and GSC are developed based on [5]. A programmable voltage source is implemented to simulate various sag conditions that can be experienced at the generator terminals.

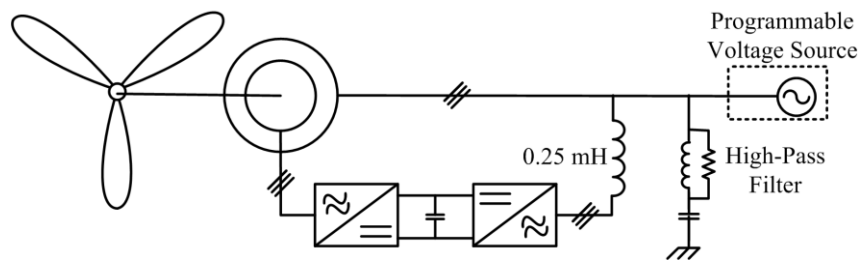


Figure 3-13 Schematic circuit diagram of the simulated network.

#### 3.5.1 Symmetrical faults and voltage recovery process

The DFIG operation under symmetrical three-phase faults is tested by imposing a 60% type A sag with zero phase-angle jump (Point B<sub>1</sub> in Figure 3-2). The fault current angle has been set to  $\psi = 80^\circ$  and the machine rotates with  $\omega_r = 1.2$  pu. It is known that the most critical electrical parameters during sag conditions are the stator voltage, rotor current and dc-link voltage [27]-[28]. Figure 3-14 to Figure 3-16 show the simulation results with three possibilities of the sag recovery (types A<sub>0</sub>, A<sub>1</sub> and A<sub>3</sub>). The stator-voltage waveforms, zoomed at the voltage recovery instant, are shown in Figure 3-14. The main observations are as follows:

- Figure 3-15: The fault causes a large transient overcurrent of 1.75 pu in the rotor winding at  $t = 0.1$  s regardless of the recovery type. This overshoot is originated from the natural response of the stator flux. The corresponding

EMF component is fixed with respect to the stationary frame; thus, it generates a current component with  $f=1.2$  PU = 60 Hz in the rotor winding. As the natural EMF decays to zero after 0.1 s, the RSC regains the controllability of the current in the rotor winding and regulates it back to the prefault command value. Note that there is no steady-state ripple during the fault because the resulting voltage sag (type A) does not include any negative-sequence component.

- Figure 3-16: Large overcurrents in the rotor winding lead to the sudden increase of the active power injected from the RSC into the dc-link capacitor. However, the partially-scaled GSC does not have enough capacity to immediately transfer the superfluous power from the capacitor to the grid. As a result, the dc-link voltage temporarily increases to 1.2 PU. Note that the GSC capability to transfer the active power has been further decreased during the fault because the grid voltage has dropped by 40%.
- Figure 3-15 and Figure 3-16: The overshoots in the rotor current and dc-link voltage at the fault clearance instant vary depending on the voltage recovery type. The most severe transients will be observed if the breakers are assumed to clear the three-phase fault in one step (unrealistic type A<sub>0</sub>). However, the overshoots at  $t_{f1}$  are still smaller than the initial point-on-wave instant ( $t_i$ ) as the GSC capacity to transfer the superfluous power will increase after the fault clearance instant due to the full availability of the grid voltage.
- Figure 3-15 and Figure 3-16: The voltage recovery process will generate smaller overshoots if the operational constraints of the circuit breakers are taken into account and three-phase faults are considered to be cleared at the natural zero-crossing points of the phase currents. By comparing the simulation results for type A<sub>0</sub> with types A<sub>1</sub> and A<sub>3</sub>, it is clear that overshoots in the rotor current and dc-link voltage decrease from 1.7 to 1.1 PU and from 1.15 to 1.03 PU, respectively. These observations can be justified by analysing the sequence components of the stator-flux during the voltage recovery process. For type A<sub>0</sub>, the full voltage recovery will take place in one step at the final point-on-wave ( $t_{f1}$ ). This would generate a large sudden change of 0.4 PU in the stator forced flux. Consequently, a large natural flux

component will be required to provide the continuity in the stator-flux trajectory and large overshoots will appear in the rotor winding. However, for types  $A_1$  and  $A_3$ , the three-phase fault will be cleared in two and three consecutive steps, respectively. According to Table 3-2, this means that the type  $A_1$  develops to type  $C_a$  and the type  $A_3$  develops to type  $E_{2a}$  and then type  $B_b$  before the full recovery, as shown in Figure 3-14. As a result, the forced component of the stator flux gradually changes in two or three consecutive steps and smaller natural flux components are required to avoid the stator-flux discontinuity at each step.

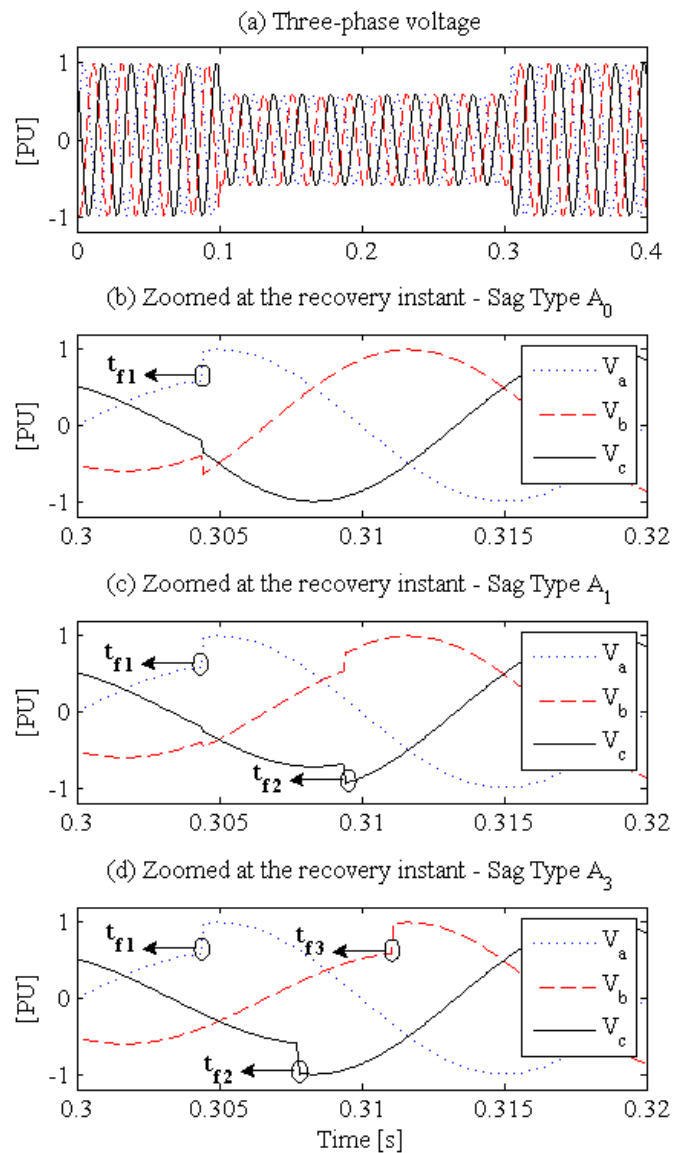


Figure 3-14 Supply voltage (zoomed at the fault clearance instant) under three-phase faults (type A) with different possibilities of the voltage recovery.

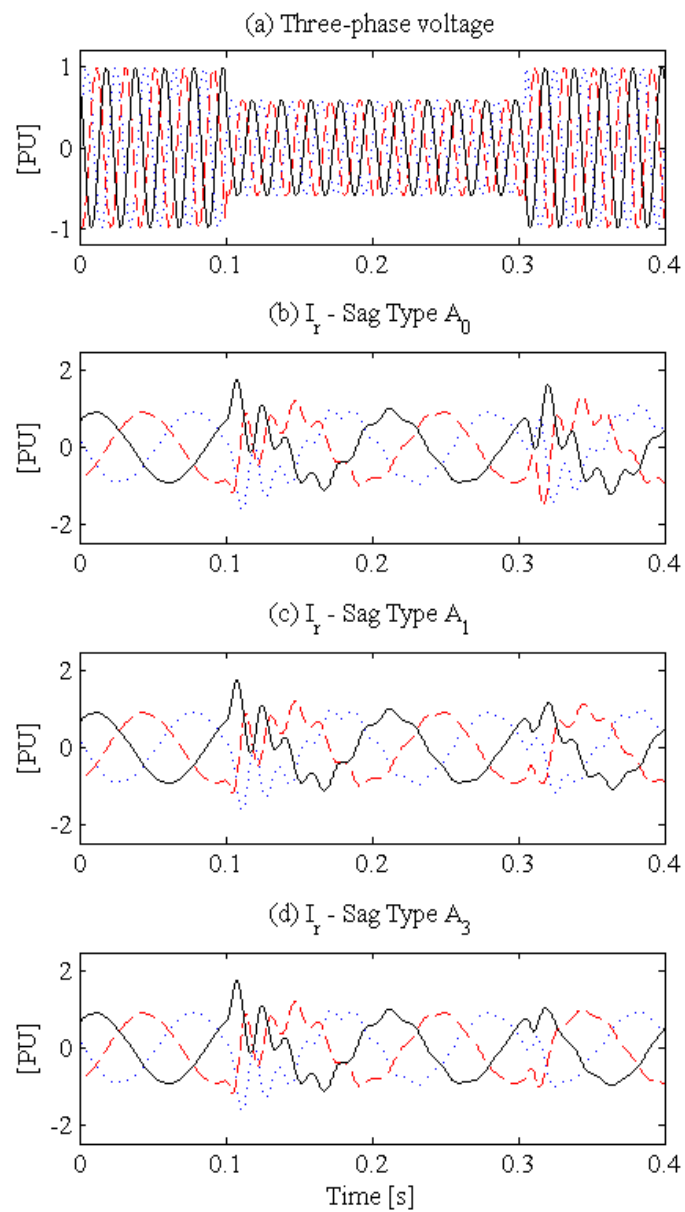


Figure 3-15 Rotor current under three-phase faults (type A) with different possibilities of the voltage recovery.



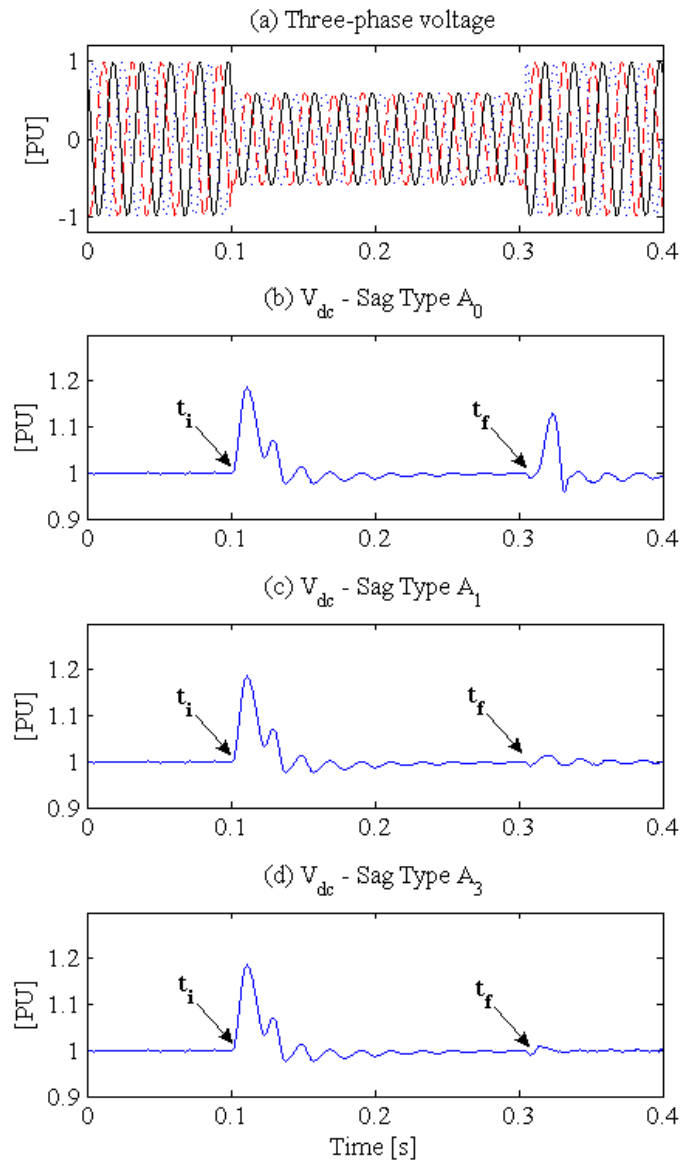


Figure 3-16 Dc-link voltage under three-phase faults (type A) with different possibilities of the voltage recovery.

Figure 3-17 shows the influence of the fault current angle on the dc-link voltage at the fault clearance instant. It can be seen that the overshoots in the dc-link voltage increases by 10% when the fault current angle changes from  $85^\circ$  to  $45^\circ$ . Therefore, it is concluded that more severe voltage recovery conditions will be experienced in the DFIG-based wind farms connected to distribution systems or located offshore. Also note that the dc-link voltage overshoot under the worst scenario ( $\psi = 45^\circ$ ) is still smaller than the unrealistic voltage recovery overshoot of 1.15 PU (experienced in type  $A_0$ ). Similar observations have been made about other types of voltage sags with different possibilities of voltage recovery.

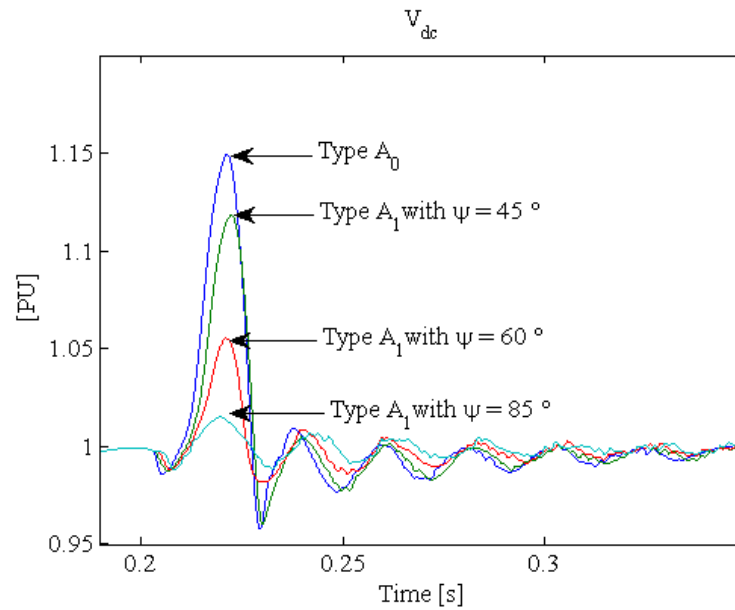


Figure 3-17 Influence of the fault current angle,  $\psi$ , on the dc-link voltage during the voltage recovery process.

### 3.5.2 Asymmetrical faults and phase-angle jump

The DFIG operation under asymmetrical faults is examined through imposing a 60% type C voltage sag at the wind generator terminals. Simulation results, presented in Figure 3-18 to Figure 3-20, show the effects of the initial point-on-wave instant and phase-angle jump on the DFIG transient response. For the theoretical analysis of simulation results, the grid voltage is decomposed into the positive and negative sequence components, given in Table 3-3. The main observations are:

- Figure 3-19: If the sag type C occurs at  $t_i = T = 20$  ms, the positive- and negative-sequence components of the grid voltage are aligned in the same direction (Point B<sub>1</sub> in Table 3-3:  $\mathbf{V}_+ = 0.8 \angle 0^\circ$  and  $\mathbf{V}_- = 0.2 \angle 0^\circ$ ). Consequently, the forced flux component will be equal to 1.0 PU just after the fault instant and no natural flux component will be required to provide the stator flux continuity. Likewise, there is no transient overshoot in the rotor current or dc-link voltage. However, the presence of the negative sequence in the stator voltage generates large current ripples in the rotor winding, with the peak-to-peak magnitude of 0.6 PU and the frequency of  $(2-s)f_s = 110$  Hz. Similar double-frequency oscillations ( $\pm 2.3\%$ ) can be observed in the dc-link voltage.

- Figure 3-19: The relative rotation speed of the positive- and negative-sequence components of the grid voltage is equal to  $2\omega_s$ . Therefore, if the sag occurs at  $t_i = T/4 = 5$  ms, the positive and negative sequence components of the supply voltage will be aligned in the opposite directions ( $\mathbf{V}_+ = 0.8 \angle 90^\circ$  and  $\mathbf{V}_- = 0.2 \angle -90^\circ$ ). In such an extreme case, the stator forced flux has the minimum possible value just after the sag (equal to  $0.6 \angle 90^\circ$ ) and the large natural flux response of 0.4 PU will be needed to avoid discontinuity in the stator flux trajectory. This will generate large transient overshoots of 2.0 PU and 1.2 PU in the rotor current and dc-link voltage, respectively. The natural response decays after 0.1 s whereas the negative-sequence oscillations remain unsuppressed during the fault period.
- Figure 3-19: For offshore wind farms, the 60% voltage sag will be associated with a phase-angle jump of  $-31^\circ$ , i.e.,  $\mathbf{V}_{\text{sag}} = 0.6 \angle -31^\circ$ . This sag condition leads to the positive- and negative-sequence components of  $\mathbf{V}_+ = 0.77 \angle -12^\circ$  and  $\mathbf{V}_- = 0.29 \angle 33^\circ$  for the type C sag starting at  $t_i = 0$  s (refer to Point B<sub>3</sub> in Table 3-3). Accordingly, if the sag occurs at  $t_i = T/4 = 5$  ms, the sequence components of the supply voltage just after the fault instant are equal to  $\mathbf{V}_+ = 0.77 \angle 78^\circ$  and  $\mathbf{V}_- = 0.29 \angle -57^\circ$ ; accordingly, the forced flux will be equal to  $0.6 \angle 58^\circ$  and a natural response of  $0.68 \angle -37^\circ$  is required in the stator flux response. This would generate very large transient overshoots of 2.7 PU and 1.35 PU in the rotor current and dc-link voltage, respectively. In addition, the double-frequency ripples in the rotor current and dc-link voltage will rise to 1.0 PU and  $\pm 4.2\%$ , respectively, due to the increase in the negative-sequence component of the supply voltage.
- Figure 3-20 (a): Under normal operation conditions, the stator-flux space vector traces a circular trajectory of 1.0 PU radius, imposed by the grid voltage. Then, as the fault takes place, the flux trajectory changes to an ellipse without any transients. The major axis of the ellipse corresponds to the instants that positive and negative sequence components are aligned in the same direction whereas the minor axis appears when they are aligned in opposite directions.<sup>3</sup>

- Figure 3-20 (b): The natural flux response of 0.4 PU forces the stator flux trajectory to be positioned away from the origin just after the fault instant. The natural flux component finally decays to zero with a speed proportional to the stator winding time constant and the stator-flux elliptic trajectory will be centred again at the origin.
- Figure 3-20 (c): Very large natural flux response of 0.68 PU has been manifested in the stator flux trajectory by the large overshoot observed just after the fault instant. Also, the axes of elliptic trajectory have been tilted by  $45^\circ$  since the positive and negative sequences of the grid voltage are in  $45^\circ$  phase difference for Point B<sub>3</sub>.

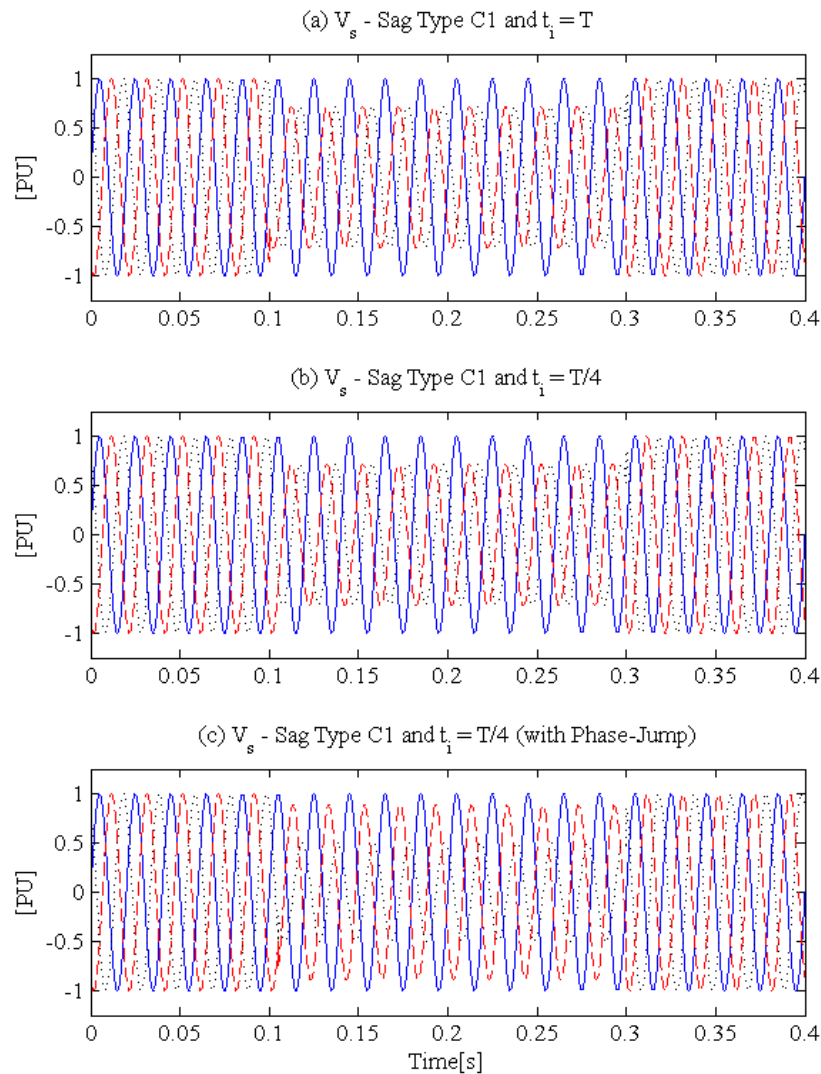


Figure 3-18 Three-phase supply voltage waveform under 60% type C voltage sag with different initial point-on-wave instants, without and with phase-angle jump.

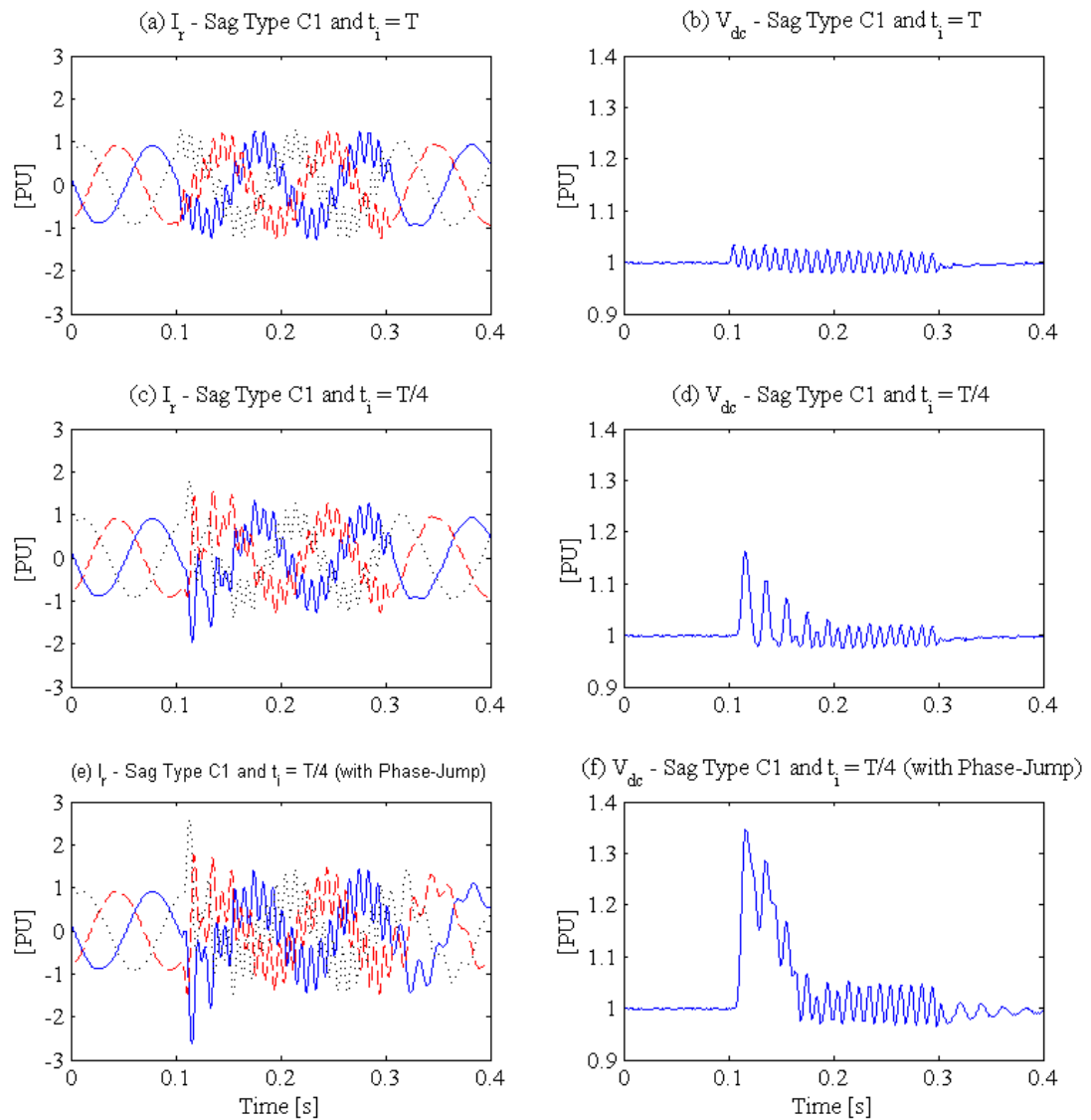


Figure 3-19 Rotor current and dc-link voltage under 60% type C voltage sag with different initial point-on-wave instants, without and with phase-angle jump.

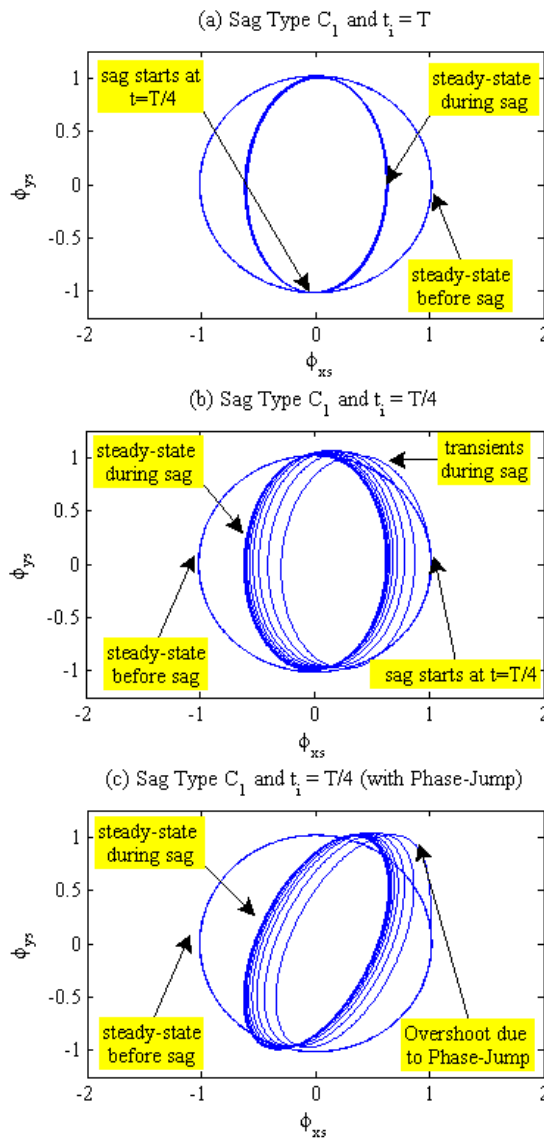


Figure 3-20 Stator flux trajectory under 60% type C voltage sag with different initial point-on-wave instants, without and with phase-angle jump.

Table 3-3 Decomposition of the supply voltage into the positive/negative sequences.

Sag Type	Point B <sub>1</sub> (0.6∠0°)		Point B <sub>3</sub> (0.6∠-31°)	
	V <sub>+</sub>	V <sub>-</sub>	V <sub>+</sub>	V <sub>-</sub>
A	0.6∠0	0.0	0.6∠-31	0.0
C*	0.85∠0	0.13∠0	0.84∠-7	0.19∠32
C	0.8∠0	0.2∠0	0.77∠-12	0.29∠33
D	0.8∠0	0.2∠-180	0.77∠-12	0.29∠-147
F	0.73∠0	0.13∠-180	0.71∠-17	0.19∠-147
G	0.73∠0	0.13∠0	0.71∠-17	0.19∠33

### 3.5.3 Influences of sag parameters on the transient response of DFIG

In this section, the influence of the initial point-on-wave instant, sag depth, and network impedance angle on the transient response of DFIG will be investigated. The parameters of interest for this study are the peak values of the rotor current and dc-link voltage, defined in per unit as

$$I_{r,peak} = \frac{\max\{|I_{ra}(t)|, |I_{rb}(t)|, |I_{rc}(t)|\}}{I_{r,base}} \quad 3-52$$

$$V_{dc,peak} = \frac{\max\{|V_{dc}(t)|\}}{V_{dc,base}} \quad 3-53$$

To examine the influence of initial point-on-wave instant, the DFIG system is subjected to various types of voltage sags with 60% remnant voltage and different impedance angles. It was observed that the peaks in the rotor current and dc-link voltage have periodic behaviour in each half cycle of the fundamental period. Simulation results also show that the initial point-on-wave instant has no influence on the peak values for three-phase faults (type A) because there is no associated negative-sequence component. In contrast, the effect of this parameter is enormous for asymmetrical faults. Figure 3-21 displays the peak values of the rotor current and dc-link voltage versus the initial point-on-wave instant for 60% types C and D voltage sags. Typical safety margins are also shown in Figure 3-21, equal to 2.0 and 1.25 PU for  $I_r$  and  $V_{dc}$ , respectively [35]. Comprehensive simulation results for sag types A, C\*, D\*, C, D, G, and F have been summarized in Table 3-4. The main observations are as follows:

- The maximum peaks for types C\*, C, and G with no phase-angle jump take place at  $t_i = T/4$  s ( $\theta_i = 90^\circ$ ), whereas the highest peaks for types D\*, D, and F occurs at the initial point-on-wave instant equal to zero (Table 3-4, 2<sup>nd</sup> column). These figures will change when the sag is associated with a phase-angle jump. Generally, the most unfavourable initial point-on-wave corresponds to the instant that the positive and negative sequence components of the grid voltage are aligned in opposite directions, e.g.,  $\theta_{peak} = 77^\circ$  and  $167^\circ$  for sag types C\* and D\* with  $\alpha = -60^\circ$ , respectively.

- 
- The overshoots in the rotor current and dc-link voltage will significantly increase and exceed the safety limits of the DFIG if the voltage sag is associated with large phase-angle jumps. For example, if the impedance angle changes from zero to  $-60^\circ$ , the overshoots in  $I_r$  and  $V_{dc}$  will increase by 45–60% and 20–40%, respectively. This observation is consistent with the increase of the negative sequence component of the supply voltage when voltage sags are associated with phase-angle jump (refer to Table 3-3). With large phase-angle jumps, the minimum possible value of the forced flux (the difference between positive and negative components) reduces and as a result, larger natural flux responses will be needed to avoid the flux discontinuity. Therefore, it is concluded that large phase-angle jumps associated with voltage sag have significant detrimental impacts on transient responses of DFIG-based WTs.
  - Under identical sag conditions, the largest overshoot of the rotor current is observed under phase-to-phase faults, i.e. sag types C and D. The rotor current under fault conditions is equal to the superposition of the positive, negative, and zero sequence components. Phase-to-phase faults generate the highest negative sequence components in the grid voltage; therefore, the largest initial overshoot will be experienced in the rotor current in types C and D as compared to other sag types (refer to Table 3-4). On the other hand, the overshoot of the dc-link voltage is directly proportional to the amplitude of the positive-sequence of the grid voltage [41]. According to Table 3-3, type A sags give the lowest positive voltage sequence values; thus, the largest overshoot in the dc-link voltage will be expected under three-phase faults.



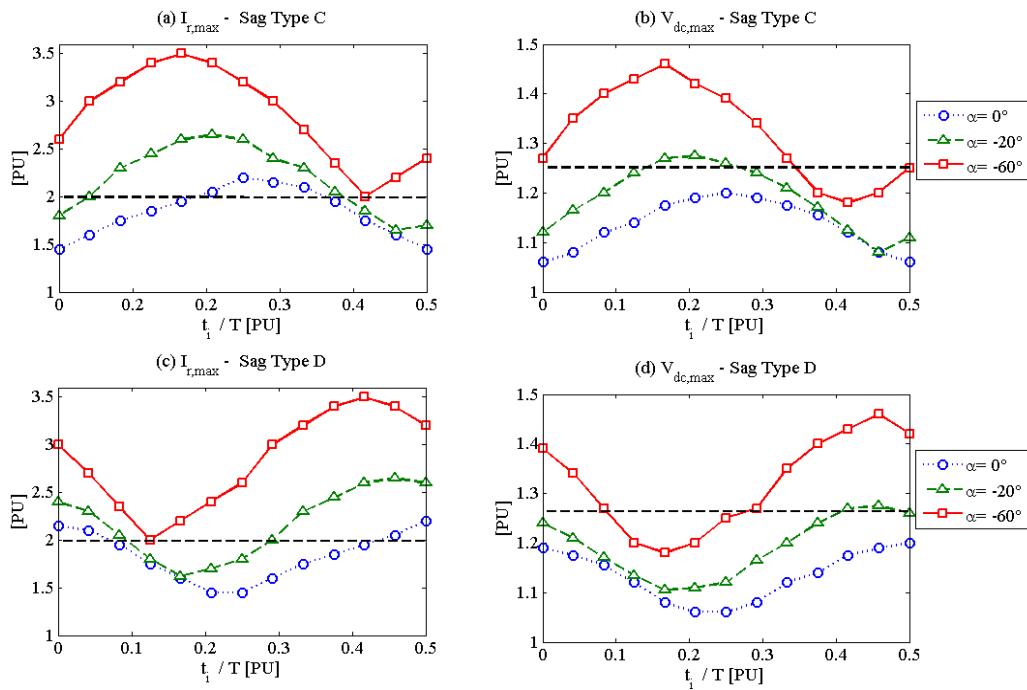


Figure 3-21 Influence of the initial point-on-wave instant on the transient response of DFIG-based WTs subjected to phase-to-phase faults (sag types C and D).

Table 3-4 Summarized simulation results for different types of faults

Fault (Sag Type)	$\alpha=0^\circ$			$\alpha=-20^\circ$			$\alpha=-60^\circ$		
	$\theta_{\text{peak}} (^\circ)$	$I_{r,p}$	$V_{dc,pk}$	$\theta_{\text{peak}} (^\circ)$	$I_{r,peak}$	$V_{dc,peak}$	$\theta_{\text{peak}} (^\circ)$	$I_{r,peak}$	$V_{dc,peak}$
$\Phi-g$ (C* & D*)	90&180	1.75	1.13	83&173	1.93	1.16	77&167	2.53	1.56*
$\Phi-\Phi$ (C&D)	90&180	2.2	1.21	84&174	2.65	1.28	80&170	3.5**	1.46
$2\Phi-g$ (G&F)	90&180	2.15	1.2	85&175	2.45	1.26	82&172	3.25	1.41
$3\Phi$ (A)	—	1.9	1.23	—	2.1	1.3	—	2.95	1.61

\*) Most severe case in terms of the overshoot in the dc-link voltage.

\*\*\*) Most severe case in terms of the overshoot in the rotor current.

Finally, to study the impact of sag depth on the DFIG transient response, the most severe initial point-on-wave instants that produce the highest peaks in the rotor current and dc-link voltage have been considered for various sag conditions. Figure 3-22 shows an almost linear relationship between the sag depth and peaks of the rotor current or dc-link voltage, i.e., higher peaks will be observed as the sag depth increases. These simulation results also confirm the validity of the observations made

in the last subsection: large phase-angle jumps have significant detrimental impacts on the DFIG response, and the most severe overshoots in the rotor current and dc-link voltage are experienced for phase-to-phase and three-phase faults, respectively.

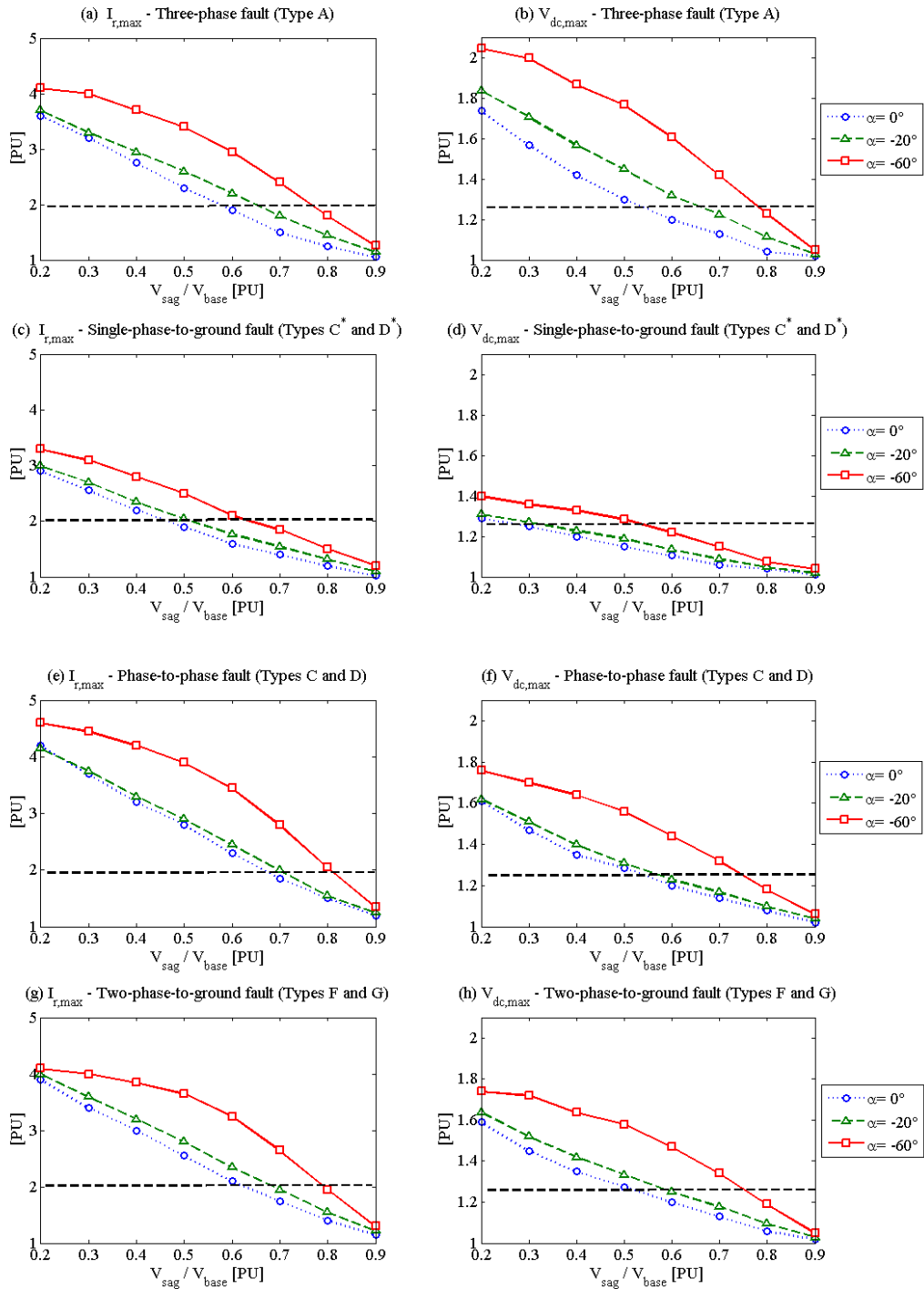


Figure 3-22 Influence of the sag depth on the transient response of DFIG-based WTs subjected to different types of faults.

### 3.6 CONCLUSIONS

In this chapter, a new analysis into the transient response of DFIG-based WTs under various symmetrical and asymmetrical fault conditions is presented. For the first time, the impacts of phase-angle jump, voltage recovery process, and various sag parameters (e.g., depth, type, instant on point-of-wave, impedance angle) are examined. Extensive simulation studies are carried out and supported by theoretical analysis. The main conclusions are summarized as follows:

- For symmetrical sags (type A), the natural response of the stator flux generates large transient overshoots in the rotor current and dc-link voltage at the beginning and the end of three-phase faults. However, if the operational constraints of the circuit breakers are taken into account, the full voltage recovery will take place in two or three consecutive steps and in turn, smaller overshoots will be experienced at the fault clearance instant. For wind farms connected to the distribution system or located offshore, overshoots during the recovery process are expected to increase as the fault current angle decreases notably.
- For asymmetrical sags (types B to G), steady-state oscillations as well as transient overshoots are observed in the rotor current and the dc-link voltage. The most unfavourable initial point-on-wave instants, with the largest overshoots, have been identified for various sag types. This corresponds to the instant that the positive and negative sequence components are aligned in the opposite directions.
- The negative-sequence component of the grid voltage increases when the voltage sag is associated with large phase-angle jumps. This has significant detrimental impacts on the transient response of DFIG-based WTs located offshore since the transient overshoots in the rotor current and dc-link voltage can increase by 45–60% and 20–40%, respectively.
- Under identical sag conditions, the largest overshoots in the dc-link voltage are experienced for three-phase faults (sag type A), while the highest peaks for the rotor current are observed under phase-to-phase faults (sag types C and D). Also, a linear relationship is obtained between the sag depth and

---

peaks of the rotor current or dc-link voltage, i.e. higher peaks will be expected as the depth increases.

In summary, this chapter identifies the difficulties associated with successful fault ride-through of DFIG-based WTs. Based on the observations made in this chapter, new current control schemes will be presented in Chapter 4 and Chapter 5 to enhance LVRT and HVRT capabilities of DFIG-based WTs in compliance with the international grid codes.

## **Chapter 4. Enhanced hysteresis-based current regulators in the vector control of DFIG-based WTs**

### **4.1 INTRODUCTION**

Simulation studies presented in Chapter 3 show that due to sluggish transient response of PI current regulators used in the RSC and GSC of DFIG-based WTs, the rotor current and dc-link voltage may exceed the safety limits of the converters under various fault conditions. As a result, the DFIG-based WT fails to comply with the LVRT regulations enforced by the international grid codes. To address this problem, new current control schemes with improved transient response must be incorporated in the vector control of DFIG-based WTs.

This chapter proposes an enhanced hysteresis-based current regulator in the vector control of DFIG-based WTs. The proposed control scheme is synchronized with the virtual grid-flux space vector, readily extractable by an enhanced PLL system. Identical variable-band VBHCRs are then used to control the output currents of the RSC and GSC. It is shown that the proposed current regulator has excellent steady-state performance and offers several advantages compared to the commonly-used PI current regulator, including very fast transient response, simple control structure, and intrinsic robustness to the machine parameters variations. Moreover, the fixed hysteresis bands in the VBHCRs are replaced with equidistant bands in order to limit the instantaneous variations of the switching frequency and reduce the maximum switching frequencies experienced in the converters. Extensive simulation studies are conducted to examine the operation of the proposed VBHCR under changing wind speed and compare its transient and steady-state performances with the PI current controller.

### **4.2 DISCRETE FORMULATION OF THE RSC VOLTAGE VECTOR**

In the conventional PI current control scheme, the RSC output voltage is considered as a continuous and linear control variables, which is not an accurate assumption. The power circuit of the RSC is shown in Figure 4-1(a). At each instant, the output voltage vector of the

converter is defined based on the three-phase gating signals, i.e.  $S_a^*$ ,  $S_b^*$ , and  $S_c^*$ . In phase  $a$ , the current is flowing through the upper switch ( $S_1$ ) if  $S_a^* = 1$ . Otherwise, the lower switch ( $S_4$ ) is conducting the phase current ( $S_a^* = 0$ ). Using the same definitions for phase  $b$  and phase  $c$ , the output voltage vector generated by the RSC can be defined as

$$\mathbf{V}_r = \frac{1}{3}V_{dc} \left[ (2S_a^* - 1) + \exp(j2\pi/3) \cdot (2S_b^* - 1) + \exp(-j2\pi/3) \cdot (2S_c^* - 1) \right] \quad 4-1$$

If all the possible combinations of gating signals are considered in (4-1), eight switching states and consequently, eight output voltage space vectors are obtained, given by

$$\begin{cases} \mathbf{V}_r = \frac{2}{3}V_{dc} \exp(j(k-1) \cdot \pi/3) & ; k = 1, 2, \dots, 6 \\ \mathbf{V}_r = \mathbf{V}_0 = \mathbf{V}_7 = 0 \end{cases} \quad 4-2$$

Based on (4-2), the available discrete output voltage vectors consist of six non-zero ( $\mathbf{V}_1$ - $\mathbf{V}_6$ ) and two zero ( $\mathbf{V}_0$ ,  $\mathbf{V}_7$ ) voltage vectors, as defined in Table 4-1 and displayed in Figure 4-1 (b) [20]. Similar discrete definitions apply to the GSC output voltage.

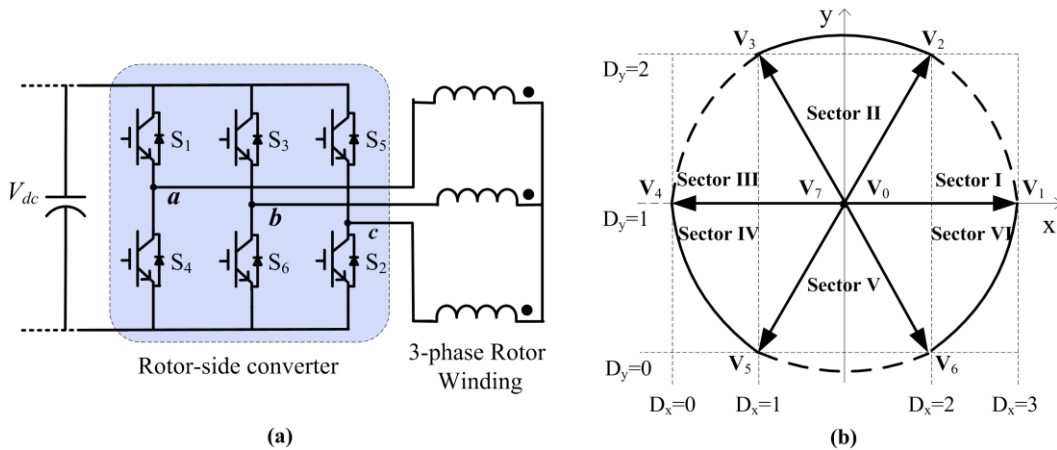


Figure 4-1 (a) Power circuit of the RSC, (b) Discrete representation of the RSC voltage vector

Table 4-1 Three-phase switching states, RSC voltage vector, and respective x-y components

$S_a^*$	$S_b^*$	$S_c^*$	$\mathbf{V}_r$	$V_x/V_{dc}$	$V_y/V_{dc}$
0	0	0	$\mathbf{V}_0$	0	0
1	0	0	$\mathbf{V}_1$	2/3	0
1	1	0	$\mathbf{V}_2$	1/3	1/√3
0	1	0	$\mathbf{V}_3$	-1/3	1/√3
0	1	1	$\mathbf{V}_4$	-2/3	0
0	0	1	$\mathbf{V}_5$	-1/3	-1/√3
1	0	1	$\mathbf{V}_6$	1/3	-1/√3
1	1	1	$\mathbf{V}_7$	0	0

## 4.3 THE PROPOSED VECTOR CONTROL SCHEME FOR DFIG

### 4.3.1 Grid-flux-orientation

The stator-flux oriented frame is the most popular synchronization technique used in the vector control of DFIG-based WTs [8]. In this method, the  $d$ -axis of the synchronous frame is fixed to the stator-flux space vector and rotates anti-clockwise at the speed of  $\omega_s$ , as shown in Figure 4-2(a). However, this synchronization technique needs the accurate estimation of the stator-flux space vector at each instant, usually estimated through an open-loop observer (refer to section 3.3.3). This means that the overall performance of the vector control scheme will be highly dependent on the accurate detection of the stator-flux position, which can be a critical problem under the distorted supply voltage condition or varying machine parameters.

As an alternative, if (3-3) is rewritten in the stationary frame, it can be observed that the space vectors of  $\mathbf{V}_s$  and  $\Phi_s$  are positioned almost orthogonally, with a small drift due to the voltage drop across the stator resistance. In medium and large induction machines, the stator resistance is very small compared to the stator reactance ( $R_s \leq 0.01L_s$ ). Therefore, the  $q$ -axis of the stator-flux frame is practically aligned with the supply-voltage space vector and in turn, the instantaneous position of the supply voltage vector can be used for the controller synchronization without any significant error [27]. Instead of directly using the supply-voltage vector, this work uses the virtual grid-flux space vector ( $\Phi_g$ ) to fully acknowledge the principle of the vector control method that requires a flux-linkage space vector for the synchronization [5]-[6]. In this method, the  $d$ -axis of the proposed synchronous frame will be aligned with the non-measurable grid flux space vector, as shown in Figure 4-2(b). Unlike the conventional stator-flux-orientation approach, the phase-angle of the proposed synchronous frame can be readily extracted using a well-known PLL system since the grid-voltage and the grid-flux space vectors are positioned vertically. This is a notable benefit in the proposed field-oriented vector control scheme.

However, the conventional PLL system cannot present accurate phase-angle estimation under asymmetrical fault conditions because the second harmonics produced by the negative-sequence component of the grid voltage will propagate through the PLL system and will be reflected in the extracted phase angle [28]. To avoid this problem, an enhanced PLL system, with an outstanding immunity to noise, harmonic and unbalance distortions, has been used in this work [29]. The proposed PLL system, referred to as UTSP, gives a clean synchronization signal extracted from the positive-sequence component of the supply voltage. Structural

simplicity and performance robustness are other salient features of the proposed UTSP. The control structure of the proposed UTSP system is given in the Appendix C.

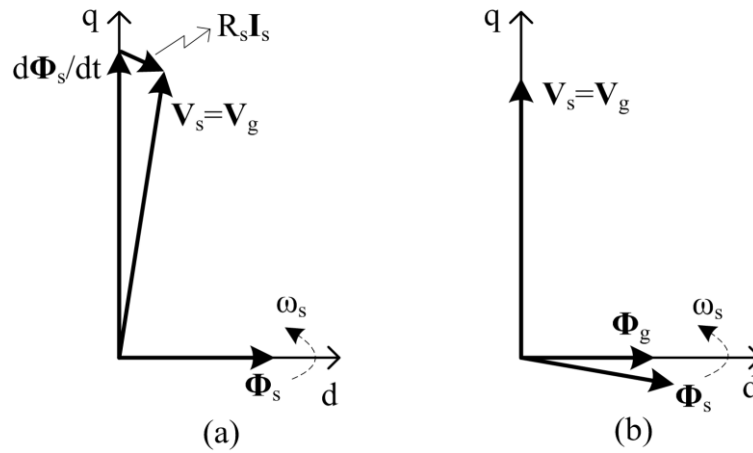


Figure 4-2 Phasor diagrams for field-oriented vector control of DFIG; (a) Conventional stator-flux-oriented frame, (b) Proposed grid-flux-oriented frame

### 4.3.2 Vector control of the DFIG-based WT

The stator voltage vector in the virtual grid-flux-orientated frame (GFOF) can be expressed by  $\mathbf{V}_s^e = jV_{sq}$ , as shown in Figure 4-2(b). Therefore, based on (3-10), the active and reactive powers of the stator winding can be defined as [4]

$$P_s = -1.5V_{sq}I_{sq} = 1.5V_{sq}I_{rq} \quad 4-3$$

$$Q_s = -1.5V_{sq}I_{sd} = 1.5V_{sq} \left( I_{rd} - \frac{V_{sq}}{\omega_s L_m} \right) \quad 4-4$$

From (4-3) and (4-4), it can be observed that the independent control of the stator active and reactive powers can be achieved through regulating the  $q$ - and  $d$ - components of the rotor current vector, respectively. Therefore, the RSC controller can be configured as shown in Figure 4-3:

1. Clarke's transformation is used to obtain the vector representation of the measured three-phase signals, i.e. to convert from  $(\mathbf{I}_{s-3\phi}$  and  $\mathbf{V}_{s-3\phi})$  to  $(\mathbf{V}_s^s$  and  $\mathbf{I}_s^s)$  and from  $\mathbf{I}_{r-3\phi}$  to  $\mathbf{I}_r^r$ .
2. The rotor angle is directly measured using a high-resolution position encoder whereas the synchronizing signal (the grid-voltage phase-angle) is extracted using the UTSP system.
3. The stator-voltage and stator current vectors are transformed from the stationary frame



to the GFOF, using (3-14).

4. Based (4-3) and (4-4), the DFIG active and reactive powers are calculated and compared to their command values. The  $P^*$  signal is calculated based on the optimal power-speed curve given by the wind turbine manufacturer and the angular speed of the rotor at each instant ( $\omega_r$ ) [30]. The  $Q^*$  signal is usually defined according to the grid-code regulations [10].
5. The error signals  $\Delta P_s$  and  $\Delta Q_s$  are fed to the PI control blocks in order to calculate the  $I_{rq}^*$  and  $I_{rd}^*$  signals, respectively.
6. The rotor command vector ( $\mathbf{I}_r^{e*}$ ) is transformed from the synchronous frame to the rotor reference frame, using (3-15).
7. The rotor command vector ( $\mathbf{I}_r^{*}$ ) along with the measured current vector ( $\mathbf{I}_r^r$ ) are fed to the proposed hysteresis-based current regulator to directly generate the appropriate gating signals for the RSC, i.e., to define  $S_a^*$ ,  $S_b^*$ , and  $S_c^*$ .

Similarly, the GSC vector controller is configured as shown in Figure 4-3:

1. Two PI control blocks are used to calculate the  $I_{gq}^*$  and  $I_{gd}^*$  current components from the error signals of  $\Delta V_{dc}$  and  $\Delta Q_g$ , respectively.
2. The GSC current command vector ( $\mathbf{I}_g^{e*}$ ) is transferred from the synchronous frame to the stationary frame, using (3-14).
3. Clarke's transformation is used to obtain the vector representation of the measured GSC three-phase current ( $\mathbf{I}_{g-3\phi}^s$ ).
4. The GSC actual current vector ( $\mathbf{I}_g^s$ ) along with the current command vector ( $\mathbf{I}_g^{s*}$ ) are fed to the proposed equidistant-band VBHCR to generate appropriate gating signals in the GSC.

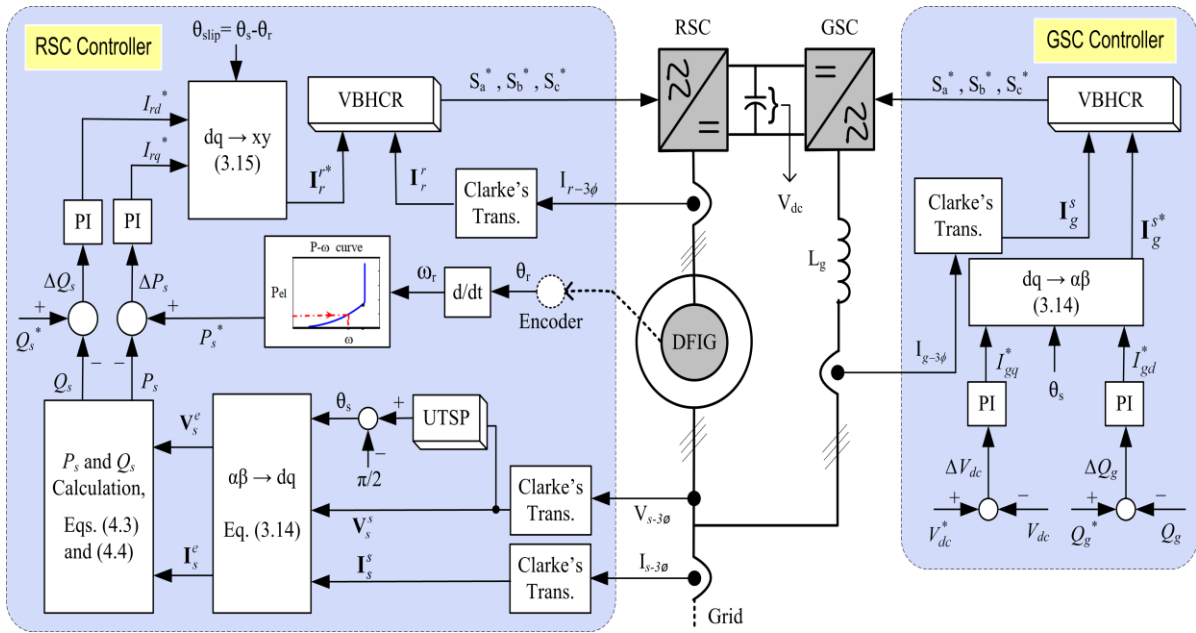


Figure 4-3 Schematic diagram of the proposed grid-flux-oriented vector control scheme for DFIG-based WT

#### 4.4 PRINCIPLES AND CONTROL STRUCTURE OF THE VBHCR

Two identical equidistant-band VBHCRs have been used to control the output current of the RSC and GSC. Based on (3-13), it can be said that the utilization of the proposed current regulator in the GSC is similar to the conventional grid-connected VSCs, as comprehensively studied in [20]. Therefore, this chapter explores the principles and the control structure of the proposed VBHCR in the RSC of DFIG-based WTs.

This current regulator was originally proposed by the author for the conventional VSCs, showing a superior performance under the steady-state and transient operation conditions [20]. It was demonstrated that the proposed VBHCR retains the inherent advantages of the conventional hysteresis method (such as the excellent transient performance, simple hardware implementation, outstanding stability, and robustness to the machine parameters variations), but removes its disadvantages in three-phase applications (such as very high average switching frequency and large oscillations in the output current) [20]. Moreover, the proposed VBHCR is superior to other vector-based methods proposed in the literature because it avoids the redundant control actions observed in [21]-[22], has a simpler structure as compared to [23], and suppresses the current vector oscillations more effectively than the methods reported in [24]-[25]. The fixed hysteresis bands in the proposed VBHCR are replaced with equidistant bands to limit the instantaneous variations of the switching frequency and reduce the maximum switching frequency experienced in the converters.

#### 4.4.1 Principle of the proposed VBHCR implemented in the RSC

The proposed VBHCR is designed to control the output current of the RSC in the rotor reference frame. Therefore, the RSC output voltage must be expressed in the  $x$ - $y$  frame. Substituting  $\omega$  with  $\omega_r$  in (3-16) results in

$$\mathbf{V}_r^r = R_r \mathbf{I}_r^r + L_\sigma \frac{d\mathbf{I}_r^r}{dt} + \frac{d\Phi_s^r}{dt} \quad 4-5$$

If the current error vector is defined as  $\mathbf{I}_{r,e}^r = \mathbf{I}_r^{r*} - \mathbf{I}_r^r$ , the differential equation describing this vector can be derived as

$$L_\sigma \frac{d\mathbf{I}_{r,e}^r}{dt} + R_r \mathbf{I}_{r,e}^r = L_\sigma \frac{d\mathbf{I}_r^{r*}}{dt} + R_r \mathbf{I}_r^{r*} - (\mathbf{V}_r^r - \mathbf{e}_0^r) \quad 4-6$$

where  $\mathbf{e}_0^r = d\Phi_s^r/dt$  is the back electromotive force (EMF) voltage vector. Based on (4-6), the current error vector changes with the time constant of  $L_\sigma/R_r$  and is influenced by the current command vector and its derivative, as well as, the RSC output voltage and the back EMF vectors. If the rotor resistance is neglected in (4-6), the desired output voltage vector to nullify the current error vector can be expressed according to

$$\mathbf{V}_r^{r*} = \mathbf{e}_0^r + L_\sigma \frac{d\mathbf{I}_r^{r*}}{dt} \quad 4-7$$

Substituting (4-7) in (4-6) gives

$$L_\sigma \frac{d\mathbf{I}_{r,e}^r}{dt} = \mathbf{V}_r^{r*} - \mathbf{V}_r^r \quad 4-8$$

From (4-7) and (4-8), it is clear that the information about back EMF voltage vector and derivative of current command vector are required to nullify the tracking error in the RSC. However, it is not practically easy to measure the back EMF voltage vector or current derivatives. An indirect technique has been used in this paper to tackle the problem and extract the required information from the desired output voltage vector [24]. Suppose that the  $\mathbf{V}_r^{r*}$  space vector is located in Sector I in Figure 4-1 (b). Based on (4-8), the error derivative vectors with respect to various output voltage vectors of the RSC ( $\mathbf{V}_0$ - $\mathbf{V}_7$ ) can be defined as shown in Figure 4-4. Small current deviations ( $d\mathbf{I}_{r,e}^r/dt$ ) are required to follow the current command with the minimum possible switching frequency. That is, the voltage space vectors adjacent to  $\mathbf{V}_r^{r*}$  must be applied in the RSC to attain the desired optimal switching pattern, e.g.  $\mathbf{V}_1$ ,  $\mathbf{V}_2$ ,  $\mathbf{V}_0$  and  $\mathbf{V}_7$  in Sector I. If this switching pattern is to be generated in the RSC, two adjacent non-zero voltage vectors along with  $\mathbf{V}_0$  and  $\mathbf{V}_7$  are the only vectors that will be selected to reduce the tracking error. Therefore, the resulting switching pattern will be similar

to the well-known SVM technique under the steady-state condition [24]. On the other hand, for fast tracking response under transient conditions, non-zero voltage vectors with high current error derivatives must be applied to force the RSC output current inside the hysteresis bands as fast as possible. It must be noted that the proposed switching method operates only based on the position of the  $\mathbf{V}_r^{r*}$  vector.

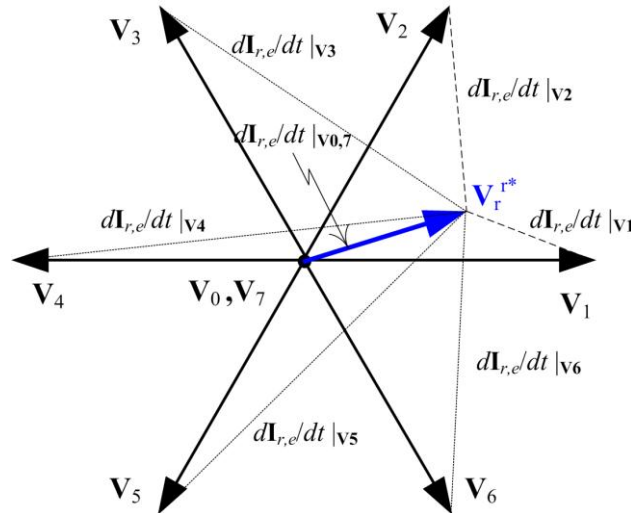


Figure 4-4 Derivatives of the current error when the  $\mathbf{V}_r^{r*}$  vector is located in Sector I

#### 4.4.2 Control structure of the proposed VBHCR

Referring to Table 4-1, it is observed that the output voltage vector of the RSC can have four and three different values in the  $x$ - and  $y$ - axes, respectively. This fact can be used to equally divide the rotor complex frame into six  $60^\circ$ -sectors, as shown in Figure 4-1 (b). Therefore, the proposed VBHCR employs 4-level and 3-level hysteresis comparators for the  $x$ - and  $y$ -current tracking errors, as displayed in Figure 4-5(a). Digital outputs of comparators ( $D_x$  and  $D_y$ ) are then fed to the switching table in order to calculate the RSC output voltage vector at each instant. Figure 4-5(b) shows the practical implementation of the 4-level hysteresis comparator, with the overall bandwidth of  $\delta + \Delta\delta$ , used in the  $x$ -axis.

The bandwidths of hysteresis comparators are tuned based on the tracking accuracy requested from the current regulator. Smaller hysteresis bands give more restricted oscillations in the RSC output current, but it is achieved at the expense of higher switching frequencies. Therefore, there is always a trade-off between the controller tracking accuracy and the consequent switching frequency.

It is clear that the proposed current regulator is a robust method because it only uses local measurements of the current and is independent of system parameters. Also, it has inherent current limiting properties and very fast transient response since it directly controls the

instantaneous value of the rotor current. The implementation of this method is very simple and the computation time is minimal [20].

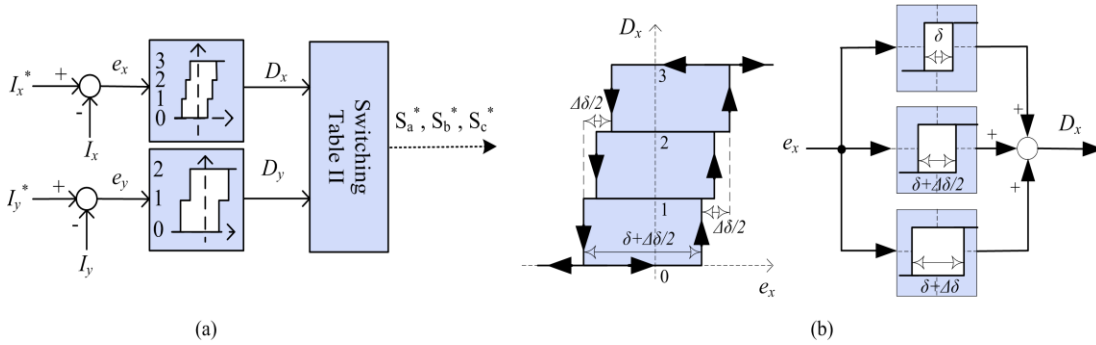


Figure 4-5 (a) Implementation of the proposed VBHCR in the RSC (b) Four-level hysteresis comparator

Table 4-2 Switching table for the proposed VBHCR

$D_y \backslash D_x$	0	1	2
0	$\mathbf{V}_5$	$\mathbf{V}_4$	$\mathbf{V}_3$
1	$\mathbf{V}_5$	$\mathbf{V}_0$	$\mathbf{V}_3$
2	$\mathbf{V}_6$	$\mathbf{V}_0$	$\mathbf{V}_2$
3	$\mathbf{V}_6$	$\mathbf{V}_1$	$\mathbf{V}_2$

For every one sixth of the fundamental period, both  $x$ - and  $y$ - comparators remain in one specific hysteresis loop, which can be used to detect the sector position of the  $\mathbf{V}_r^{r*}$  vector. Then, zero voltage vectors and two non-zero voltage vectors adjacent to  $\mathbf{V}_r^{r*}$  will be selected to reduce the tracking error of the RSC. For example, suppose that  $x$ - and  $y$ - comparators are respectively located in the middle and the top hysteresis loops, i.e.  $D_x = 1$  or  $2$  and  $D_y = 1$  or  $2$ . According to Table 4-1, the  $\mathbf{V}_r^{r*}$  position is detected in Sector II and the optimal voltage sequence of  $\mathbf{V}_0$ ,  $\mathbf{V}_2$ ,  $\mathbf{V}_3$ , and  $\mathbf{V}_7$  will be selected to be applied in the RSC. Under these circumstances, if  $e_x = I_x^* - I_x$  and  $e_y = I_y^* - I_y$  hit the higher hysteresis bands of  $\delta + \Delta\delta/2$  and  $\delta + \Delta\delta$ , respectively, digital outputs of comparators will become equal to  $D_x = 2$  and  $D_y = 2$ . This necessitates the  $\mathbf{V}_2$  voltage vector to be generated by the RSC so that both  $x$ - and  $y$ - components of the rotor current increase. Likewise, if  $D_x = 1$  and  $D_y = 2$ , the  $\mathbf{V}_3$  vector must be applied to reduce the  $I_{rx}$  component and simultaneously increase the  $I_{ry}$  component. Zero voltage vectors must be selected in other cases. Further reduction in the switching frequency can be attained by the appropriate selection of the zero voltage vector between  $\mathbf{V}_0$  and  $\mathbf{V}_7$ . The

$V_0$  vector must be chosen if the present output voltage vector of the RSC is equal to  $V_1$ ,  $V_3$ , or  $V_5$ . In this case, only one inverter leg must be switched to obtain the zero-voltage vector in the RSC output. In the same way, the  $V_7$  vector will be selected if the RSC state comes from  $V_2$ ,  $V_4$ , or  $V_6$ . It must be noted that even though the decision boundary looks like to be in a rectangular shape, the switching table has an inherent mapping characteristic that forms a hexagonal switching pattern with symmetrical  $60^\circ$  sectors (as shown in the below).

As the time passes, either the  $x$ - or  $y$ - comparator will move to the next hysteresis loop. This indicates that the position of the  $V_r^{r*}$  vector has changed to the next sector in the rotor frame; therefore, a new optimal switching sequence must be selected from Table 4-2. The resulting switching pattern will be constituted of six 4-state optimal voltage vectors sets, which matches with six  $60^\circ$ -sectors of the fundamental period. It is therefore clear that the proposed VBHCR generates an improved switching pattern similar to the widely-used SVM technique that significantly reduces the average switching frequency of the RSC and suppresses the oscillations in the output current vector.

The overall switching pattern generated by the proposed current control strategy is shown in Figure 4-6. It is evident that the generated switching pattern constituted of six consecutive 4-state optimal voltage vectors sets. This will exactly matches with six  $60^\circ$ -sectors of a fundamental period, as proven in the following. It is therefore evident that in the proposed VBHCR, the switching frequency of the VSC is significantly reduced by the systematic implementation of zero and non-zero voltage vectors, similar to the switching pattern generated by the well-known SVM technique [see Appendix D].

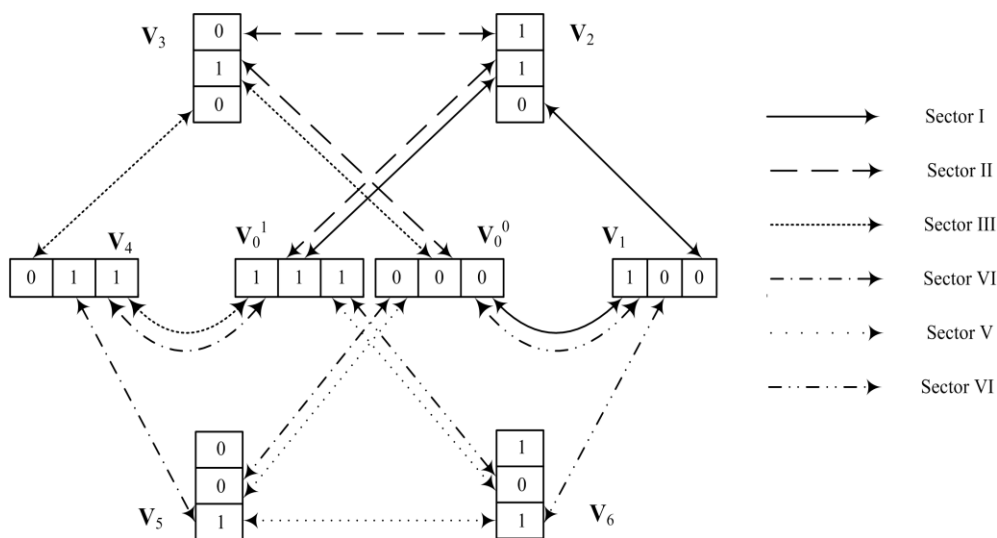


Figure 4-6 The RSC switching pattern for the proposed VBHCR

### 4.4.3 Variable hysteresis bands

The proposed VBHCR considerably reduces the average switching frequency (ASF) of the converter by the systematic application of zero voltage vectors. However, the instantaneous switching frequency varies widely during the fundamental period and may exceed the safety limits of the converter switches at certain conditions, specifically near the zero crossing points of the reference current. Therefore, lockout circuits must be incorporated to limit the maximum switching frequency (MSF), leading to severe current distortions and large error over-reaches. This problem partly arises from uneven lateral distance of hysteresis bands during the fundamental period. Very high switching frequencies occur around zero crossing points because the lateral distance of hysteresis bands is much smaller near those points as compared to the peaks of the reference current.

Two types of variable hysteresis bands have been proposed in the literature to address this problem and reduce the MSF of converter: adaptive and equidistant hysteresis bands. The former removes interphases dependency and achieve fixed switching frequency with low current ripples [31]-[33]. However, adaptive hysteresis bands typically require extra signal-processing and complex control structure, suffer from stability problems, and show degraded transient performance [33]. The equidistant hysteresis bands, on the other hand, are very simple methods to reduce the MSF and limit the instantaneous variations of the switching frequency of converter [34]. Fixed switching frequency is not achieved, but the simplicity, outstanding stability, and very fast transient response of the conventional hysteresis method are retained. It can be say that the vector-based method and equidistant hysteresis bands are complementary when applied to the converter of DFIG.

In this thesis, the fixed hysteresis bands in the proposed VBHCR are replaced with the equidistant bands proposed in [34]. In this method, a suitable percentage of the band height is subtracted at areas close to the peaks, giving almost even lateral distance from upper and lower bands during the fundamental period. The equidistant hysteresis band ( $\lambda'$ ) is defined by

$$\lambda' = \frac{\lambda}{1-k} [1 - |k \sin(\theta_r)|] \quad 4-9$$

where  $k$  is a constant with the optimal value of 0.3 [34]. If the equidistant bands defined in (4-9) are used in the proposed VBHCR, a more homogenous switching pattern will be generated with smaller variations of the instantaneous switching frequency over the fundamental period and smaller MSFs near the zero crossing points of the reference current.

## 4.5 SIMULATION RESULTS

Simulation studies have been carried out in the two phases. First, the wide-ranging behaviour of the proposed VBHCR is evaluated for a typical VSC supplying a load. Then, the proposed VBHCR is implemented in the vector control of DFIG-based WTs, where its steady state and transient performances are thoroughly examined.

- **Proposed VBHCR implemented in grid connected VSCs**

In this section, the proposed VBHCR is implemented in the conventional VSCs in motor drive applications. Simulations studies are carried out to examine the wide-ranging behavior of the proposed current regulator at extreme modulation indexes. The main reason to perform simulation for the conventional VSCs is that this system is a well-understood and less complicated as compared to the DFIG-based WTs. Therefore, the performance of the proposed current regulator can be focused more easily.

Figure 4-7 shows the circuit diagram of a conventional three-phase VSC connected to a load. The simulated load includes a three-phase sinusoidal counter-emf voltage source in series with an inductance and a resistance, which represents an induction motor with  $R$  and  $L$  are the equivalent stator resistance and inductance, respectively. Detailed discussion about the system as well as the simulation parameters are given in Appendix D.

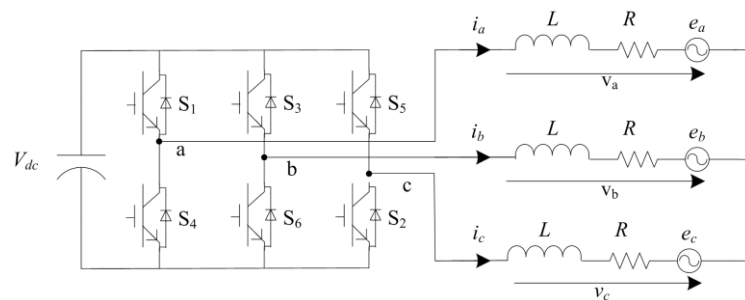


Figure 4-7 Circuit diagram of a PWM-VSI supplying an induction motor

Figure 4-8 shows the VSC output current/voltage vector components in the  $\alpha\beta$  frame and the converter phase signals when the induction machine is running close to the synchronous speed (very low counter-emf voltage). Simulation results are given for the conventional hysteresis current controller, the vector-based Method II proposed in [73], and the VBHCR proposed in this thesis (Method III). It can be seen that the interphases dependency in the conventional method causes highly oscillating currents associated with an irregular switching pattern. In contrast, vector-based methods (specially the proposed VBHCR) manage to noticeably suppress the current vector oscillations. This has been achieved by systematic



application of zero voltage vectors in the VSC switching pattern and the consequent phase voltage. Consequently, there has been a significant reduction in the VSC switching frequency, as shown in Figure 4-10(a).

Similar simulation results for the high counter-emf voltage (large slips) are presented in Figure 4-13 and Figure 4-10(b). In such an extreme case, the counter-emf vector will effectively counteracts the VSC output voltage vector as in (4-6). Hence, a reduced oscillating output current with a more regular switching pattern is produced by the conventional hysteresis current regulator. Identical observations as in the case of low counter-emf can be made in this case. It is also observed that the improvement achieved by the proposed VBHCR is more significant under low counter-emf values and the switching frequency reduces as the motor slip increases.

Further simulation results are presented in Appendix D. The main observations are as follows: 1) scrutinized evaluation of the proposed VBHCR shows that the proposed current regulator exhibits a uniform performance around the current trajectory; 2) the superior transient response of the conventional hysteresis method is retained by the proposed VBHCR, while the steady state current oscillations are suppressed notably; (3) the proposed VBHCR constrains the current error trajectory within the assigned rectangular tolerance region; 4) considerable reduction in the average switching frequency of the VSC is achieved using the proposed VBHCR (about 30% reduction); and 5) the proposed VBHCR can be successfully implemented in more demanding applications such as active power filters, where the VSC current is to track a highly non-sinusoidal current signals.

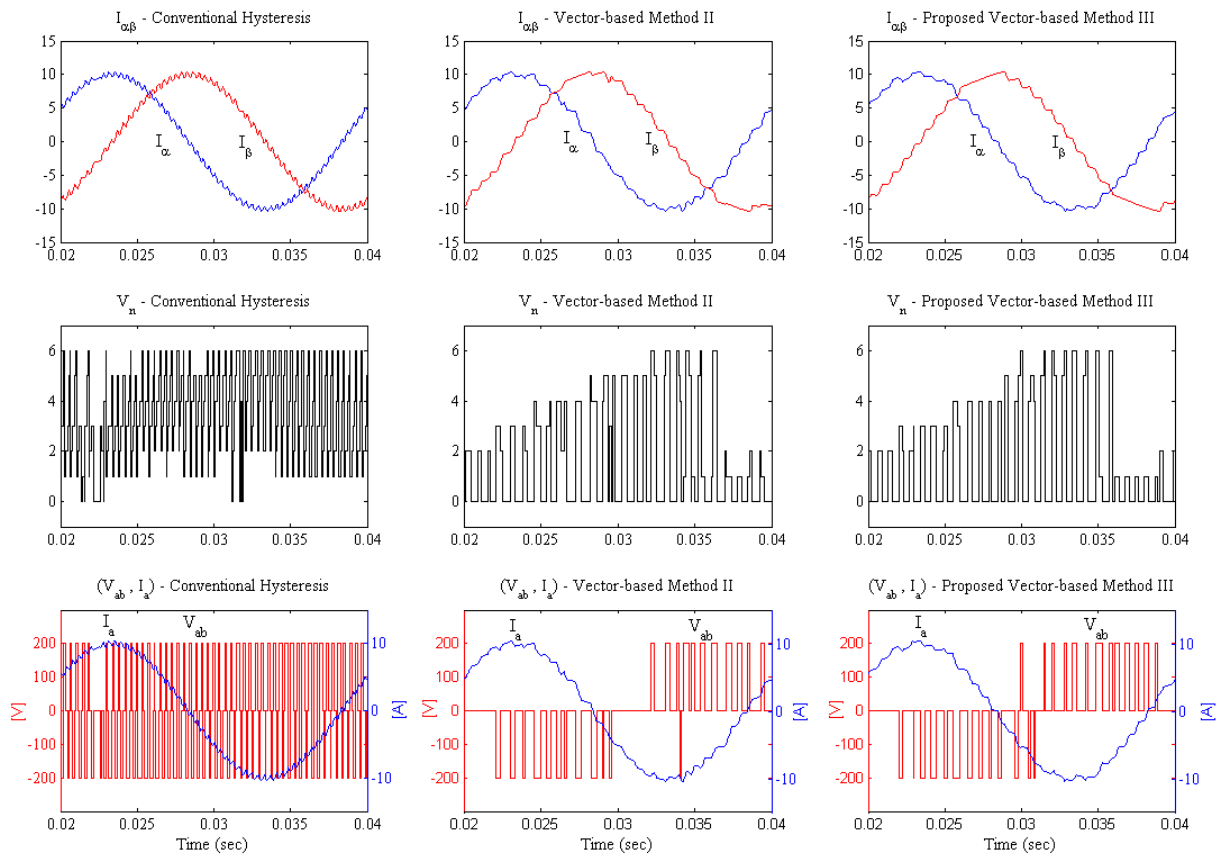


Figure 4-8  $I_{\alpha-\beta}$ ,  $V_n$ ,  $I_a$ , and  $V_{ab}$  for small counter-emf voltage ( $R=0.7 \Omega$ ,  $L=5 \text{ mH}$ , and  $e_0=25 \angle 60^\circ$ )

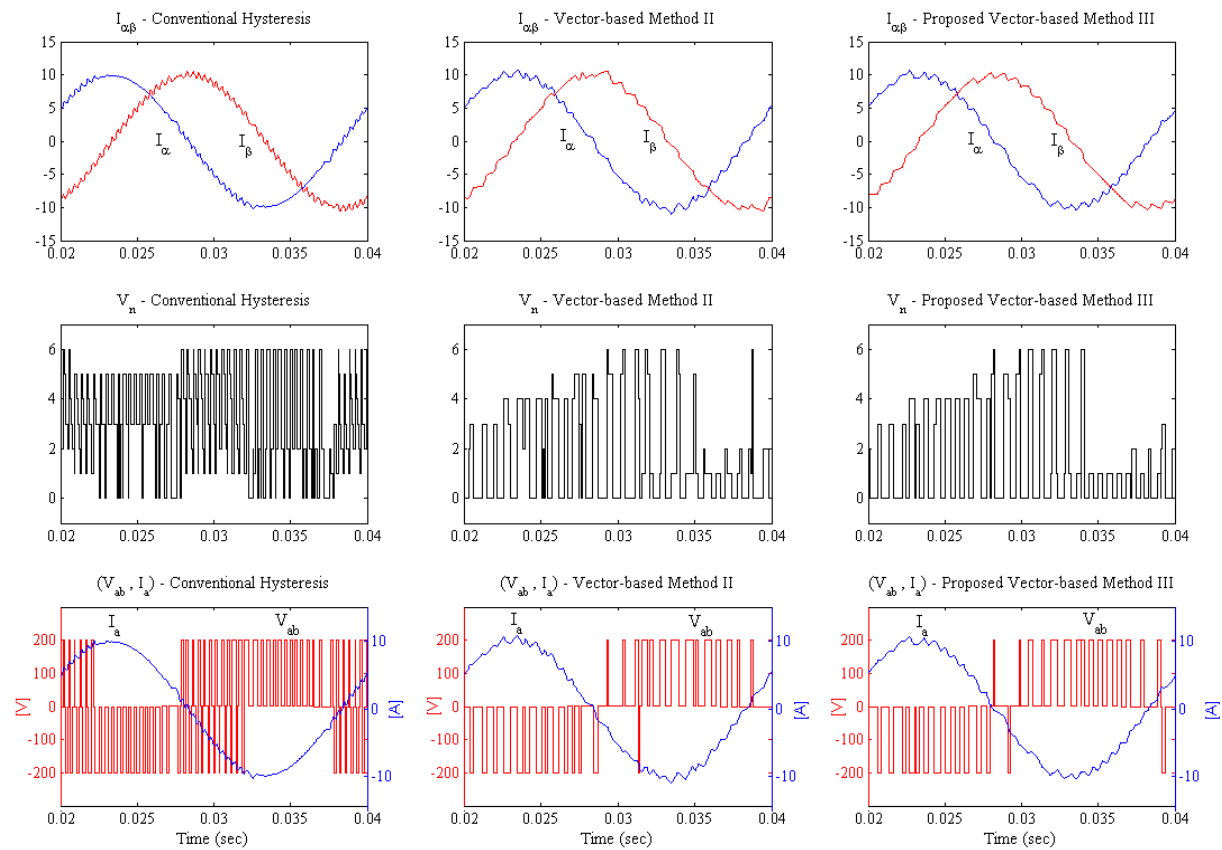


Figure 4-9  $I_{\alpha-\beta}$ ,  $V_n$ ,  $I_a$ , and  $V_{ab}$  for large counter-emf voltage ( $R=0.7 \Omega$ ,  $L=5 \text{ mH}$ , and  $e_0=75 \angle 60^\circ$ )

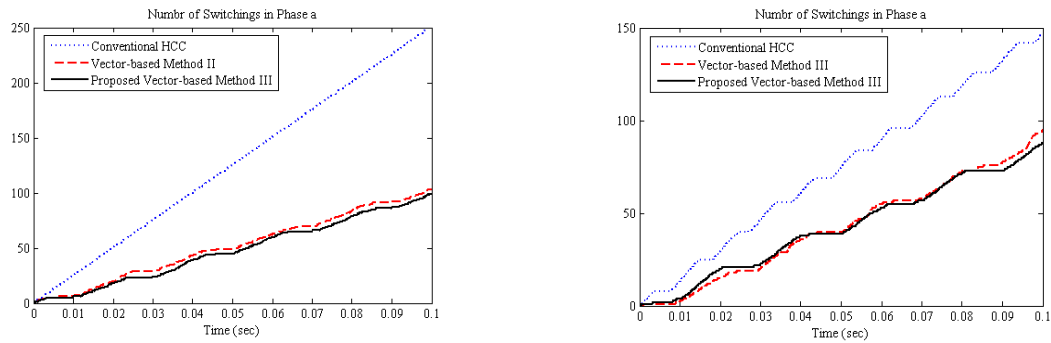


Figure 4-10 (a) Number of switching with small counter-emf voltage (b) Number of switching with large counter-emf voltage

• **Proposed VBHCR implemented in DFIG-based WTs**

Finally, simulation studies for the proposed VBHCR in the DFIG-based WT applications are carried out in three main directions, as listed in [35]: (1) the operation of the proposed vector control scheme under changing wind speed is thoroughly examined, (2) the steady-state performance of the proposed VBHCR is compared with the widely-used PI current regulator, and (3) the transient responses of current regulators are compared under the most stringent LVRT regulations enforced by the Australian grid code.

Figure 4-11 shows the schematic diagram of the simulated system with the parameters given in the Appendix B. A single DFIG-based WT is connected to the main grid through a step-up transformer and 10 km distribution feeder. Equidistant hysteresis bands have been used in the simulation studies and the bandwidths of comparators are set to  $\delta = \Delta\delta = 0.02$  PU in the RSC and  $\delta = \Delta\delta = 0.0125$  PU in the GSC. Using these parameters, an acceptable trade-off between the current tracking accuracy and the consequent switching frequency is obtained, as shown in the below.

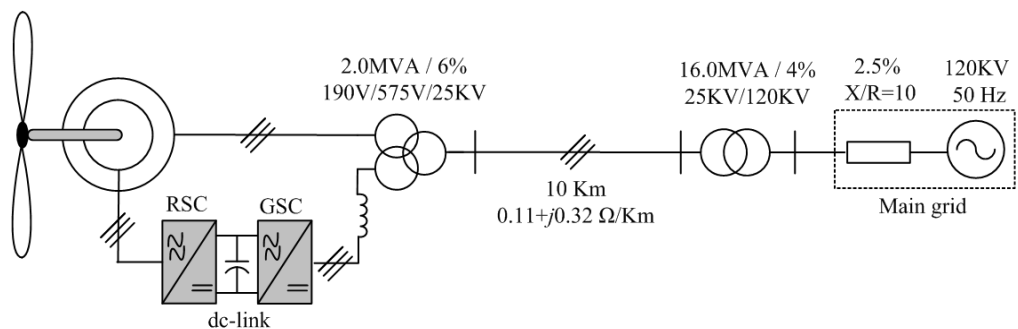


Figure 4-11 Circuit diagram of the simulated network

### 4.5.1 Operation under changing wind speed

In the first step, the mechanical input torque to the DFIG is externally specified in order to emulate the power extracted from the turbine. The lumped inertia constant of the system is intentionally set to the very small value of 0.025 s to have similar mechanical and electrical time constants and obtain a better illustration. Figure 4-12 shows the simulation results with a ramped-up wind speed between 0.3 to 0.5 s and a step-change in the reactive power command signal from zero to  $-0.2$  MVAR at  $t = 0.7$  s.

For  $0.1 < t < 0.3$  s, the wind speed is equal to 7.8 m/s and the machine rotates at  $\omega_r = 0.9$  PU based on the simulated optimal power-speed curve. This gives the active power generation of 0.4 MW in the stator winding. However, since the DFIG rotates at subsynchronous speed with  $s = +0.1$ , ten percent of the active power generated in the stator winding is fed back to the machine through the converters [30]. Accordingly, the proposed grid-flux-oriented vector control scheme regulates  $(I_{rd}, I_{rq})$  to (0.35, 0.3) PU and  $(I_{gd}, I_{gq})$  to (0,  $-0.02$ ) PU, in order to attain the desired active and reactive powers production in the machine and the GSC. The three-phase rotor current rotates with the slip frequency of 5 Hz ( $\omega_{slip} = \omega_s - \omega_r = 0.1$  PU), whereas the GSC current always has the fundamental frequency of 50 Hz, imposed by the supply voltage. As a result, the position of  $\mathbf{V}_r^{*}$  and  $\mathbf{V}_g^{s*}$  voltage vectors change in an incremental order from Sector I to Sector VI with  $f_r = 0.1$  PU = 5 Hz and  $f_s = 1.0$  PU = 50 Hz, respectively.

As the wind speed ramps up to 10.5 m/s between  $t = 0.3$  and 0.5 s, the rotor accelerates from 0.9 PU to 1.2 PU and the active power production of the DFIG-based WT increases to 0.9 MW. The machine operates in the super-synchronous mode; thus, the active power is delivered to the grid through both stator and rotor windings ( $P_s = 0.75$  MW and  $P_g = 0.15$  MW). Note that changes in the active power of the stator winding and the GSC have been obtained through the variations in the  $q$ -components of the command current signals, while the  $d$ -components are kept constant. Similarly, the  $I_{rd}^*$  component has been decreased from 0.35 to 0.1 PU at  $t = 0.7$  s to change the reactive power of the stator winding from zero to  $-0.2$  MVAR. This demonstrates the independent control of the active and reactive powers by the

proposed grid-flux-oriented vector control scheme.

For  $t > 0.5$  s, the three-phase rotor current rotates with the frequency of 10 Hz ( $\omega_{\text{slip}} = \omega_s - \omega_r = -0.2$  PU), where the negative sign of the slip frequency is manifested in the reversal of the sequence of the three-phase current flowing in the rotor winding (from  $a-b-c$  to  $a-c-b$ ). As a result, the  $\mathbf{V}_r^{r^*}$  position rotates clockwise from Sector VI to Sector I with  $f = 10$  Hz, while the  $\mathbf{V}_s^{s^*}$  position still changes incrementally from Sector I to Sector VI with  $f = 50$  Hz. It is finally worth noting that during the synchronous operation around  $t = 0.4$  s, no active power is transferred from back-to-back converters connected to the rotor. Therefore, the GSC current amplitude decreases to almost zero and the  $\mathbf{V}_r^{r^*}$  position is held unchanged in Sector I.

Simulation results, presented in Figure 4-12, show the excellent tracking performance of the proposed current regulator under extremely demanding conditions, i.e., under very fast variations of the wind speed over short period of time (0.2 s). Similar observations can be made when the DFIG works under random wind speed variations in longer periods of time.

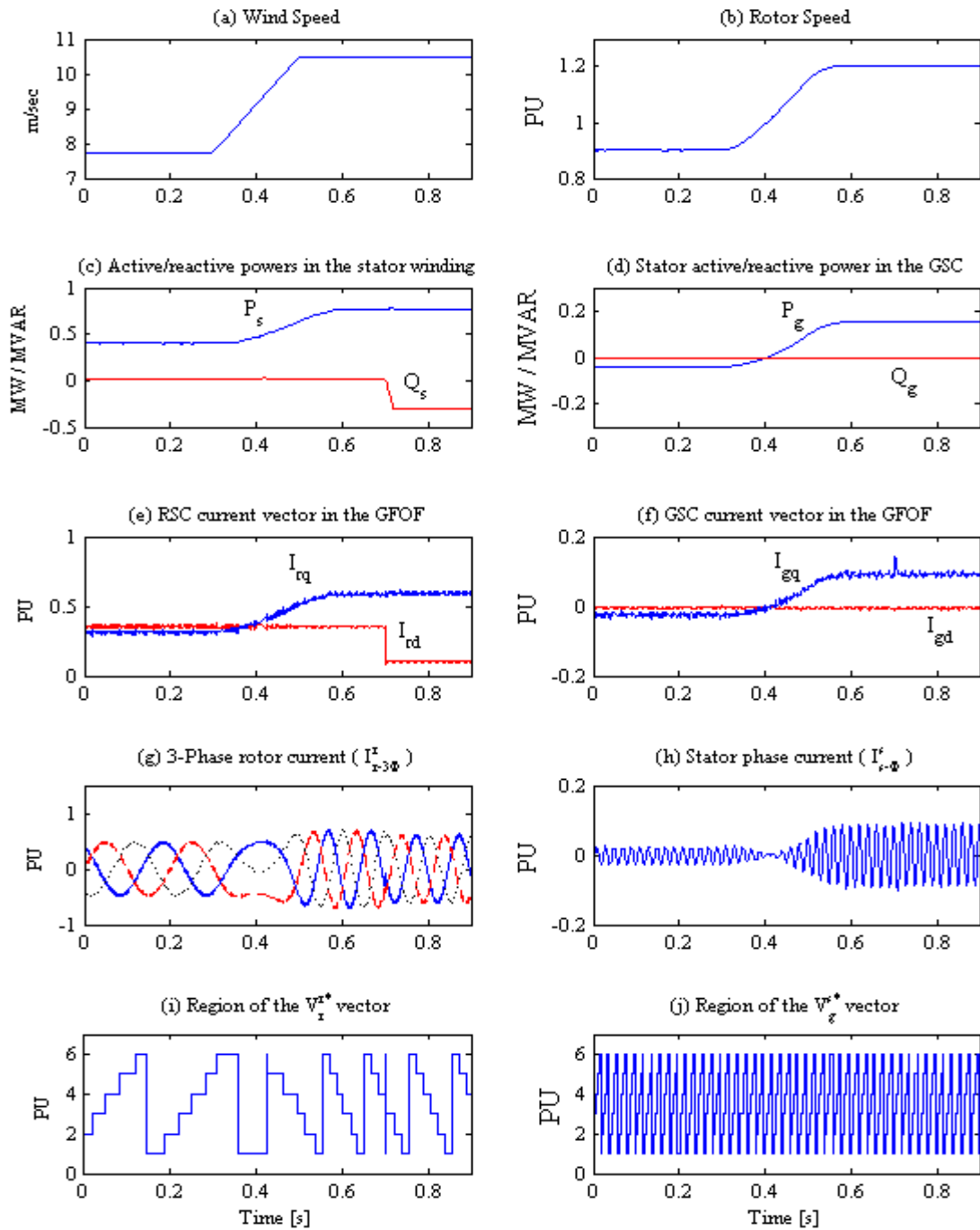


Figure 4-12 Simulation results as the wind speed varies from 7.8 m/s to 10.5 m/s.

Figure 4-13 shows the detailed operation of the proposed equidistant-band VBHCR in the RSC, subjected to a step-change in  $I_{rd}$  at  $t = 0.7$  s. Both  $x$ - and  $y$ - comparators are first located in the lowest hysteresis loop, i.e.,  $D_x = 0$  or  $1$  and  $D_y = 0$  or  $1$ . According to Table 4-1, this indicates that the  $\mathbf{V}_r^{r*}$  vector is positioned in Sector IV and the optimal switching sequence of  $\mathbf{V}_0$ ,  $\mathbf{V}_4$ ,  $\mathbf{V}_5$ , and  $\mathbf{V}_7$  is selected to be applied in

the RSC. In this case, Figure 4-13(a) and Figure 4-13(b) show that the proposed VBHCR keeps the tracking error ( $e_x$  and  $e_y$ ) within the inner hysteresis bands of ‘ $\delta$ ’. The digital outputs of multi-level comparators and the consequent switching pattern of the RSC are shown in Figure 4-13(c) and Figure 4-13(d), respectively. It is clear that under the steady-state condition, the zero voltage vectors are systematically applied in the RSC for most of the time, leading to a drastic reduction in the switching frequency of the RSC. Then, the  $I_{rd}^*$  changes at  $t = 0.7$  s and the  $\mathbf{V}_r^{r*}$  location jumps to Sector I due to the second term in (4-7). Under this transient condition, the proposed current hysteresis-based regulator selects the non-zero voltage vectors (e.g., the  $\mathbf{V}_2$  vector) to quickly force the RSC output current vector back inside the hysteresis bands within a very short response time of 2 ms. Thereafter, the steady-state operation of the current regulator is followed in Sector III.

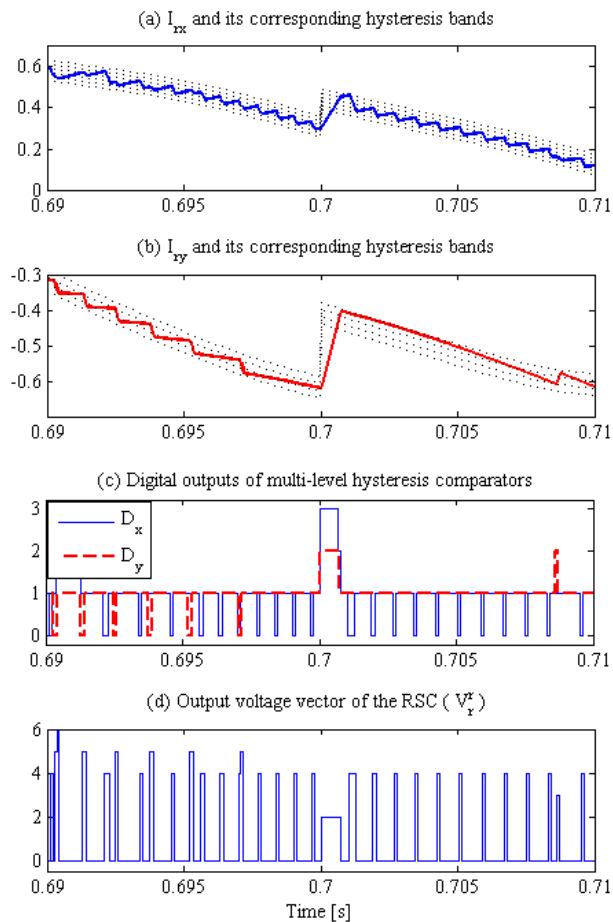


Figure 4-13 Detailed operation of the proposed VBHCR subjected to a step-change in  $I_{rd}$  (zero voltage vectors are shown as  $\mathbf{V}_0$  for the sake of clarity).

#### 4.5.2 Comparison of the steady-state performances

The steady-state performances of the proposed VBHCR and the standard PI current regulator are compared in terms of the harmonic distortions of the DFIG output current and the average switching frequencies of converters. Optimal tuning of the PI controller gains is essential to attain an accurate comparison between the current regulators. Therefore, internal mode control is first used to have an educated guess about the PI gains where the optimum bandwidth of the current control loop is estimated equal to 0.8 PU, i.e., 10%-90% rise time of 10 ms [36]. Then, numerous trail-and-error simulation sets were conducted to obtain the most optimized gains in the PI units, as given in the Appendix B.

The harmonic content of the DFIG output current varies with the rotation speed of the machine and the most severe harmonic distortion is expected at the highest slip values when a larger proportion of the total machine current is transferred through the back-to-back converters. Therefore, the rotor speed has been set to 1.25 PU to examine the output current of the DFIG under the most severe operation condition. Figure 4-14 shows the harmonic spectra when different current regulators have been used in the RSC and GSC (dashed lines show the IEEE Standard limits). In case of the PI current regulator, the total harmonic distortion (THD) is equal to 3.2% with a well-predictable frequency spectrum where harmonic components only exist at frequency orders of  $nf_{sw} \pm 1$ , e.g., 23<sup>rd</sup>, 25<sup>th</sup>, 47<sup>th</sup>, 49<sup>th</sup> etc.) [20]. In contrast, the proposed equidistant-band VBHCR gives an output current with harmonic components spread over a wide frequency range and the THD of 4.1%. However, the THD level and the amplitudes of the individual harmonic components are still well below the permitted distortion limits suggested in IEEE Standard 15471 and IEC Standards [37]-[38].



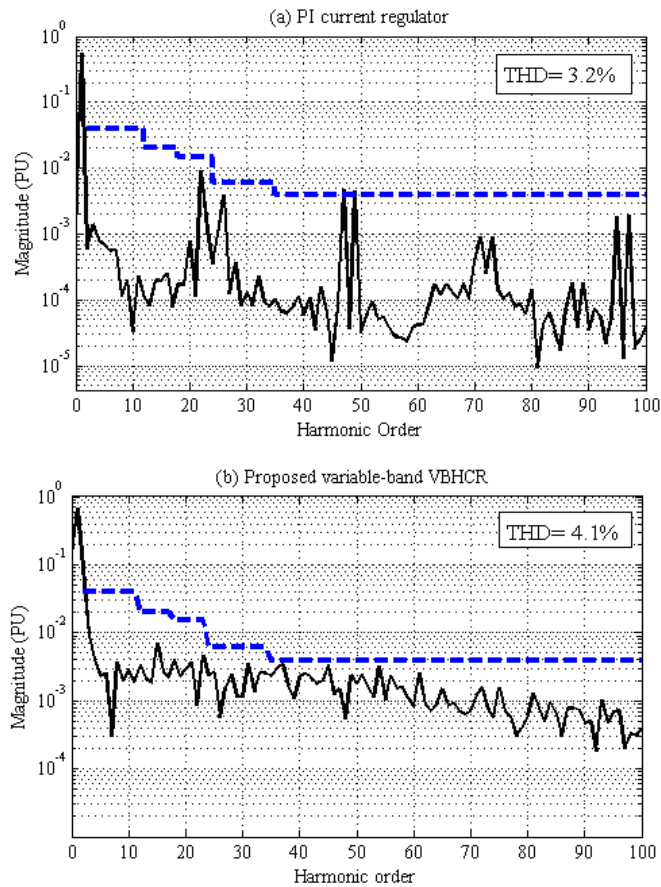


Figure 4-14 Harmonic spectrum of the DFIG output current with (a) PI current regulator (b) Proposed equidistant-band VBHCR (dashed line: IEEE harmonic limits [37])

Figure 4-15 shows the number of switching in phase ‘a’ of the RSC with different current regulators. The simulation time frames are set equal to twice the fundamental period of the rotor current, i.e., equal to 0.8 and 0.16 s when the DFIG operates with  $s = 0.05$  and  $s = 0.25$ , respectively. It can be seen that for the VBHCR, the switching frequency stops rising for half of the fundamental period, as expected from the proposed switching table [20]. Average switching frequencies of the RSC and GSC with various current regulators are summarized in Table 4-3. It is evident that: (1) the PI current regulator gives a fixed switching frequency specified by the carrier waveform, e.g., 1200 Hz in this study; (2) the switching frequency of hysteresis-based methods varies with the rotation speed of the machine; (3) the highest switching frequencies will be observed when the converters are controlled by the conventional hysteresis method and the DFIG operates with high slip values; (4) the switching frequency of the GSC is always larger than the RSC because smaller

hysteresis bands are used in the GSC; (5) the average switching frequencies decrease by 30-60% if the proposed vector-based current regulator is implemented in the RSC and GSC; and (6) a further reduction of 10-30% can be attained when the fixed hysteresis bands are replaced with the equidistant bands.

The main conclusion is that the proposed equidistant-band VBHCR will generally lead to smaller average switching frequencies as compared to the conventional PI current regulator, in view of the fact that wind generators are designed to rotate close to their synchronous speed for the most prevalent wind speed of the site. Further simulation studies have shown that by using equidistant hysteresis bands, the proposed current regulator can adequately operate with the MSF limited to 6 kHz. This figure will increase to 10 kHz when the conventional fixed bands have been used in the proposed VBHCR.

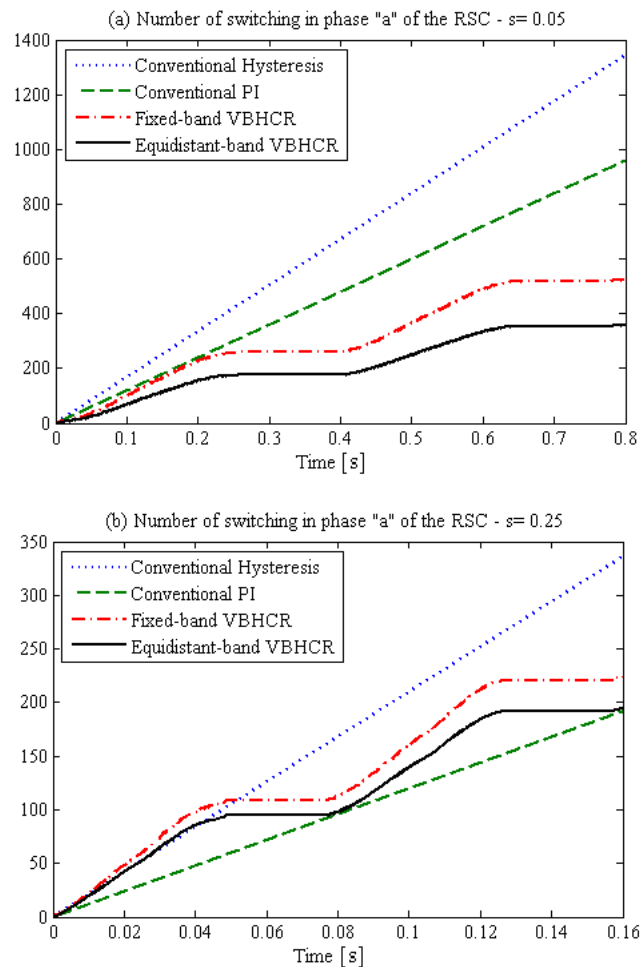


Figure 4-15 Number of switching in phase 'a' of the RSC when DFIG operates with (a)  $s = 0.05$  and (b)  $s = 0.25$ .

Table 4-3 Average switching frequency in the RSC and GSC with various types of current regulators

Current Regulator	Conv. PI with SVM	Conv. HCR		Fixed-Band VBHCR		Equidistant-Band VBHCR	
	$s = 0.0$ or $0.25$	$s = 0.05$	$s = 0.25$	$s = 0.05$	$s = 0.25$	$s = 0.05$	$s = 0.25$
RSC	1200	1680	2100	660	1410	450	1230
GSC	1200	1810	2400	780	1680	560	1430

### 4.5.3 Comparison of the transient performances

The transient responses of current regulators are evaluated under the most stringent LVRT requirements outlined in the Australian grid code. First, a three-phase fault, with the remnant voltage of 0.15 PU for 120 ms, is simulated to examine the LVRT capability of the proposed control scheme under symmetrical fault condition. Sag type  $A_1$  with the fault current angle of  $\psi = 45^\circ$  is considered, which corresponds to the most onerous fault condition experienced in offshore wind farms [see section 3.5.1]. Figure 4-16(a) and Figure 4-16(b) compare the DFIG responses to this fault condition with the PI current regulator and the proposed VBHCR.

In this thesis, comparisons are made between the proposed VBHCR and the standard PI current regulators. However, it must be noted that the PI current regulator is considered as a benchmark of the current practice because almost all of the industrial DFIG-based WTs are utilizing this control strategy, mainly due to its simplicity. That is, the standard PI current regulator is selected as the most popular control strategy but is not the optimal or ultimate control approach that exists in the literature.

From the simulation results with the conventional PI current regulator, it can be seen that the zero-sequence component of the stator flux causes the rotor current to exceed the RSC safety limit at the fault onset [34]. Also, large inrush current in the rotor winding leads to sudden increase of the active power injected from the RSC into the dc-link capacitor. The partial-scale GSC, working below the nominal voltage level, does not have enough capacity to immediately transfer the superfluous power from the capacitor to the grid [15]. As a result, the dc-link voltage rapidly increases to 1.5 PU, which is far beyond the safety limits of the capacitor. Similar observations are

---

made at the fault clearance instant. Therefore, it is evident that the DFIG-based WT cannot ride-through the fault using the conventional PI current regulators.

Figure 4-16(b) shows the fault response of DFIG with the proposed control scheme. In this case, the VBHCR used in the RSC can limit the rotor current within the designated hysteresis bands, i.e., the RSC works independent of the supply voltage waveform. Also, since the proposed VBHCR prevents large inrush currents in the rotor winding, the dc-link voltage fluctuations are significantly reduced and kept below the safety limits. Also, the electromagnetic torque overshoots are notably decreased. This alleviates the mechanical stress imposed on bearing of the turbine shaft. Hence, it can be stated that the proposed VBHCR enhances the low voltage ride-through capability of the DFIG, as requested by the Australian grid code.

It is must be noted that although the proposed VBHCR outperforms the standard PI current regulator under fault conditions, this does not mean that the proposed current regulator is the optimal controller as it needs to be further tested against other non-linear control approaches such as the predictive methods proposed in [18] and [19].

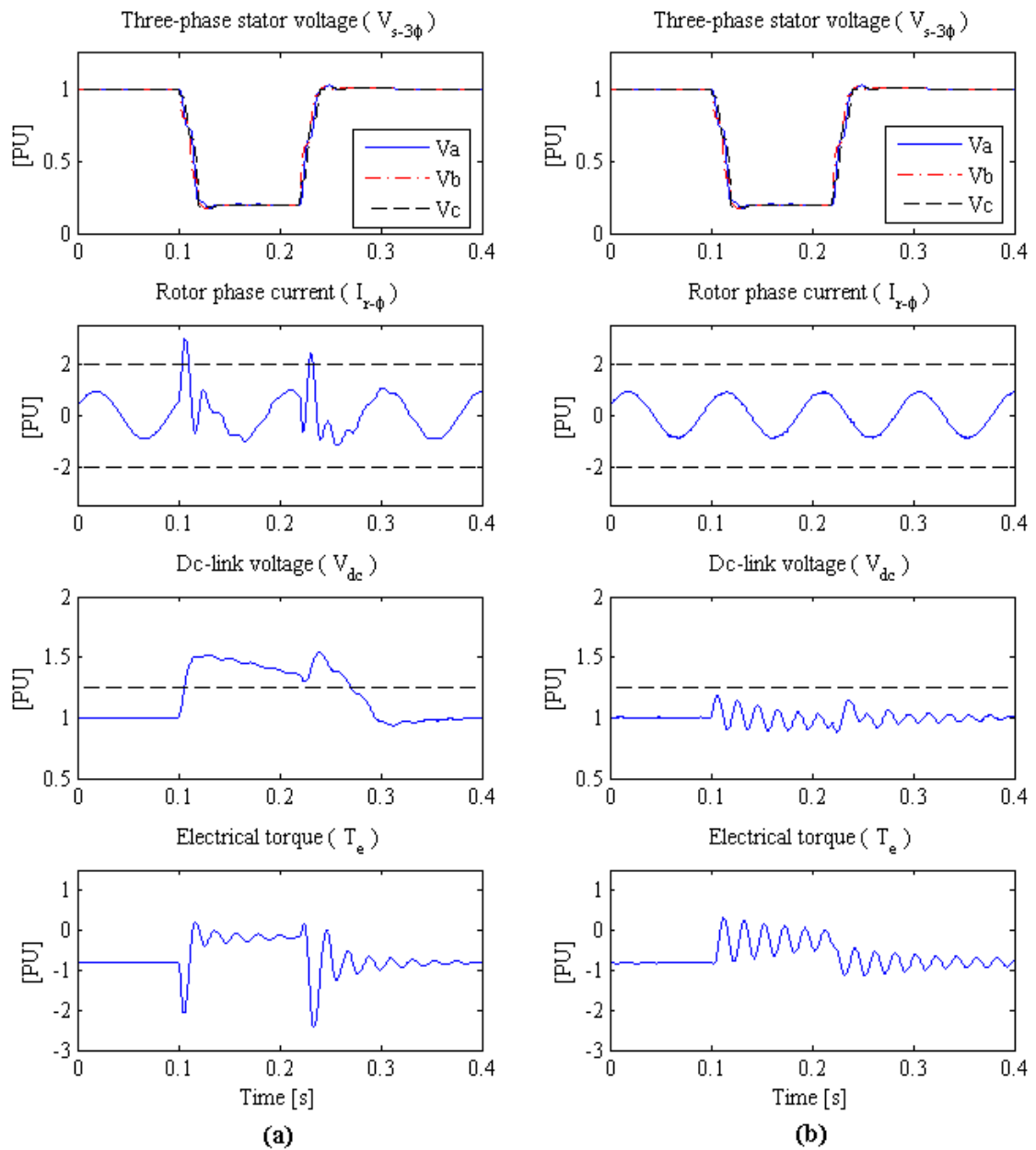


Figure 4-16 Stator voltage, rotor current, dc-link voltage, and electrical torque for DFIG under a three-phase fault with: (a) the standard PI current regulator, (b) the proposed current regulator (dashed lines show the safety margins of the rotor current and dc-link voltage).

Figure 4-17(a) and Figure 4-17(b) compare the system responses under a severe asymmetrical sag condition with  $\mathbf{V}_{sag} = 0.15 \angle -30^\circ$ . For the simulation results with the standard PI current regulator, the zero- and negative-sequence components of the stator flux cause the rotor current to exceed the safety limits of IGBTs shortly after the fault occurrence. The natural response of the stator flux decays after 50 ms while the oscillating impact of the negative-sequence component will be observed during

the fault period. This negative sequence component of the stator flux produces rotor current oscillations with a peak-to-peak value of 1.8 PU at the frequency of  $f_r = (2-s)f_s = 2.2 \text{ PU} = 110 \text{ Hz}$ . However, if the proposed VBHCR is implemented in the RSC, the rotor current oscillations will be constrained within the designated hysteresis bands and DFIG can successfully ride-through the fault. From Figure 4-17(b), it is also evident that the dc-link voltage is kept below the safety margin and pulsations in the electromagnetic torque have been reduced notably using the proposed VBHCR.

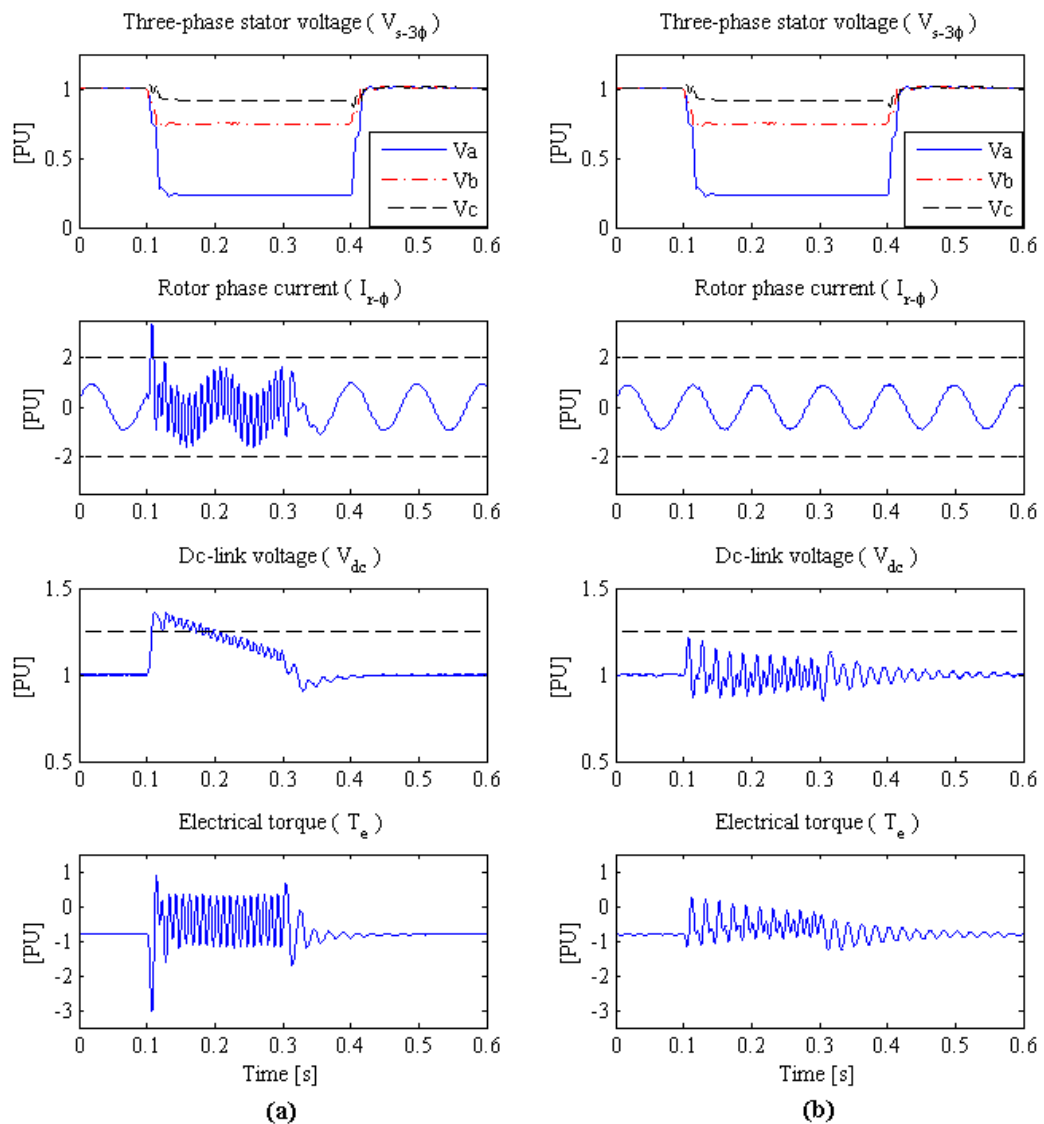


Figure 4-17 Stator voltage, rotor current, dc-link voltage, and electrical torque for DFIG under a two-phase fault with: (a) the standard PI current regulator, (b) the proposed current regulator (dashed lines show the safety margins of the rotor current and dc-link voltage).

Figure 4-18 compares the operation of the conventional PLL system and the proposed UTSP under a type C\* voltage sag with the remnant voltage of 0.6 PU. It can be seen that for the conventional PLL, the negative-sequence of the grid voltage causes a double-frequency ripple with the error amplitude of 0.45 rad in the extracted phase-angle [28]. This erroneous estimation undermines the performance of the DFIG vector control scheme as it produce non-sinusoidal current command signals for the converters. However, the proposed UTSP works completely unaffected to the distortion in the supply voltage waveform.

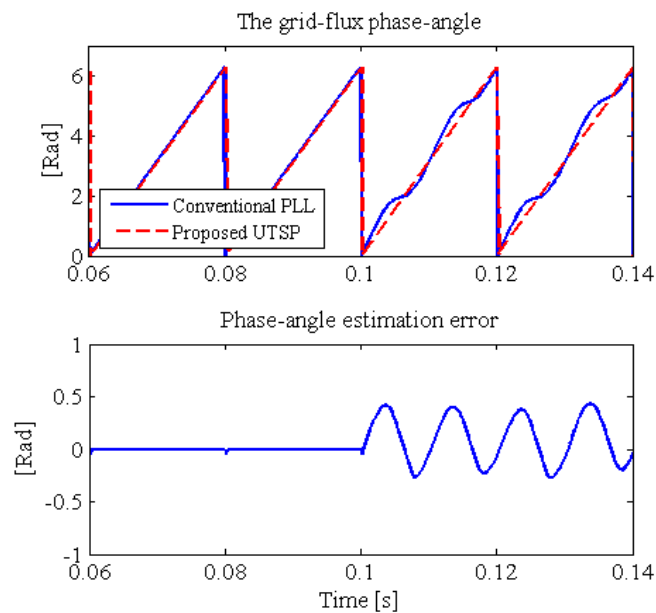


Figure 4-18 Synchronization signal estimated by the conventional PLL system and the proposed UTSP under single-phase-to-ground fault

## 4.6 CONCLUSIONS

In this chapter, a novel grid-flux-oriented vector control scheme is proposed to control the rotor-side and grid-side converters of DFIG-based WTs. The UTSP system is used to extract the synchronization signal and variable-band VBCHRs are implemented to control the output currents of the RSC and GSC. The proposed current regulator is comprised of two multi-level hysteresis comparators integrated with a switching table. The main advantages of this current regulator are its very fast transient response, simple control structure, and intrinsic robustness to the machine

---

parameters variations. It also exhibits an improved steady-state performance compared to the conventional hysteresis method.

Simulation studies confirm the validity of the proposed vector control scheme under varying wind speed conditions. It is also observed that the average switching frequency of the proposed VBHCR is smaller than the PI current regulator, with an acceptable harmonic distortion in the output current. Finally, the transient responses of the proposed VBHCR and the standard PI current regulator are compared under the most stringent LVRT requirements stipulated in the Australian grid code. Simulation results show that the proposed current regulator has a superior tracking performance and successfully complies with the Australian LVRT requirements. In the next chapter, a hybrid current control scheme is proposed as a combination of the VBHCR and the standard PI current regulator. It will be shown that the proposed hybrid current control scheme can enhance the LVRT and HVRT capabilities of DFIG-based WPPs in compliance with the latest international grid codes.



---

## **Chapter 5. Low and high voltage ride-through of DFIG-based WTs using hybrid current controlled converters**

### **5.1 INTRODUCTION**

In Chapter 4, an enhanced hysteresis-based current regulator was proposed to improve the transient response of DFIG-based WTs. The proposed VBHCR has a very fast transient response which enables the DFIG to comply with the most stringent LVRT and HVRT regulations imposed by international TSOs. There is however a problem associated with this current regulator: the switching frequency of the converter changes over one fundamental period (although the average switching frequency is less than the well-known SVM modulation method). If this variable switching frequency and its associated thermal problems can be handled by the heat sink utilized in the power converters, then the proposed VBHCR can be implemented with no problem. However, the converter designers prefer to utilize control strategies with constant switching frequency in some cases. In such cases, a combination of the conventional PI current regulator and the VBHCR could be the solution.

This chapter introduces a novel hybrid current control scheme to improve both LVRT and HVRT capacities of DFIG-based WTs, in compliance with the latest international grid code requirements. The proposed current control scheme is constituted of two different switching strategies integrated with a supervisory control unit. Under normal operating conditions, standard PI current controllers (with optimal steady-state response) are used to regulate the output currents of the RSC and GSC. However, the standard PI current controllers have very limited control bandwidth, which is not adequate for LVRT and HVRT purposes. Therefore, upon detecting a grid disturbance, the supervisory control unit transfers the switching

strategy of converters from the PI method to the hysteresis-based methods. Simulation results in Chapter 4 showed that the proposed VBHCR has very fast transient response and is insensitive to the system parameters variations. However, long-time operation of VBHCRs is preferred to be avoided due to its variable switching frequency. Therefore, the VBHCRs are kept activated only for transient fault periods in order to mitigate the rotor current oscillations and keep the dc-link voltage within the design limits. Once the DFIG operation returns within the safety margins, the standard PI current controllers will be activated again. A re-initialization mechanism is integrated to attain a seamless transition of the switching strategy used in the RSC and GSC. It must be noted that although the proposed hybrid current controller increase the control complexity to some extent, it does not raise the overall system cost as all the modifications are to be made in the control logic.

## 5.2 PROPOSED HYBRID CURRENT CONTROL SCHEME

Figure 5-1 shows the schematic diagram of the proposed hybrid current controller, consisting of four main blocks: the supervisory control unit, standard PI current regulators, the VBHCRs, and the re-initialization units. The PI current controllers regulate the RSC and GSC output currents during normal operating conditions whereas the VBHCRs will be activated when a grid disturbance is detected by the supervisory control unit. Re-initializing units are also integrated to achieve a seamless transition between the current regulators. The operation principles of the conventional PI current controller and the proposed hysteresis-based current controller are already investigated in Chapter 3 and Chapter 4, respectively. Hence, this chapter concentrates on the transition mechanism between the current regulators.

### 5.2.1 Conventional PI current controller

The principles and implementation of the conventional PI current regulators in the vector DFIG-based WTs are presented in section 3.3.3.1. It was mentioned that in the RSC, the tracking error between the reference and the actual current vectors in the synchronous frame are processed by a PI compensator in order to estimate the required voltage control vector ( $\mathbf{U}_r^{dq}$ ) at the RSC terminals and then, the converter output voltage vector is defined based on (3-26). The  $\mathbf{V}_r^{dq}$  vector is transferred from the  $d$ - $q$  frame to the rotor frame using (3-15). Finally, the estimated voltage vector

---

$(\mathbf{V}_r^{xy})$  is fed to a SVM unit in order to generate the gating signals for the RSC switches [5]. Similar PI current controller can be used in the GSC, as already presented in section 3.3.4.1.

### 5.2.2 Vector-based hysteresis current controller

The mathematic principles of the proposed VBHCR are studied in Chapter 4. Therefore, only a brief overview of the control structure and operating features of the proposed VBHCR implemented in the RSC of DFIG is presented in this chapter. Figure 5-2 shows the schematic diagram of the proposed VBHCR used in the RSC. The same control structure can be used in the GSC, but it works with the GSC output current vector represented in the stationary frame ( $\mathbf{I}_g^{\alpha\beta}$ ).

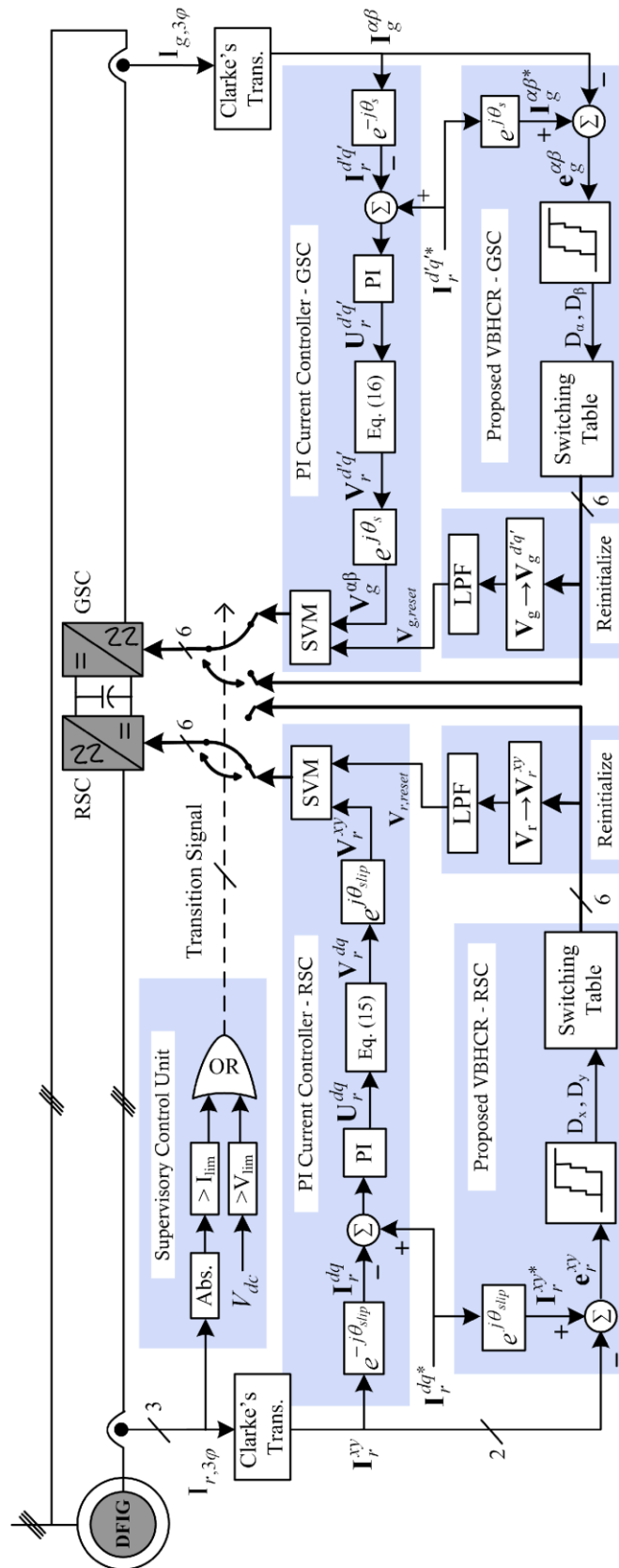


Figure 5-1 Schematic diagram of the proposed hybrid current control scheme.

In Figure 5-2,  $x$ - and  $y$ -components of the tracking error are processed by four- and three-level hysteresis comparators, respectively. Digital outputs of the comparators are fed to a simple switching table to determine the RSC output voltage vector at each instant. For every one sixth of the fundamental period, both  $x$ - and  $y$ -comparators remain in one specific hysteresis loop and this can be used to locate the position of the desired output voltage vector ( $\mathbf{V}_r^*$ ). Based on the  $\mathbf{V}_r^*$  position, zero voltage vectors and non-zero voltage vectors that are adjacent to the  $\mathbf{V}_r^*$  vector will be selected to reduce the tracking error of the current controller.

As the time passes, either  $x$ - or  $y$ - comparator will move to the next hysteresis loop. This means that the position of the  $\mathbf{V}_r^*$  vector has changed to the next sector in the rotor reference frame and accordingly, the next optimal switching sequence will be selected in the RSC from the switching table. In this way, the proposed VBHCR generates an optimal switching pattern that is similar to the widely-used SVM technique. This will significantly reduce the average switching frequency of the RSC and suppress the oscillations in the output current vector.

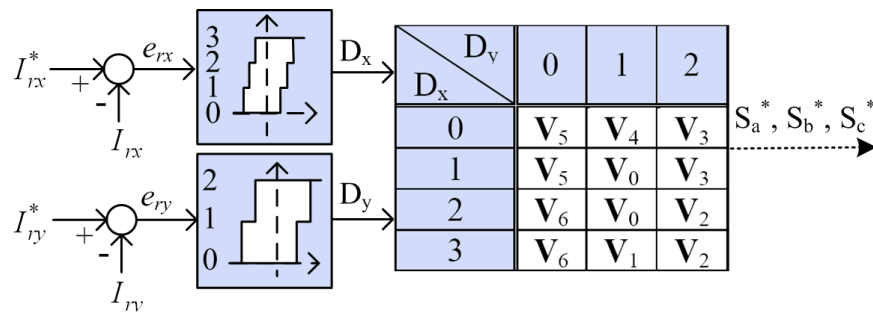


Figure 5-2 Practical implementation of the VBHCR in the RSC.

It is clear that the proposed VBHCR only needs the instantaneous measurement of the rotor current; therefore, it is very robust to the grid voltage distortions and system parameters variations. Moreover, since the modulation unit is eliminated and the gating signals of the RSC are directly generated by the switching table, the proposed current control strategy achieves very fast dynamic response and inherent current limiting behaviour. Accordingly, the RSC can be represented in the DFIG equivalent circuit as a controllable current source, which essentially works independent of the supply voltage waveform [82]. Other salient features of the proposed current

regulator are its simple control structure and minimum computational time. Nonetheless, the switching frequency of the proposed current controller is not constant and large error bands must be used to limit the maximum switching frequency of converters around the zero crossing points of the command vector. This will produce significant low-order current harmonics, which must be avoided under steady-state operating conditions.

### 5.2.3 Transition mechanism

The transition mechanism of the proposed hybrid current controller is demonstrated using Figure 5-3. Under normal operating condition ( $t < t_1$ ), the current in the rotor-side and grid-side converters are regulated using the standard PI current controllers. When a fault occurs in the grid, large transient overshoots will appear in the rotor current due to the zero- and negative-sequence components of the stator flux. The dynamic response of PI current regulator is not fast enough to maintain the precise control of the instantaneous rotor current. Consequently, the tracking error exceeds the PI error bands and rotor current hits the design limits at  $t = t_2$ . This will trigger the supervisory control unit and in turn, the converters switching strategy will be transferred to the hysteresis-based method.

The VBHCR used in the RSC has a very fast transient response and forces the rotor current inside the hysteresis error bands with a negligible response time. However, the switching frequency of converters is not constant and the error bands of VBHCRs must be designed to be larger than the PI controller bands in order to limit the maximum switching frequency of the converters. To avoid these problems, the VBHCRs need to be deactivated after a short period of time (e.g., 50 ms). Finally, the switching strategy of converters will return back to the standard PI method at  $t = t_3 = t_2 + 0.05$  s and remain in this operation mode if the rotor current oscillations have decayed enough from  $t_1$  to  $t_3$ . Otherwise, the VBHCR will be re-activated for another 50 ms (not shown in Figure 5-3).

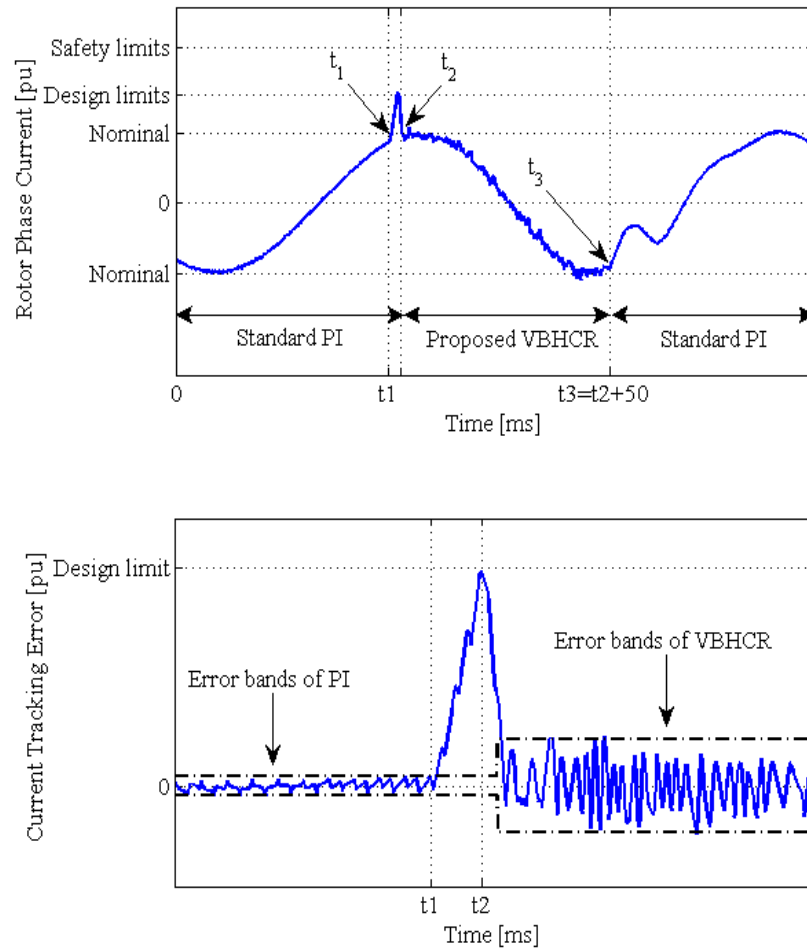


Figure 5-3 Schematic current-time diagram of the proposed hybrid current controller under voltage sag conditions.

Figure 5-3 illustrates how the proposed hybrid current controller protects the DFIG-based WT from destructive overcurrents that can appear under various voltage sag conditions. However, the situation is quite different under voltage swell conditions because the supply voltage rise has minimal impacts on the rotor current [83]. In other words, the RSC will easily handle the supply voltage rise by decreasing its modulation index; thus, the supervisory control unit cannot detect voltage swell conditions from the rotor current signal. In order to address this problem, the dc-link voltage signal is used to sense the grid voltage rise, based on the fact that severe voltage swells cause the GSC to lose its controllability over the power flow in the capacitor and as a result, large overvoltage will occur in the dc-link capacitor. Once the voltage swell condition is detected, the current control strategy in the RSC and

GSC are transferred to the proposed hysteresis method through the procedure that was already described. Note that in the supervisory control block shown in Figure 5-1, the outputs of  $I_r$  and  $V_{dc}$  comparators are fed to a logical 'OR' operator to define the transition signal. This will protect the DFIG from the destructive impacts of not only voltage sag but voltage swell conditions.

#### 5.2.4 Re-initialization process

Due to the sluggish transient response of PI current regulators, direct transition of the switching strategy from the VBHCR to the PI method is not acceptable as it generates large oscillations in the output currents of converters [82]. A re-initialization technique is developed to reset the output of PI compensators and attain a seamless transition between the current controllers. This technique uses the output voltage vectors of converters (the  $\mathbf{V}_r$  and  $\mathbf{V}_g$  vectors) to calculate the resetting values of PI compensators. As can be seen from Figure 5-1, the output voltage vectors of converters will be estimated based on the gating signals of VBHCRs after passing through first-order low-pass filters [82]. The estimated voltage vectors ( $\mathbf{V}_{r,reset}$  and  $\mathbf{V}_{g,reset}$ ) will be used to re-initialize the output voltage of the RSC and GSC upon the controller transition.

### 5.3 SIMULATION RESULTS

Simulation studies are carried out to compare LVRT and HVRT capabilities of the proposed hybrid current controller with the standard PI controller. Figure 3-13 shows the network simulated in Matlab/Simulink with the parameters given in the Appendix B. If a fault occurs at some points inside the transmission system, local voltage at the wind farm drops considerably. As a result, the DFIG-based WTs will be imposed to a sustained voltage sag condition until restores to the rated voltage upon the fault clearance. On the other hand, the DFIG-based WT can be subjected to a voltage swell condition caused by switching off large loads, energizing capacitor banks, or faults in the transmission system.

To achieve an accurate comparison between different current controllers, the outer power control loops of RSC are kept constant and mechanical parts of wind turbine are simulated based on the optimal power-speed curve used in [69]. However, since



very small speed deviation can occur during the short time period considered, simulation results are obtained under constant rotor speed condition. The rotor slip is set equal to  $s = -0.2$  PU preceding the fault in order to simulate the most onerous ride-through conditions that can be experienced by the DFIG. Low and high voltage disturbances are selected from the most onerous LVRT and HVRT regulations enforced by the Spanish and Australian grid codes, respectively. Simulation case studies are as follows:

1. a three-phase short circuit fault, causing a sag type A<sub>1</sub> with the remnant voltage of 0.2 PU at the generator terminals [corresponding to Point C in Figure 2-4]. The fault duration is set to 0.2 s to get better illustration.
2. a phase-to-phase short circuit fault, causing a sag type D with the characteristic voltage of  $\mathbf{V}_{\text{sag}} = 0.6 \angle -31^\circ$  at the generator terminals [corresponding to Point B in Figure 2-4]. In this case study, large phase-angle jump of  $-31^\circ$  is considered in order to simulate the voltage sag conditions experienced in offshore wind farms, where the fault condition is associated with large phase-angle jumps [42].
3. A symmetrical voltage swell of 1.3 PU at the generator terminals [corresponding to Point C in Figure 2-5].

The design limits of the rotor current and dc-link voltage are set to  $I_{\text{lim}} = 1.25$  PU and  $V_{\text{lim}} = 1.1$  PU, respectively. This will ensure that the VBHCRs are activated only when severe voltage sag or swell conditions endanger safe operation of the DFIG-based WT. The overall error bands of VBHCRs are adjusted to  $\pm 0.04$  PU and  $\pm 0.025$  in the RSC and GSC, respectively, in order to restrict the maximum switching frequency of converters to 6 kHz.

### 5.3.1 Operation under symmetrical voltage sag

Figure 5-4(a) and Figure 5-4(b) compare the DFIG response to a type A<sub>1</sub> voltage sag of 0.2 PU without and with the proposed hybrid current controller. Typical safety margins of 2.0 PU and 1.25 PU are considered for the rotor current and dc-link voltage, respectively [35]. From Figure 5-4(a), it can be seen that the zero-sequence component of the stator flux causes the rotor current to exceed the RSC safety limit

at the fault onset. Besides that, large inrush current in the rotor winding leads to sudden increase beyond the safety limits of the dc-bus capacitor. It is therefore evident that the DFIG-based WT cannot ride-through the sag using the standard PI current control scheme.

Figure 5-4(b) shows the simulation results with the proposed hybrid current controller. In this case, the supervisory control unit detects the fault shortly after its occurrence. The rotor current hits the design limit at  $t = 103$  ms and consequently, the switching strategies of the RSC and GSC are transferred to the hysteresis-based method for the next 50 ms. It can be seen that for  $103 < t < 153$  ms, the VBHCR used in the RSC manages to eliminate the zero-sequence oscillations and keep the rotor current inside the designated hysteresis error bands. That is, the RSC operates as a current source independent of the grid voltage waveform. Then, the RSC switching strategy is transferred back to the PI controller at  $t = 153$  ms, although the zero sequence of the stator flux has not sufficiently suppressed yet. As a result, the supervisory control unit will be triggered one more time at  $t = 157$  ms. The conventional and the proposed hybrid current controllers show similar responses for  $207 < t < 300$  ms. Finally, the VBHCRs are reactivated at the fault clearance instant.

Comparing Figure 5-4(a) and Figure 5-4(b), it is also observed that since the proposed VBHCR avoid large inrush currents to flow in the rotor winding at the fault instant, the fluctuations of dc-link voltage have been significantly reduced and kept below the safety limits. Note that using the proposed VBHCR in the GSC is the other factor that contributes to further reduction in the dc-link voltage fluctuations. Moreover, the initial torque overshoot is notably decreased from 2.2 PU to 1.4 PU. Therefore, it can be concluded that the proposed hybrid current controller improves the LVRT capability of the DFIG under three-phase faults, as requested by the Spanish grid code.

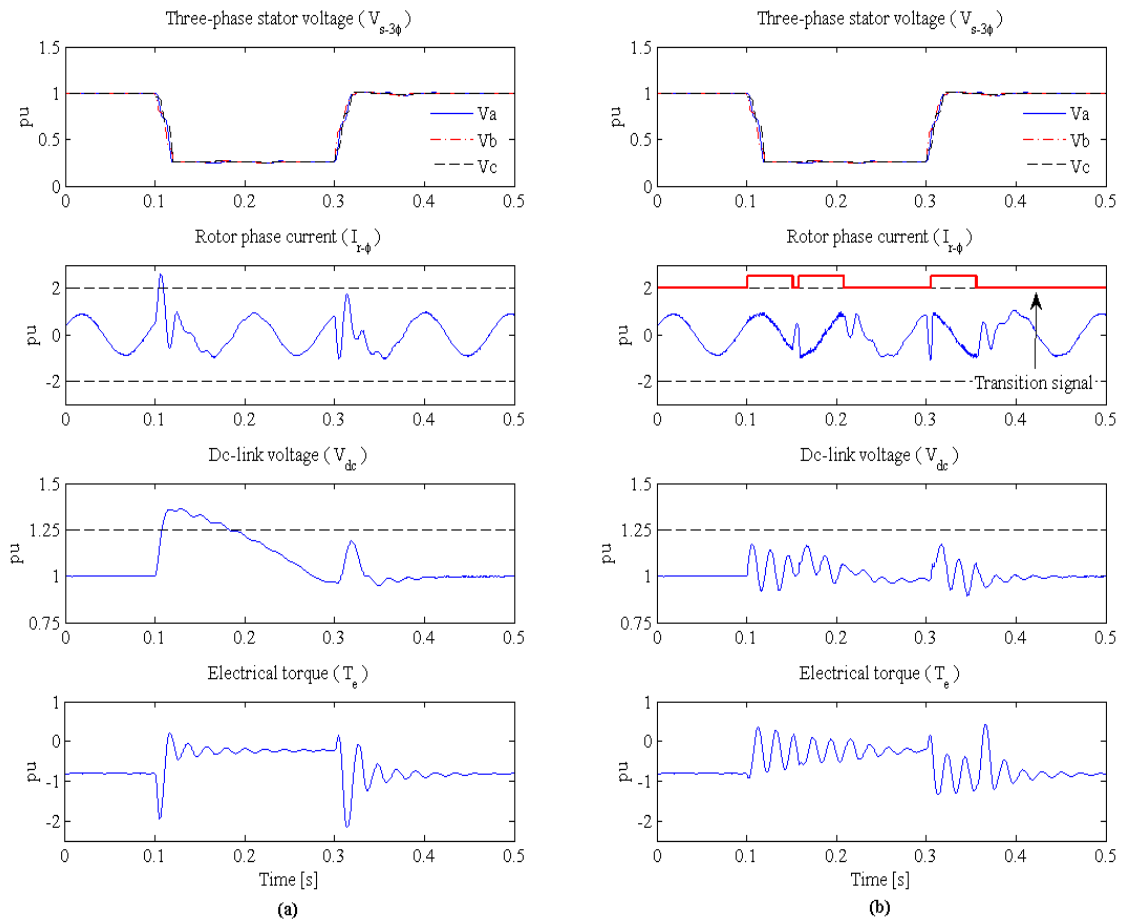


Figure 5-4 Stator voltage, rotor current, dc-link voltage, and electrical torque for DFIG under symmetrical voltage sag with: (a) the standard PI current controller, (b) the proposed hybrid current controller.

Figure 5-5 shows the detailed operation of the proposed hybrid current controller at the fault instant. Under normal operating conditions, the rotor current is regulated by the standard PI current controller with optimal steady-state performance (the gating signals are generated by the SVM unit). The fault occurs at  $t = 100$  ms and since the PI controller has a very slow dynamic response, the rotor current in phase  $b$  hits the design limits at  $t = 103$  ms. Consequently, the RSC current control strategy is transferred to the VBHCR with larger error bands of  $\pm 0.05$  PU. As expected, this will produce higher rotor current oscillations with significant low-order harmonic distortions. Note that using the proposed VBHCR, the gating signals at each instant are directly generated by a simple switching table which gives the switching pattern shown in Figure 5-5 (b). The instantaneous output voltage of the RSC and the filtered waveform are shown in Figure 5-5 (c).

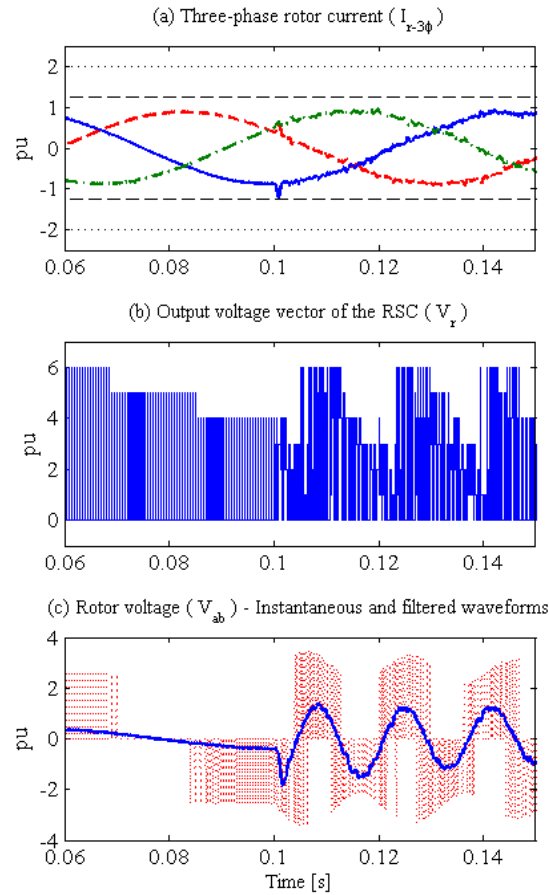


Figure 5-5 Detailed operation of the hybrid current controller at the fault instant (dashed and dotted lines show the design and safety limits of the rotor current, respectively).

### 5.3.2 Operation under asymmetrical voltage sag

Figure 5-6(a) and Figure 5-6(b) compare the DFIG responses under a severe asymmetrical fault condition, causing sag type D with  $V_{\text{sag}} = 0.6 \angle -31^\circ$  at the DFIG terminals. It is clear that using the conventional current controller, the zero- and negative-sequence components of the stator flux cause the rotor current to exceed the safety limits of IGBTs shortly after the fault occurrence. The natural response of the stator flux decays in 50 ms whereas the oscillating impact of negative-sequence component can be observed throughout the fault period. The negative-sequence component of the stator flux causes oscillations in the rotor current with the peak-to-peak value of 1.2 PU and frequency of  $f_r = (2-s)f_s = 2.2 \text{ PU} = 110 \text{ Hz}$ . However, if the proposed hybrid current control scheme is implemented in the RSC and GSC, the rotor current oscillations will be constrained within the design limits and DFIG can ride-through the fault.

From Figure 5-6(b), it is observed that once the rotor current hits the design limits at  $t = 106$  ms, the VBHCR will be activated for the next 50 ms. The current control scheme is transferred back to the conventional PI method at  $t = 156$  ms. At this instant, the zero-sequence of the stator flux has completely decayed, yet the negative-sequence of the rotor current is large enough to trigger the supervisory control unit. Therefore, the VBHCRs are kept activated throughout the fault period. In this way, the proposed hybrid current controller manages to constrain the rotor current within the safety limits of semiconductor switches used in the RSC. It is also clear that the dc-link voltage is kept below the safety limit and pulsations in the electromagnetic torque are reduced by 50%.

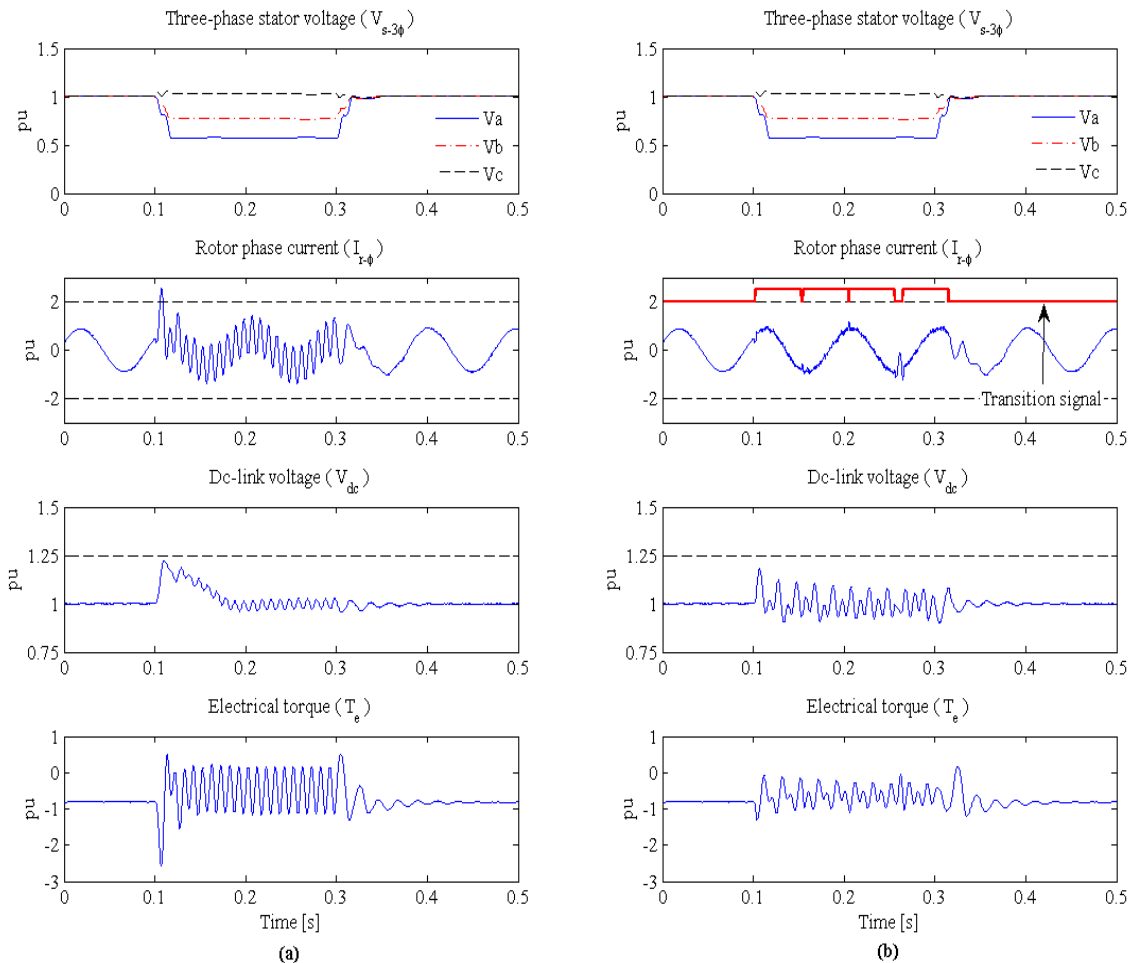


Figure 5-6 Stator voltage, rotor current, dc-link voltage, and electrical torque for DFIG under asymmetrical voltage sag with: (a) the standard PI current controller, (b) the proposed hybrid current controller.

### 5.3.3 Operation under voltage swell

Figure 5-7(a) and Figure 5-7(b) compare the DFIG responses under the voltage swell of 1.3 PU. When the conventional PI current controllers are used, the RSC handles the grid voltage rise by decreasing its modulation index, i.e., reducing the RSC voltage gain. Therefore, the rotor current oscillations are eliminated shortly after the swell onset. On the other hand, the GSC must counteract the voltage rise by increasing its modulation index in order to control the active power flow into the capacitor and keep the dc-link voltage constant. From Figure 5-7 (a), it is evident that this compensating action will drive the SVM unit into saturation. As a result, the anti-parallel diodes of the GSC are forward biased and the GSC fails to control the dc-link voltage and destructive overvoltage of 1.4 PU will appear in the capacitor. This overvoltage in the dc-link capacitor will sustain throughout the swell period.

Simulation results in Figure 5-7(b) shows that overvoltages in the dc-link capacitor can be avoided using the proposed hybrid current controller. In this case, the dc-link voltage hits the design limit of 1.1 PU and accordingly, VBHCR is activated in the DFIG converters. By using this current controller in the GSC, the modulation unit will be omitted and the dc-link voltage will be fully available at the output terminals of the GSC. Therefore, the dc-link voltage fluctuations can be limited below the safety limits of the capacitor. Moreover, the rotor current oscillations and torque pulsations are notably reduced. Hence, the DFIG-based WT can successfully ride-through the voltage swell conditions required by the Australian grid code.

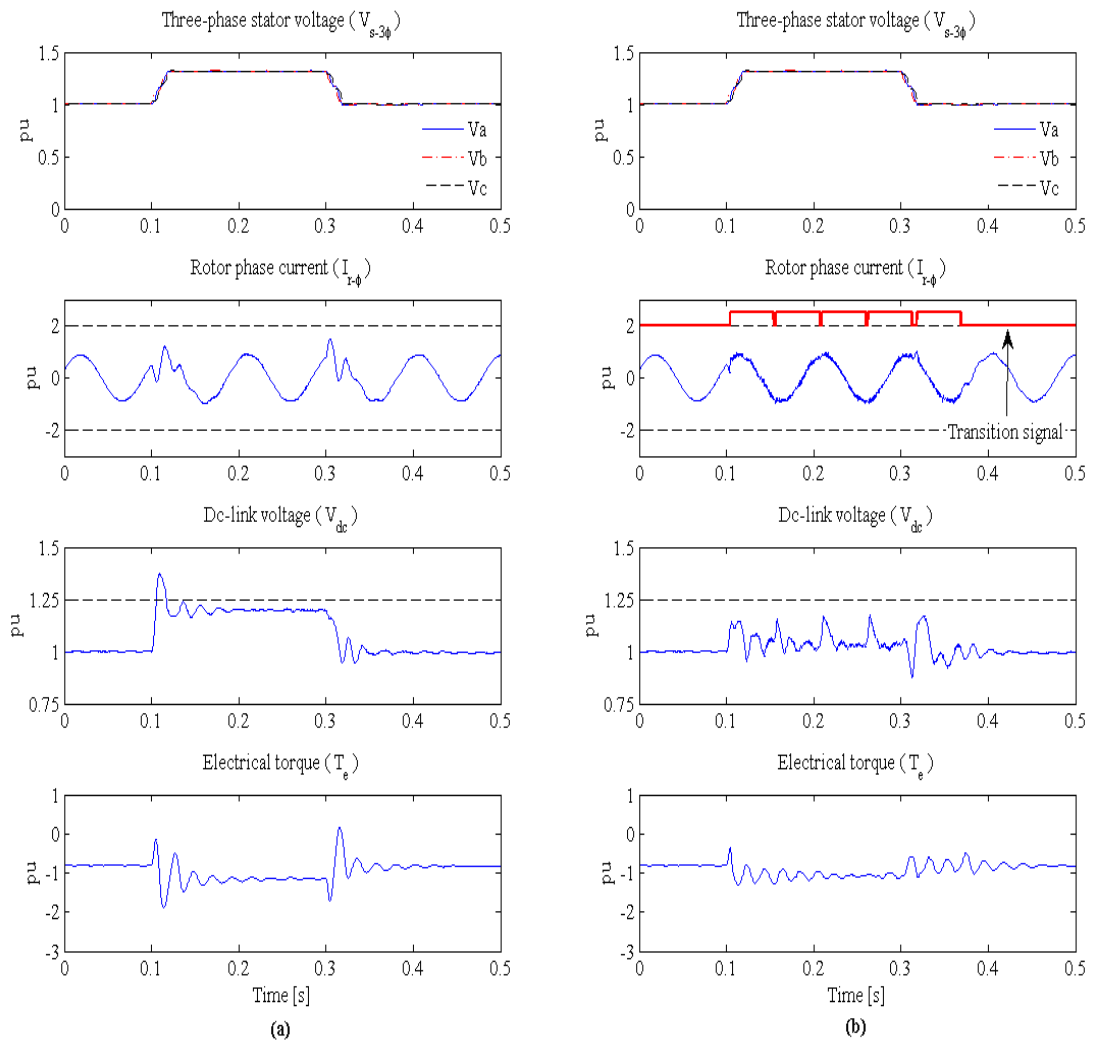


Figure 5-7 Stator voltage, rotor current, dc-link voltage, and electrical torque for DFIG under a symmetrical voltage swell of 1.3 PU with: (a) the standard PI current controller, (b) the proposed hybrid current controller.

### 5.3.4 Reactive power support

According to Australian regulation, wind generators must generate at least 4% of their maximum available reactive current for each percent of the voltage drop when the PCC voltage falls outside  $\pm 10\%$  dead band around the nominal voltage [see section 2.4.3]. After the fault clearance, the active power output of wind farm must restore to 95% of the pre-fault value within 100 ms.

Further simulation studies have been conducted to test the performance of the proposed current controller when the DFIG control scheme is modified to comply with the Australian regulations. The WT is subjected to a three-phase fault for

$0.1 < t < 0.4$  s. During the fault, the PCC voltage drops to 0.5 PU and consequently, the reactive power component of the rotor current ( $I_{rd}$ ) must ramp up to 1.0 PU. In the meanwhile, to avoid overloading the RSC, the active power component of the rotor current ( $I_{rq}$ ) must be reduced to zero as the total capacity of the converter has been dedicated to reactive current generation. Simulation results for the conventional and proposed current controllers are shown in Figure 5-8. It is evident that the hybrid current controller complies with the Australian requirement and follows the command vector with no tracking error, whereas the standard PI current controller shows a large overshoot of 1.75 PU at the fault onset.

Under normal operating conditions, the DFIG-based WT delivers 0.8 PU of the active power with unity power factor (the reactive current component of 0.3 PU only provides the machine excitation). As the fault occurs at  $t = 0.1$  s, the reactive current component of the RSC ramps up to 1.0 PU, which increase the DFIG reactive power injection to the nominal value of 0.35 PU. At the same time, the active current component ( $I_{rq}$ ) has been reduced to zero to comply with the converter rating. Consequently, the DFIG active power generation plunges to zero but returns back to the prefault value after the fault clearance. Further studies on the reactive power support of DFIG-based WPPs will be presented in the next chapter.

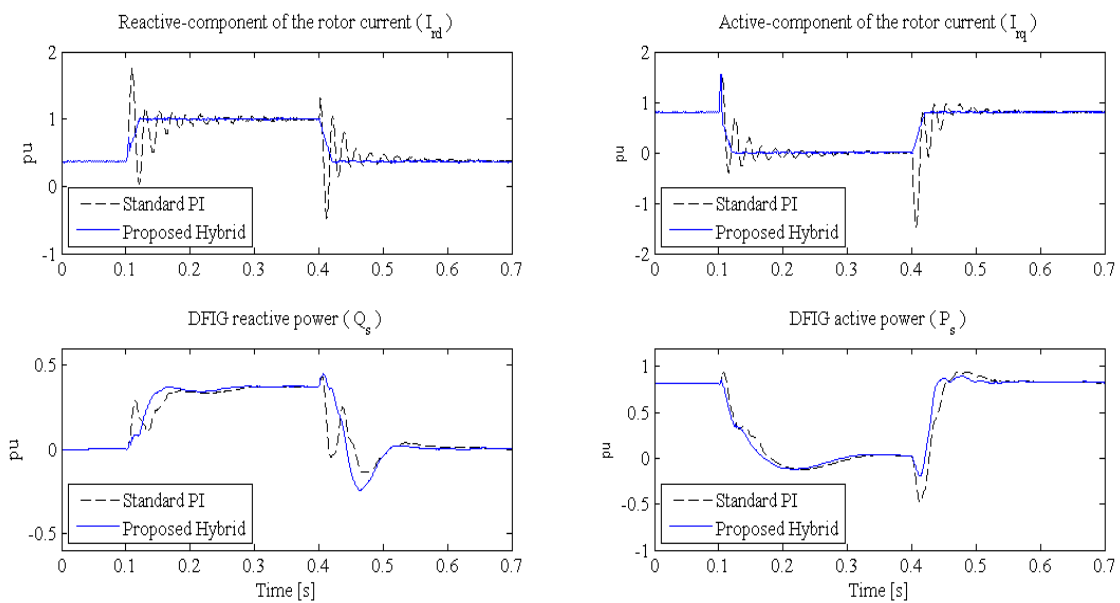


Figure 5-8 Reactive power support of the PI and the proposed hybrid controller according to Australian regulations for a 50% type A voltage sag



## 5.4 CONCLUSIONS

This chapter presents a new hybrid current control scheme to enhance both LVRT and HVRT capabilities of DFIG-based WTs, in compliance with the international grid codes. Standard PI current controllers are used to regulate the output currents of RSC and GSC under normal operating conditions. When a grid disturbance is detected by the proposed supervisory control unit, the switching strategy of converters is transferred to the VBHCR. This current regulator has very fast transient response that will effectively eliminate high frequency oscillations of the rotor current and limit the dc-link voltage fluctuations. However, long-term operation of VBHCR is not desirable due to its variable switching frequency and increased lower-order current harmonics. Therefore, the switching strategy of converters is transferred back to the PI method when the rotor current and dc-link voltage oscillations are reduced below the design limits. A re-initialization mechanism is integrated to attain a seamless transition between the current controllers.

Simulation results show that the proposed hybrid current control scheme enables the DFIG-based WTs to retain the superior steady state performance of the standard PI current regulator along with the very fast dynamic response of the VBHCRs. As a result, the DFIG-based WT can successfully comply with the stringent LVRT and HVRT regulations stipulated by the Spanish and Australian grid codes, respectively. Also, the Australian regulations on the reactive power support of DFIG-based WPPs is briefly investigated. In the next chapter, further modifications in the control structure of DFIG-based WPPs will be proposed to enhance their  $P$ - $Q$  response under various fault conditions.

## Chapter 6. Active and reactive power responses of DFIG-based WPPs following faults

### 6.1 INTRODUCTION

In Chapter 2, it was mentioned that modern grid codes require WPPs to provide reactive power support during the fault period and restore active power generation after the fault clearance. The most stringent regulations on the active and reactive power response of wind farms are stipulated in the Australian grid code. Accordingly, this chapter introduces a modified control scheme for DFIG-based WPPs to comply with the Australian grid code requirements. In the proposed control design, the UTSP system is used to not only extract the synchronization signal, but to estimate the supply voltage amplitude during grid faults. Also, current prioritization units are employed to modify the current command vectors under different operating conditions, based on the new design strategies developed in this thesis. Simulation results show that the proposed control scheme enables DFIG-based WPPs to comply with the latest regulations on the reactive and reactive power responses of wind farms as stipulated by the Australian TSO.

This chapter is organized as follows. In Section 6.2, the  $P$ - $Q$  capability curves of DFIG-based WPPs with different control designs are thoroughly studies. Section 6.3 presents the modified control scheme developed in this thesis. Time-domain simulation results are presented in Section 6.4 to test the ability of the proposed control scheme in compliance with Australian grid code requirement and to examine its impacts on the nearby grid, e.g., on fixed-speed WPPs.

## 6.2 P-Q CAPABILITY CURVES OF DFIG-BASED WPP

This section examines the  $P$ - $Q$  capability curves of DFIG-based WPPs with different control designs. First, the maximum current-carrying capacity of the RSC is calculated. Then, the original and modified control designs are presented and their corresponding  $P$ - $Q$  capability curves are obtained.

### 6.2.1 Maximum current capacity of converters

The Australian grid code requires WPPs to be capable of continuously operating at their rated active power with the power factor in the range of 0.93 capacitive to 0.93 inductive. The upper and lower limits of the supply voltage amplitude and grid frequency for the continuous operation of generating units are specified as  $|V_{s,max}| = 1.1$  PU,  $|V_{s,min}| = 0.9$  PU,  $f_{min} = 49.5$  Hz and  $f_{max} = 50.5$  Hz [refer to chapter 2].

These specifications must be taken into account to calculate the maximum current-carrying capacity of converters ( $I_{r,max}$ ). An appropriate design of  $I_{r,max}$  should make sure that the active and reactive power requirements of the DFIG-based WPP can be attained under the most onerous operating conditions without violating the thermal limits of converters.

In order to obtain the analytical expression of  $I_{r,max}$ , the active and reactive powers of DFIG are needed. If the scaling factors of Clarke's Transformation are omitted, the stator active and reactive powers in the synchronous frame are defined by

$$P_s = |V_s| I_{rq} \quad 6-1$$

$$Q_s = |V_s| I_{rd} - \frac{|V_s|^2}{\omega_s L_m} \quad 6-2$$

where  $|V_s|$  is the supply voltage amplitude and  $I_{rd}$  and  $I_{rq}$  are the quadrature components of the rotor current in the grid flux-oriented frame. Typical value of  $L_m = 3.0$  PU is considered in this study. Based on (6-1) and (6-2), the amplitude of current in the RSC can be obtained as

$$|I_r| = \sqrt{I_{rq}^2 + I_{rd}^2} = \sqrt{\left(\frac{P_s}{|V_s|}\right)^2 + \left(\frac{Q_s}{|V_s|} + \frac{|V_s|}{3\omega_s}\right)^2} \quad 6-3$$

The maximum rotor current is required when the  $P_s$  and  $Q_s$  are at their rated values,

and the supply voltage amplitude and grid frequency are at their minimum values, i.e.,  $P_s = 1.0$  PU,  $Q_s = 0.395$  PU,  $|V_s| = 0.9$  PU and  $\omega_s = 0.99$  PU. Substituting these values in (6-3), the  $I_{r-max}$  is obtained equal to 1.34 PU. This means that the rated current of the RSC must be 34% larger than its rated active power or  $I_{rq,max} = 0.75|I_{r,max}|$ . The extra current capacity in the RSC is needed to provide the machine excitation as well as generate the rated capacitive reactive power of 0.395 PU, if requested by the Australian system operator.

### 6.2.2 *P-Q* capability curve of DFIG – Design 1

Equations (6-1) and (6-2) can be used to calculate the *P-Q* response of the DFIG-based WPP with various control designs. The highest wind speed situation (i.e., the rated output active power) is considered in this study because this scenario represents the most onerous situation that can be experienced by the WPP [65].

The *P-Q* capability curve of DFIG with the conventional control design is shown in Figure 6-1. Three different operating zones are observed in this figure. Zone I corresponds to the normal operating condition when  $|V_s| > 0.9$  PU. At the start of this zone, the active current component of the RSC ( $I_{rq}$ ) is set to 0.75 PU in order to extract the rated active power from the DFIG. The DFIG is designed to work at unity power factor (UPF); therefore, the reactive current component of the RSC must only provide the machine excitation ( $I_{rd} = 0.25$  PU). As the supply voltage reduces from 1.0 PU to 0.9 PU, the  $I_{rq}$  component increases linearly to compensate for the supply voltage drop and maintain the active power at the rated value. The  $I_{rd}$  component, on the other hand, reduces slightly because the machine excitation decreases as the supply voltage drops, as projected in the second term of (6-2).

Once the supply voltage drops below 0.9 PU, the DFIG-based WPP must help the supply voltage recovery by injecting 4% reactive current component for each 1% drop in the supply voltage amplitude. Accordingly, the  $I_{rd}$  component starts linearly increasing from 0.6 PU and in the meanwhile, the  $I_{rq}$  component must decrease so that the rotor current is constrained within the limits of semiconductor switches, i.e., to ensure that  $|I_r| \leq 1.0$  PU. This implies that in Zone II, the active power production must be partially sacrificed in order to provide the reactive power support requested by the Australian regulations. Finally at  $|V_s| = 0.75$  PU, the reactive current

component of the RSC becomes equal to 1.0 PU and its active component reduces to zero. Consequently, the DFIG active power production remains at zero in Zone III, while its reactive power output reduces as the voltage drops. However, the DFIG operation with  $P_s = 0$  can force the WPP to disconnect from the grid because it leads to a large mismatch between the machine electromagnetic torque and the input mechanical torque. As a result, the shaft speed might increase beyond the safety limits of the turbine and in turn, the DFIG-based WPP must disconnect from the grid. This problem is addressed in the second control design.

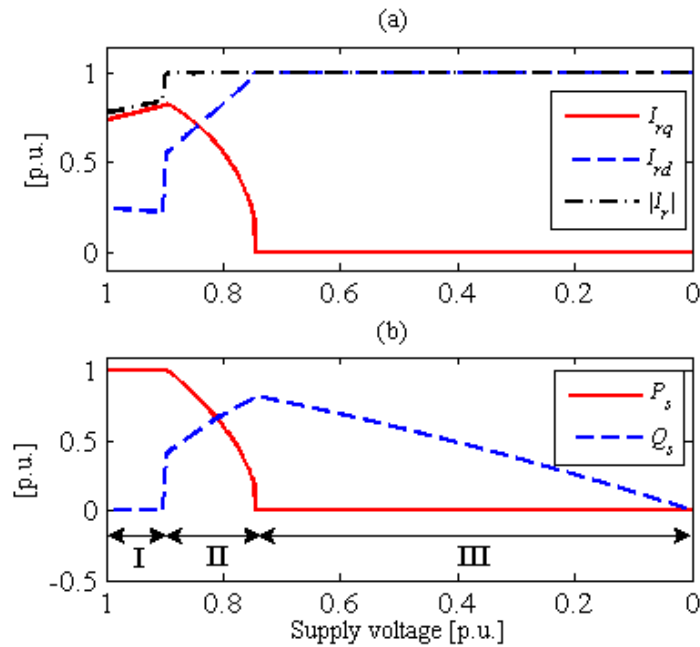


Figure 6-1  $P$ - $Q$  response of DFIG with control Design 1: (a) quadrature components of the rotor current, (b) active and reactive powers of the stator.

### 6.2.3 P-Q capability curve of DFIG – Design 2

In ‘Design 2’, the RSC output current is permitted to temporarily increase to 1.41 times of its nominal capacity during the fault period. Note that this is not a major threat for semiconductor switches because modern converters have been designed to withstand short-term overloading. For example, Semikron SKiiP<sup>®</sup> intelligent power modules can tolerate 150% overloading for 20 s [25]. The maximum fault duration requested in Australian grid code is 10 s; therefore, the RSC can be safely overloaded

by 41% during the fault period defined in the Australian Grid Code. Figure 6-2 shows the  $P$ - $Q$  capability curve of DFIG with Design 2.

This curve is different from Design 1 in the second and third operating zones. In Zone II, the active current component of the RSC is allowed to keep rising along with its reactive current component. This will retain the active power production constant while the reactive power injection from the DFIG increases. At  $|V_s| = 0.75$  PU, both  $I_{rd}$  and  $I_{rq}$  reach to 1.0 PU and in turn, the RSC output current becomes equal to 1.41 PU

It is also evident that the DFIG active power generation can be partially retained in Zone II and Zone III. This improvement in the active power response of DFIG is very valuable because it not only reduces the risk of destructive over-speeds in the shaft, but also enables the WPP to participate in the short-term frequency and transient stability support for the nearby grid. Finally, the next design strategy ('Design 3') enhances the reactive power capability of DFIG by exploiting the free current capacity of the GSC.

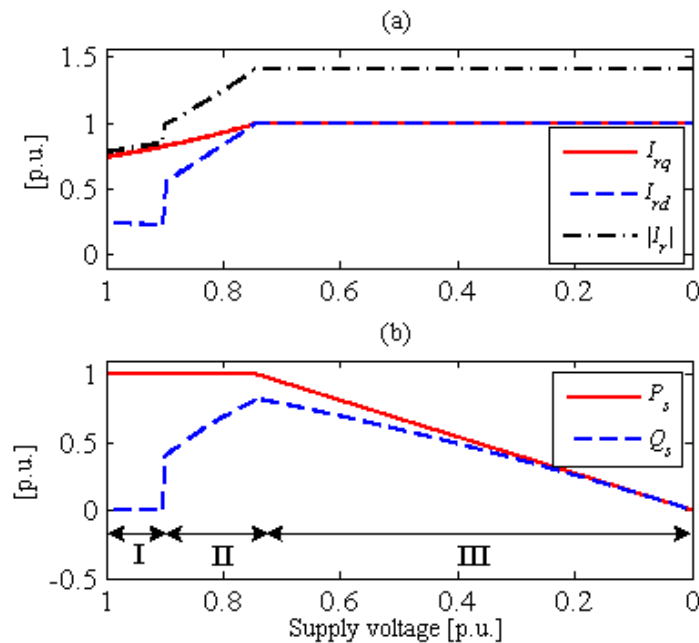


Figure 6-2  $P$ - $Q$  response of DFIG with control Design 2: (a) quadrature components of the rotor current, (b) active and reactive powers of the stator.

### 6.2.4 *P-Q* capability Curve of DFIG – Design 3

The rotor-side and grid-side converters of a DFIG, as back-to-back VSCs, are usually designed with the same rating. Therefore, there is always a free capacity in the GSC that can be deployed for providing further reactive power support during faults. However, the active power component of the GSC cannot be sacrificed for the sake of reactive power injection because it leads to destructive over-voltages in the dc-link capacitor and as a result, continuous operation of the WPP will be interrupted. In other words, the active current component of the GSC must be always prioritized to its reactive component. However, if the GSC is permitted to be overloaded during the fault period, this converter can inject both active and reactive powers to the grid. In Design 3, the reactive power generation from the GSC helps the RSC to further enhance the reactive power capability of DFIG-based WPP under fault conditions.

The operation principles of the GSC are thoroughly investigated in Section 3.3.2. The GSC active and reactive powers in the grid voltage-oriented frame are defined as

$$P_g + jQ_g = |V_s| I_{gd} + j|V_s| I_{gq} \quad 6-4$$

where  $I_{gd}$  and  $I_{gq}$  are the active and reactive components of the GSC, respectively.

Figure 6-3 shows the *P-Q* capability curve of the GSC when it is aimed to contribute to the reactive support under fault conditions. The GSC is sized at 35% of the DFIG rated power. In the start of Zone I, the active and reactive current components of the GSC are equal to 0.75 PU and zero, respectively. This operating point corresponds to rated active power production at UPF. In Zone II, the  $I_{gd}$  component increases to keep the GSC active power constant at its rated value, i.e., to maintain  $P_g$  at 0.35 PU. The  $I_{gq}$  component, on the other hand, increases by 4% for each 1% reduction in the supply voltage magnitude. Both GSC current components reach to 1.0 PU and the start of Zone III and from this point onward, the GSC active and reactive powers decrease linearly as the supply voltage drops.

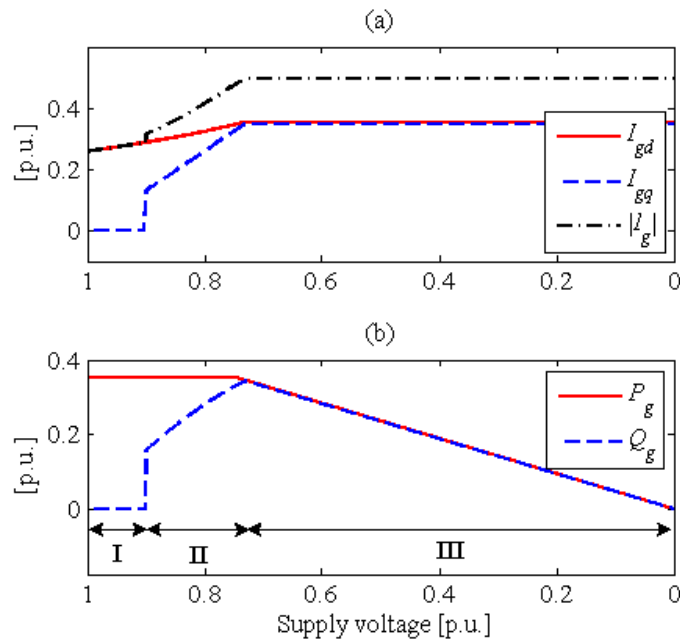


Figure 6-3  $P$ - $Q$  response of GSC with control Design 3: (a) quadrature components of the GSC, (b) active and reactive powers of the GSC.

### 6.3 PROPOSED DFIG CONTROL SCHEME

Figure 6-4 shows the schematic diagram of the proposed control scheme. The RSC controller is configured in the following steps:

1. Clarke's transformation is used to obtain the vector representation of the measured three-phase signals.
2. The rotor angle is measured using a position encoder whereas the synchronizing signal is extracted using the proposed UTSP. This signal processing unit can also estimate the amplitude of the supply voltage. The  $|V_s|$  signal will be needed to detect the fault conditions and provide the 4% reactive power support requested by the Australian grid code.
3. Using (3-14), the  $\mathbf{I}_s$  vector is transferred from the stationary frame to the synchronous frame.
4. Based on (6-1) and (6-2), the active and reactive powers produced in the stator winding of DFIG are calculated and compared to their command values. The active power command signal,  $P^*$ , is calculated based on the



optimal power-speed curve. The  $Q^*$  signal is defined based on the grid code regulation. The Australian TSO, for instance, may request power factor in the range of 0.93 capacitive to 0.93 inductive.

5. Under normal operating condition ( $0.9 < |V_s| < 1.1$  PU), the error signals of  $\Delta P_s$  and  $\Delta Q_s$  are fed to the PI compensators in order to calculate the  $I_{rq}^*$  and  $I_{rd}^*$  signals, respectively. However, if the supply voltage drops below 0.9 PU, the reactive current component of the RSC must ramp up by 4% of the RSC nominal current for each 1% reduction in the supply voltage amplitude.
6. The quadrature components of the rotor command vector are fed to a current prioritization unit to avoid hazardous overloading of the RSC, based on different  $P$ - $Q$  control designs that are already studied in section 6.2.
7. Using (3-15), the rotor command vector is transformed from the synchronous frame to the rotor frame.
8. Finally, the command and the measured rotor current vectors are fed to a variable-band VBHCR unit in order to generate the gating signals of the RSC. Note that the proposed VBHCR can also be replaced with the hybrid current control scheme proposed in Chapter 5. This will not cause any notable difference in the operation of the proposed overall vector control scheme.

In the same manner, the GSC controller can be configured in the following steps:

1. Two PI control blocks are used to calculate the  $I_{gd}^*$  and  $I_{gq}^*$  current components from the error signals of  $\Delta V_{dc}$  and  $\Delta Q_g$ , respectively.
2. The quadrature components of the GSC command vector are fed to a current prioritization unit. This unit will only work under fault conditions with Design 3. It does not change the active current component of the command vector, but exploits the free current capacity of the GSC to contribute to the reactive power support under fault conditions (through modifying  $I_{gq}^*$ ).
3. The GSC current command vector is transferred from the synchronous frame to the stationary frame, using (3-14).
4. The GSC current vector and the current command vector are fed to the variable-band VBHCR unit to generate the gating signals for the GSC.

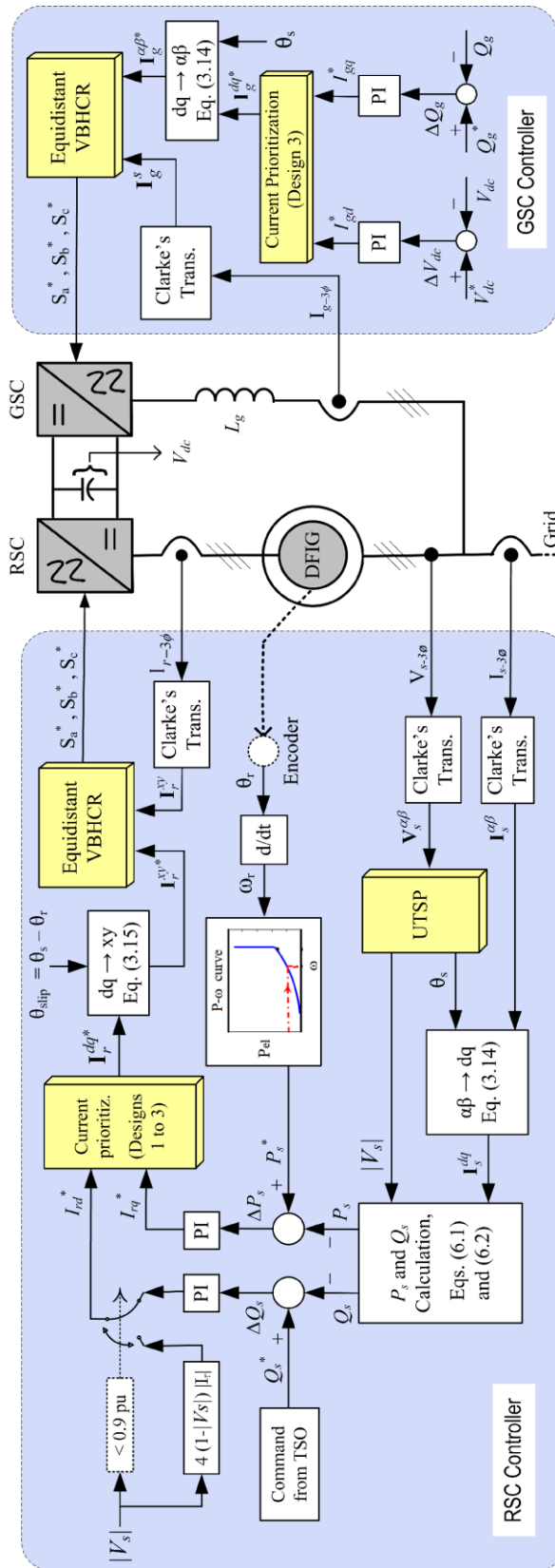


Figure 6-4 Schematic diagram of the proposed control scheme.

## 6.4 SIMULATION RESULTS

Extensive simulation studies are carried out to examine the transient response of the proposed control scheme in compliance with the Australian grid code. Figure 6-5 shows the simple distribution network simulated in Matlab/Simulink with the parameters given in the Appendix B. A wind farm, consisting of six 1.5 MW DFIG-based WTs, is connected to the medium-voltage bus through a step-up transformer and 10 km transmission line. The distribution feeder B25 and its local load are weakly connected to the main grid (B120) via 20 km transmission line. Simulation studies are conducted in two main directions: (i) to investigate the  $P$ - $Q$  response of DFIG with different control designs, and (ii) to evaluate impacts of the fault response of the DFIG-based WPP on the nearby grid.

The transient and steady-state performances of the VBHCR used in DFIG-based WTs are already studied in Chapter 4. Therefore, simulation studies in this chapter will focus not on the detailed operation of the proposed VBHCR, but on its overall performance in the proposed control scheme. The machine slip is set equal to  $s = -0.2$  PU preceding the fault in order to impose the most onerous condition on DFIG when a larger amount of power is transferred through the converters.

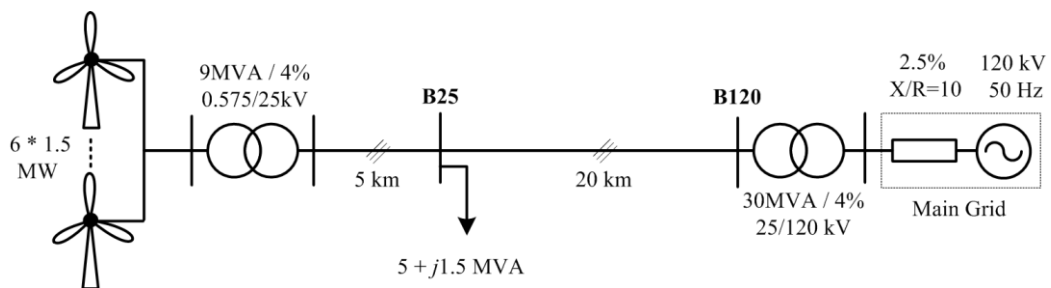


Figure 6-5 Circuit diagram of the simulated network.

Figure 6-6 shows the detailed operation of the proposed UTSP under fault conditions. Before the fault occurrence, the three-phase supply voltage is equal to 1.0 PU, with no tracking error from the UTSP. At  $t = 0.1$  s, a phase-to-phase short circuit takes place and a type D voltage sag with the characteristic voltage of  $\mathbf{V}_{\text{sag}} = 0.3 \angle 0^\circ$  appears at the DFIG terminals [see Fig. 7(a)]. This voltage sag condition corresponds to the positive and negative sequence components of 0.65 PU and 0.35 PU,

respectively. From Fig. 7(b), it can be observed that the UTSP accurately estimates the magnitudes of sequence components in almost one fundamental period and consequently, the tracking error reduces to zero in 20ms after the fault onset. On the other hand, Fig. 7(d) shows that the proposed UTSP extracts the synchronization signal (i.e., the supply voltage phase-angle) completely unaffected from the grid voltage condition. This will enhance the overall control performance under grid disturbances whereas distorted voltage condition causes serious stability problems for the commonly-used stator flux oriented vector control schemes.

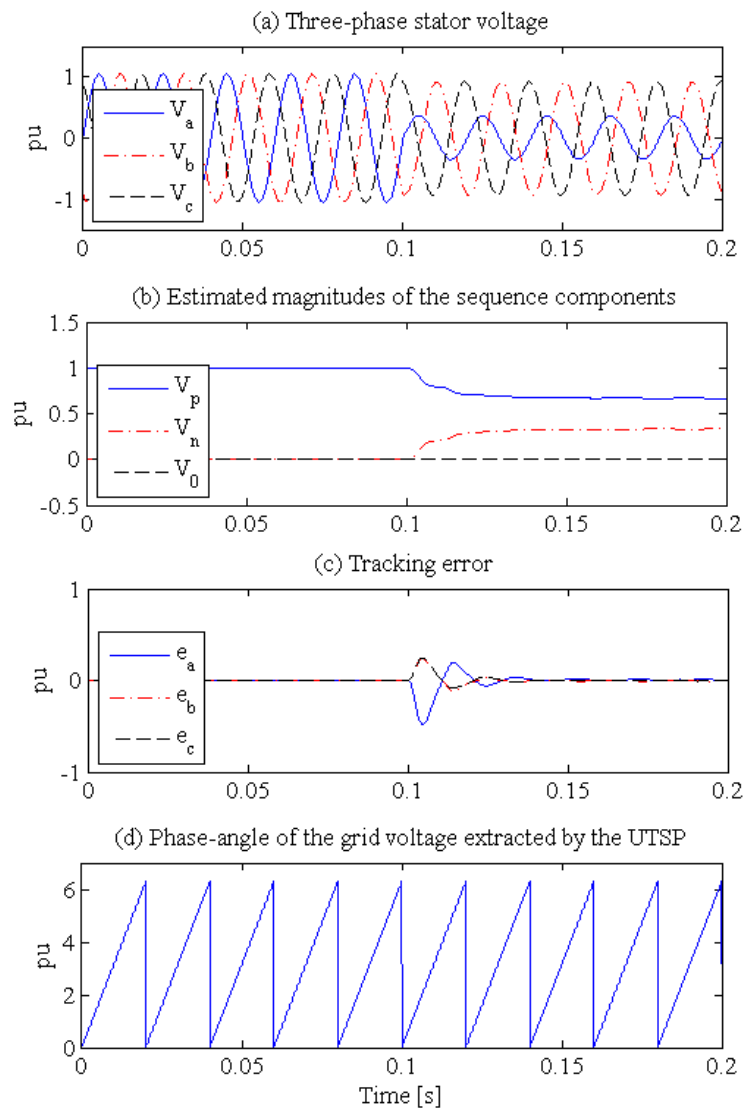


Figure 6-6 Tracking performance of the proposed UTSP: (a) three-phase grid voltage, (b) estimated magnitudes of the sequence components, (c) tracking error signals, and (d) extracted synchronizing phase-angle.

According to the Australian regulations, WPPs must inject 4% reactive current for each 1% reduction in the supply voltage. To test the proposed control scheme in compliance with this requirement, a three-phase fault with the remnant voltage of 0.4 PU at B120 is simulated. Figure 6-7 to Figure 6-10 compare the  $P$ - $Q$  responses of the DFIG-based WPP with different control designs.

Figure 6-7 shows the  $P$ - $Q$  response of the DFIG when no modifications are applied to the controller. During normal operating conditions, the  $I_{rq}$  and  $I_{rd}$  components are adjusted to 0.65 and 0.33 PU respectively, which corresponds to the active power production of 0.9 PU at UPF. As the fault takes place, the  $I_{rq}$  component increases to 1.0 PU in order to maximize the active power that can be exported from the wind generator to the grid. The  $I_{rd}$  component, on the other hand, reduces to zero so that the current-carrying capacity of converters is not exceeded. This leads to small reactive power absorption from the grid, needed for the machine excitation. It is also worth noting that the DFIG response would not change if the WPP is designed to work in voltage control mode, because there is no free capacity for the reactive current component of the RSC to manoeuvre.

Besides that, if the proposed VBHCRs were not used in the controller, the rotor current might exceed the safety limits of the RSC switches which, in turn, activates the crowbar. When the crowbar is engaged, vector control is lost and the DFIG resembles a high-resistance single fed machine, operating at very high slips. This temporary configuration is a worst-case combination of poor active power output and high reactive power demand, which exacerbates the fault condition [25].

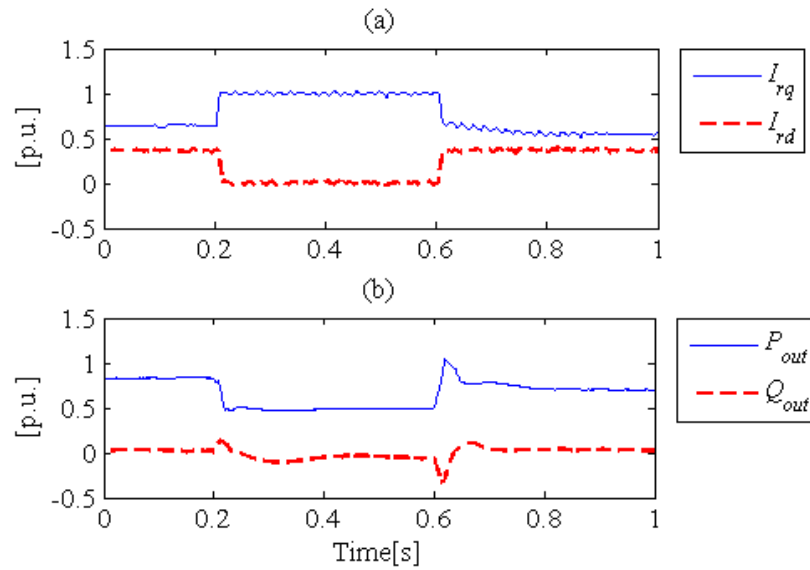


Figure 6-7 Conventional controller: (a) quadrature components of the rotor current (b) DFIG active and reactive powers.

Figure 6-8 shows that P-Q response of the DFIG-based WPP when it is designed to comply with the Australian regulations using Design 1. The DFIG response under normal operating condition is similar to Figure 6-7. However, during the fault period, the  $I_{rd}$  component rises to 1.0 PU because the supply voltage drops by more than 25%. Accordingly, the DFIG reactive power increases to 0.5 PU, but its active power drops to zero due to the reduction of the  $I_{rq}$  component. Since the electromagnetic torque of DFIG-based WT is reduced to zero during the fault period, the turbine shaft accelerates (as discussed in the following). This means that the rotor speed has increased at the fault clearance instant. Therefore, WPP temporarily injects more active power to the grid after the fault clearance and then, reduces back to the pre-fault value. The normal operation of the DFIG-based WPP (i.e., active power restoration to 95% of the pre-fault value) is attained in less than 100 ms after the fault clearance instant.

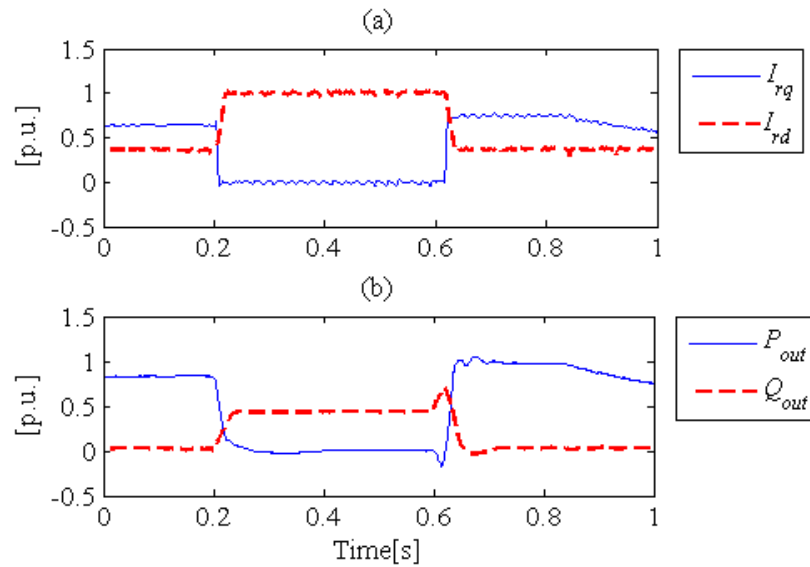


Figure 6-8 Design 1: (a) quadrature components of the rotor current (b) DFIG active and reactive powers.

Figure 6-9 shows the  $P$ - $Q$  response of DFIG-based WPP with the second design strategy. In this design, the RSC is permitted to be overloaded by 41% during the fault period. Accordingly, both  $I_{rq}$  and  $I_{rd}$  components increase to 1.0 PU upon the fault occurrence. As a result, the active power generation is mostly retained while the reactive power increases to 0.5 PU in order to support the grid voltage recovery. Finally, the DFIG regains its normal operating condition shortly after the fault clearance, i.e., in less than 100 ms.

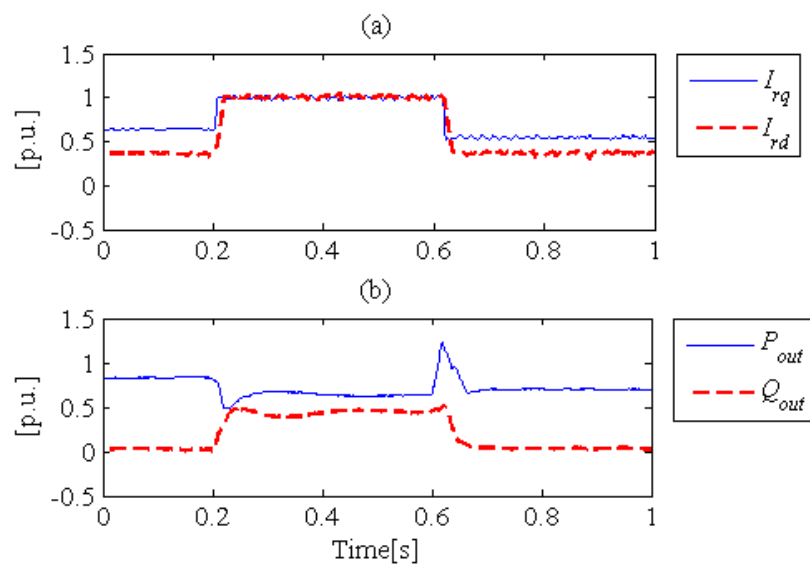


Figure 6-9 Design 2: (a) quadrature components of the rotor current (b) DFIG active and reactive powers.

Figure 6-10 shows that  $P$ - $Q$  response of DFIG with Design 3. The rotor current components ( $I_{rd}$  and  $I_{rq}$ ) are similar to Design 2, but the reactive power injected by the DFIG-based WPP increases from 0.5 PU to 0.82 PU in view of the fact that the free capacity of the GSC is exploited to generate more reactive power from the DFIG. The normal operation of DFIG-based WPP will be restored in less than 100 ms after the fault clearance.

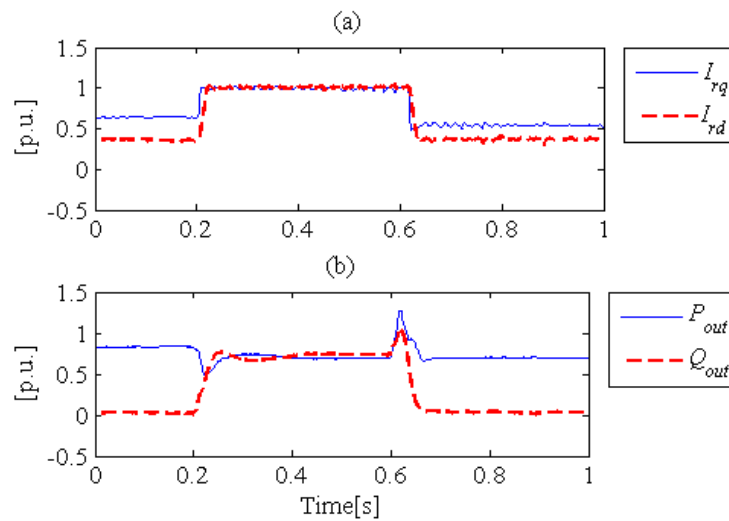


Figure 6-10 Design 3: (a) quadrature components of the rotor current (b) DFIG active and reactive powers.

Figure 6-11 compares the quadrature components of the GSC current for Design 2 and Design 3. In Design 2, the  $I_{gd}$  component oscillates to its limit (0.35 PU) in order to suppress the double-frequency fluctuations of the dc-link voltage, whereas the  $I_{gq}$  component is fixed at zero in order to attain UPF operation at the GSC terminals. In Design 3, the  $I_{gd}$  component does not change because the GSC active power control is always prioritized to its reactive power generation. However, the GSC current limit is temporarily increased to 0.5 PU and the free current capacity of the GSC has been instantaneously used for the reactive power generation.



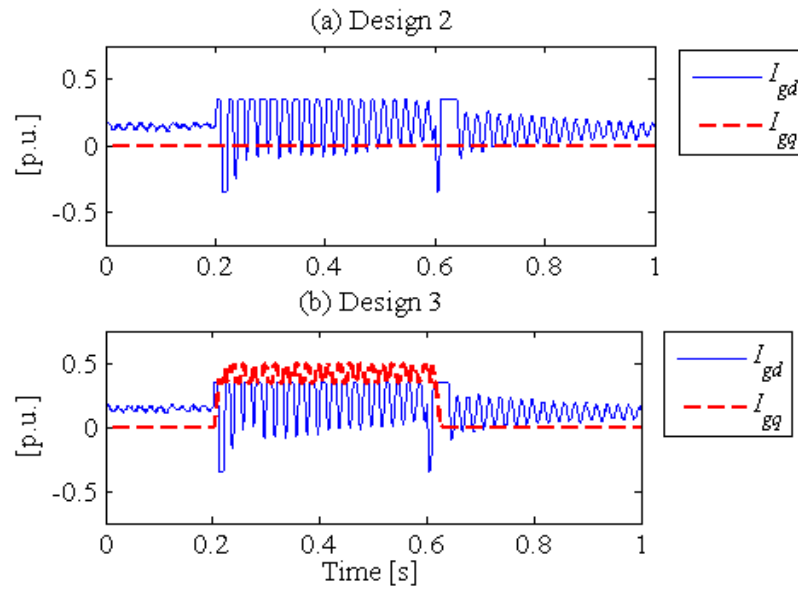


Figure 6-11 Quadrature components of the GSC current with (a) Design 1 (b) Design 2.

Figure 6-12 illustrates how the reactive power support from the DFIG-based WPP can improve the voltage profile at the nearby distribution feeder. Fault in the main grid causes the voltage at B120 to drop to 0.4 PU, but the voltage profile at B25 varies depending of the control design adopted in the DFIG. If the conventional control scheme is implemented, the voltage at B25 is slightly less than 0.4 PU due to the machine excitation current. However, the local voltage profile significantly improves if the WPP is designed to comply with the Australian regulations. The minimum voltage drop (i.e., the highest improvement in the voltage profile) is obtained in Design 3 because the DFIG-based WPP injects its maximum reactive power to the grid. Design 1 and Design 2 have similar reactive power responses, but the voltage profile for Design 2 is slightly better because the DFIG active power reduces to zero in Design 1. Consequently, the local load at B25 must be fed from the main grid, leading to a voltage drop caused by the resistive part of the transmission line and active power transfer from the main grid to the local load.

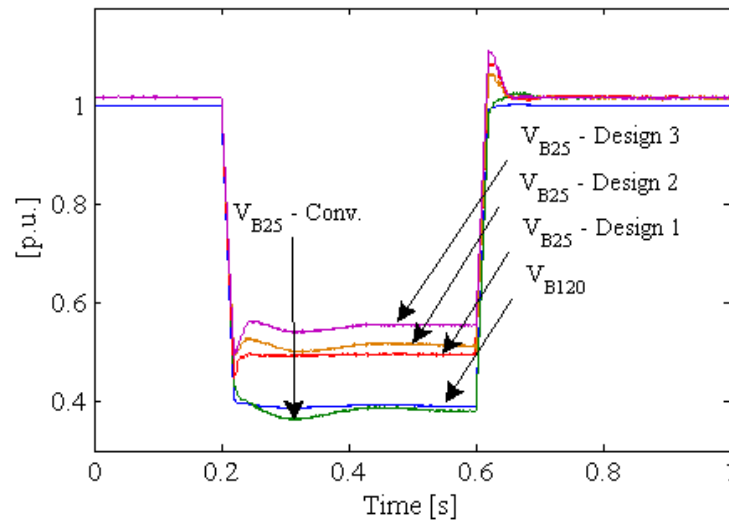


Figure 6-12 Voltage profile at B120 and B25 during the fault with different control designs adopted in the DFIG-based WPP.

Figure 6-13 compares the rotor speed when the DFIG is controlled according to Design 1 and Design 2. For the former, as the active power reduces to zero during the fault period, a large mismatch appears between the input mechanical torque from the turbine and the electromagnetic torque developed by the machine. As a result, the rotor accelerates to 1.225 PU. This can lead to dangerous over-speeds under more severe fault conditions. In contrast, Design 2 mostly retains the active power output during the fault and as a result, very slight increase is observed in the rotor speed.

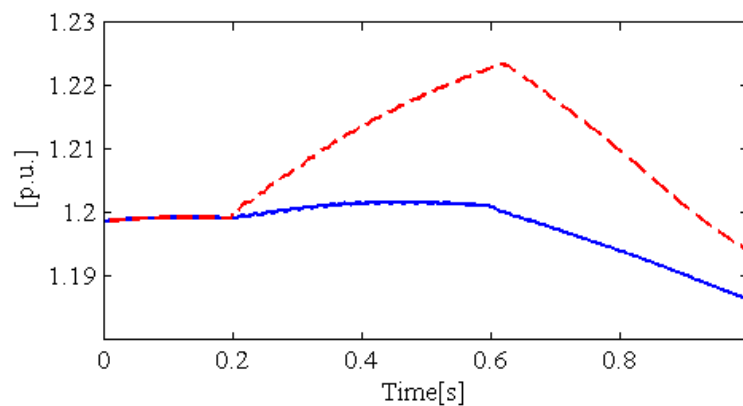


Figure 6-13 Rotor speed with Design 1 (dashed line) and Design 2 (solid line).

### 6.4.1 Impacts of the DFIG operation on the nearby grid

To investigate the impacts of the DFIG-based WPP on the nearby grid, the local load connected to B25 is replaced with 2\*1.5 MW pitch-controlled squirrel cage WTs with the parameters given in the appendix B. A remote three-phase fault with the remnant voltage of 0.65 PU is simulated at B120 when both WPPs are operating near their nominal output conditions, i.e., with their rated wind speeds. The system response to this fault is studied when the DFIG-based WPP is controlled by the conventional design strategy or when it is targeted to comply with the Australian grid code using Design 3.

Figure 6-14 shows the  $P$ - $Q$  response of DFIG-based WPP with two different control designs. It can be seen that the active power response of both cases are relatively similar but in Design 3, the reactive power injection of DFIG during the fault increases from zero to 8 MVar. This reactive power injection provides the reactive power needed by the induction generator to restore its electromagnetic torque. As a result, the turbine speed and terminal voltage of the induction generator quickly return to the pre-fault values after the fault clearance (see Figure 6-15). In contrast, the induction generator fails to ride-through the fault if the DFIG is controlled by the conventional design strategy with no reactive power support during the fault period.

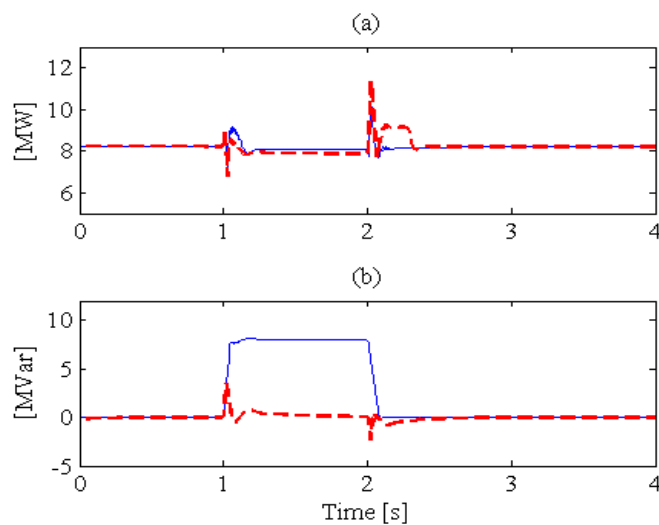


Figure 6-14 Active and reactive power of DFIG with the conventional design strategy (dashed line) and the proposed Design 3 (solid line).

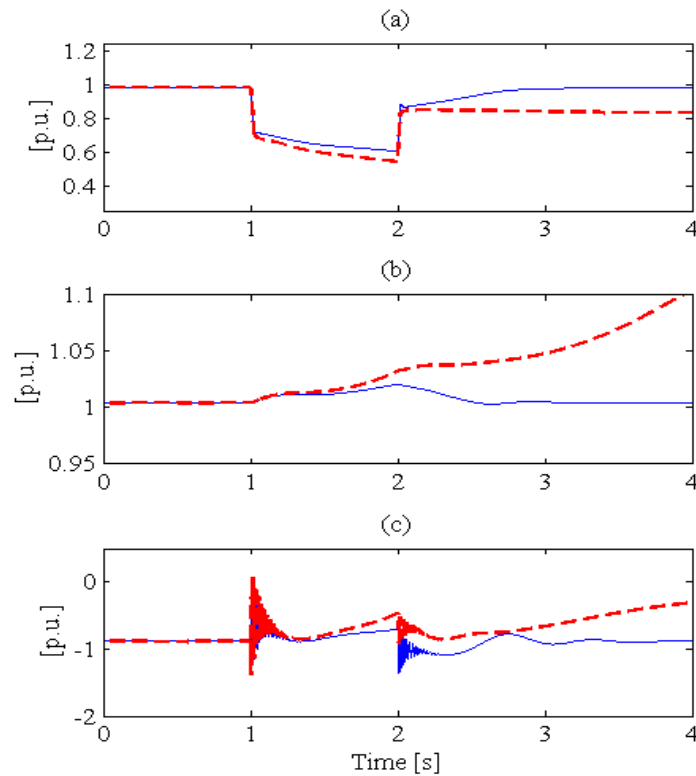


Figure 6-15 (a) Voltage at B25, (b) shaft speed of the induction generator, and (c) electromagnetic torque of the induction generator with the conventional design strategy (dashed line) or with the proposed Design 3 (solid line).

## 6.5 CONCLUSIONS

This chapter introduces an enhanced control scheme for DFIG-based WPPs to comply with the Australian grid code. New control designs are developed and their corresponding  $P$ - $Q$  capability curves are studied. The proposed control scheme consists of an enhanced PLL system to extract the amplitude and phase-angle of the supply voltage, variable-band VBHCRs used to control the output currents of the converters, and current prioritization units that function based on targeted design strategies. Simulation results show that the 4% reactive current requirement can be attained with three different control designs. Simulation results show that Design 3 (that allows temporary overloading of the converters and utilizes the free capacity of the GSC) is the most advantageous control strategy because it not only provides enhanced reactive power support, but retains the active power production of DFIG-

based WPP under severe fault conditions. It is finally shown that DFIG-based WPP with the proposed control scheme can assist the nearby fixed-speed wind generator to successfully ride-through the fault.

## Chapter 7. Conclusions

This thesis proposes modified transient control schemes for DFIG-based WPPs to comply with the latest international grid codes. After a literature review conducted in chapter 1, chapter 2 presents a comparative study on the international regulations defined for large WPPs. This study covers the latest grid codes of Australia, Denmark, Canada, Germany, Ireland, New Zealand, Spain, UK and USA. The technical regulations are classified and compared in five major groups: (1) LVRT and HVRT curves; (2) active and reactive power responses of WPPS following faults; (3) extended variation range of the supply frequency; (4) active power control or frequency regulation support; and (5) reactive power control or voltage regulation capability. The ultimate objective of this comparison is to identify the most stringent regulations enforced on the transient response of WPPs. It is found that Australia and Spain have the most onerous LVRT and HVRT regulations, and Australia has the most stringent regulations on the active and reactive power responses following a fault. Therefore, the regulations outlined in these grid codes are selected to be examined in the following chapters.

Chapter 3 presents a comprehensive study on the transient response of DFIG-based WTs under various symmetrical and asymmetrical faults. The relevant features and constraints of power networks are taken into account, including the effects of transformers' configuration, submarine/underground AC cables, and fault clearing mechanism of the circuit breakers. Extensive simulation results are presented and supported by theoretical analysis. The main outcomes of this chapter are as follows: (1) if the operational constraints of the circuit breakers are taken into account, the full voltage recovery for three-phase faults will take place in two or three consecutive steps and in turn, smaller overshoots in the rotor current and dc-link voltage will be experienced at the fault clearance instant; (2) since the fault current angle decreases for WPPs connected to the distribution system or located offshore, overshoots during the recovery process will increase notably; (3) the overshoots observed under

asymmetrical faults depend on the initial point-on-wave instants. The most unfavourable initial point-on-wave point corresponds to the instant that the positive and negative sequence components of the supply voltage are aligned in the opposite directions; (4) phase-angle jump has large detrimental impacts on the transient response of WPPs located offshore; and (5) the largest overshoots in the dc-link voltage are experienced for three-phase faults (sag type A), whereas the highest peaks for the rotor current are observed under phase-to-phase faults (sag types C and D). These observations help researchers to identify the problems that hinder successful fault ride-through of DFIG-based WTs under realistic operating conditions and accordingly, modifications in the conventional control scheme of DFIG can be suggested to overcome these deficiencies.

In chapter 4, the transient response of DFIG-based WTs is improved through implementing variable-bands VBHCR in the RSC and GSC. Moreover, an enhanced PLL system, referred to as UTSP, is utilized to readily extract the synchronization signal from the supply voltage. Simulation results show the validity of the overall control scheme under changing wind speed. It is also shown that the average switching frequency of converters using the proposed VBHCR is less than the conventional PI current regulator and the harmonic content of the DFIG output current with the proposed current regulator is below the IEEE standard limits. On the other hand, the VBHCR presents very fast and robust transient response, which enables the WT to fulfil the most stringent LVRT regulations imposed by the Australian grid code (for both symmetrical and asymmetrical faults).

Chapter 5 introduces a hybrid current control scheme for DFIG-based WTs. The proposed control scheme uses the conventional PI current regulators under steady-state conditions. Once a voltage sag or swell condition occurs at the DFIG terminals, the supervisory control unit detects it from the rotor current or dc-link voltage signal. Then, the switching strategy of the RSC and GSC is transferred to the VBHCR until the current and voltage fluctuation suppress to below the safety operating limits of the DFIG. In this way, the proposed current control scheme exploits the excellent steady-state and transient performances of the PI and hysteresis-based current regulators, respectively. Simulation results show that with the proposed current control scheme, the DFIG-based WTs can comply with the LVRT and HVRT

regulations stipulated in the Australian and Spanish grid codes.

In chapter 6, the transient  $P$ - $Q$  response of DFIG-based WPPs is examined according to the Australian regulations. Three different control designs are proposed to comply with the 4% reactive current injection requirements stipulated by the Australian grid code. The  $P$ - $Q$  capability curves corresponding to each control design is thoroughly studied. Simulation results show that all design strategies can fulfil the reactive current injection regulations, but the most advantageous response is obtained with Design 3. In this design methodology, the converters of DFIG are permitted to overload by 41% under the transient fault period. As a result, the active power production of the WPPs can be retained which in turn, prevents destructive shaft acceleration and contributes to the transient stability of the network. On the other hand, the free capacity of the GSC is exploited to provide further reactive power support to the grid. It is finally shown that if the DFIG-based WPP provides the reactive current injection requested by the Australian grid code, it can assist increase the nearby fixed-speed WP to ride-through various fault conditions.

## 7.1 CONTRIBUTIONS

The main results of this these have been released in 15 papers as listed in Section 1.5. The primary contributions of this thesis are as follow.

1. The latest international grid codes for large WPPs are compared and the most stringent regulations are identified.
2. The transient response of DFIG-based WT under symmetrical and asymmetrical faults are studied through comprehensive simulation and theoretical studies. This study, for the first time, investigates detrimental impacts phase-angle jump, voltage recovery process, and voltage sag parameters.
3. A new variable-band VBHCR is proposed to be implemented in the vector control of DFIG-based WTs. This current regulator has very fast transient response and as a result, the DFIG-based WT can fulfil the most stringent LVRT regulations enforced by the international grid codes.
4. A hybrid current control scheme is introduced to enhance both LVRT and HVRT



capabilities of DFIG-based WTs. The proposed current control scheme uses the standard PI current regulators under normal operating conditions and the hysteresis-based current regulators under transient fault periods. Using this hybrid controller, the DFIG-based WT can comply with the most onerous LVRT and HVRT requirements outlined in the international grid codes.

5. The conventional vector control scheme of DFIG-based WPPs is modified in order to meet the Australian regulations on the reactive current injection during the fault periods. New design strategies are developed and their corresponding  $P$ - $Q$  capability curves are studied. The most promising design strategy proposes temporary overloading of the DFIG converters by 41% as well as exploiting the free capacity of the GSC to inject further reactive power.

## 7.2 FUTURE WORKS

The following topics are suggested for future research in continuation of this work.

1. The LVRT and HVRT capabilities of DFIG-based WPP with other types of current regulators, such as predictive methods, must be studied.
2. Modified GSC control schemes or dc-choppers can be integrated with the proposed current controllers to further limit the dc-link voltage fluctuations under various voltage sag or swell conditions.
3. The transient response of DFIG-based WTs under extremes frequency excursions must be studied and modification shall be suggested to enhance the ride-through capability of the wind generator according to the international grid codes.
4. The overall control scheme of DFIG-based WPPs must be equipped with supplementary control loops to fulfill the requirements that are expected to appear in future grid codes, such as emulating inertia response or providing power system stabilization.

The DFIG-based WPP with the proposed transient control scheme can be simulated in a more realistic power network with several conventional generation units and load centers. Thereby, the impacts of  $P$ - $Q$  response of WPPs on the transient stability of the system can be studied accurately.

---

## References

*Every reasonable effort has been made to acknowledge the owners of copyright material. I would be pleased to hear from any copyright owner who has been omitted or incorrectly acknowledged.*

- [1] T. Ackermann, *Wind Power in Power Systems*. Wiley, NJ, 2005.
- [2] C. Jauch, J. Matevosyan, T. Ackermann, and S. Bolik, “International comparison of requirements for connection of wind turbines to power systems”, *Wind Energy*, vol. 8, no. 8, pp. 295–306, Jul. 2005.
- [3] F. Iov, A. Hansen, P. Sorensen, N. Cutululis, *Mapping of grid faults and grid codes*, Riso National Laboratory, Denmark, 2007
- [4] M. Tsili and S. Papathanassiou, “A review of grid code technical requirements for wind farms,” *IET Renew. Power Gener.*, vol. 3, no. 3, pp. 308–332, Sep. 2009.
- [5] R. Pena, J.C. Clare, and G.M. Asher, “Doubly fed induction generator using back-to-back PWM converters and its application to variable-speed wind-energy generation,” *IEEE Proc. Electric Power Appl.*, vol. 143, no. 3, pp. 231–241, May 1996.
- [6] G.B. Hopfensper, D.J. Atkinson, and R.A. Lakin, “Stator-flux oriented control of a doubly-fed induction machine with and without position encoder,” *IEE Proc. Electr. Power Appl.*, vol. 147, no. 4, pp. 241–250, July 2000.
- [7] A. Tapia, G. Tapia, J.X. Ostolaza, and J.R. Saenz, “Modelling and control of a wind turbine driven doubly fed induction generator,” *IEEE Trans .Energy Convers.*, vol. 18, no. 2, pp. 194–204, Jun. 2003.
- [8] W. Leonhard, *Control of Electrical Drives*. London: Springer, 2001.

- 
- [9] A. Petersson, L. Harnefors, and T. Thiringer, "Evaluation of current control methods for wind turbines using doubly-Fed induction machines", *IEEE Trans. Power Electron.*, vol. 20, no.1, pp. 2270–235, Jan. 2005.
- [10] J.P.A. Vieiral, M.V.A. Nunes, U.H. Bezerra, and A.C. Nascimento, "Designing optimal controllers for doubly fed induction generators using a genetic algorithm," *IET Gener. Transm. Distrib.*, vol. 3, no. 5, pp. 472–484, 2009.
- [11] R. Datta and V.T. Ranganathan, "Direct power control of grid-connected wound rotor induction machine without rotor position sensors," *IEEE Trans. Power Electron.*, vol. 16, no. 3, pp. 390–399, May 2001.
- [12] K.P. Gokhale, D.W. Karraker, and S.J. Heikkila, "Controller for a wound rotor slip ring induction machine," U.S. Patent 6448735B1, Sept. 2002.
- [13] L. Xu and P. Cartwright, "Direct active and reactive power control of DFIG for wind energy generation," *IEEE Trans. Energy Convers.*, vol. 21, no. 3, pp. 750–758, Sept. 2006.
- [14] J. Kang and S. Sul, "New direct torque control of induction motor for minimum torque ripple and constant switching frequency," *IEEE Trans. Ind. Appl.*, vol. 35, no. 5, pp. 1076–1082, Sept./Oct. 1999.
- [15] N.R.N. Idris and A.H.M. Yatim, "Direct torque control of induction machines with constant switching frequency and reduced torque ripple," *IEEE Trans. Ind. Electron.*, vol. 51, no. 4, pp. 758–767, Aug. 2004.
- [16] G. Abad, M.A. Rodriguez, and P. Poza, "Two-level VSC-based predictive direct power control of the doubly fed induction machine with reduced power ripple at low constant switching frequency," *IEEE Trans. Energy Convers.*, vol. 23, no. 2, pp. 570-580, June 2008.
- [17] Barros L.S., Mota W.S., d Silva J.J., Barros C.M.V., "An optimal control strategy for DFIG", *IEEE International Conference on Industrial Technology 2010*, pp. 1727-1732.
- [18] Castilla M., Miret J., Matas J., Borrell A. de Vicuna L.G., " Direct Rotor Current Mode Control Improves the Transient response of Doubly Fed Induction

- 
- Generator-Based Wind Turbines”, *IEEE Trans. Energy Convers.*, vol. 25, no. 3, pp. 722–731, Sept. 2010.
- [19] L. Xu, D. Zhi, and A. Williams, “Predictive current control of doubly fed induction generators,” *IEEE Trans. Ind. Electron.*, vol. 56, no. 10, pp. 4143–4153, Oct. 2009.
- [20] V. Akhmatov, “Analysis of dynamic behavior of electric power systems with large amount of wind power,” Ph.D. thesis, *Electr. Power Eng., Tech. Univ.*, Copenhagen, Denmark, Apr. 2003 (available online).
- [21] J. G. Slootweg, S.W. H. de Haan, H. Polinder, and W. L. Kling, “General model for representing variable speed wind turbines in power system dynamics simulations,” *IEEE Trans. Power Syst.*, vol. 18, no. 1, pp. 144–151, Feb. 2003.
- [22] J. B. Ekanayake, L. Holdsworth, X. G. Wu, and N. Jenkins, “Dynamic modeling of doubly fed induction generator wind turbines,” *IEEE Trans. Power Electron.*, vol. 18, no. 2, pp. 803–809, May 2003.
- [23] Y. Lei, A. Mullane, G. Lightbody, and R. Yacamini, “Modeling of the wind turbine with a doubly fed induction generator for grid integration studies,” *IEEE Trans. Energy Convers.*, vol. 21, no. 1, pp. 257–264, Mar. 2006.
- [24] I. Erlich, J. Kretschmann, J. Fortmann, S. M.-Engelhardt, and H. Wrede, “Modelling of Wind Turbines Based on Doubly-Fed Induction Generators for Power System Stability Studies,” *IEEE Trans. Power Syst.*, vol. 22, no. 3, pp. 909-919, August 2007.
- [25] J. Morren and S. de Haan, “Ride-through of wind turbines with doubly fed induction generator during a voltage dip,” *IEEE Trans. Energy Convers.*, vol. 20, no. 2, pp. 435–441, Jun. 2005.
- [26] J. Lopez, E. Gubia, E. Olea, J. Ruiz, and L. Marroyo, “Ride through of wind turbines with doubly fed induction generator under symmetrical voltage dips,” *IEEE Trans. Ind. Electron.*, vol. 56, no. 10, pp. 4246-4254, Oct. 2009.
- [27] A. Petersson, T. Thiringer, L. Harnesfors, and T. Petru “Modeling and experimental verification of grid interaction of a DFIG wind turbine,” *IEEE Trans. Energy Convers.*, vol. 20, no. 4, pp. 878–886, Dec. 2005.

- 
- [28] S. Seman, J. Niiranen, and A. Arkkio, "Ride-through analysis of doubly fed induction wind-power generator under unsymmetrical network disturbance," *IEEE Trans. Power Syst.*, vol. 21 no. 4, pp. 1782–1789, Nov. 2006.
- [29] S. Seman, J. Niiranen, S. Kanerva, A. Arkkio, and J. Saitz, "Performance study of a doubly fed wind-power induction generator under network disturbances," *IEEE Trans. Energy Convers.*, vol. 21, no. 3, pp. 883–890, Dec. 2006.
- [30] P.S. Flannery and G. Venkataramanan, "A fault tolerant doubly fed induction generator wind turbine using a parallel grid side rectifier and series grid side converter," *IEEE Trans. Power Electron.*, vol. 23, no. 3, pp. 1126–1134, May 2008.
- [31] P.S. Flannery and G. Venkataramanan, "Unbalanced voltage sag ride-through of a doubly fed induction generator wind turbine with series grid-side converter," *IEEE Trans. Ind. Appl.*, vol. 45, no. 5, pp. 1879–1887, Sep./Oct. 2009.
- [32] O. A. Baqi and A. Nasiri, "A dynamic LVRT solution for doubly fed induction generators," *IEEE Trans. Power Electron.*, vol. 25, no.1, pp. 193–196, Jan. 2010.
- [33] J. Yang, J. E. Fletcher, and J. O'Reilly, "A series-dynamic-resistor-based converter protection scheme for doubly-fed induction generator during various fault conditions," *IEEE Trans. Energy Convers.*, vol. 25, no. 2, pp. 422–432, June 2010.
- [34] X. Yan, G. Venkataramanan, P. S. Flannery, Y. Wang, Q. Dong, and B. Zhang, "Voltage-sag tolerance of DFIG wind turbine with a series grid side passive-impedance network," *IEEE Trans. Energy Convers.*, accepted for publication (DOI. 10.1109/TEC.2010.2054097).
- [35] D. Xiang, L. Ran, P. Tavner, and S. Yang, "Control of a doubly fed induction generator in a wind turbine during grid fault ride through," *IEEE Trans. Energy Convers.*, vol. 21, no. 3, pp. 652–662, Sep. 2006.
- [36] L. Xu and Y. Wang, "Dynamic modeling and control of DFIG based wind turbines under unbalanced network conditions," *IEEE Trans. Power Syst.*, vol. 22, no. 1, pp. 314–323, Feb. 2007.

- 
- [37] L. Xu, "Coordinated control of DFIG's rotor and grid side converters during network unbalance," *IEEE Trans. Power Electron.*, vol. 23, no. 3, pp. 1041–1049, May 2008.
- [38] O. G. Bellmunt, A. J. Ferre, A. Sumper, and J. B. Jane, "Ride-through control of a doubly-fed induction generator under unbalanced voltage sags," *IEEE Trans. Energy Convers.*, vol. 23, no. 4, pp. 1036–1045, Dec. 2008.
- [39] Y. Zhou, P. Bauer, J. Pierik, and J. A. Ferreira, "Operation of grid-connected DFIG under unbalanced grid voltage condition," *IEEE Trans. Energy Convers.*, vol. 24, no. 1, pp. 240–246, March 2009.
- [40] M. Rahimi and , "Coordinated control approaches for low-voltage ride-through enhancement in wind turbines with doubly fed induction generators ," *IEEE Trans Energy Convers.*, vol. 25, no. 3, pp. 873–873, Sep. 2010.
- [41] J. Yao, H. Li, Y. Liao, and Z. Chen, "An improved control strategy of limiting the DC-link voltage fluctuation for a doubly fed induction wind generator," *IEEE Trans. Power Electron.*, vol. 23, no. 3, pp. 1205–1213, May 2008.
- [42] M. H. J. Bollen, G. Olguin, and M. Martins, "Voltage dips at the terminals of wind power installations," *Wind Energy*, vol. 8, no. 3, pp. 307–318, Jul. 2005.
- [43] C. Feltes, S. Englehardt, J. Kretschmann, J. Fortmann, F. Koch and I. Erlich, "High voltage ride Through of DFIG Based Plants," in *Proc. IEEE Power Eng. Soc. Gen. Meet.*, 2008, pp. 1–8.
- [44] J. G. Slootweg, S. W. H. de Haan, H. Polinder, and W. L. Kling, "Voltage control methods with grid connected wind turbines: a tutorial review," *Wind Eng.*, vol. 25, no. 6, pp. 353–365, 2001.
- [45] A. Tapia, G. Tapia, J. X. Ostolaza, and J. R. Saenz, "Modeling and control of a wind turbine driven doubly fed induction generator," *IEEE Trans. Energy Convers.*, vol. 18, no. 2, pp. 194–204, Jun. 2003.
- [46] P. Ledesma and J. Usaola, "Contribution of variable-speed wind turbines to voltage control," *Wind Eng.*, vol. 26, no. 6, pp. 347–358, 2002.

- 
- [47] M. Kayikci and J. Milanovic, "Reactive power control strategies for DFIG based plants," *IEEE Trans. Energy Convers.*, vol. 22, no. 2, pp. 389–396, Jun. 2007.
- [48] R. J. Konopinski, P. Vijayan, and V. Ajjarapu, "Extended reactive capability of DFIG wind parks for enhanced system performance," *IEEE Trans. Power Syst.*, vol. 24, no. 3, pp. 1346–1355, Aug. 2009.
- [49] F. M. Hughes, O. A. Lara, N. Jenkins, and G. Strbac, "Control of DFIG based wind generation for power network support," *IEEE Trans. Power Syst.*, vol. 20, no. 4, pp. 1958–1966, Nov. 2005.
- [50] N. R. Ullah, T. Thiringer, and D. Karlsson, "Temporary primary frequency control support by variable speed wind turbines— Potential and Applications," *IEEE Trans. Power Syst.*, vol. 22, no. 4, pp. 1647–1656, Nov. 2007.
- [51] M. Kayikci and J. Milanovic, "Dynamic contribution of DFIG-based wind plants to system frequency disturbances," *IEEE Trans. Power Syst.*, vol. 24, no. 2, pp. 859–867, May 2009.
- [52] WWEA, *World wind energy report 2009*, Aug. 2010. Available at < <http://www.wwindea.org>>.
- [53] IEA, 2009 *IEA wind annual report*, May 2010. Available at < <http://www.ieawind.org>>.
- [54] Australian Government, *Enhanced Renewable Energy Target*, Sep. 2010. Available at < <http://www.climatechange.gov.au>>.
- [55] Union for the Co-ordination of Transmission of Electricity, *Final report on the disturbances on 4 November 2006*, Available at <http://entsoe.eu/>
- [56] REE, *Grid Code number 12.3 of the Spanish grid operator*, Oct. 2008. Available at [http://www.ree.es/operacion/procedimientos\\_operacion.asp](http://www.ree.es/operacion/procedimientos_operacion.asp)
- [57] AEMC, *National Electricity Rules, Version 33*, Nov. 2009. Available at < <http://www.aemc.gov.au/>>
- [58] EWEA, *Harmonising Europe's Grid Codes for the Connection of Wind Power Plants to the Electricity Network*, Nov. 2009. Available at < <http://www.ewea.com/>>

- 
- [59] M. Altin, O. Goksu, R. Teodorescu, P. Rodriguez, B. K. Jensen, and L. Helle, "Overview of recent grid codes for wind power integration," in *Proc. 12th International Conference on Optimization of Electrical and Electronic Equipments*, Romania, 2010.
- [60] J. Enquist, "Ride-through of offshore wind parks," M.Sc. thesis, Dept. of Electr. Power Eng., Chalmers University of Technology, Goteborg, Sweden, 2007 (available online).
- [61] M.H.J. Bollen, *Understanding power quality problems: voltage sags and interruptions*, IEEE Press, New York, 2000.
- [62] A. Perdana, "Dynamic models of wind turbines," PhD thesis, Dept. of Electr. Power Eng., Chalmers University of Technology, Goteborg, Sweden, 2008 (available online).
- [63] G.R. Slemon, "Modelling of induction machines for electric drives," *IEEE Trans. Ind. Appl.*, vol. 25, no. 6, pp. 1121-1131, Nov./Dec. 1989.
- [64] J. Lopez, P. Sanchis, X. Roboam, and L. Marroyo, "Dynamic behaviour of the doubly-fed induction generator during three-phase voltage dips," *IEEE Trans Energy Convers.*, vol. 22, no. 3, pp. 709-717, Sep. 2007.
- [65] J. Lopez, E. Gubia, P. Sanchis, X. Roboam, and L. Marroyo, "Wind turbines based on doubly fed induction generator under asymmetrical voltage dips," *IEEE Trans Energy Convers.*, vol. 23, no. 1, pp. 321-330, March 2008.
- [66] A. Peterson, L. Harnefors, and T. Thiringer, "Comparison between stator-flux and grid flux oriented rotor current control of doubly-fed induction generators," in *Proc. 35<sup>th</sup> IEEE Power Electronics Specialist Conference 2004*, pp. 482-486.
- [67] V. Kaura and V. Blasko, "Operation of a phase locked loop system under distorted utility conditions," *IEEE Trans. Ind. Appl.*, vol. 33, no. 1, pp. 58-63, Jan./Feb. 1997.
- [68] M. Karimi-Ghartemani and H. Karimi, "Processing of symmetrical components in time-domain," *IEEE Trans. Power Syst.*, vol. 22, no. 2, pp. 572-579, May 2007.
- [69] Siegfried Heier, *Grid Integration of Wind Energy Conversion Systems*, 2<sup>nd</sup> ed., John Wiley & Sons Ltd, 2006.



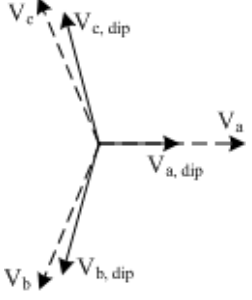
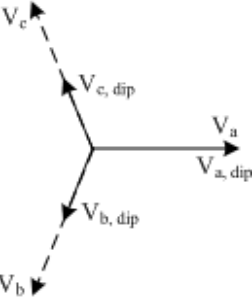
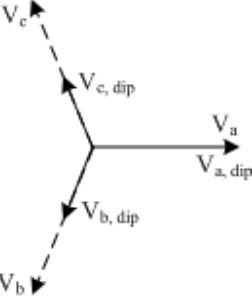
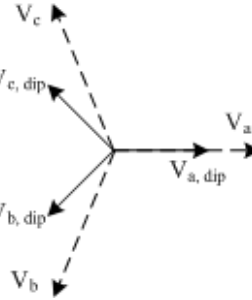
- 
- [70] M.P. Kazmierkowski, M.A. Dzieaniakowski, and W. Sulkowski, "Novel space vector based current controllers for PWM-inverters," *IEEE Trans. Power Electron.*, vol. 6, no.1, pp. 158–166, Jan. 1991.
- [71] C. T. Pan and T. Y. Chang, "An improved hysteresis current controller for reducing switching frequency," *IEEE Trans. Power Electron.*, vol. 9, no.1, pp. 97–104, Jan. 1994.
- [72] A. Tilli and A. Tonielli, "Sequential design of hysteresis current controller for three-phase inverter," *IEEE Trans. Ind. Electron.*, vol. 45, no. 5, pp. 771–781, Oct. 1998.
- [73] B.H. Kwon, T.W. Kim, and J.H. Youn, "A novel SVM-based hysteresis current controller," *IEEE Trans. Power Electron.*, vol. 13, no.2, pp. 297–307, Mar. 1998.
- [74] B.H. Kwon, B.D. Min, and J.H. Youm, "An improved space-vector-based hysteresis current controller," *IEEE Trans. Ind. Electron.*, vol. 45, no. 5, pp. 752–760, Oct. 1998.
- [75] K.M. Rahman, M.R. Khan, M.A. Choudhury, and M.A. Rahman, "Variable band hysteresis current controllers for PWM voltage source inverters," *IEEE Trans. Power Electron.*, vol. 12, no. 6, pp. 964–970, Nov. 1997.
- [76] L. Malesani and P. Tenti, "A novel hysteresis control method for current controlled VSI PWM inverters with constant modulation frequency," *IEEE Trans. Ind. Applicat.*, vol. 26, pp. 88–92, Jan./Feb. 1990.
- [77] L. Malesani, P. Mattavelli, and P. Tomasin, "Improved constant-frequency hysteresis current control for VSI inverters with simple feedforward bandwidth prediction," *IEEE Trans. Ind. Appl.*, vol. 33, pp. 1194–1202, Sep./Oct. 1997.
- [78] P.N. Tekwani, R.S. Kanchan, and K. Gopakumar, "Novel current error space phasor based hysteresis controller using parabolic bands for control of switching frequency variations," *IEEE Trans. Ind. Electron.*, vol. 54, pp. 2648–2656, Oct. 2007.
- [79] L. Harnefors and H.-P. Nee, "Model-based current control of ac machines using the internal model control method," *IEEE Trans. Ind. Applicat.*, vol. 34, no. 1, pp. 133–141, Jan./Feb. 1998.

- [80] IEEE Standard for Interconnecting Distributed Resources with Electric Power Systems, IEEE Standard 15471, 2003.
- [81] Wind Turbines, Measurement and Assessment of Power Quality Characteristics of Grid Connected Wind Turbines—Part 21, IEC Standard 61400-21, Ed. 2.0, Standard, 2008.
- [82] M. S. Khan and R. Iravani “Hybrid control of a grid-interactive wind energy conversion system,” *IEEE Trans. Energy Convers.*, vol. 23, no. 3, pp. 895–902, Sep. 2008.
- [83] V. Kaura and V. Blasko, “Operation of a voltage source converter at increased utility voltage,” *IEEE Trans. Power Electron.*, vol. 12, no. 1, pp. 132–137, Jan. 1997.

## Appendix A – Voltage sag classification

Phasor diagram and mathematic expression of different types of voltage sags are given in the below.

Sag type	3- $\Phi$ Voltage Expression	Phasor Diagram
A	$\begin{cases} U_a = \mathbf{V}_{dip} \\ U_b = -\frac{1}{2} \mathbf{V}_{dip} - j \frac{\sqrt{3}}{2} \mathbf{V}_{dip} \\ U_c = -\frac{1}{2} \mathbf{V}_{dip} + j \frac{\sqrt{3}}{2} \mathbf{V}_{dip} \end{cases}$	
B	$\begin{cases} U_a = \mathbf{V}_{dip} \\ U_b = -\frac{1}{2} \mathbf{V} - j \frac{\sqrt{3}}{2} \mathbf{V} \\ U_c = -\frac{1}{2} \mathbf{V} + j \frac{\sqrt{3}}{2} \mathbf{V} \end{cases}$	
C	$\begin{cases} U_a = \mathbf{V} \\ U_b = -\frac{1}{2} \mathbf{V} - j \frac{\sqrt{3}}{2} \mathbf{V}_{dip} \\ U_c = -\frac{1}{2} \mathbf{V} + j \frac{\sqrt{3}}{2} \mathbf{V}_{dip} \end{cases}$	

D	$\begin{cases} U_a = \mathbf{V}_{dip} \\ U_b = -\frac{1}{2} \mathbf{V}_{dip} - j \frac{\sqrt{3}}{2} \mathbf{V} \\ U_c = -\frac{1}{2} \mathbf{V}_{dip} + j \frac{\sqrt{3}}{2} \mathbf{V} \end{cases}$	
E	$\begin{cases} U_a = \mathbf{V} \\ U_b = -\frac{1}{2} \mathbf{V}_{dip} - j \frac{\sqrt{3}}{2} \mathbf{V}_{dip} \\ U_c = -\frac{1}{2} \mathbf{V}_{dip} + j \frac{\sqrt{3}}{2} \mathbf{V}_{dip} \end{cases}$	
F	$\begin{cases} U_a = \mathbf{V}_{dip} \\ U_b = -\frac{1}{2} \mathbf{V}_{dip} - j \left( \frac{\sqrt{3}}{3} \mathbf{V} + \frac{\sqrt{3}}{6} \mathbf{V}_{dip} \right) \\ U_c = -\frac{1}{2} \mathbf{V}_{dip} + j \left( \frac{\sqrt{3}}{3} \mathbf{V} + \frac{\sqrt{3}}{6} \mathbf{V}_{dip} \right) \end{cases}$	
G	$\begin{cases} U_a = \frac{2}{3} \mathbf{V} + \frac{1}{3} \mathbf{V}_{dip} \\ U_b = -\frac{1}{3} \mathbf{V} - j \left( \frac{\sqrt{3}}{2} \mathbf{V}_{dip} + \frac{1}{6} \mathbf{V}_{dip} \right) \\ U_c = -\frac{1}{3} \mathbf{V} + j \left( \frac{\sqrt{3}}{2} \mathbf{V}_{dip} - \frac{1}{6} \mathbf{V}_{dip} \right) \end{cases}$	

## Appendix B – Simulation parameters

Simulation parameters for the DFIG and induction wind generators are given in Table I and Table II, respectively.

TABLE I. SIMULATION PARAMETERS FOR DFIG-BASED WT

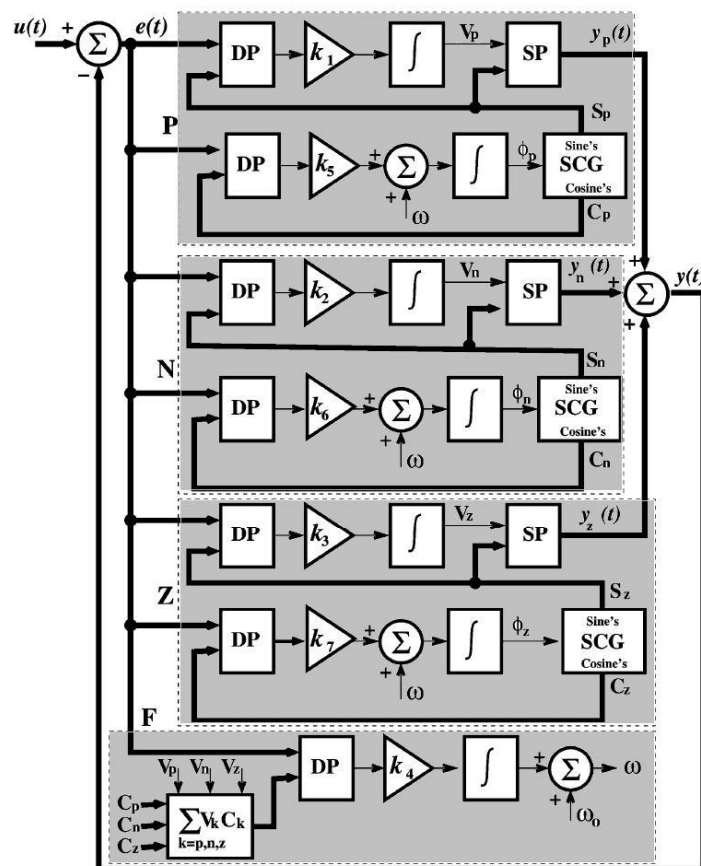
Generator Parameters	
Rated apparent power	1.6 MVA
Rated power	1.5 MW
Rated voltage / Rated frequency	575 V , 50 Hz
Stator / Rotor resistances	0.007 , 0.005 p.u.
Leakage / Mutual inductances	0.3 , 3.0 p.u.
Dc-link capacitor / Dc rated voltage	15 mF , 1200 V
Rated power of the RSC and GSC	0.55 MVA
Wind Turbine Parameters	
Nominal mechanical output power	1.5 MW
Base wind speed	11 m/s
Maximum power at base wind speed	1.1 p.u.
Initial pitch angle	0°
Inertia constant	4.5 s
DFIG Control System Parameters	
$K_p$ and $K_i$ – RSC $P$ regulator	1.0 , 100
$K_p$ and $K_i$ – RSC $Q$ regulator	0.05 , 5
$K_p$ and $K_i$ – RSC current regulator	0.5 , 9.0
$K_p$ and $K_i$ – GSC $V_{dc}$ regulator	0.002 , 0.05
$K_p$ and $K_i$ – GSC $Q$ regulator	0.5 , 25
$K_p$ and $K_i$ – GSC current regulator	2.75 , 500.0

TABLE II. SIMULATION PARAMETERS FOR THE FIXED-SPEED WT

Generator Parameters	
Rated apparent power	1.6 MVA
Rated power	1.5 MW
Rated voltage / Rated frequency	575 V , 50 Hz
Stator / Rotor resistances	0.005 , 0.005 p.u.
Leakage / Mutual inductances	0.4 , 5 p.u.
Local capacitor bank	0.2 MVar
Wind Turbine Parameters	
Nominal mechanical output power	21.5 MW
Base wind speed	9 m/s
Maximum power at base wind speed	1.0 p.u.
Turbine inertia constant	3.0 s

## Appendix C – The UTSP system

Schematic diagram of the proposed UTSP system is shown in the below. It is constituted of four estimations loops: ‘P’ loop which extracts the amplitude and phase-angle of the positive-sequence component of the supply voltage, ‘N’ loop which extracts the amplitude and phase-angle of the negative-sequence component of the supply voltage, and ‘Z’ loop which extracts the amplitude and phase-angle of the zero-sequence component of the supply voltage. The estimation loop ‘F’ extracts the synchronization signal and the synchronous speed ( $\omega$ ). The mathematical principles and control structure of the proposed signal processing unit are explored in [68].



**Appendix D – IEEE Transaction on Power Electronics:  
A New Vector-Based Hysteresis Current Control Scheme  
for Three-Phase PWM Voltage-Source Inverters**



# A New Vector-Based Hysteresis Current Control Scheme for Three-Phase PWM Voltage-Source Inverters

Mansour Mohseni, *Student Member, IEEE*, and Syed M. Islam, *Senior Member, IEEE*

**Abstract**—This paper presents a new vector-based hysteresis current controller (HCC) for three-phase pulsewidth modulation (PWM) voltage-source inverters (VSI). The HCC is intrinsically robust to the load parameters variations, exhibits very fast transient performance, and is suitable for simple implementations. Despite these advantages, the conventional HCC has a major drawback when applied to the three-phase PWM-VSI: interphases dependency leads to very high-switching frequencies in the inverter. This paper starts with a review on the vector-based HCCs reported in the literature to address this problem. Then, a new vector-based method is proposed using multilevel hysteresis comparators integrated with a switching table. The proposed method works with the inverter current vector represented in the stationary  $\alpha - \beta$  frame and produces a coordinated switching pattern. The current error is kept inside a square tolerance region without significant increase in the complexity of the hardware implementation. Simulation results show that the proposed vector-based method can retain the advantages of the conventional HCC. However, the steady-state performance of the proposed current regulator is significantly improved by reducing the switching frequency and minimizing oscillations of the inverter current vector. The proposed current controller is finally compared with other reported vector-based methods and its advantages are illustrated.

**Index Terms**—Hysteresis current controller (HCC), three-phase pulsewidth modulation (PWM) voltage-source inverter (VSI), vector-based methods.

## I. INTRODUCTION

THE CURRENT controller of three-phase voltage-source inverters (VSI) is an essential part in the overall control structure of many applications, such as active power filters, ac motor drives, and uninterruptible power supplies [1]. The quality of the applied current controller greatly influences the overall control system performance. Therefore, over the past few decades, considerable research has been done on current control techniques, and from this work three major classes of current controller have evolved: predictive controllers, linear proportional-integral (PI) controllers, and hysteresis con-

trollers [1], [2]. Predictive controllers are the most complex method and require the knowledge of load parameters. Extensive hardware implementation is another disadvantage of this technique. Linear PI current controller can limit the switching frequency of the inverter and produce a well-defined harmonic content. However, parameters of PI controllers must be carefully tuned with a tradeoff between maintaining the system stability over the whole operation range and achieving an adequate dynamic response during transients. This can result in degraded transient performance, which in turn, hinders the application of PI current controller in high-demanding situations, such as active power filters [1]–[3]. Finally, hysteresis current controllers (HCC) have been widely used because of the noncomplex implementation, outstanding stability, absence of any tracking error, very fast transient response, inherent limited maximum current, and intrinsic robustness to load parameters variations [1], [2]. However, it is well known that conventional HCCs have several drawbacks when applied to three-phase VSIs [2]. Very high switching frequency happens at lower modulation index due to the lack of the coordination between three-phase hysteresis comparators (referred to as “interphases dependency”). Occasional hysteresis band violation up to twice the permitted bandwidth is another disadvantage of this current controller.

Several methods have been proposed to address these problems. The substitution of fixed hysteresis bands with variable bands was suggested to reduce the switching frequency [4], [5]. This solution, although very simple, produces significant low-frequency current harmonics and leads to very high switching frequencies around zero crossing points of the reference current. Adaptive hysteresis band current controllers have been proposed to achieve fixed switching frequency and remove the interphases dependency [6]–[10]. This approach gives satisfactory frequency spectra and minimized inverter current oscillations. However, fixed modulation frequency is usually obtained at the expense of extra signal processing and control complexity requirements, which jeopardizes the simplicity of conventional HCCs. Moreover, these techniques typically suffer from stability problems and limited transient performance [10]. In digital implementations of HCCs, the sampling rate can be controlled to reduce the switching frequency [11], [12]. The main disadvantages of this approach are highly distorted current waveform and frequency jitter. A digital predictive hysteresis controller has been proposed to remove these problems [13]. This method gives a very satisfactory transient and steady-state performance, but still requires complex online computations.

Manuscript received April 26, 2009; revised July 29, 2009, December 22, 2009, and February 16, 2010; accepted March 16, 2010. Date of current version September 17, 2010. Recommended for publication by Associate Editor J. R. Espinoza.

The authors are with the Department of Electrical and Computer Engineering, Curtin University of Technology, Perth 6845, W.A., Australia (e-mail: mansour.mohseni@postgrad.curtin.edu.au; s.islam@curtin.edu.au).

Color versions of one or more of the figures in this paper are available online at <http://ieeexplore.ieee.org>.

Digital Object Identifier 10.1109/TPEL.2010.2047270

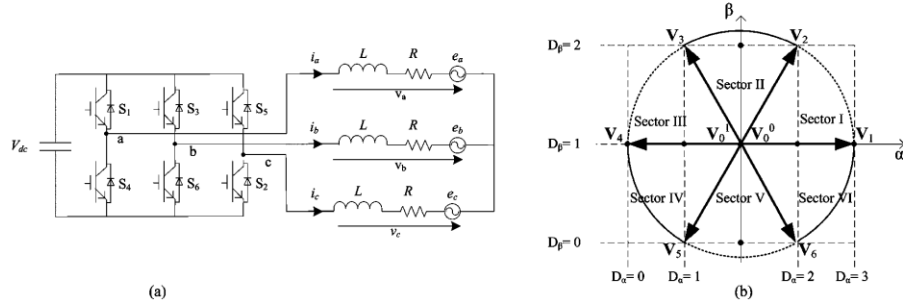


Fig. 1. (a) Circuit diagram of the PWM-VSI feeding an induction motor. (b) Space-vector representation of the VSI output voltage.

Finally, vector-based methods were suggested to reduce the inverter switching frequency [14]–[20]. The current error is measured in a space-vector form, and vector-based techniques will be employed to keep the error within the assigned tolerance region. Vector-based methods systematically select zero and nonzero voltage vectors to follow the current command vector. This significantly reduces the inverter switching frequency. Besides simple control structure, vector-based HCCs exhibit very satisfactory transient and steady-state performance, as will be thoroughly discussed in following sections.

This paper presents a new vector-based HCC after a brief review on other reported methods. The proposed control technique works with current vector represented in the coordinated stationary frame ( $\alpha - \beta$  complex frame). Multilevel hysteresis comparators are employed to generate an optimal switching pattern that keeps the current error vector inside a square tolerance region. The proposed method retains all advantages of the conventional HCC. Furthermore, it gives a significantly reduced switching frequency with minimized current vector oscillations. Simulation results also demonstrate the superior performance of the proposed current controller compared to other reported vector-based methods.

## II. THREE-PHASE PULSEWIDTH MODULATION (PWM) VSI

Fig. 1(a) shows the circuit diagram of a three-phase VSI connected to a load. The load includes a three-phase sinusoidal-counter-emf voltage source in series with an inductance and a resistance. This simulates an induction motor, where  $R$  and  $L$  are the equivalent stator resistance and inductance. Three-phase output voltage of the inverter ( $v_{abc}$ ) can be transformed to a vector represented in the stationary frame, where  $\mathbf{X}(t) = x_\alpha(t) + jx_\beta(t)$  is defined by

$$\begin{bmatrix} x_\alpha \\ x_\beta \end{bmatrix} = \frac{2}{3} \begin{bmatrix} 1 & -\frac{1}{2} & -\frac{1}{2} \\ 0 & \frac{\sqrt{3}}{2} & -\frac{\sqrt{3}}{2} \end{bmatrix} \begin{bmatrix} x_a \\ x_b \\ x_c \end{bmatrix}. \quad (1)$$

Conduction states of the inverter legs determine the VSI output voltage vector at each instant ( $\mathbf{V}_n$ ). There are two states for each inverter leg: if the upper switch in phase  $a$  ( $S_1$ ) conducts the current, then  $S_a^* = 1$ . Otherwise  $S_a^* = 0$ , indicating  $S_4$  is

TABLE I  
THREE-PHASE SWITCHING STATES, RESPECTIVE VOLTAGE SPACE VECTOR, AND THE  $\alpha - \beta$  VALUES

$S_a^*$	$S_b^*$	$S_c^*$	$\mathbf{V}_n$	$V_\alpha/V_{dc}$	$V_\beta/V_{dc}$
0	0	0	$\mathbf{V}_0^0$	0	0
1	0	0	$\mathbf{V}_1$	2/3	0
1	1	0	$\mathbf{V}_2$	1/3	1/√3
0	1	0	$\mathbf{V}_3$	-1/3	1/√3
0	1	1	$\mathbf{V}_4$	-2/3	0
0	0	1	$\mathbf{V}_5$	-1/3	-1/√3
1	0	1	$\mathbf{V}_6$	1/3	-1/√3
1	1	1	$\mathbf{V}_0^1$	0	0

ON. Accordingly, the  $\mathbf{V}_n$  vector can be expressed as follows:

$$\mathbf{V}_n = \frac{1}{3} V_{dc} [(2S_a^* - 1) + \exp(j2\pi/3)(2S_b^* - 1) + \exp(-j2\pi/3)(2S_c^* - 1)]. \quad (2)$$

Substituting different conduction states in (2) gives eight possible output voltage vectors with the following discrete description:

$$\begin{cases} \mathbf{V}_n = \frac{2}{3} V_{dc} \exp(j(k-1)2\pi/3), & k = 1, 2, \dots, 6 \\ \mathbf{V}_0^0 = \mathbf{V}_0^1 = 0. \end{cases} \quad (3)$$

Based on (3), the inverter output voltage includes six nonzero vectors ( $\mathbf{V}_1 - \mathbf{V}_6$ ) and two zero vectors ( $\mathbf{V}_0^0, \mathbf{V}_0^1$ ), as given in Table I and graphically presented in Fig. 1(b).

## III. PRINCIPLE OF VECTOR-BASED CURRENT CONTROLLER

Implementing Kirchhoff's voltage law in Fig. 1(a) results in

$$\begin{cases} \frac{di_a}{dt} = \frac{1}{3L} [2(v_a - e_a) - (v_b - e_b) - (v_c - e_c)] - \frac{R}{L} i_a \\ \frac{di_b}{dt} = \frac{1}{3L} [2(v_b - e_b) - (v_a - e_a) - (v_c - e_c)] - \frac{R}{L} i_b \\ \frac{di_c}{dt} = \frac{1}{3L} [2(v_c - e_c) - (v_a - e_a) - (v_b - e_b)] - \frac{R}{L} i_c. \end{cases} \quad (4)$$

The vector representation of (4) can be obtained using (1), as follows:

$$\frac{d\mathbf{i}_o}{dt} = \frac{1}{L} (\mathbf{V}_n - \mathbf{e}_o) - \frac{R}{L} \mathbf{i}_o \quad (5)$$

where  $\mathbf{i}_o$  is the output current vector and  $\mathbf{e}_0$  is the counter-emf voltage vector. By defining  $\mathbf{i}_{ref}$  as the current command vector and  $\mathbf{i}_e$  as the current error vector

$$\mathbf{i}_e = \mathbf{i}_{ref} - \mathbf{i}_o. \quad (6)$$

From (5) and (6), the differential equation describing the current error vector is derived as follows:

$$L \frac{d\mathbf{i}_e}{dt} + R\mathbf{i}_e = L \frac{d\mathbf{i}_{ref}}{dt} + R\mathbf{i}_{ref} - (\mathbf{V}_n - \mathbf{e}_0). \quad (7)$$

It is observed from (7) that the current error vector ( $\mathbf{i}_e$ ) varies with  $L/R$  time constant and is influenced by the current command vector and its derivative ( $\mathbf{i}_{ref}$  and  $d\mathbf{i}_{ref}/dt$ ) as well as the inverter output voltage vector ( $\mathbf{V}_n$ ) and the counter-emf voltage vector ( $\mathbf{e}_0$ ). Neglecting  $R$  in (7), the desired inverter output voltage to achieve zero error can be defined by

$$\mathbf{V}_n^* = \mathbf{e}_0 + L \frac{d\mathbf{i}_{ref}}{dt}. \quad (8)$$

Rewriting (7) based on (8) leads to

$$L \frac{d\mathbf{i}_e}{dt} = \mathbf{V}_n^* - \mathbf{V}_n. \quad (9)$$

Based on (8) and (9), it can be seen that the information about the counter-emf voltage vector and the derivative of the current command vector are required to nullify the inverter tracking error. However, it is not practically easy to measure the counter-emf vector and the computation of derivatives is usually susceptible to noise.

Different vector-based methods apply various control strategies to address this problem. Suppose that the desired output voltage vector ( $\mathbf{V}_n^*$ ) is located in Sector I in Fig. 1(b). Based on (9), current error derivative vectors with respect to  $\mathbf{V}_0 - \mathbf{V}_6$  can be calculated, as shown in Fig. 2 [19], [20]. Small  $d\mathbf{i}_e/dt$  is required to follow the command vector with the minimum switching frequency. Thus, discrete voltage vectors adjacent to  $\mathbf{V}_n^*$  must be selected in order to obtain the desired optimal switching pattern (e.g.,  $\mathbf{V}_1, \mathbf{V}_2, \mathbf{V}_0^0$ , and  $\mathbf{V}_0^1$  for Sector I). In this way, the  $\mathbf{V}_0$  vector and adjacent nonzero voltage vectors are the only vectors selected by the inverter to reduce the tracking error. Accordingly, the proposed vector-based current controller generates a switching pattern similar to the well-known space-vector modulation (SVM) under steady-state condition. Note that to produce this optimal switching pattern, only the  $\mathbf{V}_n^*$  sector needs to be determined not the exact value of the vector. However, for fast tracking response during transient conditions, nonoptimal voltage vectors with high-current error derivatives must be applied to force the error vector into the hysteresis bands as fast as possible. This would provide a very fast transient response for the proposed vector-based current controller.

#### IV. VECTOR-BASED CURRENT CONTROL SCHEMES

The general block diagram of vector-based HCCs is shown in Fig. 3 [16]. It includes the following main parts: 1) a set of summing elements to compute the current error vector; 2) a set of comparators to define the tolerance region; 3) a switching table derived based on the applied control strategy; and 4) a

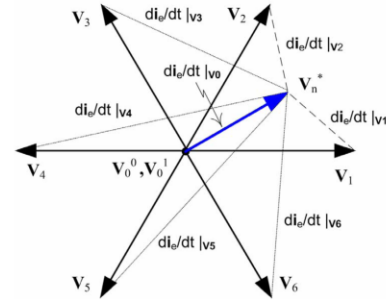


Fig. 2. Current error derivative vectors when the  $\mathbf{V}_n^*$  vector is located in Sector I.

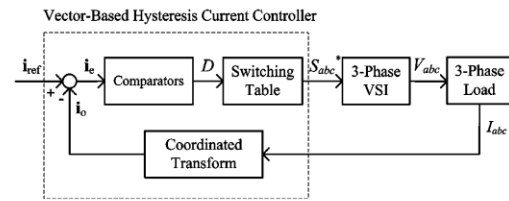


Fig. 3. General block diagram of vector-based HCCs.

coordinated transformation to convert three-phase current signals into the appropriate reference frame, when needed [16]. Reported vector-based methods are different in terms of the adopted reference frame, comparators' configuration, and the applied switching tables. The assigned tolerance region will be different accordingly. Most of the reported methods have used Clarke's transformation to convert the three-phase current signal into a space-vector represented in the stationary frame to eliminate the interphases dependency [14]–[18]. Although different hysteresis comparators and control strategies were used, the resulting tolerance region is identical for these methods. Therefore, the vector-based method presented in [14] is selected, as this group representative to be examined. A more complex sequential approach has been proposed in [16]. This can achieve further reduction in the inverter switching frequency, as will be discussed. However, Kwon *et al.* [19] and [20] suggested vector-based current controllers working in the three-phase  $abc$  frame. Since the comparators configuration, control strategies, and the consequent tolerance region are entirely different from other reported methods, the control technique proposed in [20] is also examined in this paper. To summarize, this section starts with presenting the conventional three-phase HCC as the base method, followed by studying the vector-based current controllers proposed by [14] and [20]. Finally, a new vector-based HCC will be suggested.

##### A. Conventional Three-Phase HCC

In this current controller, hysteresis bands of width  $\delta_{hys}$  are defined around each reference value of three-phase currents. Therefore, the inverter phase current will be controlled using a



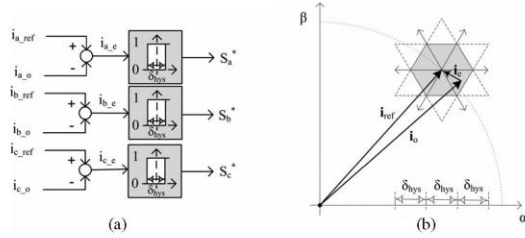


Fig. 4. Conventional HCC. (a) Schematic diagram. (b) Designated error surface.

two-level hysteresis comparator, as shown in Fig. 4(a). When the inverter current becomes greater (or less) than the reference value by the hysteresis band  $\delta_{hys}$ , the inverter leg in the corresponding phase is switched in the negative (or positive) direction. This gives a controller that is targeted to keep the current error within the hexagonal tolerance region shown in Fig. 4(b) [3]. At each instant, the hexagon center is pointed by the reference current vector, rotating around the origin of the  $\alpha - \beta$  frame with the fundamental frequency. Once the inverter current vector touches the hexagon surface (i.e., the error tends to exceed the  $\delta_{hys}$  band), the current controller will select the appropriate output voltage vector in order to force the output current back into the hexagon area.

However, in three-phase applications, there is a mutual interaction between phase currents if the load neutral is isolated. Due to this interphase dependency, when the conduction state of an inverter leg changes by the current controller, the resulting voltage vector will vary based on the conduction states of other two legs. This causes two major problems: unnecessary high-switching frequencies at low counter-emf voltage and the current error exceeding twice the permitted hysteresis band ( $2\delta_{hys}$ ), shown by the dashed area in Fig. 4(b) [3].

### B. Vector-Based HCC Method I

Kazmierkowski *et al.* [14] suggested a vector-based HCC to avoid the drawbacks of the conventional hysteresis method. Interphases dependency is removed using the vector representation of three-phase current signals in the stationary  $\alpha - \beta$  frame. The proposed current controller includes two three-level hysteresis comparators integrated with a switching table, as shown in Fig. 5(a). The overall bandwidth of three-level hysteresis comparators is equal to  $\delta + \Delta\delta$ . With the switching table given in Table II, this vector-based method limits the current error within the square tolerance region shown in Fig. 5(b). Squares centers are pointed by the reference current vector at each instant. If the inverter current touches a surface of the squares, the inverter output voltage will be selected according to Table II in order to force the error back inside the designated tolerance region. This vector-based method noticeably reduces the inverter switching frequency by the systematic utilization of zero voltage vectors. However, the presence of redundant situations in the control action can lead to nonoptimal switching pattern in some occasions.

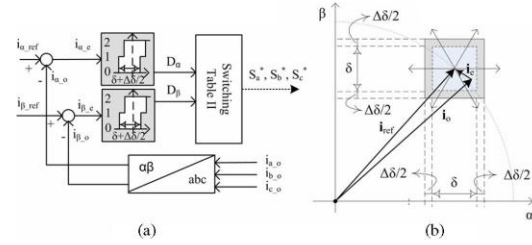


Fig. 5. Vector-based HCC method I. (a) Schematic block diagram. (b) Designated error surface.

TABLE II  
SWITCHING TABLE OF THE VECTOR-BASED HCC METHOD I

$D_\alpha \backslash D_\beta$	0	1	2
0	$V_2$	$V_1$	$V_6$
1	$V_2$ or $V_3$	$V_0$	$V_5$ or $V_6$
2	$V_3$	$V_4$	$V_5$

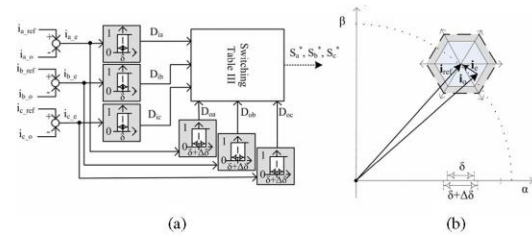


Fig. 6. Vector-based HCC method II. (a) Schematic block diagram. (b) Designated error surface.

### C. Vector-Based HCC Method II

Kwon *et al.* [20] proposed a vector-based HCC using a region detector. Two sets of hysteresis comparators are employed in the three-phase  $abc$  frame, as shown in Fig. 6(a). Outer comparators with bandwidth of  $\delta + \Delta\delta$  determine the position of the desired voltage vector ( $V_n^*$ ). That is, they define the optimal set of voltage vectors to be applied. Then, inner hysteresis comparators with narrow band of  $\delta$  track the command current by the appropriate selection of the inverter output voltage from the optimal voltage vectors confined by the region detector. The employed switching table is given in Table III, which leads to the tolerance region shown in Fig. 6(b). While the current error vector is kept inside the inner hexagonal tolerance region for most of the time, it moves toward the outer hexagon bands when the region of  $V_n^*$  varies. Once the outer band is touched, the change in  $V_n^*$  region will be detected and error current will be forced back again inside the inner hexagonal tolerance region. This vector-based works with current signals represented in the three-phase  $abc$  frame; thus the oscillations of load current vector in the coordinated  $\alpha - \beta$  frame cannot be removed effectively.

TABLE III  
SWITCHING TABLE OF THE VECTOR-BASED HCC METHOD II

$D_{a1} D_{a2} D_{a3} D_{a4}$	000	001	010	100	011	101	110	111
100	$V_0^1$	$V_0^1$	$V_0^1$	$V_1$	$V_0^1$	$V_6$	$V_2$	$V_0^1$
110	$V_0^0$	$V_0^0$	$V_2$	$V_1$	$V_0^0$	$V_0^0$	$V_2$	$V_0^0$
010	$V_0^1$	$V_0^1$	$V_3$	$V_0^1$	$V_4$	$V_0^1$	$V_2$	$V_0^1$
011	$V_0^0$	$V_3$	$V_3$	$V_0^0$	$V_4$	$V_0^0$	$V_0^0$	$V_0^0$
001	$V_0^1$	$V_3$	$V_0^1$	$V_0^1$	$V_4$	$V_6$	$V_0^1$	$V_0^1$
101	$V_0^0$	$V_3$	$V_0^0$	$V_1$	$V_0^0$	$V_6$	$V_0^0$	$V_0^0$

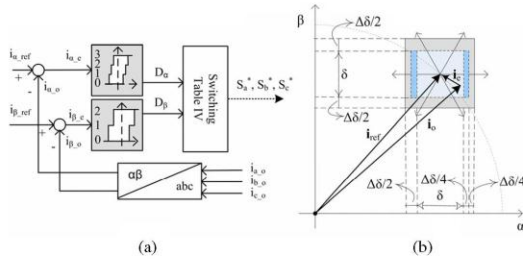


Fig. 7. Proposed vector-based HCC method III. (a) Schematic block diagram. (b) Designated error surface.

D. Proposed Vector-Based HCC Method III

This paper presents a new vector-based current controller using multilevel hysteresis comparators. The proposed method is developed based on the fact that if the actual inverter current crosses the tolerance region on one side, a new voltage vector with the opposite component on that side must be applied. That is, if the actual current crosses the top (or left) side of the tolerance region, the next inverter voltage vector must have a smaller  $\beta$ -component (or a larger  $\alpha$ -component) to keep the tracking error inside the tolerance region. For instance, suppose that the desired voltage vector ( $V_n^*$ ) is located in Sector I, and both  $i_{e,\alpha} = i_{ref,\alpha} - i_{o,\alpha}$  and  $i_{e,\beta} = i_{ref,\beta} - i_{o,\beta}$  hit upper hysteresis bands. This means that the inverter output current vector tends to exceed the tolerance region from the bottom-left side; thus the next voltage vector with positive  $\alpha$  and  $\beta$  components ( $V_2$ ) needs to be applied to force the inverter current back inside the designated tolerance region. Similarly, the  $V_1$  vector with positive  $\alpha$  component must be selected if the inverter current vector touches the left side of the assigned tolerance region. The switching logic of the proposed current controller must select zero voltage vectors in other cases in order to achieve the desired optimal switching pattern.

According to Table I,  $\alpha$  and  $\beta$  components of the inverter output voltage can have four and three values for nonzero voltage vectors, respectively. This can be used to divide the complex  $\alpha - \beta$  frame into six  $60^\circ$  sectors, as displayed in Fig. 1(b). Therefore, the proposed current controller implements four-level and three-level comparators in  $\alpha$  and  $\beta$  axes, as shown in Fig. 7(a). The practical implementation of the four-level hysteresis comparators with the overall bandwidth of  $\delta + \Delta\delta$  is illustrated in Fig. 8.

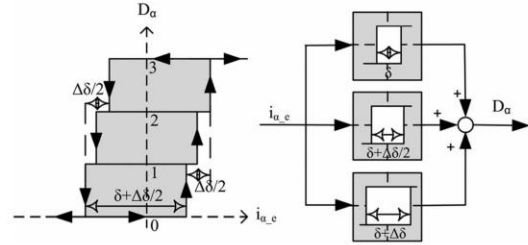


Fig. 8. Schematic block diagram of the four-level hysteresis comparator.

TABLE IV  
SWITCHING TABLE OF THE PROPOSED VECTOR-BASED HCC METHOD III

$D_\alpha \backslash D_\beta$	0	1	2
0	$V_5$	$V_4$	$V_3$
1	$V_5$	$V_0$	$V_3$
2	$V_6$	$V_0$	$V_2$
3	$V_6$	$V_1$	$V_2$

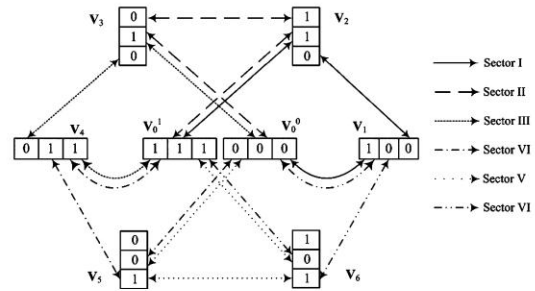


Fig. 9. VSI switching pattern for the proposed vector-based HCC method III.

The selection of bandwidths of the hysteresis comparators greatly depends on the accuracy requested from the current controller. Smaller hysteresis bands give more restricted oscillations of the inverter current around the reference signal, but it is achieved at the expense of higher switching frequency. Thus, there is always a tradeoff between the current controller accuracy and the resulting switching frequency. Simulation studies need to be conducted to achieve the optimized performance, since depending on the load parameters, there is always a minimum bandwidth behind that the vector-based HCC cannot generate the expected optimal switching pattern.

At each instant, digital outputs of the hysteresis comparators ( $D_\alpha$  and  $D_\beta$ ) determine the discrete state of the inverter output voltage according to Table IV. If a comparator output varies, the inverter output voltage changes accordingly in order to reduce the corresponding component of the error vector. Thereby, the current error is always kept inside the square tolerance region shown in Fig. 7(b). Note that depending on the  $V_n^*$  sector, the tolerance region will be selected from two internal regions and the external region shown in Fig. 7(b). For every one sixth of the fundamental period, both  $\alpha$  and  $\beta$  comparators remain in specific

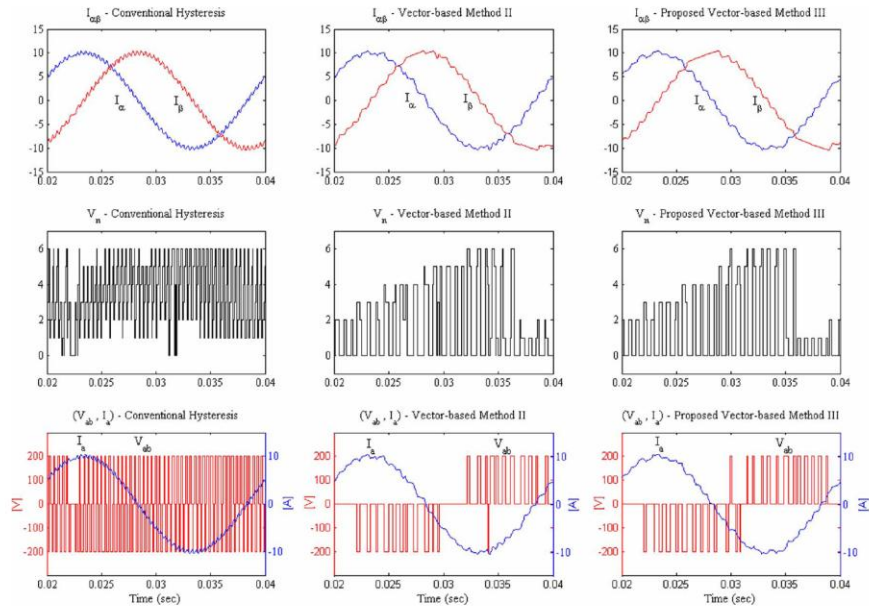


Fig. 10.  $I_{\alpha-\beta}$ ,  $V_n$ ,  $I_a$ , and  $V_{ab}$  for small counter-emf voltage ( $R = 0.7 \Omega$ ,  $L = 5 \text{ mH}$ , and  $e_o = 25 \angle 60^\circ$ ).

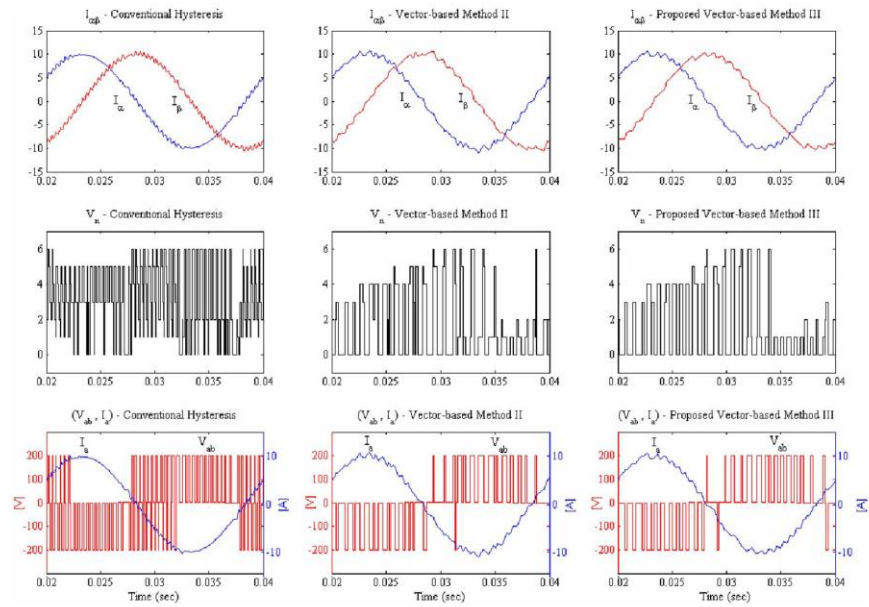


Fig. 11.  $I_{\alpha-\beta}$ ,  $V_n$ ,  $I_a$ , and  $V_{ab}$  for large counter-emf voltage ( $R = 0.7 \Omega$ ,  $L = 5 \text{ mH}$ , and  $e_o = 75 \angle 60^\circ$ ).



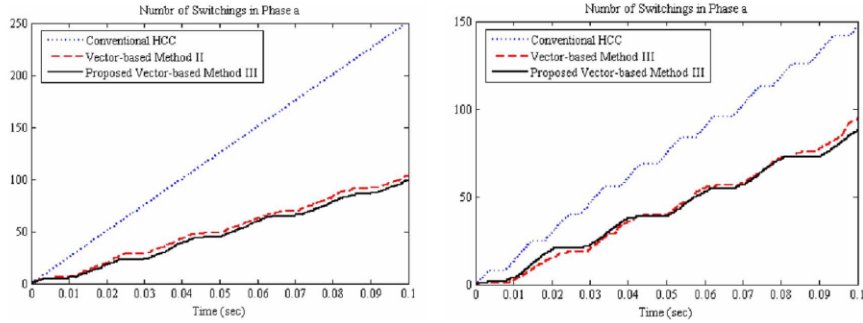


Fig. 12. (a) Number of switching with small counter-emf voltage. (b) Number of switching with large counter-emf voltage.

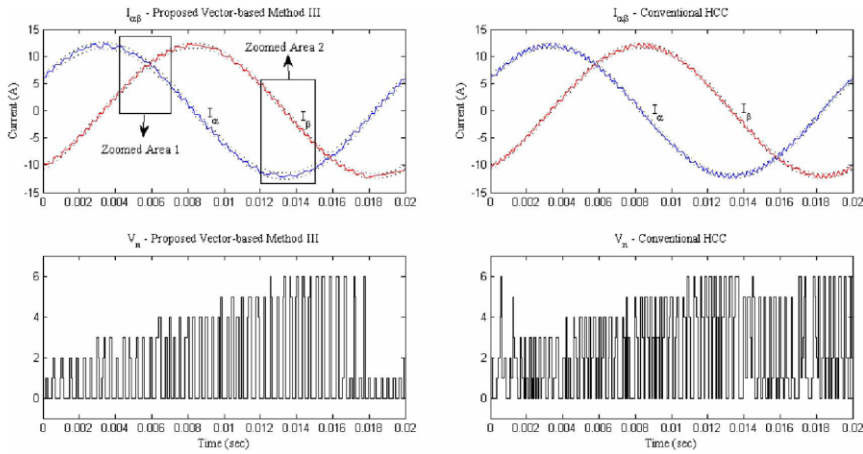


Fig. 13.  $I_{\alpha-\beta}$  and  $V_n$  for the (a) proposed vector-based HCC method III and (b) conventional HCC.

hysteresis comparator loops, which determines the position of the desired output voltage vector ( $\mathbf{V}_n^*$ ). In this time period, only zero voltage vectors and two nonzero voltage vectors adjacent to  $\mathbf{V}_n^*$  will be selected by the controller. For instance, as long as  $\mathbf{V}_n^*$  is located in Sector V,  $D_\alpha$  and  $D_\beta$ , respectively, remain in the middle and the lowest hysteresis loops ( $D_\alpha = 1$  or 2 and  $D_\beta = 0$  or 1), and the optimal voltage set of  $\mathbf{V}_0^0$ ,  $\mathbf{V}_0^1$ ,  $\mathbf{V}_5$ , and  $\mathbf{V}_6$  is selected to be applied. In this case, the current error is kept inside the rectangular tolerance region shown in Fig. 7(b). Once the inverter current vector hits the hysteresis band of either  $\alpha$  or  $\beta$  component, the corresponding comparator will move to the next loop. Thereby, the change of  $\mathbf{V}_n^*$  position to the next sector is detected, and a new optimal switching set will be selected according to the Table IV.

The overall switching pattern generated based on this control strategy is shown in Fig. 9. It is observed that the proposed method gives a switching pattern constituted of six consecutive four-state optimal voltage vectors sets, which matches with six  $60^\circ$  sectors of a fundamental period. The inverter switching frequency is significantly reduced by the systematic

implementation of zero and nonzero voltage vectors, similar to the SVM technique. Furthermore, where the zero state is to be applied, the  $\mathbf{V}_0^0$  vector will be chosen if the present inverter voltage is equal to  $\mathbf{V}_1$ ,  $\mathbf{V}_3$ , or  $\mathbf{V}_5$ . In this case, only one inverter leg must be switched. Likewise,  $\mathbf{V}_0^1$  will be selected if the inverter state is coming from  $\mathbf{V}_2$ ,  $\mathbf{V}_4$ , or  $\mathbf{V}_6$ . This yields further reduction of switching frequency, as suggested by [16].

A set of simulation studies is conducted to examine the wide-ranging behavior of the proposed vector-based HCC at extreme modulation indexes. Fig. 10 shows the VSI output current/voltage vectors as well as the inverter phase signals when the machine is running close to the synchronous speed (very low counter-emf voltage). Simulation results are given for the conventional HCC, the vector-based method II, and the proposed vector-based method III. It can be seen that the inter-phases dependency in the conventional method causes predominantly oscillating currents associated with an irregular switching pattern. In contrast, vector-based methods (specially the proposed method) manage to noticeably suppress current vector

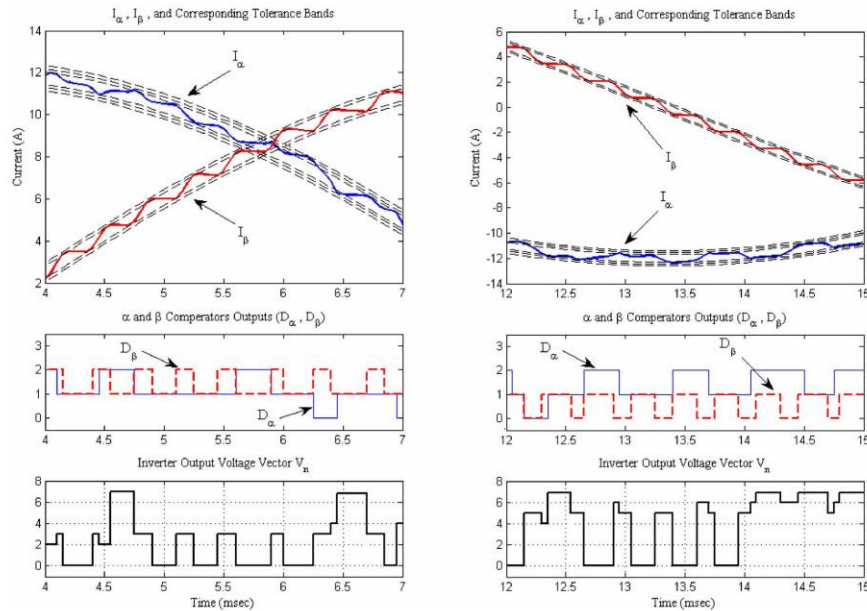


Fig. 14. Detailed operation of the proposed vector-based HCC for the zoomed areas.

oscillations through the systematic application of zero voltage vectors in the VSI switching pattern and the consequent phase voltage. This will significantly reduce the VSI switching frequency, as shown in Fig. 12(a). Similar simulation results for the high counter-emf voltage (very large slips) are presented in Figs. 11 and 12(b). In this case, the counter-emf vector ( $\mathbf{e}_0$ ) effectively counteracts  $\mathbf{V}_n$  in (7); thus, a reduced oscillating output current with a more regular switching pattern is generated by the conventional HCC. Identical observations, though less noticeable, can be made for the vector-based current controllers. It is therefore concluded that the improvement achieved by the proposed vector-based method is more significant under low counter-emf values and the switching frequency reduces as the motor slip increases.

#### V. SIMULATION STUDIES

Simulation studies are carried out in two main directions: verifying the validity of the proposed current controller and comparing its performance with other reported vector-based methods. The circuit diagram shown in Fig. 1 is simulated in MATLAB/Simulink with parameters given in Appendix I.

First, the sinusoidal three-phase command signal is set to 15 A, and the tolerance region is formed with  $\delta = 0.3$  A and  $\Delta\delta = 0.1$  A. These parameters are set with a compromise between the accuracy of the controller and the resulting switching frequency. Simulation results show that with the selected hysteresis bandwidths, the current control accuracy, and the inverter switching frequency are satisfactorily equal to 2.5% and 2400 Hz. The inverter output current vector and the switch-

TABLE V  
SWITCHING FREQUENCIES (IN HERTZ)

Method	SW <sub>a</sub>	SW <sub>b</sub>	SW <sub>c</sub>	$f_{sw,avg}$	SUF %
Conventional HCC	3320	3320	3319	3320	0
Method I	2812	3071	2345	2743	14.5
Method II	2381	2379	2376	2379	0
Method III	2441	2209	2048	2233	8.0

ing pattern are shown in Fig. 13(a). For the sake of clarity,  $\mathbf{V}_0^0$  and  $\mathbf{V}_0^1$  are both depicted by  $\mathbf{V}_n = 0$ , and only outer hysteresis bands are shown. Fig. 13(b) presents similar waveforms for the conventional HCC. Since the inverter error in the conventional method reaches twice of the permitted hysteresis band, the tolerance region is formed with  $\delta_{hys} = 0.5(\delta + \Delta\delta) = 0.2$  A to achieve the same current control accuracy. Comparing Fig. 13(a) and 13(b), it is clear that the proposed vector-based method keeps  $\mathbf{I}_{\alpha-\beta}$  inside the tolerance region with fewer changes of the inverter output voltage, i.e., a more regular switching pattern.

Fig. 14 illustrates detailed operation of the proposed vector-based method for two areas zoomed in Fig. 13(a), where  $I_\alpha$  and  $I_\beta$  are located in the peak and zero-crossing points and where these signals are both in the middle. The  $\mathbf{V}_0^1$  vector is shown as  $\mathbf{V}_7$  to visualize the influence of the present nonzero voltage vector on the next zero voltage vector. For  $4 < t < 6.25$  ms,  $\alpha$  and  $\beta$  comparators are located in the middle and top hysteresis loops, respectively, which indicates the position of  $\mathbf{V}_n^*$  in Sector II. Therefore, the optimal voltage set of  $\mathbf{V}_2, \mathbf{V}_3, \mathbf{V}_0^0$ , and  $\mathbf{V}_0^1$  is selected to be applied. At  $t = 6.25$  ms,  $\mathbf{V}_n^*$  location moves from Sector II to Sector III, since the digital output of the



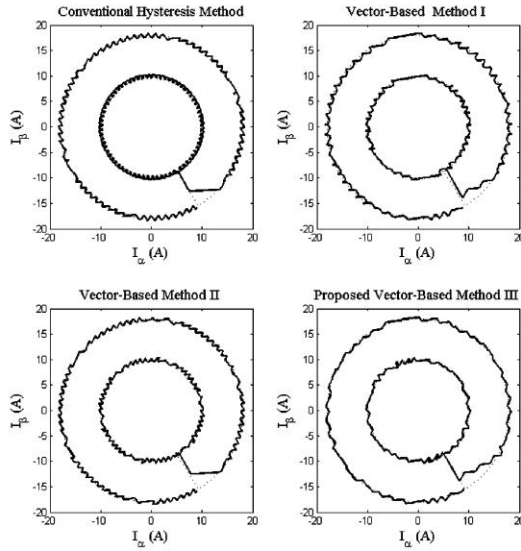


Fig. 15. Load current trajectory ( $I_{\alpha,\beta}$ ) for the conventional three-phase HCC, vector-based method I, method II, and proposed method III.

$\alpha$ -comparator varies from the middle to the lowest hysteresis loop. Thereafter, the optimal voltage set of  $V_3$ ,  $V_4$ ,  $V_0^0$ , and  $V_0^1$  is selected to be applied by the inverter. For  $12.5 < t < 15$  ms, the  $V_n^*$  vector is located at Sector V and optimal voltage set of  $V_5$ ,  $V_6$ ,  $V_0^0$ , and  $V_0^1$  is selected, as shown in Fig. 14(b). It is thus demonstrated that the proposed vector-based method can limit the error vector inside the assigned tolerance region throughout the fundamental period, using an optimal switching pattern.

To compare the steady-state and transient performance of the proposed current controller with other reported vector-based methods, a command current with a step change from 10 to 18 A at  $t = 20$  ms is applied. Fig. 15 shows the load current trajectory for different control schemes. It can be seen that the vector-based method I and the proposed method (method III) can considerably suppress load current oscillations in the  $\alpha - \beta$  frame. The best current trajectory with smallest oscillations around the command signal is obtained by the proposed method (see Fig. 16). In contrast, current oscillations cannot be effectively suppressed using the vector-based method II as it works with current signals represented in the three-phase  $abc$  system. This does not guarantee a coordinated control of load current vector in the  $\alpha - \beta$  frame. The superior transient behavior of the conventional HCC is retained by all vector-based methods. That is, all vector-based methods follow the command signal in less than 1 ms (equal to  $18^\circ$  in the complex frame). This important advantage is achieved by the application of nonoptimal voltage vectors with high current error derivatives during transient conditions.

Fig. 14 shows that all controllers successfully limit the current error inside their assigned tolerance regions. As expected, the

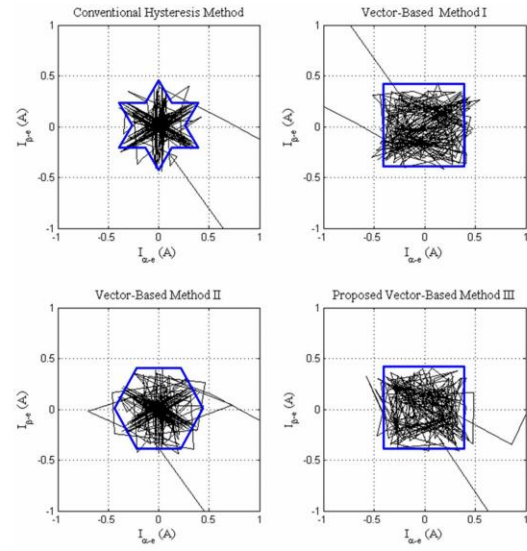


Fig. 16. Current error trajectory ( $I_{\alpha,\beta-e}$ ) for the conventional three-phase HCC, vector-based method I, method II, and proposed method III.

inverter error for the conventional HCC reaches  $2\delta_{\text{hys}} = 0.4$  A because of the interphases dependency. Note that in Fig. 14, the few observed violations from the tolerance region are related to the negligible transient time that takes for current controllers to follow the step change of command signal. The switching frequency of the inverter controlled by different methods is reported in Table V. It is clear that all vector-based methods achieve considerable reduction in the inverter switching frequency and among them, the proposed method presents the minimum switching frequency with 30% reduction. Almost a third of the reduction in the switching frequency for methods II and III is contributed from the appropriate selection of the zero voltage vector, which can be also implemented in method I [16]. Furthermore, switching frequencies in various inverter legs are not equal in methods I and III, since they control the current in stationary  $\alpha - \beta$  frame not in three-phase  $abc$  frame. Defining the switching unbalance factor (SUF) as follows:

$$\text{SUF}\% = \max \left| f_{\text{sw,avg.}} - \frac{S_i}{f_{\text{sw,avg.}}} \right| \times 100 \quad i = a, b, c \quad (10)$$

it can be seen that the SUF is quite high for method I. This causes unequal heating of three-phase inverter legs due to unbalanced switching losses.

Fig. 17 shows the frequency spectra of the inverter phase current, where the conventional HCC and the proposed vector-based method are implemented. It is observed that the resulting harmonic components are spread over a wide frequency range, but their amplitudes are well below the permitted limits. Total harmonic distortion (THD) is equal to 3% for the proposed vector-based method, which slightly increases for the conventional HCC. Note that the proposed vector-based method

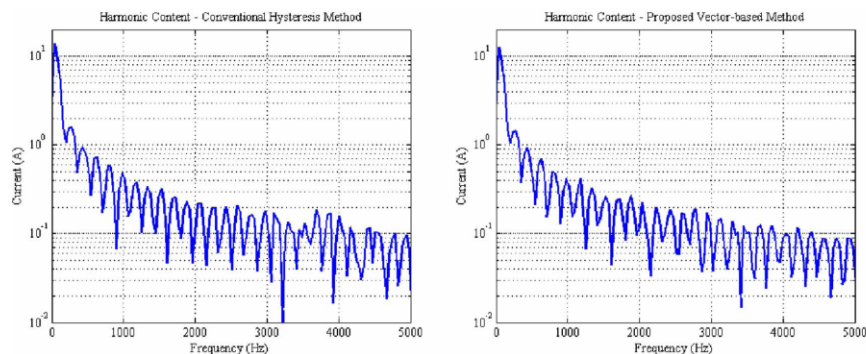
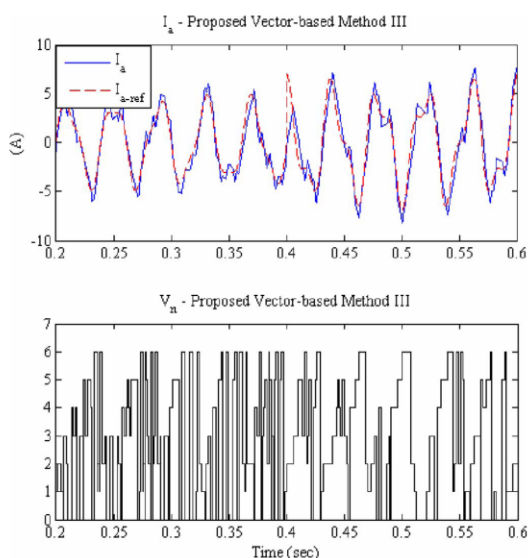
Fig. 17. Harmonic contents of the phase  $a$  inverter current.

Fig. 18. Operation of the proposed vector based method in an APF application.

suppresses current vector oscillations in the complex  $\alpha - \beta$  frame, which does not guarantee a significant improvement in the harmonic content of the inverter phase current. However, the proposed vector-based method gives a moderately enhanced harmonic content, as shown in Fig. 17.

Finally, the proposed vector-based method is used to track a highly nonsinusoidal command signal. This can further examine the performance of the proposed current controller in more demanding applications, such as active power filters (APFs). As shown in Fig. 18, the command signal includes 5th and 11th harmonic components with step changes at  $t = 0.4$  s. It is observed that the proposed method exhibits an excellent tracking performance that keeps the inverter current within the designated hysteresis bands ( $\delta = 0.4$  A and  $\Delta\delta = 0.2$  A). In the generated switching pattern, the  $V_n^*$  position rotates several times faster than the fundamental frequency as the command signal includes

higher order frequency components. Very fast transient behavior of the proposed method can be seen at  $t = 0.4$  s, where the inverter output current follows the command step-change within 10 ms.

## VI. CONCLUSION

In this paper, a new vector-based HCC was presented for three-phase PWM-VSIs. The proposed method implements two multilevel hysteresis comparators in the  $\alpha$ - and  $\beta$ -axes to divide the stationary complex frame into six  $60^\circ$  sectors. The position of the desired voltage vector will be determined based on the digital outputs of hysteresis comparators, which is needed to achieve an optimal switching pattern. At each instant, the inverter output voltage is selected from four voltage vectors: two nonzero vectors adjacent to the desired voltage vector and two zero voltage vectors. In this way, the proposed vector-based method significantly reduces the inverter switching frequency and keeps the current error inside a square tolerance region. Further reduction of the switching frequency is achieved by the systematic selection of the appropriate zero-voltage vector based on the previous state of the inverter.

Simulation results illustrated the considerable improvement achieved by the proposed current controller. It was also shown that the proposed method is superior to other reported vector-based methods. That is, the proposed controller gives the smallest output current oscillations with the lowest switching frequency (almost 30% reduction compared to the conventional method). It finally was observed that vector-based methods exhibit a very fast transient response similar to the conventional HCC.

## APPENDIX I

Squirrel-cage induction motor parameters as follows:

10 hp, 220 V, 1470 r/min, 50 Hz, three-phase, four poles.

Stator Parameter—resistance: 0.68  $\Omega$ , leakage inductance: 0.005 H;

Rotor Parameter—resistance: 0.45  $\Omega$ , leakage inductance: 0.0025 H;

Magnetizing inductance: 0.1486 H.

DC-link voltage: 200 V.

## REFERENCES

- [1] M. P. Kazmierkowski and L. Malesani, "Current control techniques for three-phase voltage-source PWM converters: A survey," *IEEE Trans. Ind. Electron.*, vol. 45, no. 5, pp. 691–703, Oct. 1998.
- [2] D. M. Brod and D. W. Novotny, "Current control of VSI-PWM inverters," *IEEE Trans. Ind. Appl.*, vol. IA-21, no. 3, pp. 562–570, May/Jun. 1985.
- [3] S. Buso, L. Malesani, and P. Mattavelli, "Comparison of current control techniques for active filter Applications," *IEEE Trans. Ind. Electron.*, vol. 45, no. 5, pp. 722–729, Oct. 1998.
- [4] A. Tripathi and P. C. Sen, "Comparative analysis of fixed and sinusoidal band hysteresis current controllers for voltage source inverters," *IEEE Trans. Ind. Electron.*, vol. 39, no. 1, pp. 63–73, Feb. 1992.
- [5] K. M. Rahman, M. R. Khan, M. A. Choudhury, and M. A. Rahman, "Variable band hysteresis current controllers for PWM voltage source inverters," *IEEE Trans. Power Electron.*, vol. 12, no. 6, pp. 964–970, Nov. 1997.
- [6] B. K. Bose, "An adaptive hysteresis-band current control technique of a voltage-fed PWM inverted for machine drive system," *IEEE Trans. Ind. Electron.*, vol. 37, no. 5, pp. 402–408, Oct. 1990.
- [7] L. Malesani and P. Tenti, "A novel hysteresis control method for current controlled VSI PWM inverters with constant modulation frequency," *IEEE Trans. Ind. Appl.*, vol. 26, no. 1, pp. 88–92, Jan./Feb. 1990.
- [8] L. Malesani, L. Rossetto, L. Sonaglioni, P. Tomasin, and A. Zuccato, "Digital adaptive hysteresis current control with clocked commutations and wide operating range," *IEEE Trans. Ind. Appl.*, vol. 32, no. 2, pp. 1115–1121, Mar./Apr. 1996.
- [9] L. Malesani, P. Mattavelli, and P. Tomasin, "Improved constant-frequency hysteresis current control for VSI inverters with simple feedforward bandwidth prediction," *IEEE Trans. Ind. Appl.*, vol. 33, no. 5, pp. 1194–1202, Sep./Oct. 1997.
- [10] P. N. Tekwani, R. S. Kanchan, and K. Gopakumar, "Novel current error space phasor based hysteresis controller using parabolic bands for control of switching frequency variations," *IEEE Trans. Ind. Electron.*, vol. 54, no. 5, pp. 2648–2656, Oct. 2007.
- [11] S. Buso, S. Fasolo, L. Malesani, and P. Mattavelli, "A dead-beat adaptive hysteresis current control," *IEEE Trans. Ind. Appl.*, vol. 36, no. 4, pp. 1174–1180, Jul./Aug. 2000.
- [12] R. R. Ramos, D. Biel, E. Fossas, and F. Guinjoan, "A fixed-frequency quasi-sliding control algorithm: Application to power inverters design by means of FPGA implementation," *IEEE Trans. Power Electron.*, vol. 18, no. 1, pp. 344–355, Jan. 2003.
- [13] W. Stefanutti and P. Mattavelli, "Fully digital hysteresis modulation with switching-time prediction," *IEEE Trans. Ind. Appl.*, vol. 42, no. 3, pp. 763–769, May/Jun. 2006.
- [14] M. P. Kazmierkowski, M. A. Dzieciakowski, and W. Sulkowski, "Novel space-vector based current controllers for PWM-inverters," *IEEE Trans. Power Electron.*, vol. 6, no. 1, pp. 158–166, Jan. 1991.
- [15] C. T. Pan and T. Y. Chang, "An improved hysteresis current controller for reducing switching frequency," *IEEE Trans. Power Electron.*, vol. 9, no. 1, pp. 97–104, Jan. 1994.
- [16] A. Tilli and A. Tonielli, "Sequential design of hysteresis current controller for three-phase inverter," *IEEE Trans. Ind. Electron.*, vol. 45, no. 5, pp. 771–781, Oct. 1998.
- [17] J. F. A. Martins, A. J. Pires, and J. F. Silva, "A novel and simple current controller for three-phase PWM power inverters," *IEEE Trans. Ind. Electron.*, vol. 45, no. 5, pp. 802–805, Oct. 1998.
- [18] E. Aldabas, L. Romeral, A. Arias, and M. G. Jayne, "Software-based digital hysteresis-band current controller," in *Proc. Electric Power Appl.*, Mar. 2006, pp. 184–190.
- [19] B.-H. Kwon, T.-W. Kim, and J.-H. Youn, "A novel SVM-based hysteresis current controller," *IEEE Trans. Power Electron.*, vol. 13, no. 2, pp. 297–307, Mar. 1998.
- [20] B.-H. Kwon, B.-D. Min, and J.-H. Youm, "An improved space-vector-based hysteresis current controller," *IEEE Trans. Ind. Electron.*, vol. 45, no. 5, pp. 752–760, Oct. 1998.



**Mansour Mohseni** (S'09) received the B.Sc. and M.Sc. degrees in electrical engineering from Shahid Chamran University, Ahwaz, Iran, in 2004 and 2007, respectively. He is currently working toward the Ph.D. degree from Curtin University of Technology, Perth, Australia.

His current research interests include wind power generation, grid integration of renewable energy systems, and power electronics.



**Syed M. Islam** (S'82–M'89–SM'93) received the B.Sc., M.Sc., and Ph.D. degrees from King Fahd University of Petroleum and Minerals, in 1979, 1983, and 1988, respectively, all in electrical power engineering.

He is currently the Chair Professor in electrical power engineering and Head of Department of Electrical and Computer Engineering, Curtin University of Technology, Perth, Australia. He has authored or coauthored more than 170 technical papers.

His research interests include condition monitoring of transformers, wind energy conversion, power quality and harmonics, and power systems.

Dr. Islam was the recipient of the IEEE T Burke Haye's Faculty Recognition Award in 2000. He has been a Keynote Speaker and an Invited Speaker at many international workshops and conferences. He is the current Vice-Chair of the Australasian Committee for Power Engineering and a member of the Board of Directors of the Australian Power Academy. He is a Fellow of the Engineers Australia, a Senior Member of the IEEE Industry Applications Society, Power Engineering Society, Dielectrics and Electrical Insulation Society, a Fellow of the Institution of Engineering and Technology, and a Chartered Engineer in the United Kingdom. He is a Regular Reviewer for the IEEE TRANSACTIONS ON ENERGY CONVERSION AND POWER DELIVERY. He is an Editor of the IEEE TRANSACTION ON SUSTAINABLE ENERGY.